UNIVERSITY OF LONDON THESIS

Degree PhD Year 2007 Name of Author BURNSIDE, Paul William

Mass spectrometric studies of dication reactions

by

Paul William Burnside

A thesis submitted for the degree of Doctor of Philosophy

to the

University of London

in

2007

Gas Phase Ion Chemistry Group,
Christopher Ingold Laboratories,
University College London.

ProQuest LLC
789 East Eisenhower Parkway
P.O. Box 1346
Ann Arbor, MI 48106-1346

With thanks to all those I have worked with over the years at University College, and particularly of course to Steve Price.

Abstract

This thesis describes work conducted using a linear time-of-flight (TOF) mass spectrometer concerning the gas phase reactivity of atomic and small molecular doubly charged positive ions (dications) with neutral species at low collision energies (below 20 eV).

The process of analysis by which measured ion intensities gathered using this instrument are converted into reaction cross-sections is completely redeveloped, permitting for the first time the cross-sections of all ionic products of bimolecular reactions to be derived. The new methodology calculates reaction cross-sections in arbitrary units; furthermore the absolute size of these arbitrary units depends only on the absolute value of the number density distribution of the neutral reactant and thus is independent of collision energy and changes from one collision system to another only due to differences in the effusive properties of the neutral reactant.

While a number of collision systems have been observed, three were selected for more rigorous study: SF^{2+} + Ar, Cl^{2+} + CO and HCl^{2+} + CO, and these are reported herein. The first and second of these collisions are particularly novel because their chemistry includes reaction channels that produce a doubly charged product containing new chemical bonds (ArS^{2+} and CCl^{2+} respectively). This class of dication-neutral reaction is highly unusual and only a very limited number of examples have been reported previously. The chemistry of HCl^{2+} with CO, while bearing similarities to that of Cl^{2+}, also exhibits proton transfer (to form HCO^{+}) that occurs with a branching ratio similar to electron transfer. The new procedure of analysis is applied to each system, allowing calculation of the reaction cross-sections for all charged products and is demonstrated to perform suitably well. The mechanism of electron transfer in dication-neutral systems is well understood, and computational calculations are conducted to complement the experimental results, but consideration of energetics also allows the observation of bond-forming products to be rationalized.

The development of a more satisfactory means of extracting reaction cross-sections from experimental measurements, while an achievement, has highlighted a number of shortcomings in the present experimental design and a number of suggestions have also been made for a future upgrade of the experiment that would facilitate simpler analysis as well as improved resolution and flexibility.

Declaration

I, Paul William Burnside, confirm that the work presented in this thesis is my own. Where information has been derived from other sources, I confirm that this has been indicated in the thesis.

Publications

The following publications are based on work discussed in this thesis:

Electron transfer and bond-forming reactions following collisions of SF^{2+} *with Ar* International Journal of Mass Spectrometry 249: 279 (2006)

Electron transfer and bond-forming reactions following collisions of Cl^{2+} *and* HCl^{2+} *with Ar* Physical Chemistry Chemical Physics DOI:10.1039/b704645f (2007)

Definition of axes

Throughout this thesis, reference is frequently made to the directions x, y and z. Since the setting is in most cases a TOF mass spectrometer, unless stated otherwise these directions are defined in the laboratory frame as follows:

i) the z-axis is defined as being the direction of flight and coincident with the axis of cylindrical symmetry of the spectrometer;

ii) the x-axis is defined as the direction of the incident ion beam when injected orthogonally in crossed-beam experiments (as is the case for the experiment described in this thesis);

iii) the y-axis is the third mutually perpendicular direction, along which the neutral reactant is introduced in crossed-beam experiments;

iv) the origin is taken to be the centre (in all three directions) of the source region of the spectrometer.

Contents

Chapter 1: Introduction

1.1 The study of the bimolecular reactivity of gas phase dications

Dications are doubly positively charged atomic or molecular species and possess markedly different properties to singly charged cations. Monocations have been studied extensively for many years and a great deal is known both about their structure and reactivity.[1-18] Monocations play important roles as reactive species in a range of environments, including planetary atmospheres, the interstellar medium and etching plasmas. In the interstellar medium for instance, ion-neutral reactions are key, because, due the induction of dipoles in neutral species by charged species, their rate increases, rather than decreases, at low temperatures.[19,20] Wherever monocations occur, dications will normally also be present but usually in far lower abundances. It is perhaps partly the low abundance of naturally-occurring dications and partly the frequent instability of doubly charged species that explains the scarcity of research into doubly charged cations in comparison to their singly charged analogues. Indeed, when modelling the behaviour of energized media, such as planetary atmospheres, the processes involving singly charged species is often complex enough, and additional contributions from multiply charged ions are commonly deemed to be negligible. In recent years, however, increasing attention has been directed towards the study of gas phase dications for a number of reasons, outlined below.

Firstly, the typical cross-section for double ionization in electron-molecule collisions, relative to single ionization, has been shown to be much larger than previously thought. This is because experiments often failed to detect many of the energetic fragment ions produced in dissociative double ionization. Double ionization, long thought to account for less than 2% of total ionization cross-sections, is in fact more commonly 5%-10%[21-26], as is the case for the precursor gases SF_6 and HCl which are used in the experiments detailed in Chapters 5-6.

Secondly, many molecular dications have been shown, either experimentally or theoretically, to possess electronic states with lifetimes of microseconds and upwards.[27-30] Such 'long-lived' states can be probed using traditional techniques, such as time-of-flight (TOF) mass spectrometry.

Thirdly, the separation of a double charge through fragmentation of a molecular dication is accompanied by a large release of energy, because of the Coulombic repulsion between like charges. As a consequence, monocations formed via the dissociation of a dication tend to have much larger kinetic energies than those formed directly in a single ionization process. This additional kinetic energy may open mechanistic pathways involving product monocations that would not be available in the absence of dications.

Spectroscopic probe techniques, discussed later in this chapter, have now characterized electronic and even vibrational states of an increasing number of dications, and unimolecular properties such as the lifetimes and fragmentation channels are also commonly studied.[31] However, the published literature on bimolecular reactions of dications in the gas phase is still severely limited, so much so that experimental work is still focussed on understanding the chemistry that simple dications undergo in collisions with neutral species, rather than attempting to recreate atmospheric or interstellar conditions and model the role of doubly charged ions in the chemistry of these environments.

The most important reactive process open to a dication is transfer of charge, which dications undergo very readily. The ubiquity of electron transfer reactions in the bimolecular collisions of dications has lead to the mechanism being reasonably well understood thanks to the development over recent years of the Reaction Window model. However, in addition to electron transfer, the experimental work around which this

thesis is based pays particular attention to bond-forming reactions, which are still rarely reported and mechanistically less straightforward.

1.2 Properties of molecular dications

Small doubly-charged molecules are, as one might expect, frequently unstable and often readily dissociate to form a pair of singly charge ions (sometimes accompanied by further neutral species).

$$XY_n^{2+} \rightarrow XY_{n-m-1}^{+} + Y^{+} + mY \qquad (1.1)$$

The non-adiabatic potential surface associated with a molecular dication, however, asymptotically corresponds to a smaller (or atomic) dication and a neutral species. Unless steric factors are significant, which is unlikely in small molecules, such a potential surface will always have a bound minimum, however weak, simply through polarization interactions. Molecular dications can decay by making an adiabatic transfer to the purely repulsive surface corresponding to a monocation pair that intersects the bound potential surface[32], see Figure 1.1.

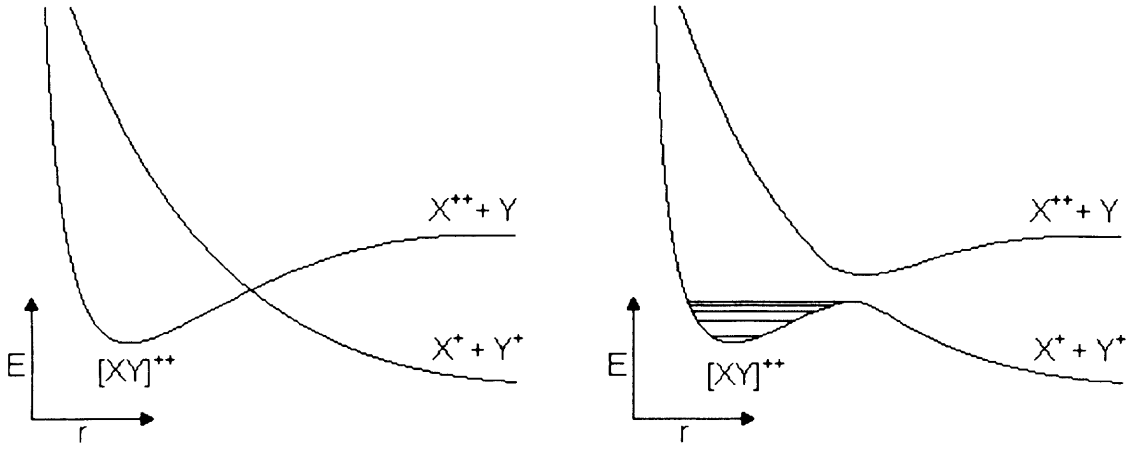

Figure 1.1 In a non-adiabatic picture potential curves do not interact (left-hand image), but in an adiabatic picture the system adopts the lowest energy configuration (right-hand image). This results in an 'avoided crossing' and can create a local minimum that can sustain vibrational levels.

Consider a diatomic dication, XY^{2+}. The stability of this dication will depend upon the energy at which the intersection with the repulsive surface occurs relative to the energy of the bound minimum. This can be estimated using the depth of the bound minimum and the appropriate ionization potentials of the component atoms.

The energy difference between the dication/neutral asymptote ($X^{2+} + Y$) and the monocation pair ($X^{+} + Y^{+}$) can be calculated by:

$$\Delta E = IP(X^{+}) - IP(Y) \qquad (1.2)$$

In cases in which the two potential surfaces cross at all we find three possible outcomes depending on the relative energetics:

a) If the monocation pair asymptote lies higher in energy than the bound minimum then the molecular dication is thermodynamically stable and cannot spontaneously dissociate.

b) If the monocation pair asymptote lies significantly lower in energy than the bound minimum then the crossing between surfaces will occur in the region of the bound minimum and the molecular dication will immediately dissociate.

c) If the monocation pair asymptote lies slightly lower in energy than the bound minimum an energy barrier to dissociation is created. While the molecular dication is still thermodynamically unstable, lying as it does above the dissociation asymptote to a monocation pair, it possesses a degree of kinetic stability depending on the height of the barrier. Such dications are termed 'metastable'.

In the unlikely case that the potential surface of the monocation pair lies wholly below the dication neutral potential surface then the molecular dication is metastable inasmuch as it can, in principle, dissociate to a monocation pair only by losing energy through radiative or collisional decay. In practice, of course, excited states come in to play and the molecular dication will almost certainly be able to cross to an excited potential surface of the monocation pair.

By inspection of these energetics arguments, it can be seen that stable doubly charged molecular cations are favoured when the second IP of X is relatively low, while

the first IP of Y is relatively high. Consequently, heavy metal oxides and halides, such UF_4^{2+} and LaO_2^{2+} are often thermodynamically stable. A number of other stable molecular dications have been either observed or postulated.[33] In contrast, molecular species containing only non-metals have only unstable or metastable doubly charged electronic states.

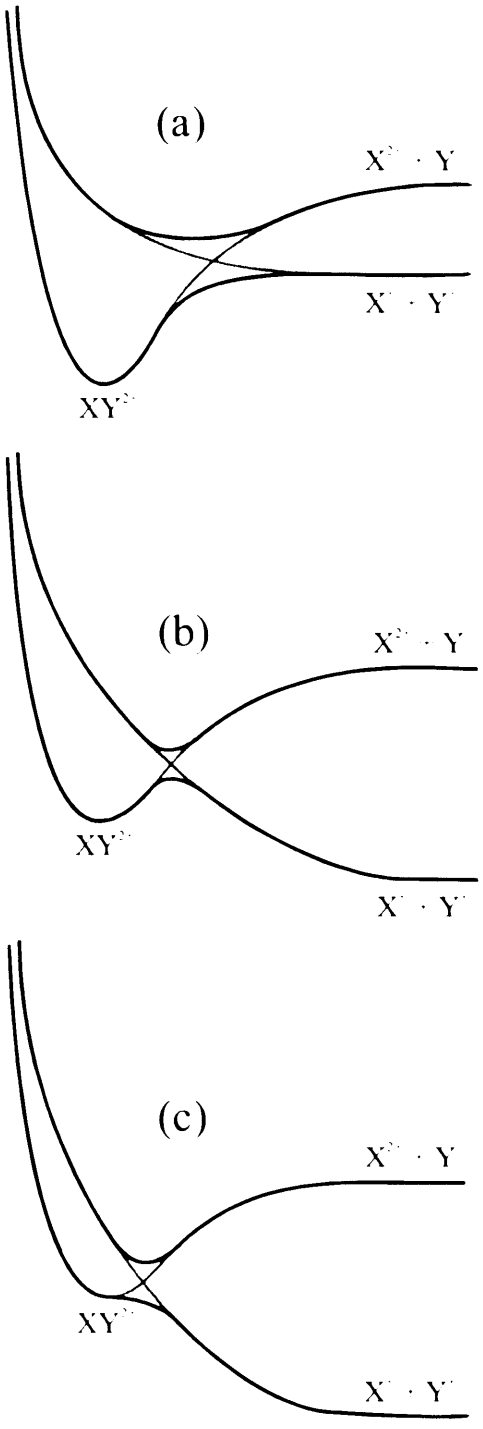

Figure 1.2 Prototypical potential energy curves for a diatomic dication from an adiabatic (black lines, foreground) and non-adiabatic (grey lines, background) perspective. If the lowest-energy dissociation asymptote lies above the bound minimum (a), the molecular dication is thermodynamically stable; if the asymptote lies below the minimum but is separated by an energy barrier (b), the molecular dication is metastable; if there is no barrier to dissociation (c), the molecular dication is thermodynamically unstable.

In the case of a metastable molecular dication, the bound minimum is a local minimum rather than a global minimum. The global potential minimum corresponds to the asymptotic energy of a monocation pair, which can be reached by tunnelling through the energy barrier confining the local minimum. The lifetime of a metastable state depends on the tunnelling rate, which in turn depends on the mass of the species and, more importantly the width of the energy barrier. In cases where the local minimum is deep enough to support a number of vibrational levels, dications in higher vibrational states, where the width of the barrier rapidly decreases will have much shorter lifetimes than those in the ground vibrational state. Doubly charged ions were first observed using mass spectrometric methods, so it was immediately clear that electronic states must exist with lifetimes of the order of, at least, microseconds, simply by virtue of their detection. The lifetimes of metastable dications are typically measured by storage ring experiments but some have been found to live for so long that it is difficult for such experiments to place an upper limit on their lifetimes. The lifetime of low-lying vibrational levels of the ground electronic states of CO^{2+} [34], N_2^{2+} [35] and SH^{2+} [27] for instance, are known to be considerably greater than 1s.

In fact, it has been shown that tunnelling rates are negligible for all but the highest vibrational states.[36] Low vibrational levels in deep local potential wells cannot tunnel through the energy barrier, so unless the potential surface is crossed by another which allows pre-dissociation these states may be expected to be very long-lived. Larger molecular dications may dissociate via a multiple step process called deferred charge-separation.[37] In this case, the parent dication loses neutral fragments until it reaches a state that can dissociate by charge-separation. This is common in large molecules where structural changes to the dication result in relatively small changes to the potential energy surface.

$$XY_n^{2+} \rightarrow XY_{n-1}^{2+} + Y, \; XY_{n-1}^{2+} \rightarrow XY_{n-2}^{2+} + Y, \text{ etc} \qquad (1.3)$$

$$XY_{n-m}^{2+} \rightarrow XY_{n-m-1}^{+} + Y^{+} \qquad (1.4)$$

1.3 Ionization techniques

Molecular dications may be formed by the double ionization of a suitable precursor gas. The most common means of achieving double ionization is by bombardment of precursor molecules with either electrons or photons. Both of these techniques are destructive, in that they deposit significant amounts of energy in a molecule that often causes fragmentation. More recently, however, 'soft' methods of multiple ionization have been developed to service the ever-growing interest in bio-molecules.

The crossed-beam experiment that is the subject of this thesis employs an electron-ionization source, which is described in detail in Chapter 3. An electron-ionization source was chosen because such sources are relatively cheap and simple to construct, while being robust and capable of producing large quantities of ions. The disadvantages of such a source are that it is indiscriminate and, as mentioned above, destructive. However, these problems can often be solved experimentally, with a mass-filter in the first instance and appropriate choice of precursor gas in the second.

1.3.1 Electron ionization

"Electron ionization"[38-41] is the IUPAC-approved term for what is often known as "electron-impact ionization" and has been a commonly used technique for many years. Electrons are generated by thermionic emission, whereby a current is passed through a wire filament, and collimated into a beam. The electron beam intersects a neutral gas target; when an electron strikes a molecule, some of the electron's kinetic energy is transferred to the molecule. If sufficient energy is transferred, the molecule will eject an electron, producing a molecular ion. Multiply charged molecular ions are formed in a single event when a large amount of energy is transferred rather than successive ionization caused by repeated electron-molecule collisions. The formation of a doubly charged molecular ion by electron ionization may be represented as:

$$M + e^- \rightarrow M^{2+} + 3e^- \qquad (1.5)$$

However, the energy imparted to a molecule may excite the molecule vibrationally, as well as electronically, which often leads to fragmentation of the molecular ion.

The efficiency of ionization is a function of the kinetic energy of the colliding electrons. Clearly, if the electron energy is less than the energy required to ionize the target, no ions will be formed at all. Above this threshold, the total ionization cross-section increases with electron energy because statistically more electrons will transfer enough energy to ionize a molecule in a collision. However, as the electron energy increases further, the total ionization cross-section begins to fall. This is because the faster the electrons are moving the less they interact with the target gas. Another way of looking at this is in terms of the De Broglie wavelength of the ionizing electrons. Energy transfer is most efficient when this wavelength is comparable to a bond length in the target molecule, but as the energy of the ionizing electrons increases so their De Broglie wavelength decreases and the target gas becomes transparent to the electron beam.

Electron ionization is a vertical process, because the interaction time between an ionizing electron and a target molecule is very short. This means that the product ion is formed at the equilibrium geometry of its neutral precursor because the nuclei do not have sufficient time to move relative to each other in the course of the ionization event. In cases where the equilibrium geometry of the ion is significantly different to that of the neutral molecule, this means that the minimum energy required to ionize the target may be considerably larger than the energy difference between the bound minimum of the precursor molecule and the product ion.

Double-ionization cross-sections via electron-ionization represent only a small fraction of the total ionization cross-section of a molecule and since electron ionization also usually produces a range of fragments the resulting ion mixture must be effectively and efficiently mass-selected in order to generate a suitable ion beam to use in experiments.

1.3.2 Photon ionization

The principles of using photons to generate multiply charged ions[42-44] have long been understood, but practical difficulties in generating photons of the required energy prevented its widespread experimental application until relatively recently. The development and increasing availability of synchrotron radiation sources and tuneable UV and VUV lasers has now greatly improved the practicality of photon ionization. Single-photon ionization may be represented as:

$$M + h\nu \rightarrow M^{+} + e^{-} \qquad (1.6)$$

Ionizing photons are most easily generated by discharge lamps, but this method severely restricts the photon energies available. Synchrotron radiation and lasers provide access to a much greater wavelength range of photons, allowing much wider applicability of the photon ionization technique. The main advantage of photon ionization is that the whole of the photon energy is transferred to the target and so since the photon energy is accurately known, the energy deposited into the target is also known.

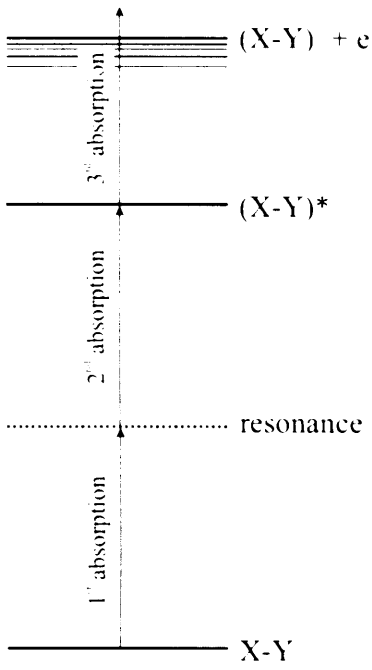

Figure 1.3 Schematic diagram of a (2+1) REMPI process.

An important sub-category of photon ionization is resonance-enhanced multi-photon ionization[45-48] (REMPI). REMPI involves the excitation of a neutral molecule or atom prior to ionization, thereby allowing state-selection of product ions. The target species can be excited to a desired electronic state by using a laser tuned to the appropriate wavelength based on knowledge of the electronic spectrum of the target. In principle this excitation can be done using a single photon, but often this requires photons beyond the near UV, which are difficult to produce on a laboratory scale. Instead, it is possible for a target species to absorb multiple photons to reach the desired electronic state via a number of intermediate resonances. The excited species is then ionized by absorption of further photons. A REMPI process is labelled with the number of photons used in the

excitation step and the number used in the ionization step. Most commonly, two photons are used to excite the target and a single subsequent photon to ionize, so this is termed (2+1) REMPI.

The energy, E, of the product ion and hence its quantum state, can be determined provided that the kinetic energy release (the difference in translational energy between the target and the ion), the ionization potential of the target and the energy of the n photons are all known.

$$E_{\text{ion}} = \sum_{i=0}^{i=n} h\nu_i - \text{KER} - \text{IP}_{\text{neutral}} \quad [49] \qquad (1.7)$$

1.3.3 Soft ionization

TOF spectrometry has received a great deal of additional interest from a biochemical perspective since the development of soft ionization techniques, specifically matrix-assisted laser desorption ionization[50-52] (MALDI) and electrospray ionization[53,54] (ESI). Soft ionization allows large, fragile molecules, such as proteins, to be ionized without the degree of fragmentation associated with conventional ionization techniques. Biochemical applications of TOF spectrometry require very high resolution spectrometers to distinguish small changes of mass in very heavy biomolecules. Commercial MALDI-TOF spectrometers tend to couple ion mirrors and long drift lengths and can achieve mass resolutions in excess of 20,000, meaning that the full-width half-maximum of peaks from molecules of 20,000 and 20,001 are spatially distinct in the TOF spectrum.

In MALDI, analyte molecules (those to be ionized) are stabilized in a matrix material. The sample is prepared by dissolving the analyte molecule, along with an appropriate crystalline molecule (the matrix), in a solvent (or a mixture of solvents if ambiphaticity is required). This solution is deposited on a plate and the solvent evaporates leaving analyte molecules co-crystallized in the matrix. The sample is the subjected to laser photons, which primarily ionize the crystalline matrix. The matrix then relaxes by transferring some of its energy to the trapped analyte molecules. The products of MALDI are usually singly charged ions formed by the addition of a light atomic ion from the matrix to analyte molecules.

Electrospray ionization is another soft ionization technique that minimizes fragmentation when ionizing fragile molecules. Once again the analyte is dissolved in a mixture of volatile solvents, either acidic or basic, so that the analyte exists either in a protonated cationic form or an anionic form. The solution is drawn into an appropriately charged capillary so that the charged analyte molecules are repelled and forced along the capillary. As a result, the solution is expelled as an aerosol, of droplets approximately 10 μm in diameter, from the capillary aperture. As the solvent evaporates from the surfaces of the droplets, the analyte ions become ever more closely packed until the density of charge brings about fragmentation of the droplets in a process termed Coulombic fission. This fission continues as the solvent molecules continue to evaporate until the analyte is left as isolated ions in the gas phase. A carrier gas, such as nitrogen or argon, is commonly used both to aid formation of the aerosol and evaporation of the neutral solvent. The mechanism of ESI is not well understood but product ions are both preformed in the solution and produced in the Coulombic fission processes.

In common with MALDI, ESI does not involve the direct removal of electrons, but rather the transfer of charged atoms. In practice, this most often means the transfer of protons and common products would be $[M + nH]^{n+}$ or $[M - nH]^{n-}$, where M is the initial analyte molecule. However, electrospray ionization generates many more multiply charged ions than MALDI and can generate very highly charged ions in proton rich systems. Similarly to MALDI, ESI is usually paired with a high resolution TOF mass spectrometer and used to study biomolecules.

1.4 Probe techniques

There are a number of probe techniques in common use that are designed to study positively charged ions in addition to the type of apparatus described in Chapter 3. An overview of experimental types of historical and contemporary importance is included here. In many cases different information is yielded by different techniques and separate experiments may be operated co-operatively; for instance the gas-phase chemistry group at UCL also includes an ion-ion coincidence spectrometer with position-sensitive detection. Position-sensitive experiments, including a technique called velocity imaging, are powerful and rapidly evolving probes of dication reactivity and are given particular attention as those topics will be drawn upon in Chapter 7.

1.4.1 Coincidence experiments

Although a multitude of variants exist, all coincidence experiments involve the simultaneous detection of two or more species (either ions, electrons and/or photons) that are formed coincidentally, i.e. in a single event. Measuring the flight times and/or angular distribution of two products simultaneously allows a much greater insight into a reactive event than traditional TOF spectrometry, which is not event specific.

The earliest and simplest coincidence technique to study dications, ion-ion coincidence[55], involves the detection of a pair of ions formed in dissociative multiple ionization of a precursor gas by electron impact. This technique has been used to investigate the dissociation channels of many doubly-charged molecules, both organic, such as the benzene dication[56], and inorganic, such as the ozone dication[57]. Ion-ion coincidence spectroscopy is most commonly a one-dimensional technique, where only the time difference, Δt, between the arrivals of a pair of ions is measured. Consider the dissociation of a diatomic dication:

$$XY + e^- \rightarrow XY^{2+} + 3e^- \rightarrow X^+ + Y^+ + 3e^- \qquad (1.8)$$

When the product ions, X^+ and Y^+ are detected in coincidence, the first ion to hit the detector (i.e. the lighter one) starts the timing cycle, which runs until the second ion reaches the detector. If the initial velocity of X^+ is perpendicular to the time-of-flight axis, then its partner must also have zero on-axis velocity and each ion will have the zero-energy flight time associated with its mass, $t_0(X^+)$ and $t_0(Y^+)$, as will its partner. The minimum flight time for X^+ is $t_0(X^+) - t^-(X^+)$, corresponding to the initial velocity being directed towards the detector, and the maximum is $t_0(X) + t^-(X)$, corresponding to the initial velocity being entirely in the opposite direction. The quantity t^- is defined here as the time it takes for an ion whose velocity is initially directed against the electric field (directly away from the detector) to slow down and reach its turning point. Similarly, the maximum and minimum flight times of Y^+ are $t_0(Y) \pm t^-(Y)$. However, in order to maintain zero overall momentum (assuming the parent dication to be stationary), X^+ and Y^+ must separate with fixed speeds at a mutual angle of 180°. Consequently, if the flight time of an X^+ ion is at its maximum, that of its partner Y^+ ion must be at its minimum, and vice versa, so the maximum difference in flight time that is recorded is:

$$\Delta t_{max} = [t_0(X) + t(X)] - [t_0(Y) - t(Y)] \quad (1.9)$$

while the minimum is:

$$\Delta t_{min} = [t_0(X) - t(X)] - [t_0(Y) + t(Y)] \quad (1.10)$$

By subtracting Equation (1.10) from Equation (1.9), we find the width of a peak in a 1D coincidence spectrum:

$$\Delta t_{max} - \Delta t_{min} = 2[t(X) - t(Y)] \quad (1.11)$$

In a 1D coincidence spectrum, a reaction channel producing a pair of singly charged ions, such as Equation (1.8), appears as a square peak with a width determined by Equation (1.11).

For an ion of mass m, charge q and initial speed v in an electric field E, the turnaround time t is given by:

$$t = \frac{mv}{qE} \quad (1.12)$$

Hence, by determining the limits of a peak in the coincidence spectrum, the times $t(X)$ and $t(Y)$ can be derived, which, for a known electric field, allows the velocity of both the ions to be calculated.

$$v = \frac{qEt}{m} \quad (1.13)$$

These velocities are, of course, dependent upon the total amount of energy liberated by the dissociation, ΔT, which can in turn be obtained.

$$\Delta T = \tfrac{1}{2} m_X v_X^2 + \tfrac{1}{2} m_Y v_Y^2 \qquad (1.14)$$

If a time reference point can be obtained, then the absolute flight times of X^+ and Y^+ can be measured, and two-dimensional plot of t_{X^+} against t_{Y^+} can be obtained. A time reference may be achieved by pulsing beam of ionizing electrons, but the pulse must be very short compared to the flight times of ions for this method to be accurate. A more precise time reference can be obtained when using a pulsed laser (see PIPICO, below) or by detecting a photoelectron in addition to the ion pair (see PEPIPICO, below). In a 2D coincidence spectrum, true peaks, that is those originating from genuine coincidences, appear as 45° straight lines because the product ions must have equal and opposite momentum so t_{X^+} and t_{Y^+} are correlated. Deviations of the gradient of a peak from −1 are indicative of multiple step mechanisms, which cannot be probed using 1D coincidence spectroscopy. Dissociations that also form a third, neutral, species also have different gradients because the momenta of the two ionic products are no longer required to be equal and opposite. The true peaks in a coincidence spectrum arising from different dissociation channels will be superimposed on a background of false coincidences caused by either one or both of the detected pair being a stray ion not produced by the reactive event. False coincidences are clear to spot because there is no correlation between the times of the two ions.

Photoion-photoion coincidence[58] (PIPICO) differs from normal ion-ion coincidence solely by virtue of using photons as the means of ionization rather than electrons. The ionizing photons may be generated by a gas discharge or a laser. The advantage of photoionization of electron impact ionization is that the energy deposited in the precursor molecule is precisely known. A number of molecules that have been studied in crossed-beam experiments by the Price group have been investigated by others using the PIPICO method including CF_4^{2+}[59] and SO_2^{2+}[60].

Photoelectron-photoelectron coincidence[61] (PEPECO) detects the electrons generated by a double ionization event, rather than the ions. The energy of the photoelectrons may be determined using time-of-flight methods or hemispherical energy analysers. Electrons are much harder to analyze using TOF methods than ions because, being so much lighter, they travel extremely fast when accelerated by electric fields. This means that very long drift tubes are required for electrons of slightly different energies to have measurably different flight times. While the drift tube for an

ion collection experiment is usually a few tens of centimetres, that for an electron collection experiment may be several metres in length. On the other hand, energy analyzers have good resolution even at high electron energies, but have very limited collection efficiency, since only electrons of a selected energy are detected.

A particular advantage of PEPECO is that the energies of the electrons emitted by ionization, $E(e_1)$ and $E(e_2)$ allow the energy of the parent dication, $E(XY^{2+})$, to be calculated directly, because the electrons have no internal energy.

$$E(XY^{2+}) = h\nu \quad E(e_1) \quad E(e_2) \tag{1.15}$$

Eland has obtained the double photoionization spectra of a wide range of small molecules using this technique.[62]

Photoelectron-photoion coincidence[63,64] (PEPICO) detects both ions and electrons in coincidence. In the case of TOF detection, this is achieved by mounting two spectrometers of opposite polarity at either end of the source region, one to extract and detect positive particles, the other negative particles. In most laser-based time-of-flight techniques, a product angular distribution may be described by a single anisotropy parameter, β, since the molecules in the incident molecular beam are randomly orientated. The anisotropy parameter is consequently dependent on the alignment of the laser polarization axis. The molecules must be in a known orientation, that is the direction of the molecular axis and electric moment vector must be known, in order to obtain the fixed-molecule angular distribution (FMAD). However, since the distributions of ions and electrons are correlated to each other, simultaneous measurements of both these distributions allows the FMAD of a reaction to be obtained. The direct relationship between the electron and ion distributions holds providing:

i) the time delay between ionization (production of photoelectons) and fragmentation (production of photoions) is small compared to the rotational period of the molecule;

ii) the correlation between the angular distributions and the polarization vector of the laser is negligible compared to the correlation between the angular distributions and the molecular orientation.

The mathematics behind the measurement of fixed-molecule angular distributions and experimental results using the PEPICO technique have been reviewed by Baer.[65]

Threshold photoelectrons coincidence[66-68] (TPEsCO) detects the pair of zero kinetic energy (ZEKE) photoelectrons that are emitted each time a scanned photon source passes through the resonant frequency of a dication state threshold. One means of detecting zero (or very low) energy electrons is to employ time-of-flight methods[69,70], applying a delayed electric pulse to extract ZEKE electrons after non-ZEKE electrons have left the source region under their own velocity, but this is not ideal for resolving genuine ZEKE electrons. In many cases, the penetrating field technique is used to efficiently collect zero energy electrons, by creating a saddle-shaped potential in the source region that separately focuses electrons emitted on either side of its plane of symmetry to one of two exit apertures.[66,71] A pair of energy analyzers is then used to select only zero energy electrons and record coincident pairs. Since the energy of the ionizing photons is precisely known and can be accurately controlled, both the electronic and vibrational structure of the dication can be observed. Although the TPEsCO technique is capable of very high resolution it relies on achieving direct valence ionization and results can be complicated by indirect double ionization, such as Auger processes. Nonetheless, TPEsCO spectroscopy is today a very important tool for determining the vibrational structure of doubly charged molecules, such as Ar^{2+}[72], HCl^{2+}[68], HBr^{2+}[73], N_2^{2+}[67], CO^{2+}[67] and $C_6H_6^{2+}$[74].

More complicated methods detect more than two particles in coincidence and attract even longer acronyms. For instance **photoelectron-photoion-photoion coincidence**[75] (PEPIPICO) is a triple coincidence technique that measures the flight time of each of a pair of ions relative to the detection of one of the photoelectrons. This puts the ionic flight times on an absolute scale and allows direct calculation of their masses. This makes PEPIPICO particularly useful for studying the double ionization of organic molecules that have many possible fragmentation channels, which would be difficult to identify unambiguously without the benefit of an absolute mass scale. For instance, Leach et al. have used PEPIPICO to observe a number of similar pathways in the dissociation of the naphthalene and azulene isomers of $C_{10}H_8^{2+}$.[76]

1.4.2 Doppler-free kinetic energy release spectroscopy[77] (DFKER)

The resolution of coincidence techniques that detect a pair of ions is limited by Doppler broadening in the kinetic energy distribution of the products as a result of the non-zero thermal energies of the reactants.

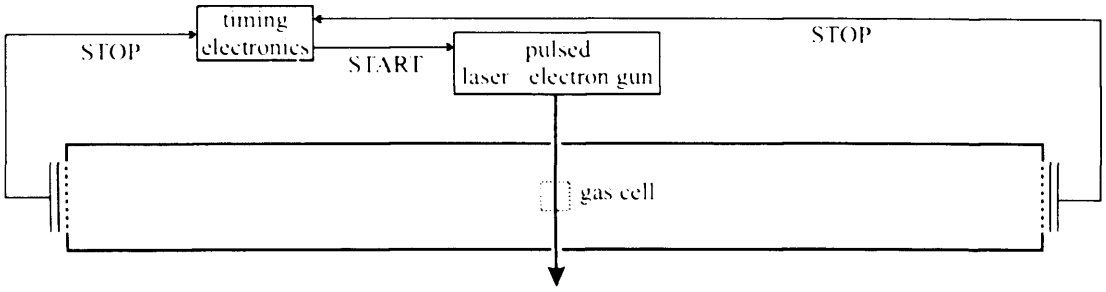

Figure 1.4 Schematic of a DFKER instrument.

DFKER uses a field-free arrangement to detect fragment ion pairs at two separate detectors. Ion pairs formed in the source region (Figure 1.4) separate solely due to the kinetic energy release of the dissociation (i.e. no external electric fields are applied). In cases where the precursor molecule is appropriately orientated, one of the fragment ions will hit each detector and a coincidence will be recorded. The thermal motion of the precursor molecule manifests itself as a non-zero value of the velocity of the centre-of-mass of the system, but by measuring the kinetic energies of both fragments, the contribution of the motion of the centre-of-mass towards the LAB frame energy can be removed.

The experiment allows the relative velocity of a pair of ions, v_{rel}, to be ascertained, which is independent of the motion of the centre-of-mass, v_{CM}.

$$v_1 = w_1 + v_{CM} \tag{1.16}$$

$$v_2 = w_2 + v_{CM} \tag{1.17}$$

$$\Rightarrow v_{rel} = (w_1 + v_{CM}) - (w_2 + v_{CM}) = w_1 - w_2 \tag{1.18}$$

The kinetic energy of the product ions in the CM frame, T_p, is determined using the following relationship between the reduced mass of the system, μ, and the relative velocity of the product ions:

$$T_p = \frac{1}{2}\mu v_{rel}^2 \quad (1.19)$$

Further information on the use of the centre-of-mass frame, and the division of energy in collisions and fragmentations is found in Chapter 2.

The proponents of DFKER spectroscopy demonstrated the technique by distinguishing the vibrational structure of a number of electronic states of CO^{2+}[78], and subsequently observed vibrational structure in dissociation spectra of O_2^{2+}[79], N_2^{2+}[80] and NO^{2+}[81].

1.4.3 Translational energy spectroscopy (TES)

TES techniques involve measuring the kinetic energy of a species before and after a collision to deduce the energy required for, or released by, the collision. The aim is to establish electronic, vibrational and, in some cases, even rotational energies of ions by comparing translational energies before and after a collision. Double charge transfer (DCT) spectroscopy[82] is a variant of TES that observes the products of double electron transfer in high energy (keV) collisions between incident ions and a neutral analyte. For instance, protons of known energy may be collided with a neutral target M, and the hydride ions produced in DCT collected and energy analyzed. Hydride ions may be formed in a single collision[83,84]:

$$H^+ + M \rightarrow H^- + M^{2+} \quad (1.20)$$

or a double collision:

$$H^+ + M \rightarrow H + M^+ \quad (1.21)$$

$$H + M \rightarrow H^- + M^+ \quad (1.22)$$

In the case of the single collision, the difference in translational energy of the H^+ reactant and H^- product indicates the energy imparted to the target molecule:

$$\Delta T = 2IP_M + E_{H^-} + T_M \quad (1.23)$$

It has been shown that in such collisions hydride ions are formed in the ground electronic state ($E_{H^-} = 0$), and providing the mass of the target is much greater than a proton, the recoil energy of the neutral target (T_M) will also be negligible. The translational energy loss, therefore, is a measure of the energy required to doubly ionize the target.

Energy loss spectra are often capable of resolving vibrational levels of the target molecule, for instance Furuhashi et al. used DCT spectroscopy to successfully probe vibrational structure of the acetylene dication for the first time.[85] Indeed, DCT spectroscopy can offer advantages over TPEsCO spectroscopy, for which indirect processes, whereby the electrons are ejected sequentially via a singly charged intermediate, can complicate spectra.[67] Experiments have shown that the charge transfer observed in DCT spectroscopy occurs only via a direct process (i.e. a vertical transition) and can consequently be well modelled by considering the appropriate Franck-Condon factors.[86]

1.4.4 Afterglow techniques

Afterglow techniques are used to detect the products of ion-molecule reactions occurring within a tube filled with an inert carrier gas, allowing experiments to be conducted on thermalized reactant ions. The simplest such technique, the stationary afterglow method[87-89], mixes both the precursor gas and the other reactant gas with the carrier gas in the same region and exposes this mixture to a short pulse of ionizing radiation. The period after the ionizing pulse is removed is termed the 'afterglow' and populations of ions in the mixture is monitored over time. A major disadvantage of the stationary afterglow technique is that as the partner reactant, which is intended to remain neutral, is subjected to the same ionizing radiation as the precursor molecule, additional, unwanted ionic species may be produced, complicating the interpretation of results. For this reason, stationary afterglow has been largely supplanted by the flowing afterglow technique[90] in which the carrier gas flows along a tube, carrying the reactant species along with it. This allows the precursor gas to be injected (and ionized) downstream of the point where the neutral reactant is injected.

A related technique is selected ion flow-tube (SIFT) mass spectrometry[91], which ionizes the precursor gas and, as the name suggests, selects a particular ionic fragment using a mass analyser (usually a quadrupole (see Section 1.4.5) before

injecting the ions into the flow tube. This technique has proved particularly successful in physiological applications because of its ability to output absolute concentrations of neutral molecules in physiological samples, such as breath. In such instances, an ion such as H_3O^+ or NO^+ that has well established reaction rates with common molecules is used and reacted with the sample. Given that the reaction rates are known, monitoring the ionic products of the reactions allows the absolute concentrations of neutral molecules, such as alcohol, in the sample to be determined.

All these techniques that rely on thermalizing ions in a carrier gas are not suitable for use with doubly charged ions because dications would readily transfer charge to the carrier gas molecules.

1.4.5 Guided ion beam experiments

GIB techniques employ a multipolar (usually quadru- or octo-polar) radio frequency electric field to generate a cylindrical potential to confine and transport ions.[92] The strength of the applied oscillating electric field determines the depth of the potential well in the centre of the multipole. Ion-molecule collision experiments often use an octopole placed around the collision cell to confine product ions in tandem with a quadrupole mass spectrometer.[93,94]

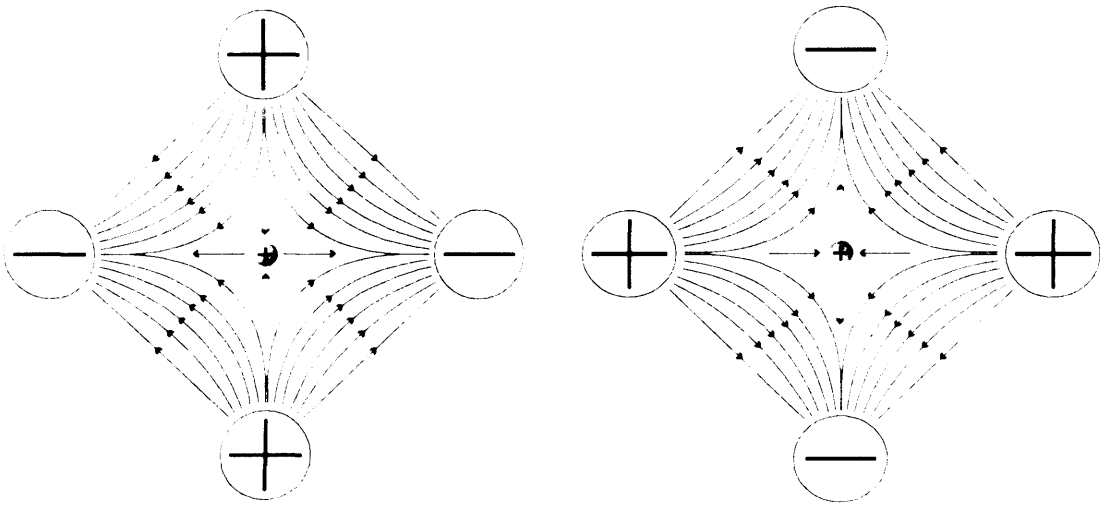

Figure 1.5 Illustration of the potential field created by a quadrupole mass spectrometer. The polarity is rapidly alternated between the left-hand image and right-hand image. The electric field is shown in green and the forces exerted on a positively charged particle are shown in black.

Multipoles can be used as mass analyzers by superimposing a DC voltage over the RF field to propel ions through the multipole. For ions of a particular mass only a certain ratio of voltages will produce a stable trajectory and allow the ions to pass along the multipole; ion trajectories in a multipole cannot be calculated analytically, but can be determined numerically. In practice, mass selection is achieved by scanning the applied voltages.

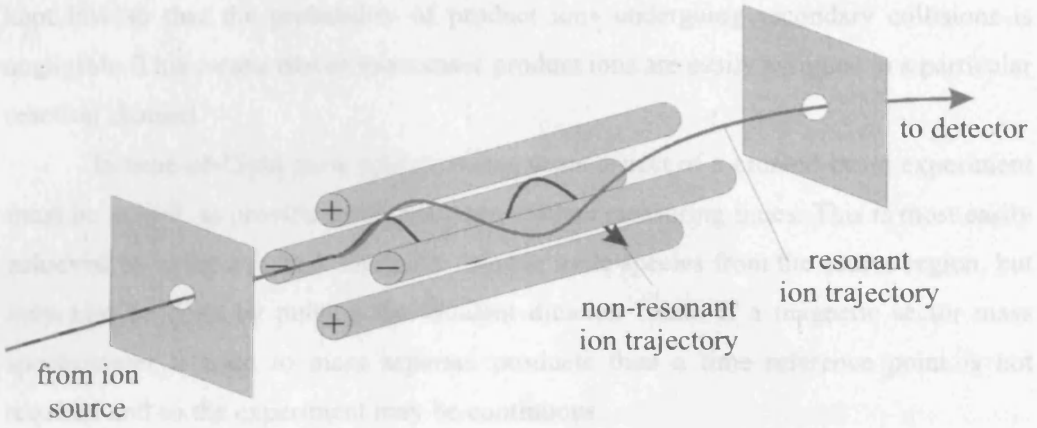

Figure 1.6 Mass selection using a quadrupole. Varying the applied voltages changes the mass of ions that are able to pass along the entire length of the quadrupole.

Higher order multipoles are also sometimes used, for example the 22-pole ion trap designed by Gerlich[95]. Higher order multipoles produce a larger region of flat potential in the centre of the trap, with the potential rising very steeply close to the electrodes.

GIBs are particularly useful when studying relatively low energy ions because they ensure complete collection of ions and are thus well suited to determining total cross-sections and branching ratios. However, GIBs are less widely employed when working with dications because the energetic ions formed in charge separation processes are difficult to confine.

1.4.6 Crossed-beam experiments

The early investigations into the collisional reactivity of dications were performed using conventional (magnetic sector) mass spectrometers, at high (keV) collision energies.[18,96] In order to study such collisions at more realistic collision

energies, purpose-built spectrometers were needed with optics capable of collimating a beam of dications at low energies (such as the spectrometer described in Chapter 3). Typically, crossed-beam experiments rely on photons or electrons as the means of ionizing the precursor gas, then mass select and collimate a beam of a particular dication and intersect this beam orthogonally with a narrow beam or jet of some neutral reactant.[97-100]

The pressure of the neutral reactant and the current of the ion beam must both be kept low so that the probability of product ions undergoing secondary collisions is negligible. This means that in most cases product ions are easily assigned to a particular reaction channel.

In time-of-flight mass spectrometry, some aspect of a crossed-beam experiment must be pulsed, to provide a reference point when measuring times. This is most easily achieved by using a pulsed voltage to remove ionic species from the source region, but may also be done by pulsing the incident dication beam. If a magnetic sector mass spectrometer is used to mass separate products then a time reference point is not required and so the experiment may be continuous.

The products of crossed-beam reactions may be detected using a time-of-flight mass spectrometer, multipole mass spectrometer (see Section 1.4.5) or a magnetic sector mass spectrometer[97]. In some instances the detector may be rotated with respect to the direction of the dication beam to provide measurements of angular scattering, or position-sensitive detection may be used to reveal dynamical information. Generally, a crossed-beam source may be used in conjunction with the same spectrometric detection methods used for observing the products of photoionization, but achievable resolutions are usually lower because the interaction region between two beams is inevitable larger than the focal point of a laser.

1.4.7 Imaging/position-sensitive experiments

Imaging experiments, that record not only temporal but also spatial information, have become extremely widespread in the field of time-of-flight mass spectrometry in recent years and indeed may be a useful addition to the apparatus discussed in this thesis. In essence, the recording of an ion's position at the point of detection, in addition to its flight time, allows the ion's initial speed and direction to be determined, rather than simply its kinetic energy. The first experiments to study reaction dynamics were

one-dimensional, recording only temporal information. This approach is, of course, extremely useful and still widely used in many different forms, however, a number of techniques have been developed that also record spatial information. Position-sensitive experiments are potentially very powerful probes into reaction dynamics, particularly angular properties.

As far back as 1971, Solomon et al. had demonstrated the anisotropic nature of three-dimensional product distributions by conducting photodissociations inside a coated bulb and producing etched patterns on its inner surface.[101] However, quantitative techniques remained one-dimensional until the advent of ion-imaging in 1987.[102]

Ion-imaging simply involved placing a phosphor screen behind the MCP detector of a normal Wiley-McLaren-type mass spectrometer and capturing the images produced using an optical or CCD camera. The Wiley-McLaren source optics (see Section 1.5.2) focus ions of the same mass so that they reach the detector at approximately the same time. However, the position where an ion hits the detector (x,y) depends on its off-axis velocity components (v_{xy}), which are unaffected by the electric field, and its initial position. Since the energy released by a reaction is fixed, each type of product ion forms a ring in the image, corresponding to different alignments of the initial velocity vector. Unfortunately, the z-component of velocity (i.e. parallel to the time-of-flight axis) does not affect the impact position and cases where the z-component is large leads to broadening of the ring (in principle, an ion with $v_{xy} = 0$ would hit the centre of the detector, regardless of its kinetic energy). Anisotropy of the angular distribution of a product ion is seen as variations of intensity with position in the image.

Ion imaging was of fairly limited application due to the restricted energy resolution of which it was capable, but the introduction of velocity map imaging[103] (or simply velocity imaging) in the late 1990s has brought about renewed interest in imaging experiments. Velocity imaging uses gridless optics to achieve greatly improved resolution with the added benefit of mapping ions as a function of their initial velocity. Velocity imaging and some subsequent refinements to the technique are discussed separately, in Section 1.4.8.

It is standard practice in ion-imaging and velocity imaging to reconstruct a three-dimensional angular velocity distribution from a two-dimensional image using a Fourier-type transform called the inverse-Abel transform.[104] The most important

caveat of the inverse-Abel transform is that it is only applicable to three-dimensional distributions that display cylindrical symmetry about an axis perpendicular to the detector face.

Each row of pixels in a two-dimensional image corresponds to the projection of a slice of a spherical distribution as shown in Figure 1.7. Each row is associated with a single value of y and each column with a single value of x, and for any particular mass the positions y and x are proportional to v_y and v_x, respectively. The intensity of each pixel is proportional to the distribution in the z-direction. The inverse-Abel transform back-projects the measured distribution (x,y) to obtain the original three-dimensional distribution in polar co-ordinates (r,θ).

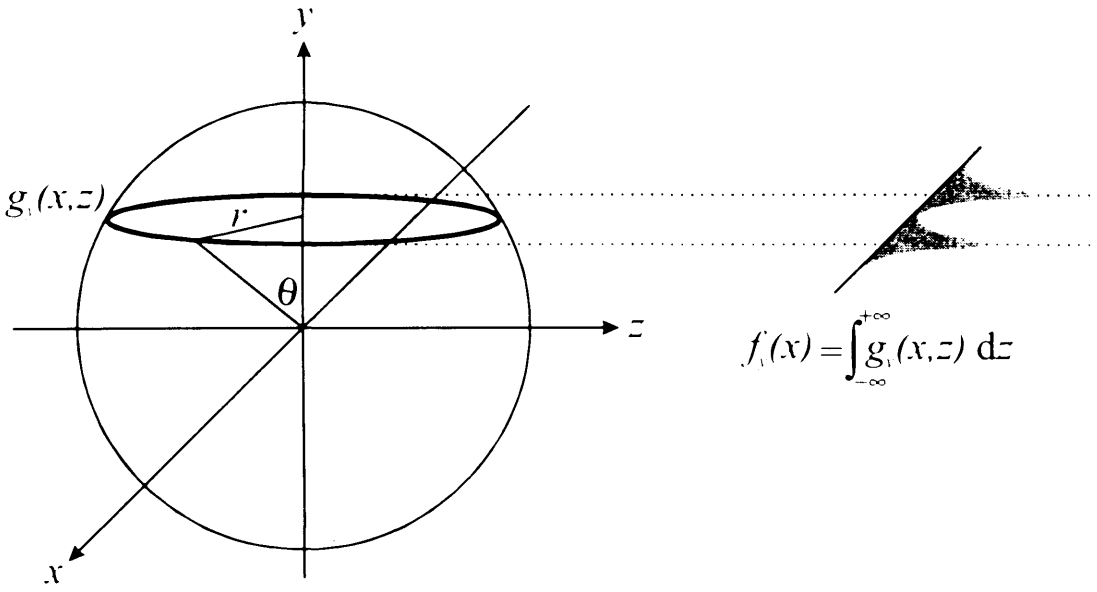

Figure 1.7 Illustration of the projection of a two-dimensional slice of a three-dimensional distribution onto a one-dimensional array. The time-of-flight axis is denoted z, while the detector is in the xy plane.

In Cartesian co-ordinates, the Abel transform is defined as the relationship between the one-dimensional function $f_i(x)$ that describes the intensity of a row of pixels defined by a particular value of y, and the two-dimensional function $g_i(x,z)$ that describes the original angular distribution in the xz plane:

$$f_i(x) = \int_{-\infty}^{+\infty} g_i(x,z)\,dz \qquad (1.24)$$

which, by the required property of cylindrical symmetry, is:

$$f_x(x) = 2\int_0^\infty g_x(x,z)\,dz \tag{1.25}$$

which, in polar co-ordinates becomes:

$$f_x(x) = 2\int_x^\infty \frac{g(r)r}{\sqrt{r^2 - x^2}}\,dr \tag{1.26}$$

The inverse of the Abel transform is, unfortunately, not immediately apparent from Equation (1.26), but transform mathematics[105] can be used to show that it has the Equation (1.26), but transform mathematics[105] can be used to show that it has the form[104]:

$$g(r) = \frac{1}{\pi}\int_r^\infty \frac{df_x(x)/dx}{\sqrt{r^2 - x^2}}\,dx \tag{1.27}$$

There are two main problems with the inverse-Abel transform in addition to the requirement of cylindrical symmetry. Firstly, Equation (1.27) is not well-behaved; the integrand approaches ∞ as $x \to r$. This results in a line through the centre of an image which cannot be reconstructed. Secondly, the dependence of Equation (1.27) upon the differential of $f_x(x)$ amplifies noise present in the image, since noise in any distribution will obviously cause significant local changes in gradient.

The problem of reconstructing an image representing the superposition of many ion arrivals may be circumvented by using a detector that directly measures both positions and flight times as part of a coincidence experiment. Price et al. employ such a position-sensitive coincidence (PSCO) experiment that has proved to be a powerful probe of reaction dynamics.[106]

Positional data is recorded by placing a two-dimensional delay-line anode behind the MCP detector. The anode consists of two pairs of wire-wound propagation delay lines. These pairs of wire are wound perpendicularly to each other and independently record the x- and y-co-ordinates of an ion arrival. The electron pulse generated by an ion hitting the MCP hits the anode and propagates along the delay lines.

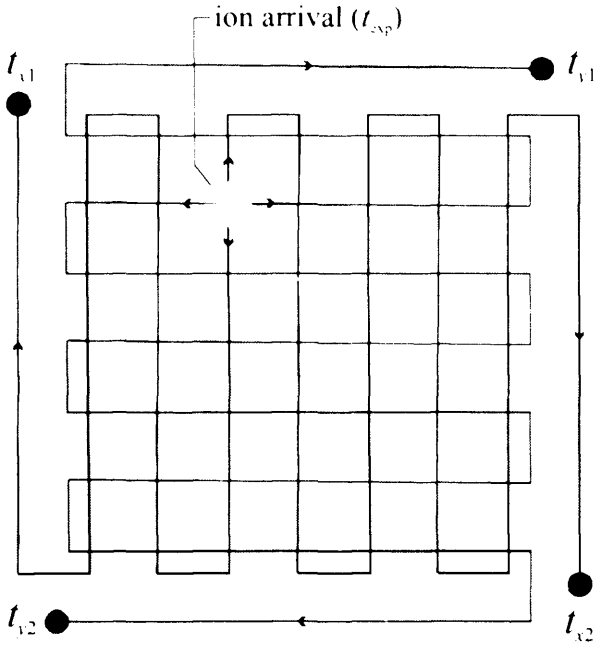

Figure 1.8 Schematic diagram of a delay line anode. In reality, each wire is wound approximately 10 times per centimetre.

In addition to the flight time of an ion, t_{exp}, the times for the signal to reach both ends of the delay lines are also measured, namely t_{x1}, t_{x2}, t_{y1} and t_{y2}. The x-position of the source of the signal is then proportional to the difference between t_{x1} and t_{x2} (and t_{y1} - t_{y2} for the y-co-ordinate). Since the rate at which a signal propagates along the delay-lines, denoted Θ, is known, the delay times of the arrival of an ion j can be converted directly to a position (x,y).

$$x_j = \frac{t_{x1}(j) - t_{x2}(j)}{2\Theta} \tag{1.28}$$

$$y_j = \frac{t_{x1}(j) - t_{x2}(j)}{2\Theta} \tag{1.29}$$

The lab frame velocity vectors $v_x(j)$ and $v_y(j)$ can then be calculated from the position recorded for ion j (x_j,y_j) relative to the position recorded for unreacted dications (x_d,y_d).

$$v_{jx} = \frac{x_j - x_d}{t_{tot}} \tag{1.30}$$

$$v_{jy} = \frac{y_j - y_d}{t_{tot}} \tag{1.31}$$

In Equations (1.30) and (1.31), t_{tot} is the total flight time of ion j and is equal to the experimental flight time t_{exp}, corrected for timing delays.

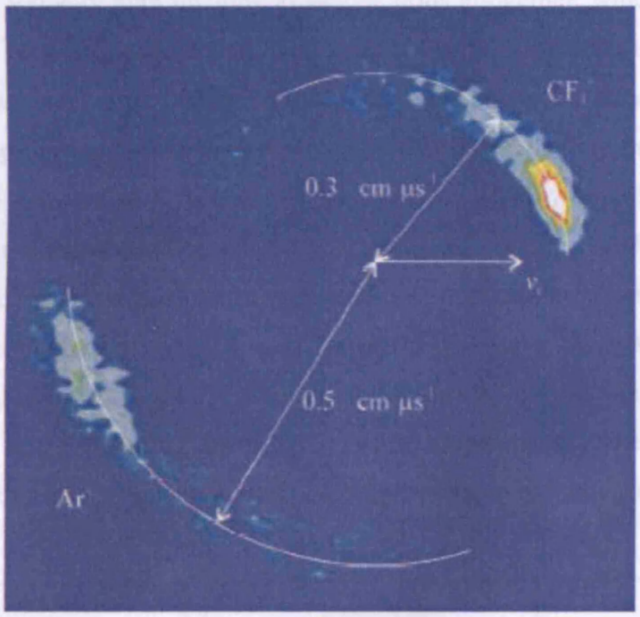

Figure 1.9 An example of a Newton diagram representing experimental PSCO data[107], in this case the non-dissociative electron transfer products of the collision CF_3^{2+} + Ar. The COM frame velocities of the products are shown relative to the velocity of the centre-of-mass. Since scattering angles of $n°$ and $(180\text{-}n)°$ are equivalent, the top half of the diagram shows the distribution of CF_3^+ and the bottom half shows Ar^+.

The principal advantage of the PSCO apparatus is that by measuring the lab frame velocity of every ion directly, the 3D angular distribution of products can be obtained simply by converting values into the centre-of-mass frame, rather than indirectly recovering the angular distribution using the inverse-Abel transform.

1.4.8 Velocity imaging[103,108]

The crucial difference between velocity map imaging and other time-of-flight methods is the use of aperture electrodes instead of grid electrodes. The technique was

discovered somewhat serendipitously when David Chandler (also an early proponent of ion-imaging) and Andre Eppink tried to solve the problems caused by the use of grid electrodes. Traditional time-of-flight methods, including ion-imaging, use linear electric fields to linearly accelerate ions. Plate electrodes, necessary to produce ideal linear fields, are clearly useless because ions must be able to pass through them. Grid electrodes are consequently used to approximate a linear electric field. However, there is an inevitable compromise between minimising field curvature and maximising ion transmission. Velocity map imaging abandons grids altogether, which results in curved source fields and less simple ion trajectories, but does permit 100% transmission. However, it was found that the non-linear source field also acts as an electrostatic lens, which, by appropriate tuning of the electrode potentials, has the property of mapping ions onto the detector as a function of their initial velocity, regardless of their initial position (over a small fraction of the source region). Unfortunately velocity imaging maps only the components of velocity that are perpendicular to the time-of-flight axis; a velocity map image of a particular product ion state thus appears as a ring, corresponding purely x and y velocity components, but within the ring there is considerable noise resulting from non-zero v_z components. The three-dimensional velocity distribution can be recovered using the inverse-Abel transform.

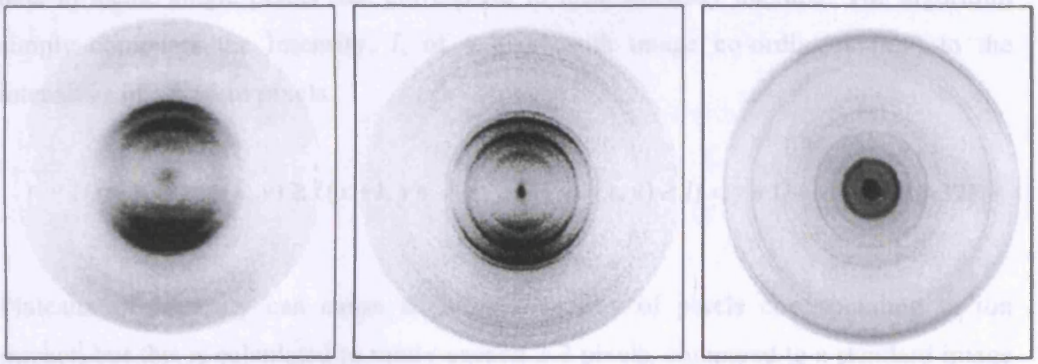

Figure 1.10 Images recorded by Eppink and Parker following the photodissociation of O_2.[103] Left: O^+ imaged using ion-imaging (with grids). Centre: O^+ imaged using velocity map imaging (without grids). Right: photoelectrons imaged by reversing the polarity of the VMI optics. The diameter of a ring indicates the off-axis speed of the product and the velocity images are of sufficient resolution not only to discern electronic levels of O^+ but also vibrational levels of the O_2^+ precursor.

It should be noted that velocity imaging was designed for, and has principally been applied to, photolytic experiments. The lensing properties of velocity imaging are very good at compensating for a spatial distribution in the x-direction, but less effective in the z-direction and the high resolution of which the technique is capable is partly due to the very small interaction region (particularly in the z-direction) formed where a laser beam intersects a molecular beam. The technique is perfectly applicable to crossed molecular beam experiments, but the resolution will inevitably be reduced by the increased size of the interaction region in such experiments.

1.4.9 Real-time ion counting[109]

CCD cameras are widely used to capture images in ion-imaging experiments, but dealing with a composite image rather than counting events individually places some severe restrictions on resolution. Firstly, an image will always include a degree of background noise, which becomes more problematic for weaker ion channels. Secondly, although a single ion is much, much smaller than a detection element in a CCD camera, the amplified signal generated by MCP plates can cover 20-30 pixels of an image, causing a major reduction in resolution.

Noise levels can be greatly reduced by applying a threshold filter to image data and discarding all pixels that fail the test. An algorithm is then applied to the remaining data to locate single pixels that correspond to local intensity maxima. The algorithm simply compares the intensity, I, of a pixel with image co-ordinates (x,y) to the intensities of adjacent pixels.

$$I(x-1,y) < I(x,y) \geq I(x+1,y),\ I(x,y-1) < I(x,y) \geq I(x,y+1) \qquad (1.32)$$

Plateaux of intensity can cause slight mis-location of pixels corresponding to ion impact, but this is calculated to rarely exceed 2-3 pixels, compared to a standard image size of 640×480 pixels.

An additional benefit of real-time ion-counting is that it greatly reduces the amount of data that must be processed in the course of an experiment.

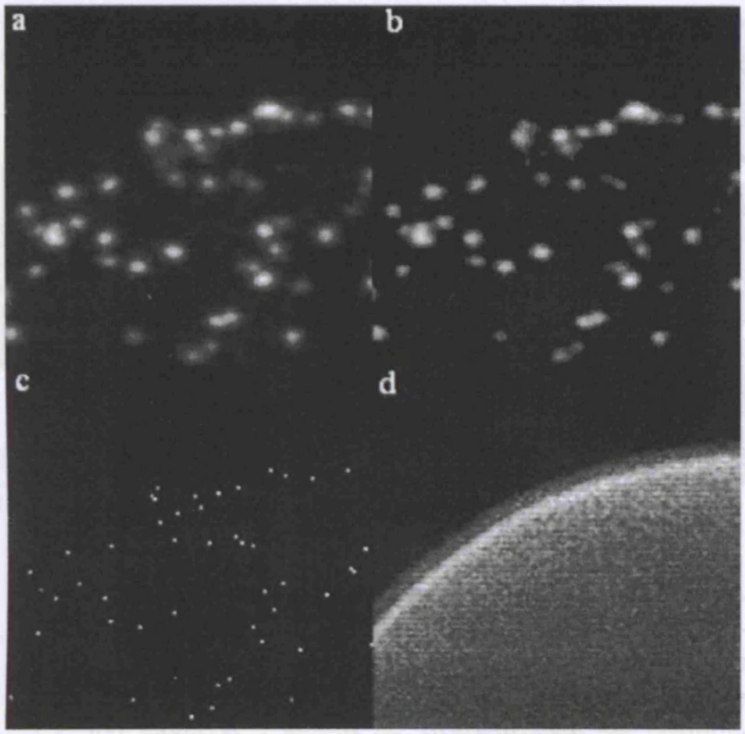

Figure 1.11 Typical partial images demonstrating the real-time ion counting at various stages of the process: a) raw data; b) after applying threshold discrimination; c) after applying the algorithm in Equation (1.32); d) accumulation of 18,000 images.

1.4.10 Slice imaging[110]

In most time-of-flight experiments studying unimolecular events, the Newton sphere (see Chapter 2) is deliberating 'pancaked', i.e. focussed so that ions of the same mass reach the detector at approximately the same time. The inverse-Abel transform then back projects the recorded image to recover the distribution of the original Newton sphere. In contrast slice-imaging delays the application of the repeller plate pulse following ionization to allow the Newton sphere to expand. This broadens the time window over which ions of the same mass are detected typically from a few tens of nanoseconds to a few hundred. The detector is then gated to detect for only a small fraction of this time and thus records a slice through the actual three-dimensional distribution.

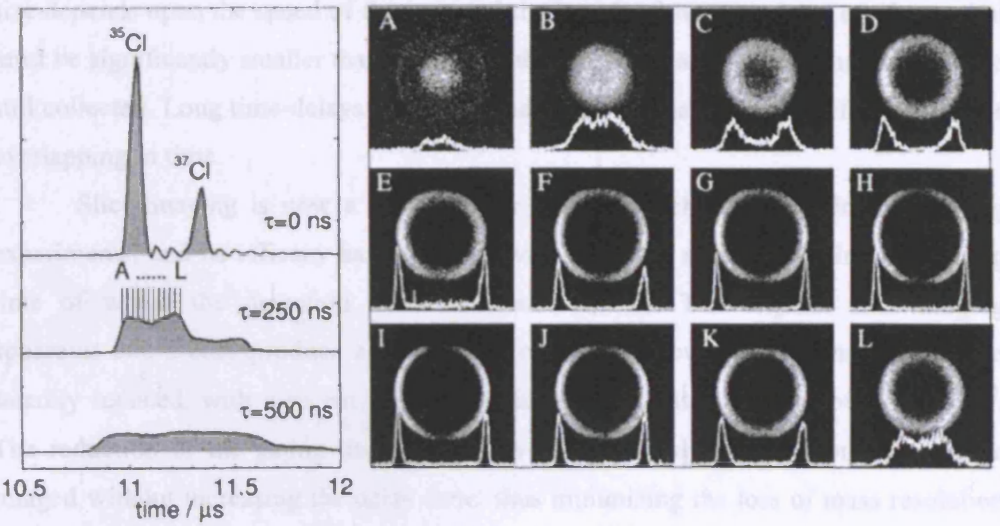

Figure 1.12 Application of slice-imaging to the photo-dissociation of Cl_2. The left-hand panel shows how the time-intensity profile changes with the delay time of the extractor pulse, τ. The right-hand panel shows slice-images through the $^{35}Cl^+$ ion cloud at τ = 250 ns, overlaid with the position-intensity profile. A normal velocity map image would be equivalent to the superimposition of all the slice images.

Each slice image is much sharper than a transformed image that contains contributions of the entire sphere. Slice imaging has been compared with experiments that used the inverse-Abel transform to obtain the angular distribution of products and the two have been found to be mutually consistent, which shows that the inverse-Abel transform, while being a purely mathematical construct, is valid in its application to ion-imaging. However, slice imaging has further advantages over transform experiments:

i) noise introduced by the inverse-Abel transform is entirely eliminated;

ii) experimental geometries are not restricted by inverse-Abel transform requirements;

iii) portions of an image can be analysed separately, while the inverse-Abel transform requires the entire distribution.

The lower limit of the time window for which the detector is gated is governed by the detection electronics, so the number of slices into which an ion cloud may be divided is dependent on the size to which the Newton sphere is initially allowed to expand. This

size depends upon the speed of the ions and the length of the time-delay employed, but must be significantly smaller than the size of the ion optics assembly so that the ions are still collected. Long time-delays may also lead to the clouds of ions of different masses overlapping in time.

Slice-imaging is now a very popular auxiliary technique in velocity imaging experiments, and its efficacy has increased with efforts to reduce the minimum gating time of which the detection electronics are capable. The original slice-imaging apparatus could only produce a 40 ns slice of the ion cloud, but this has since been steadily reduced, with a recent experiment achieving a gated window of just 6ns[111]. The reduction of the gating time allows a very narrow slice of the ion cloud to be imaged without increasing the delay time, thus minimizing the loss of mass resolution associated with slice-imaging.

1.4.11 Einzel magnification[112]

An Einzel lens is a simple device comprised of three gridless electrodes that is commonly used in time-of-flight experiments to counteract divergence of ions in the drift tube. The two outer electrodes are unbiased (relative to the surrounding region) while a large voltage (usually positive in the case of positive ions) is applied to the centre electrode. This creates a curvature of the potential that has the effect of focussing ions towards a point on the time-of-flight axis, but the symmetrical nature of the lens means that the kinetic energy of an ion is unchanged after passing through the lens. In normal use, the lens is tuned so that the focal point coincides with the detector face.

Following the advent of velocity imaging it was realised that by altering the focal point, an Einzel lens could be used to produce a magnified (and inverted) image. The degree of magnification, for otherwise fixed experimental conditions, is simply determined by the depth of the potential well produced by the lens. Importantly this is genuine magnification, resulting in improved image resolution, as opposed to enlargement of the image, which, since the resolution of the phosphor screen is limited by its component pixels, does not bring with it any increase in resolution.

Offerhaus et al. demonstrated that an Einzel lens could be used to magnify their velocity map images by more than a factor of 20 and improve the resolution of their apparatus by up to a factor of 2.5. Although magnification improves image resolution, it must be remembered that high magnification is only possible if the un-magnified image

is very small (i.e. the imaged particles have very low velocities perpendicular to the time-of-flight axis): the Offerhaus experiment detected slow electrons from the photoionization of excited Xe atoms, which produced an un-magnified image of <5 mm diameter.

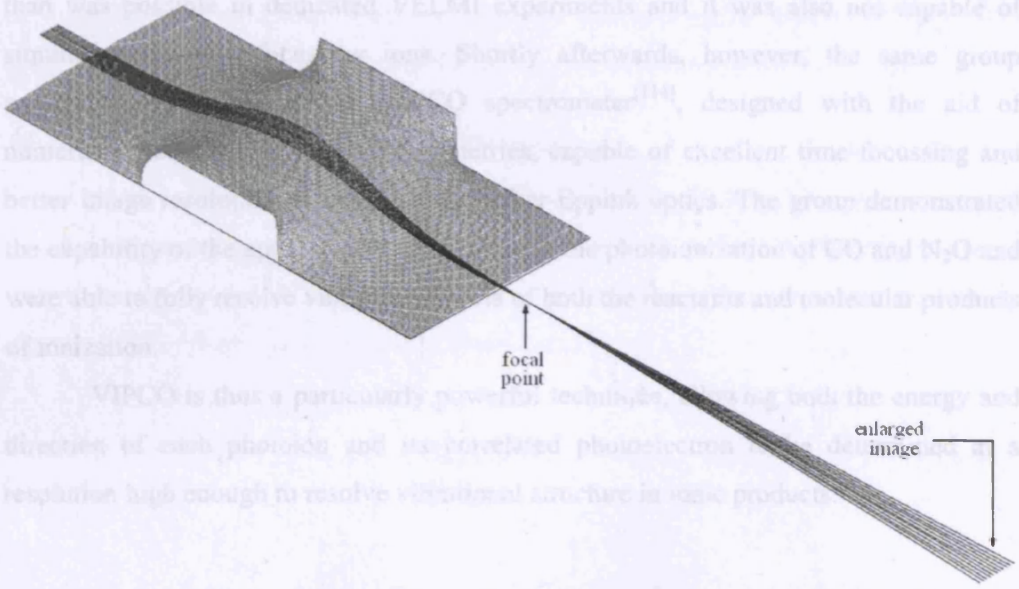

Figure 1.13 Comparison of ion trajectories with different initial displacements from the time-of-flight axis when passed through an Einzel lens. The ions shown all have initial velocities parallel to the time-of-flight axis, but an Einzel lens is a means of restraining divergent ions.

1.4.12 Velocity imaging photoionization coincidence (VIPCO) spectroscopy

Velocity imaging has also been incorporated into coincidence experiments, further advancing the information that can potentially be extracted. Velocity imaging, as it was designed, measures the angular distribution of either photoions or photoelectrons from photodissociation events. The coincidence technique PEPICO (see Section 1.4.1) is an established way of obtaining the fixed-molecule angular distribution of a reaction. Replacing both the ion and electron collecting portions of a PEPICO spectrometer with a velocity imaging set-up allows orientation information to be attributed to velocity imaging data, because the technique is 'event-wise', that is each point in either distribution (ions or electrons) can be directly paired with its corresponding pair in the other.

The first attempt to use velocity imaging in conjunction with coincidence detection was made by Eland et al. in 1999.[113] This apparatus used Parker-Eppink type optics to achieve velocity imaging of electrons, but retained gridded optics in the positive particle collector, relying on conically shaped electrodes to achieve the required lensing. The velocity imaging of ions using this spectrometer was of lower resolution than was possible in dedicated VELMI experiments and it was also not capable of simultaneously time-focussing ions. Shortly afterwards, however, the same group constructed a high-resolution VIPCO spectrometer[114], designed with the aid of numerical modelling of different geometries, capable of excellent time-focussing and better image resolution of cations than Parker-Eppink optics. The group demonstrated the capability of the apparatus by application to the photoionization of CO and N_2O and were able to fully resolve vibrational levels of both the reactants and molecular products of ionization.

VIPCO is thus a particularly powerful technique, allowing both the energy and direction of each photoion and its correlated photoelectron to be determined at a resolution high enough to resolve vibrational structure in ionic products.

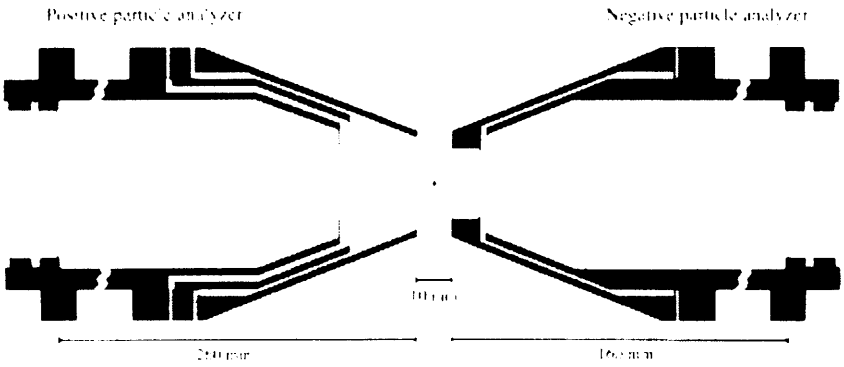

Figure 1.14 Diagram of a high resolution VIPCO spectrometer. A single grid is used to prevent field interference between the positive particle analyzer and the negative particle analyzer; electrostatic lensing is achieved by using aperture electrodes rather than shaped electrodes.

1.5 Ion optics

The arrangement of electrodes (the 'source optics') is crucial to the performance of a time-of-flight mass spectrometer. At present, our apparatus employs a pair of closely spaced grids, but there are a number of alternative source optics in common use. Reflectron instruments employ further ion optics at the end of one drift-tube to reflect ions into a second drift tube. Many of the topics discussed in this section will be drawn upon in Chapter 7 when considering the design of a new spectrometer.

1.5.1 Time-of-flight (TOF) mass spectrometry

Many of the experimental techniques covered in Section 1.4 rely on time-of-flight spectrometry to identify ionic products. This simple method has been in extensive use for many years and utilizes the fact that charged particles are accelerated by an electric field in proportion to their mass-to-charge ratio:

$$a = \frac{F}{m} = \frac{qE}{m} = \frac{ze}{m}\frac{\Delta V}{l} \tag{1.33}$$

where F is the force exerted by an electric field of magnitude E created by application of a potential difference ΔV across a distance l, on a particle of mass m and charge q (or z units of electron charge e). TOF mass spectrometers comprise source optics that create an electric field to accelerate ions of different m/z values to different velocities, a drift region with no electric field that allows ions of different velocities to be separated in time, and a detector to record flight times. The relationship between flight times and m/z value can be calculated either analytically (see Appendix A) or empirically calibrated from peaks of known mass (see Chapter 3).

The focussing properties and resolving power of a TOF mass spectrometer is crucially dependent on the source optics employed. These optics may be grid electrodes (used to produce uniform electric fields) or aperture electrodes (used to produce non-uniform electric fields) or indeed, a combination of both. It is most common to apply source fields until all ions have been extracted into the drift region, thereby accelerating ions over an equal distance and thus to an equal kinetic energy, but an alternative is to apply the source field for a fixed time, which, providing all ions remain in the electric fields for the duration of the pulse, accelerates all ions to an equal momentum[115].

The sources of aberration in a TOF mass spectrometer that are responsible for non-zero peak widths in TOF spectra can be summarized[116] as:

i) the inaccuracy of focussing in the source region because of the finite thickness of the ion formation zone or other reasons resulting in an ion energy spread;
ii) broadening due to the angular spread in ion trajectories;
iii) the deviation of the source and detector planes from perpendicularity to the instrument axis;
iv) the effective depth of the microchannel plate (the detector);
v) the effect of ions that formed in the same source plane, but with different initial energies;
vi) the slope of the leading edge of the extraction pulse;
vii) broadening of the output pulses from the detector caused by electron avalanches in the microchannel plate and in the course of amplification;
viii) the effect of stray fields in the field electrode grids;
ix) the laser pulse length (in the case of photodissociation experiments);
x) the influence of space charge created by ions.

In practice, the resolution of an experiment is limited by (i), the spatial distribution of ion formation, and (v), the initial energy distribution of ions in the source. The spatial distribution is of course much greater in crossed beam experiments, where it is determined by the volume of overlap between the ion beam and molecular beam, than in photodissociation experiments, where it is determined by the focal width of the laser. As will be discussed in the appropriate sections, source optics are designed to counteract spatial distributions, while ion mirrors are used to deal with energy distributions.

1.5.2 Wiley-McLaren source optics

Most TOF mass spectrometers in use today employ source optics based on those designed by Wiley & McLaren over fifty years ago. A Wiley-McLaren source[117] comprises three successive electrodes: a repeller, an extractor and a ground electrode. The repeller electrode is usually a plate, while the extractor and ground electrode are composed of wire mesh. The 'ground' electrode need not necessarily be grounded but

must be held at the same potential as the drift region. Reactions, be they bimolecular or unimolecular, take place half-way between the repeller plate and the extractor grid.

The source optics of a TOF mass spectrometer are used to focus ions that are formed at different positions along the z-axis. It is simple to see that an ion formed towards the rear of the source has further to travel to hit the detector than an identical ion formed towards the front of the source, but also will be accelerated to a greater velocity by virtue of spending longer in the electric fields. Thus, there will be some point in the field-free region that both our ions will reach in the same time. This point is termed the space-focus. Since the advent of velocity imaging, which maps ions as a function of velocity, the term space-focus, referring to the focussing in time of isobaric ions with different initial positions, has become a little confusing because of the term 'spatial resolution' referring to the ability to focus isobaric ions of different initial velocity but the same initial position to different positions on the detector. For this reason, the term 'time-focus' is sometimes used to indicate the temporal focussing of ions of equal mass, and is synonymous with the term 'space-focus'. Source optics produce a space-focus with respect to initial position, while ion mirrors produce a space-focus with respect to initial energy.

Mathematically, space-focussing is defined in terms of the rate of change of TOF as a function of source position, for a fixed mass:charge ratio, at the centre of the source. For a spatial displacement from the centre of the source along the z-axis, s_z, the first-order space-focussing condition is:

$$\left[\frac{\partial t}{\partial s_z}\right]_{s_z=0} = 0 \qquad (1.34)$$

Likewise, n^{th} order space-focussing requires the n^{th} differential to be zero.

$$\left[\frac{\partial^n t}{\partial s_z^n}\right]_{s_z=0} = 0 \qquad (1.35)$$

Notice that these conditions apply to the centre of the source ($s_z = 0$) and do not explicitly describe how the focussing behaves across the source region. However, the

order of space-focussing at the centre of the source is a good indicator of how rapidly flight times will change with small displacements in source position.

A single linear electric field can only achieve first-order space-focussing, in fact the best space-focussing that can be obtained from an n-stage source is n^{th}-order. Hence, ideal (infinite-order) space-focussing requires an infinite number of linear source fields, or, in other words, a non-linear source field. Constructing electrodes that produce the correct field curvature for such non-linear electric fields, is extremely difficult, and most experimentalists settle for second- or even first-order space-focussing.

The uniform electric fields employed in a Wiley-McLaren source allow ion trajectories to be calculated using simple equations of motion. The optimum parameters for the source geometry can be found by deriving focussing conditions from these calculated trajectories. A full derivation of the focussing conditions of a Wiley-McLaren source is included in Appendix A, but the original authors found that a linear two-stage source could achieve first-order space-focussing if it satisfied the condition:

$$l_{ff} = l_s k^{\frac{3}{2}} \left(1 - \frac{l_a}{\frac{1}{2} l_s (k + k^{-1})} \right) \tag{1.36}$$

where l_s, l_a and l_{ff} are the lengths of the first electric field (called the source region), the second electric field (the acceleration region) and the field-free region respectively, and k is defined as:

$$k = 1 + \frac{l_a a_a}{\frac{1}{2} l_s a_s} \tag{1.37}$$

where a refers to acceleration, using the same subscripts as before.

Much later, Eland demonstrated that another solution to Wiley & McLaren's equations allowed second-order space-focussing to be achieved using a two-stage source.[115] The field-free path length required to reach the focal point now became:

$$l_{ff} = l_s k^{\frac{1}{2}} \left(\frac{k^{\frac{1}{2}} - 1}{k + k^{\frac{1}{2}} - 2} \right) \tag{1.38}$$

with a further condition relating the drift length to the length of the second source field:

$$\frac{l_{ff}}{l_a} = 2 + \frac{6}{k - 3} \tag{1.39}$$

The principal result of these second-order focussing conditions is to significantly lengthen the acceleration region in proportion to the source region. The ratio l_a/l_s is usually 0.5 in a standard Wiley-McLaren spectrometer, but 5 using an Eland-type source.

1.5.3 Velocity imaging source optics

The velocity imaging technique has already been discussed in Section 1.4.8. The important difference between velocity imaging and traditional linear field source is the absence of grids. This creates a non-uniform electric field that acts as an electrostatic lens and spatially focuses ions as a function of their initial velocity.

1.5.4 Summary of source optics

The principal purpose of source optics in TOF mass spectrometry is to accelerate ions of different mass to different velocities, allowing them to be identified by differences in flight time. Ideally ions of the same mass should be time-focussed so that they have the same flight time regardless of their initial position. The use of aperture electrodes to produce curved source fields allows ions to be mapped onto a position sensitive detector as a function of their initial velocity, independently of their initial position, and in addition to time-focussing ions by mass. No source is able to time-focus ions as a function of their initial energy, however ion mirrors can be used for this purpose (see Section 1.5.5). The most important source geometries are compared in Figure 1.15.

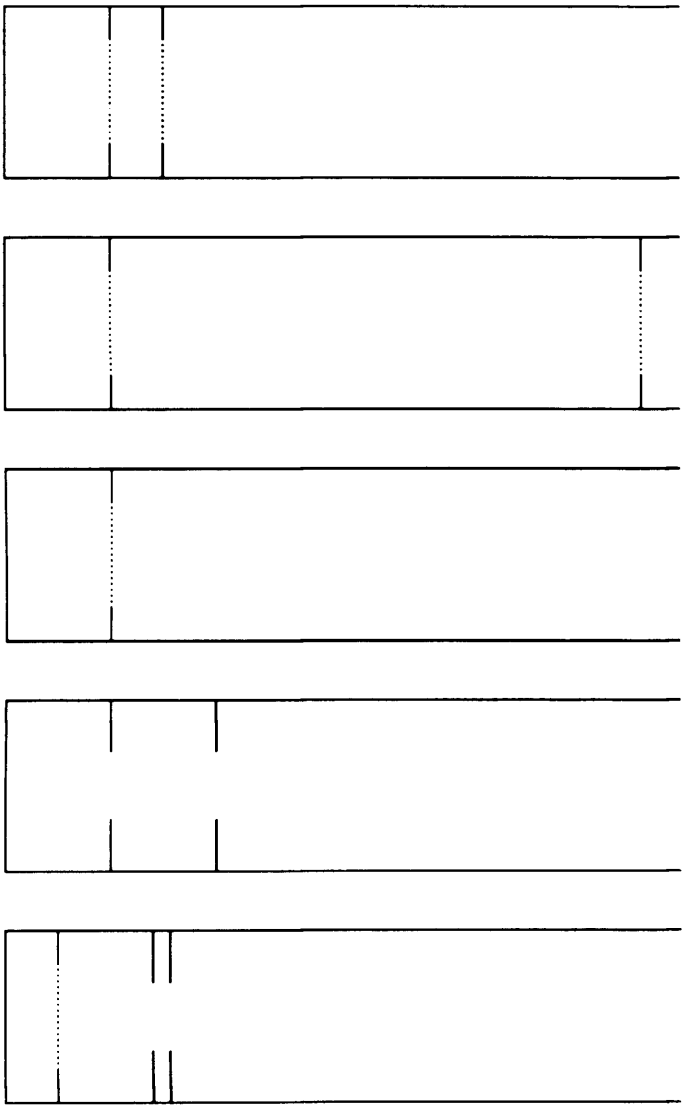

Figure 1.15 Summary of the principal source geometries employed in TOF mass spectrometry. Voltages can be applied independently to all electrodes whether plates, grids or apertures. The distance from the centre of the source to the time-focus will depend on the source geometry and the applied voltages. From top: Wiley-McLaren linear source (1^{st}-order space-focussing); the Eland-type linear source (2^{nd}-order space focussing); an ion-imaging source; Parker & Eppink's velocity imaging source; high-resolution VIPCO source (positive particle collector only).

1.5.5 Ion mirrors (reflectrons)

While source optics are used to focus in time ions of the same mass and the same initial velocity but different initial positions, ion mirrors are used to focus in time ions of the same mass and the same initial position but different initial velocities. In fact, ion mirrors correct for different initial z-components of velocity, which may be ions with the same kinetic energy but different directions, or ions with the same direction but different kinetic energies; for this reason the term 'energy-focussing' is often used. An ion mirror is simply a retarding electric field (or fields) that reverses the direction of incoming ions. Ions of the same mass but different speeds penetrate varying distances into the ion mirror. The speed of an ion is the same as it exits an ion mirror as

when it entered, but the time spent in the mirror is longer for faster ions. Thus an ion mirror allows the flight times of faster moving ions to be extended relative to those of slower moving ions. In this way, a focal point will occur in the field-free region that all ions (ideally) will reach at the same time, regardless of their initial velocity.

The development of reflectron time-of-flight (RTOF) mass spectrometry has been driven largely by the interest biochemistry, and much literature has been published on the subject. Experiments conducted on biological molecules, while operating on the same principle, have significant practical differences to those that we conduct, which involve lower mass species and employ relatively low electric fields. Firstly, microchannel plates, which are commonly used as ion detectors, have a detection threshold dependent on momentum ($\propto v$) so massive ions must be accelerated to very high kinetic energies ($\propto v^2$) in order to be efficiently detected and consequently very large electric fields are required. Ionizing large molecules is also problematic, because simple techniques such as photoabsorption or electron-impact tend to fragment the target molecules. It is only in the past twenty years that soft ionization techniques, such as MALDI and ESI (see Section 1.3.3), have been developed to allow non-dissociative ionization of biomelecules. Another factor is that the greater the mass of the target molecule, the higher the mass resolution required of the spectrometer. By recalling the basic formula $t^2 \propto m/z$, it can be seen that the spacing between adjacent mass peaks decreases as the mass increases:

$$\frac{t_{m+1}}{t_m} = \sqrt{\frac{m+1}{m}} \tag{1.40}$$

We can seen from this that the TOF of D^+ is $\sqrt{2}$ times greater than that of H^+, but this factor becomes $\sqrt{1.001}$ for masses of 1000 and 1001 amu. Mass resolution is defined as the ratio of the ion mass to the mass difference that can be distinguished, $m/\Delta m$. The mass limit of an experiment is the highest mass for which $\Delta m > 1$ (in the case of singly charged ions). So, as resolutions improve, larger and larger biomolecules can be studied using TOF mass spectrometry. Multiple reflectron instruments (which have several mirrors and flight tubes) can achieve resolutions in excess of 10^4, which allows large proteins to be studied using the technique.[116] In contrast, in the low mass ranges we

study (m < 100 amu) much lower resolution is still sufficient to resolve peaks. However, reflectrons can still have a role in analysing metastable decay, as will be discussed later.

The first RTOF mass spectrometry apparatus was devised by Boris Mamyrin in the 1970s.[119,120] The electric fields of a Mamyrin reflector are linear along the axis of cylindrical symmetry and uniform in the radial direction. Mamyrin reflectors may be single stage, but are usually dual-stage, comprising a short, high-field deceleration region and a longer, lower-field reflection region.

The electrodes of an ion mirror must be at some small angle to the source grids to avoid ions being reflected back at the source, although a few machines deal with this by having a 'transparent' source with the detector directly behind it. The angle between the mirror and source should be as small as possible, because the mirror only focuses components of velocity perpendicular to the grids. In fact, small angles make very little difference to flight times, which are dependent on the z-component of velocity (since $\cos 3^\circ \approx 0.999 \approx 1$) but must be considered for the x,y displacement of ions, which is dependent on the transverse components of velocity (since $\sin 3^\circ \approx 0.052 \neq 0$).

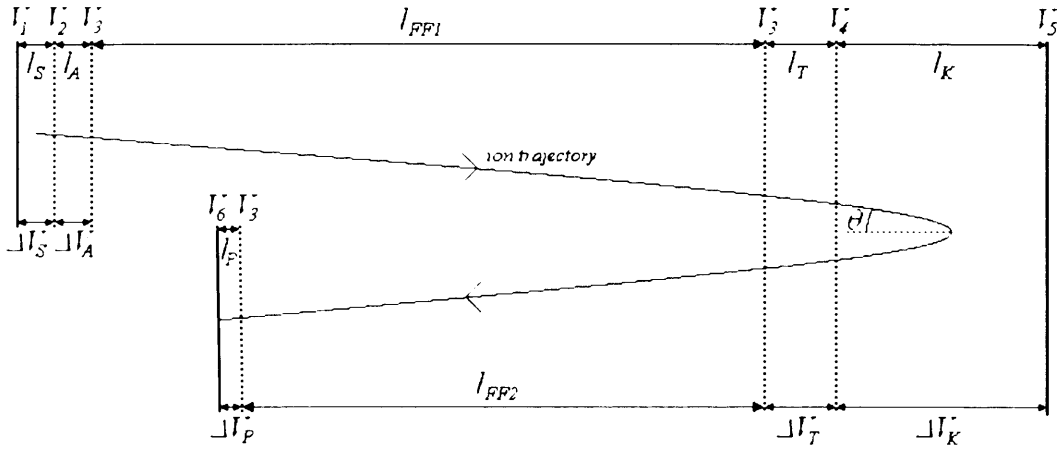

Figure 1.16 Schematic of a Mamyrin-type RTOF mass spectrometer. The regions of importance are the source (S), acceleration (A), first drift (FF1), deceleration (T), reflection (K), second drift (FF2) and pre-detection (P). The electrodes have been drawn parallel to each other, but in reality the ion mirror must be at a small angle θ with respect to the source fields in order to transversely displace ions so that they are reflected towards the detector rather than back at the source.

The order of energy focussing of which a linear field ion mirror is capable is equal to the number of stages, in the same way that the space-focusing power of a Wiley-McLaren source increases with the number of stages. Although an ideal parabolic reflecting field gives ideal space-focussing, such a field is very difficult to produce in practice. A good approximation of a parabolic field requires complex 3D electrode arrangements, such as stacks of thin ring electrodes or hyperbolic bar electrodes. Electrodes like this are expensive to produce to the required precision and difficult to adjust from experiment to experiment. Consequently, considerable research has been directed towards generating non-linear ion mirrors with good space-focussing properties using simpler electrode geometries.

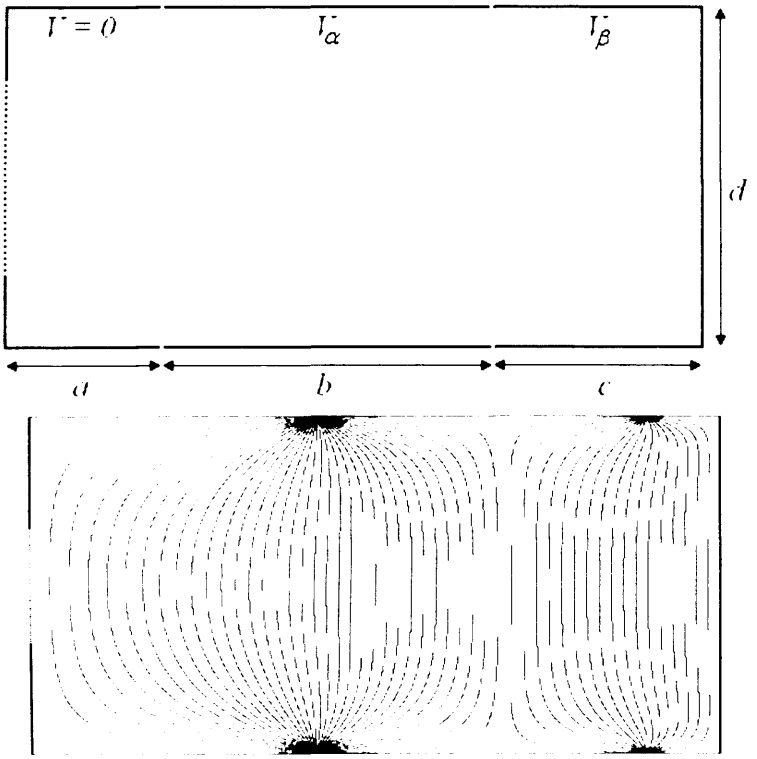

Figure 1.17 Cross-section of a Zhang-Enke mirror. The properties of the mirror can be modelled for different dimensions a, b, c and d and voltages V_α and V_β (top image). The equipotentials are shown in the bottom image.

The most successful product of these endeavours is the Zhang-Enke mirror[121-123], first described in 2000. The Zhang-Enke mirror is simply a cylinder comprised of three elements held at different potentials and enclosed by a grid where it adjoins the drift tube (Figure 1.17). The Zhang-Enke mirror is a good approximation of a parabolic field,

but the amount of deviation from the ideal field increases with radial distance from the symmetry axis.

1.6 Bimolecular reactivity of dications

The principal objective of this thesis is to observe, understand and descibe the bimolecular reactivity of dications with neutral species. This reactivity may be broadly classified as electron transfer, collision-induced fragmentation and bond-formation; these types of reaction are discussed in the following sections.

1.6.1 Electron transfer

In most dication-neutral collision systems, transfer of a single electron is seen to be the strongest reaction channel.

$$AB^{2+} + CD \rightarrow AB^{+} + CD^{+} \qquad (1.41)$$

Reaction (1.41) represents non-dissociative electron transfer, but either, or indeed both, of the products may be formed in a dissociative electronic state and rapidly fragment to form an ion-neutral pair.

The mechanism of single electron transfer (SET) is often understood using the Reaction Window model[124], which is based on the Landau-Zener theory[125,126] of adiabatic transitions. This model is explained in detail in Chapter 2, but is essentially concerned with calculating the quantity δ, defined as the probability of remaining on a non-adiabatic potential energy surface as it makes an intersection with another surface. In the course of a collision, considering only a single reactant potential and a single product potential, such an intersection will be encountered twice and so the probability of SET occurring is maximized when $\delta = 0.5$. In a dication-neutral collision system, the reaction window is the term given to the range of interspecies separation in which the surface intersection must lie in order for SET to be significant. The reaction window may be described in terms of separation or exothermicity since the point of intersection between a dication-neutral potential energy surface and a monocation-monocation surface is determined largely by the asymptotic exothermicity, rather than the exact chemical identity of the species involved. As a consequence, the reaction window of electron transfer in a dication neutral system may be approximated as 3-5 Å or ~4 eV

(Figure 1.18). Note that this behaviour is in marked contrast to singly charged systems, in which both the reactants and products of SET are a monocation-neutral pair. Therefore, the similarity between the shapes of the product and reactant potentials means that intersection will only occur at all due to slight differences in curvature and thus only at very low exothermicities. It is a principal difference between dication and monocation chemistry that electron transfer of the former is most efficient at much larger exothermicities than the latter.

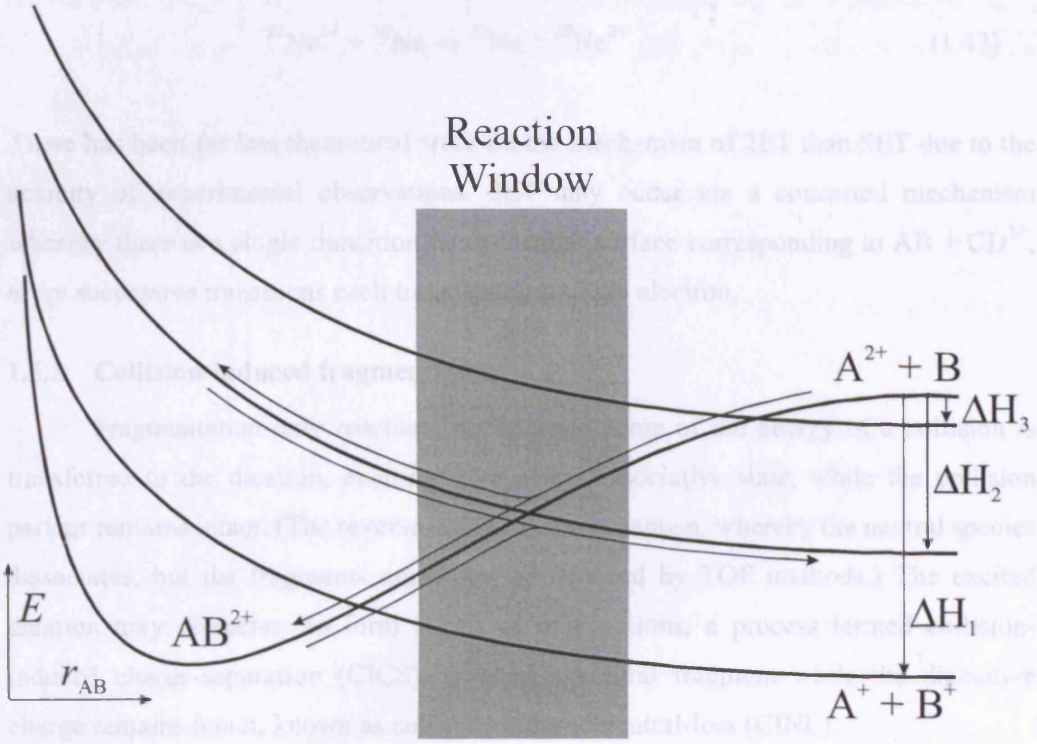

Figure 1.18 Diagram showing the interrelationship between separation r and asymptotic exothermicity ΔH for SET between a dication and a neutral species. The reaction window is a qualitative region for which SET is most efficient. Only intersections inside the reaction window have a significant probability of resulting in SET; these correspond to moderate exothermicities (i.e. ΔH_2), typically a few eV.

Double electron transfer (2ET) is the transfer of a pair of electrons from the neutral collision partner to the dication.

$$AB^{2+} + CD \rightarrow AB + CD^{2+} \quad (1.42)$$

Although 2ET is common in the collisions of higher multiply charged ions, it is very rarely observed in the collisions of dications. One such example is between isotopic Ne[127]:

$$^{22}Ne^{2+} + {}^{20}Ne \rightarrow {}^{22}Ne + {}^{20}Ne^{2+} \quad (1.43)$$

There has been far less theoretical work on the mechanism of 2ET than SET due to the scarcity of experimental observations. 2ET may occur via a concerted mechanism whereby there is a single transition to a potential surface corresponding to $AB + CD^{2+}$, or by successive transitions each transferring a single electron.

1.6.2 Collision-induced fragmentation

Fragmentation-only reactions occur when some of the energy of a collision is transferred to the dication, exciting it to a pre-dissociative state, while the collision partner remains intact. (The reverse could of course happen, whereby the neutral species dissociates, but the fragments could not be detected by TOF methods.) The excited dication may dissociate to form a pair of monocations, a process termed collision-induced charge-separation (CICS), or shed a neutral fragment while the dipositive charge remains intact, known as collision-induced neutral-loss (CINL).

$$AB^{2+} + C \rightarrow A^{+} + B^{+} + C \quad (1.44)$$

$$AB^{2+} + C \rightarrow A^{2+} + B + C \quad (1.45)$$

It is worth noting at this point that if a reactive event results in n products, then n-1 products must be detected in coincidence in order to derive the full dynamics of the reaction (the properties of the undetected product being calculated using conservation of momentum). Consequently, any reaction that produces two or more neutral products,

such as the CINL reaction above, cannot be fully kinematically understood using TOF methods.

Collision-induced fragmentation reactions are not discussed further in this thesis, since neither CICS or CINL channels are observed in the systems that comprise the reported experimental results.

1.6.3 Bond-formation

In some low energy collision systems, bimolecular reactions that form new chemical bonds have been observed. Reports in the literature regarding this class of dication reactivity is limited, but growing.[100] Bond-forming reactions tend to be much weaker than other reaction channels, sometimes 100 times weaker than electron transfer.

Most bond-forming reactions in dication-neutral systems involve the separation of the dipositive charge, thus yielding a pair of monocations.

$$AB^{2+} + CD\ (\rightarrow ABCD^{\ulcorner 2+}) \rightarrow ABC^{+} + D^{+} \qquad (1.46)$$

Bond-forming reactions are usually thought to proceed via a collision complex because of the broad angular distributions associated with the products. However, the most simple bond-forming reactions, hydride transfer to the dication and proton transfer to the neutral reactant, are often considered as 'heavy' electron transfer and treated with Landau-Zener theory.

Hydride transfer (for example, Reaction 1.47[128]) is most common in collisions of transition metal dications, because the relatively low second ionization potential of these species means that the exothermicity between the reactants (TM^{2+} + HX) and the electron transfer products (TM^{+} + HX^{+}) is usually small and hence electron transfer is suppressed. In contrast, in the collisions of molecular dications, the electron transfer dominates because these products (AB^{+} + HX^{+}) tend to lie lower in energy than the hydride transfer products.

$$Y^{2+} + C_2H_6 \rightarrow YH^{+} + C_2H_5^{+} \qquad (1.47)$$

Proton transfer (for example Reaction 1.48[129]) is often seen in the reactions of H-bearing dications. A recent study[129] has compared a wide number of reactions between HCX^{2+} (where X is any halogen from F to I) and a variety of neutral collision partners. Polar collision partners were found to favour proton transfer over electron transfer, similarly to the proton transfer between HCl^{2+} and CO described in Chapter 6.

$$HCBr^{2+} + CO \rightarrow CBr^{+} + HCO^{+} \qquad (1.48)$$

In 1999, Bassi et al. observed the first dication-neutral reaction to form a doubly charged product[130]:

$$Ar^{2+} + N_2 \rightarrow ArN^{2+} + N \qquad (1.49)$$

The same group have since reported a number of such reactions[94,131,132], including the formation of ArC^{2+}, which proceeds from both atomic and molecular dication reactants.

$$Ar^{2+} + CO \rightarrow ArC^{+} + O \qquad (1.50)$$

$$CO^{2+} + Ar \rightarrow ArC^{+} + O \qquad (1.51)$$

The schematic energy diagram, Figure 1.19, demonstrates why the formation of a doubly charged product is so improbable. Consider a simple triatomic system, X^{2+} + YZ, ignoring, for simplicity, the possibility of vibrational or electronic excitation. Firstly, to reach a collision complex (XYZ^{2+}), the system must avoid crossing to a repulsive potential surface (electron transfer) as the reactants approach. The collision complex may then separate via the X–Y bond or the Y–Z bond. In the former case, the system returns to its initial reactants (or may undergo electron transfer when passing through intersection [A] again). In the latter case, the separating complex must avoid crossing onto another repulsive potential surface (corresponding to $XY^{+} + Z^{+}$) and possess sufficient kinetic energy to surmount any barrier associated with the formation of $XY^{2+} + Z$, which is often endothermic with respect to the reactants. Additionally, in order to be detected, the doubly charged product XY^{2+} must be formed in a stable or metastable electronic state that lives long enough to reach the detector.

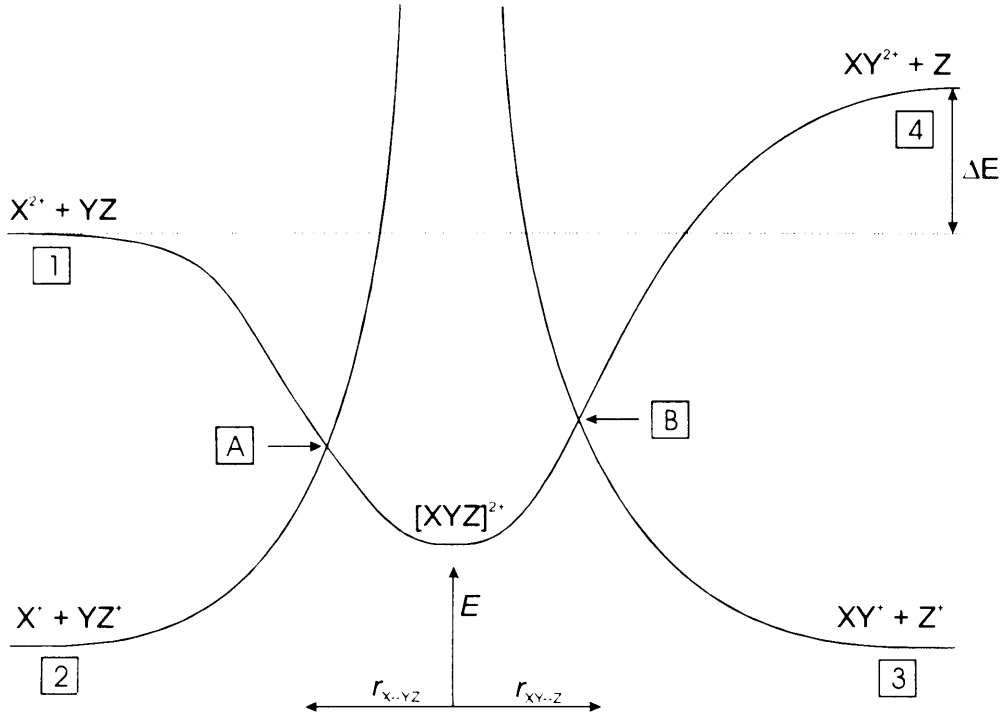

Figure 1.19 Schematic diagram of the possible (non-dissociative) products of a dication-neutral collision. The numbered asymptotes correspond to: [1] reactants; [2] SET products; [3] bond-formation w/ charge separation; [4] bond-formation w/o charge separation. In this prototypical model (neglecting excited states) there are two intersections at which an adiabatic transfer may occur ([A] and [B]), and a doubly charged collision complex en route to chemically new products.

1.7 Summary

This chapter puts the subject of this thesis into context by explaining the motivation behind the work and providing an overview of the most common experimental techniques employed in the field of ion chemistry. The following chapters provide more detail on a number of aspects of theory that are important to understanding the collision systems investigated in later chapters. The object of the experimental work is to obtain relative reaction cross-sections for the products of dication-neutral reactions, and to this end a great deal of work has been done to improve the analysis of experimental data. Over the course of the past three years, a wide number of collision systems have been surveyed, but those reported here have been selected for their novel chemistry. The final chapter includes a proposed designed for upgrading the apparatus to be a more powerful probe into reaction dynamics.

1.8 References

[1] N.M.M. Nibbering, *Mass Spectrom. Rev.* **25:** 962 (2006)
[2] J. Caillat, A. Dubois, I. Sundvor and J.P. Hansen, *Phys. Rev. A* **70:** (2004)
[3] J.S. Brodbelt, *Mass Spectrom. Rev.* **16:** 91 (1997)
[4] M. Speranza, *Int. J. Mass Spectrom.* **232:** 277 (2004)
[5] S. Gronert, *Chem. Rev.* **101:** 329 (2001)
[6] P.B. Armentrout, *Int. J. Mass Spectrom.* **200:** 219 (2000)
[7] W. Lindinger, A. Hansel and Z. Herman (2000) in *Advances in Atomic, Molecular, and Optical Physics, Vol 43 (Advances in Atomic Molecular and Optical Physics)* vol 43, p 243
[8] G.V. Karachevtsev and P.S. Vinogradov, *Uspekhi Khimii* **68:** 605 (1999)
[9] B. Brutschy, *Chem. Rev.* **92:** 1567 (1992)
[10] P. Tosi, *Chem. Rev.* **92:** 1667 (1992)
[11] H. Nakamura, *Adv. Chem. Phys.* **82:** 243 (1992)
[12] N.M.M. Nibbering, *Accounts Chem. Res.* **23:** 279 (1990)
[13] P.M. Guyon and E.A. Gislason, *Top. Curr. Chem.* **151:** 161 (1989)
[14] E.E. Ferguson, *Annu. Rev. Phys. Chem.* **26:** 17 (1975)
[15] B.H. Mahan, *Accounts Chem. Res.* **3:** 393 (1970)
[16] J.L. Franklin, P.K. Ghosh and Studniar.S, *Advances in Chemistry Series* 59 (1969)
[17] L. Friedman, *Annu. Rev. Phys. Chem.* **19:** 273 (1968)
[18] M.J. Henchman, *Annu. Rep. Prog. Chem.* **62:** 39 (1965)
[19] E. Herbst, *Annu. Rev. Phys. Chem* **46:** 27 (1995)
[20] D. Smith and P. Spanel, *Mass Spectrom. Rev.* **14:** 255 (1995)
[21] N.A. Love and S.D. Price, *Phys. Chem. Chem. Phys.* **6:** 4558 (2004)
[22] N.A. Love and S.D. Price, *Int. J. Mass Spectrom.* **233:** 145 (2004)
[23] S. Harper, P. Calandra and S.D. Price, *Phys. Chem. Chem. Phys.* **3:** 741 (2001)
[24] H.C. Straub, M.A. Mangan, B.G. Lindsay, K.A. Smith and R.F. Stebbings, *Rev. Sci. Instrum.* **70:** 4238 (1999)
[25] B.G. Lindsay, M.A. Mangan, H.C. Straub and R.F. Stebbings, *J. Chem. Phys.* **112:** 9404 (2000)
[26] M.A. Mangan, B.G. Lindsay and R.F. Stebbings, *J. Phys. B* **33:** 3225 (2000)
[27] D. Mathur, L.H. Andersen, P. Hvelplund, D. Kella and C.P. Safvan, *J. Phys. B* **28:** 3415 (1995)
[28] I. Ben-Itzhak, J.P. Bouhnik, B.D. Esry, I. Gertner and B. Rosner, *Chem. Phys. Lett.* **307:** 287 (1999)
[29] H. Hogreve, *Chem. Phys.* **314:** 49 (2005)
[30] T. Sedivcova, P.R. Zd'anska, V. Spirko and J. Fiser, *J. Chem. Phys.* **124:** (2006)
[31] S.G. Cox, A.D.J. Critchley, P.S. Kreynin, I.R. McNab, R.C. Shiell and F.E. Smith, *Phys. Chem. Chem. Phys.* **5:** 663 (2003)
[32] D. Mathur, *Phys. Rep. - Rev. Sec. Phys. Lett.* **225:** 193 (1993)
[33] D. Schroder and H. Schwarz, *J. Phys. Chem. A* **103:** 7385 (1999)
[34] L.H. Andersen, J.H. Posthumus, O. Vahtras, H. Agren, N. Elander, A. Nunez, A. Scrinzi, M. Natiello and M. Larsson, *Phys. Rev. Lett.* **71:** 1812 (1993)
[35] J. Senekowitsch, S. Oneil, P. Knowles and H.J. Werner, *J. Phys. Chem.* **95:** 2125 (1991)
[36] F.R. Bennett and I.R. McNab, *Chem. Phys. Lett.* **251:** 405 (1996)
[37] S. Leach, J.H.D. Eland and S.D. Price, *J. Phys. Chem.* **93:** 7575 (1989)

[38] K.L. Bell, H.B. Gilbody, J.G. Hughes, A.E. Kingston and F.J. Smith, *J. Phys. Chem. Ref. Data* **12:** 891 (1983)
[39] H. Tawara and T. Kato, *Atomic Data and Nuclear Data Tables* **36:** 167 (1987)
[40] H. Deutsch, K. Becker, S. Matt and T.D. Mark, *Int. J. Mass Spectrom.* **197:** 37 (2000)
[41] J. Berakdar, A. Lahmam-Bennani and C. Dal Cappello, *Phys. Rep. - Rev. Sec. Phys. Lett.* **374:** 91 (2003)
[42] J. Morellec, D. Normand and G. Petite, *Adv. Atom. Mol. Phys.* **18:** 97 (1982)
[43] P.M. Johnson, *Accounts Chem. Res.* **13:** 20 (1980)
[44] K.W.D. Ledingham and R.P. Singhal, *Int. J. Mass Spectrom. Ion Process.* **163:** 149 (1997)
[45] L. Zandee and R.B. Bernstein, *J. Chem. Phys.* **70:** 2574 (1979)
[46] L. Zandee and R.B. Bernstein, *J. Chem. Phys.* **71:** 1359 (1979)
[47] K. Kimura, *J. Elec. Spec. Rel. Phenom.* **100:** 273 (1999)
[48] S. Mark, T. GlenewinkelMeyer and D. Gerlich, *Int. Rev. Phys. Chem.* **15:** 283 (1996)
[49] K.-M. Weitzel (2000) in *Advanced Series in Physical Chemistry* Ng C-Y (ed) vol 10A, World Scientific Publishing Co. Ltd
[50] K. Tanaka, H. Waki, Y. Ido, S. Akita, Y. Yoshida and T. Yoshida, *Rapid Commun. Mass Spectrom.* **2:** 151 (1988)
[51] M. Karas, D. Bachmann and F. Hillenkamp, *Anal. Chem.* **57:** 2935 (1985)
[52] M. Karas, D. Bachmann, U. Bahr and F. Hillenkamp, *Int. J. Mass Spectrom. Ion Process.* **78:** 53 (1987)
[53] J.B. Fenn, M. Mann, C.K. Meng, S.F. Wong and C.M. Whitehouse, *Mass Spectrom. Rev.* **9:** 37 (1990)
[54] J.B. Fenn, M. Mann, C.K. Meng, S.F. Wong and C.M. Whitehouse, *Science* **246:** 64 (1989)
[55] K.E. McCulloh, T.E. Sharp and Rosensto.Hm, *J. Chem. Phys.* **42:** 3501 (1965)
[56] H.M. Rosenstock, K.E. McCulloh and F.P. Lossing, *Int. J. Mass Spectrom. Ion Process.* **25:** 327 (1977)
[57] K.A. Newson and S.D. Price, *Int. J. Mass Spectrom. Ion Process.* **153:** 151 (1996)
[58] G. Dujardin, S. Leach, O. Dutuit, P.M. Guyon and M. Richardviard, *Chem. Phys.* **88:** 339 (1984)
[59] T. Masuoka, A. Okaji and A. Kobayashi, *Int. J. Mass Spectrom.* **218:** 11 (2002)
[60] I.W. Griffiths, D.E. Parry and F.M. Harris, *Chem. Phys.* **238:** 21 (1998)
[61] S.D. Price and J.H.D. Eland, *J. Elec. Spec. Rel. Phenom.* **52:** 649 (1990)
[62] J.H.D. Eland, *Chem. Phys.* **294:** 171 (2003)
[63] M.E. Gellender and A.D. Baker, *Int. J. Mass Spectrom. Ion Process.* **17:** 1 (1975)
[64] B.P. Tsai, T. Baer, A.S. Werner and S.F. Lin, *J. Phys. Chem.* **79:** 570 (1975)
[65] T. Baer, *Int. J. Mass Spectrom.* **200:** 443 (2000)
[66] R.I. Hall, A. McConkey, K. Ellis, G. Dawber, L. Avaldi, M.A. Macdonald and G.C. King, *Meas. Sci. Technol.* **3:** 316 (1992)
[67] G. Dawber, A.G. McConkey, L. Avaldi, M.A. Macdonald, G.C. King and R.I. Hall, *J. Phys. B* **27:** 2191 (1994)
[68] A.G. McConkey, G. Dawber, L. Avaldi, M.A. Macdonald, G.C. King and R.I. Hall, *J. Phys. B* **27:** 271 (1994)

[69] M. Sander, L.A. Chewter, K. Mullerdethlefs and E.W. Schlag, *Physical Review A* **36:** 4543 (1987)
[70] B. Krassig and V. Schmidt, *J. Phys. B* **25:** L327 (1992)
[71] Cvejanov.S and F.H. Read, *J. Phys. B* **7:** 1180 (1974)
[72] L. Avaldi, G. Dawber, N. Gulley, H. Rojas, G.C. King, R. Hall, M. Stuhec and M. Zitnik, *J. Phys. B* **30:** 5197 (1997)
[73] A.J. Yencha, A.M. Juarez, S.P. Lee and G.C. King, *Chem. Phys. Lett.* **381:** 609 (2003)
[74] R.I. Hall, L. Avaldi, G. Dawber, A.G. McConkey, M.A. Macdonald and G.C. King, *Chem. Phys.* **187:** 125 (1994)
[75] J.H.D. Eland, *Mol. Phys.* **61:** 725 (1987)
[76] S. Leach, J.H.D. Eland and S.D. Price, *Journal of Physical Chemistry* **93:** 7575 (1989)
[77] M. Lundqvist, P. Baltzer, D. Edvardsson, L. Karlsson and B. Wannberg, *Phys. Rev. Lett.* **75:** 1058 (1995)
[78] M. Lundqvist, P. Baltzer, D. Edvardsson, L. Karlsson and B. Wannberg, *Physical Review Letters* **75:** 1058 (1995)
[79] M. Lundqvist, D. Edvardsson, P. Baltzer, M. Larsson and B. Wannberg, *J. Phys. B* **29:** 499 (1996)
[80] M. Lundqvist, D. Edvardsson, P. Baltzer and B. Wannberg, *J. Phys. B* **29:** 1489 (1996)
[81] D. Edvardsson, M. Lundqvist, P. Baltzer, B. Wannberg and S. Lunell, *Chem. Phys. Lett.* **256:** 341 (1996)
[82] F.M. Harris, *Int. J. Mass Spectrom. Ion Process.* **120:** 1 (1992)
[83] J. Appell, J. Durup, Fehsenfe.Fc and P. Fournier, *J. Phys. B* **6:** 197 (1973)
[84] J. Appell, J. Durup, Fehsenfe.Fc and P. Fournier, *J. Phys. B.* **7:** 406 (1974)
[85] O. Furuhashi, T. Kinugawa, S. Masuda, C. Yamada and S. Ohtani, *Chem. Phys. Lett.* **342:** 625 (2001)
[86] P.G. Fournier, H. Aouchiche, V. Lorent and J. Baudon, *Physical Review A* **34:** 3743 (1986)
[87] D.B. Dunkin, Fehsenfe.Fc, Schmelte.Al and E.E. Ferguson, *J. Chem. Phys.* **49:** 1365 (1968)
[88] Schmelte.Al, E.E. Ferguson and Fehsenfe.Fc, *J. Chem. Phys.* **48:** 2966 (1968)
[89] J. Berkowitz, W.A. Chupka and G.B. Kistiakowsky, *J. Chem. Phys.* **25:** 457 (1956)
[90] R.B. Norton, E.E. Ferguson, Fehsenfe.Fc and Schmelte.Al, *Planet. Space Sci.* **14:** 969 (1966)
[91] N.G. Adams and D. Smith, *Int. J. Mass Spectrom. Ion Process.* **21:** 349 (1976)
[92] E. Teloy and D. Gerlich, *Chem. Phys.* **4:** 417 (1974)
[93] J. Jasik, J. Roithova, J. Zabka, R. Thissen, I. Ipolyi and Z. Herman, *Int. J. Mass Spectrom.* **255:** 150 (2006)
[94] W.Y. Lu, P. Tosi and D. Bassi, *J. Chem. Phys.* **112:** 4648 (2000)
[95] D. Gerlich, *Phys. Scrip.* **T59:** 256 (1995)
[96] Z. Herman, J. Kerstett, T. Rose and R. Wolfgang, *Discuss. Farad. Soc.* 123 (1967)
[97] Z. Herman, *Int. Rev. Phys. Chem.* **15:** 299 (1996)
[98] Z. Herman, *Int. J. Mass Spectrom.* **212:** 413 (2001)
[99] S.D. Price, *Int. J. Mass Spectrom.* **260:** 1 (2007)
[100] S.D. Price, *Phys. Chem. Chem. Phys.* **5:** 1717 (2003)

[101] J. Solomon, C. Jonah, P. Chandra and R. Bersohn, *J. Chem. Phys.* **55:** 1908 (1971)
[102] D.W. Chandler and P.L. Houston, *J. Chem. Phys.* **87:** 1445 (1987)
[103] A. Eppink and D.H. Parker, *Rev. Sci. Instrum.* **68:** 3477 (1997)
[104] B.J. Whitaker (2001) in *American Chemical Society Symposium Series #770* Suits AG, Continetti RE (eds), ACS
[105] R.N. Bracewell (2000) The Fourier Transform and its Applications. McGraw-Hill
[106] S.M. Harper, S.W.P. Hu and S.D. Price, *Meas. Sci. Technol.* **13:** 1512 (2002)
[107] W.P. Hu, S.M. Harper and S.D. Price, *Mol. Phys.* **103:** 1809 (2005)
[108] D.H. Parker and A. Eppink, *J. Chem. Phys.* **107:** 2357 (1997)
[109] B.Y. Chang, R.C. Hoetzlein, J.A. Mueller, J.D. Geiser and P.L. Houston, *Rev. Sci. Instrum.* **69:** 1665 (1998)
[110] C.R. Gebhardt, T.P. Rakitzis, P.C. Samartzis, V. Ladopoulos and T.N. Kitsopoulos, *Rev. Sci. Instrum.* **72:** 3848 (2001)
[111] M.L. Lipciuc and M.H.M. Janssen, *Phys. Chem. Chem. Phys.* **8:** 3007 (2006)
[112] H.L. Offerhaus, C. Nicole, F. Lepine, C. Bordas, F. Rosca-Pruna and M.J.J. Vrakking, *Rev. Sci. Instrum.* **72:** 3245 (2001)
[113] M. Takahashi, J.P. Cave and J.H.D. Eland, *Rev. Sci. Instrum.* **71:** 1337 (2000)
[114] Y. Hikosaka and J.H.D. Eland, *Chem. Phys.* **281:** 91 (2002)
[115] S.T. Tsai, C.K. Lin, Y.T. Lee and C.K. Ni, *Review of Scientific Instruments* **72:** 1963 (2001)
[116] B.A. Mamyrin, *Int. J. Mass Spectrom.* **206:** 251 (2001)
[117] W.C. Wiley and I.H. McLaren, *Rev. Sci. Instrum.* **26:** 1150 (1955)
[118] J.H.D. Eland, *Meas. Sci. Technol.* **4:** 1522 (1993)
[119] B.A. Mamyrin, V.I. Karataev and D.V. Shmikk, *Sov. Phys. - Tech. Phys.* **16:** 1177 (1972)
[120] B.A. Mamyrin, V.I. Karataev, D.V. Shmikk and V.A. Zagulin, *Zhurnal Eksperimentalnoi I Teoreticheskoi Fiziki* **64:** 82 (1973)
[121] J. Zhang and C.G. Enke, *Eur. J. Mass Spectrom.* **6:** 515 (2000)
[122] J. Zhang and C.G. Enke, *J. Am. Soc. Mass. Spectrom.* **11:** 759 (2000)
[123] J. Zhang, B.D. Gardner and C.G. Enke, *J. Am. Soc. Mass. Spectrom.* **11:** 765 (2000)
[124] S.A. Rogers, S.D. Price and S.R. Leone, *J. Chem. Phys.* **98:** 280 (1993)
[125] L.D. Landau, *Phys. Z. Sowjetunion* **2:** 46 (1932)
[126] C. Zener, *Proc. Roy. Soc. London, Series A* **137:** 696 (1932)
[127] O. Hadjar, D. Ascenzi, D. Bassi, P. Franceschi, M. Sabidò and P. Tosi, *Chem. Phys. Lett.* **400:** 476 (2004)
[128] Y.D. Hill, Y.Q. Huang, T. Ast and B.S. Freiser, *Rapid Commun. Mass Spectrom.* **11:** 148 (1997)
[129] J. Roithova, Z. Herman, D. Schroder and H. Schwarz, *Chem.-A Eur. J.* **12:** 2465 (2006)
[130] P. Tosi, R. Correale, W.Y. Lu, S. Falcinelli and D. Bassi, *Phys. Rev. Lett.* **82:** 450 (1999)
[131] D. Ascenzi, P. Franceschi, P. Tosi, D. Bassi, M. Kaczorowska and J.N. Harvey, *J. Chem. Phys.* **118:** 2159 (2003)
[132] P. Tosi, W.Y. Lu, R. Correale and D. Bassi, *Chem. Phys. Lett.* **310:** 180 (1999)

Chapter 2: Reaction Mechanics

2.1. Introduction

Having put the subject of this thesis into context, this chapter deals with a number of theoretical aspects that are crucial to understanding the dynamics of dication-neutral collisions. The first few sections deal with a number of mechanical concepts that are required to understand gas-phase collisions. In general these are applicable to all collisions, but given the focus of this thesis, wherever specifics are called upon it is assumed that the collision system comprises a dication and a neutral molecule. These concepts of mechanics are drawn upon in the process of analysing experimental data (detailed in Chapter 4) and also in the formulation of Reaction Window theory, described later in this chapter. Additionally, reaction mechanisms and selection rules appropriate to dication-neutral collisions are introduced towards the end of the chapter.

2.2. The centre-of-mass frame

When describing the experimental conditions and making physical measurements, it is most natural and most convenient to use the laboratory (LAB) frame as the frame of reference. However, when using such measurements to understand the physics of a collision it is more informative and mathematically straightforward to use

the centre-of-mass frame (CM) as the frame of reference.[11] The CM frame moves relative to the LAB frame in such a way that its origin is always coincident with the centre-of-mass of the two particles. In the LAB frame we assume that the neutral reactant is stationary, since thermal velocities are far less than the speed of the dication beam. However, in the CM frame, both reactants are moving towards their common centre-of-mass. The energy of a collision in the LAB frame is, in itself, of little use since a proportion of this energy must conserve the linear momentum of the centre-of-mass of the system relative to the LAB frame. In the CM frame, on the other hand, total linear momentum is always zero and all of the kinetic energy of the collision is available for reactive processes.

The position vector of the centre-of-mass of a two-body system, relative to any pre-defined location, depends upon the mass and position of the constituent bodies:

$$\mathbf{R}_{CM} = \frac{m_1\mathbf{r}_1 + m_2\mathbf{r}_2}{m_1 + m_2} \tag{2.1}$$

Consequently the velocity vector of the centre-of-mass in the LAB frame, $\mathbf{v}_{CM}$ is:

$$\mathbf{v}_{CM} = \frac{m_1\mathbf{v}_1 + m_2\mathbf{v}_2}{m_1 + m_2} \tag{2.2}$$

The velocity of a particle in the LAB frame, $\mathbf{v}_j$, is simply the sum of its velocity in the centre-of-mass frame, $\mathbf{w}_j$, and the velocity in the LAB frame of the centre-of-mass, $\mathbf{v}_{CM}$.

$$\mathbf{v}_j = \mathbf{w}_j + \mathbf{v}_{CM} \tag{2.3}$$

Hence, if a product particle, j, is back-scattered in the CM frame (i.e. $\mathbf{w}_j$ is in the opposite direction to $\mathbf{v}_{CM}$) with a velocity $|\mathbf{w}_j| < \mathbf{v}_{CM}$, it will actually be moving *forward* in the LAB frame. Clearly, if a particle is back-scattered in the CM frame with a velocity $|\mathbf{w}_j| > \mathbf{v}_{CM}$, it will also be moving backwards in the LAB frame, while in principle a product particle with velocity $\mathbf{w}_j = -\mathbf{v}_{CM}$, would be stationary in the LAB frame.

If, for the moment, we assume all particle motion is co-linear, we can replace the velocity vectors **v** and **w** with their magnitudes v and w. The total kinetic energy of the LAB frame is given by:

$$T_{LAB} = \tfrac{1}{2} m_1 v_1^2 + \tfrac{1}{2} m_2 v_2^2 \tag{2.4}$$

The total kinetic energy of the CM frame is succinctly given by:

$$T_{CM} = \tfrac{1}{2} \mu v_{rel}^2 \tag{2.5}$$

where μ, the reduced mass of the system, is:

$$\mu = \frac{m_1 m_2}{m_1 + m_2} \tag{2.6}$$

and the relative velocity of the two particles, v_{rel}, is simply:

$$v_{rel} = v_1 - v_2 = w_1 - w_2 \tag{2.7}$$

If we apply these equations to our collisions of dications (d), with neutral molecules (n), then by assuming that $v_d >> v_n$, the second term in Equation 2.4 may be approximated as zero and $v_{rel} \approx v_d$. Now dividing Equation 2.5 by Equation 2.4, we get:

$$\frac{T_{CM}}{T_{LAB}} = \frac{\mu}{m_d} \tag{2.8}$$

Hence the kinetic energy of the CM frame can be straightforwardly derived from the LAB kinetic energy using the relation:

$$T_{CM} = \frac{\mu T_{LAB}}{m_d} \tag{2.9}$$

2.2.1. Internal frames of reference

In addition to the centre-of-mass and laboratory frames of reference it may also be useful to define a frame of reference relative to one particle in a system. While the angular scattering distributions of all products are usually plotted relative to the direction of the motion of the centre-of-mass, further information can be revealed by using the direction of motion of one product against which to plot the angular scattering of the others[2] (for instance to distinguish different mechanistic pathways, see Section 2.9). However, since angular distributions are not measured by the experiment to which this thesis pertains, internal frames of reference are not employed in the analysis of data.

2.2.2. Headlight effect

In the centre-of-mass frame, the products of a reaction must have a mutual scattering angle of 180°, in order to conserve linear momentum. However, the directions of the products in the LAB frame depend of the velocity of the centre-of-mass: the bigger the velocity of the centre-of-mass relative to the velocity of a particle in the centre-of-mass frame, the smaller the LAB frame scattering angle. This is known as the headlight effect and means that off-axis scattering effects will be more noticeable at lower collision energies.

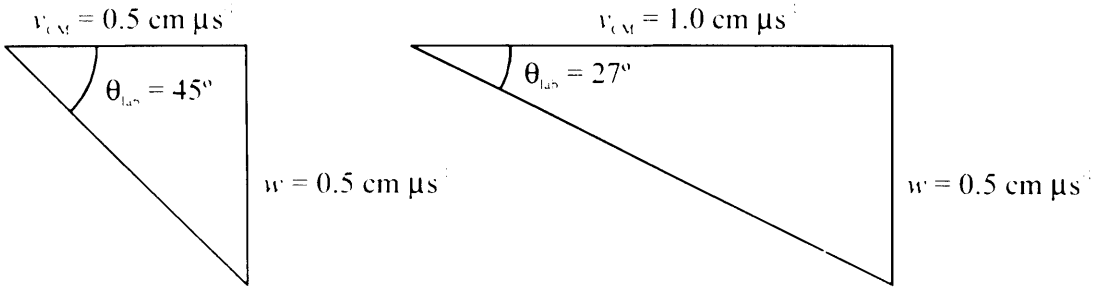

Figure 2.1 Headlight effect: in each case an initially stationary particle is scattered at 90° in the centre-of-mass frame with a velocity of 0.5 cm μs^{-1}. The velocities of collision products in the centre-of-mass frame do not depend on the collision energy, hence if the collision energy is increased, the scattering angle in the lab frame decreases.

2.3. The impact parameter and the collision cross-section

The impact parameter, denoted b, is an important quantity when considering atomic and molecular collisions.[1] In a collision between a moving particle and a stationary partner, it may be defined as the distance between a line drawn through the moving particle along its velocity vector, and a parallel line drawn through the stationary particle *at infinite separation*. If this definition is applied to the most simple of collision molecules, that which approximates atoms and molecules as hard spheres, then the impact parameter does not change as the centre-centre interspecies separation r decreases, and the maximum value of b for which a collision will occur, b_{max}, is equal to the sum of the radii of the two spheres, this being termed the collision diameter, d. Moreover, the minimum interspecies separation is also equal to the collision diameter.

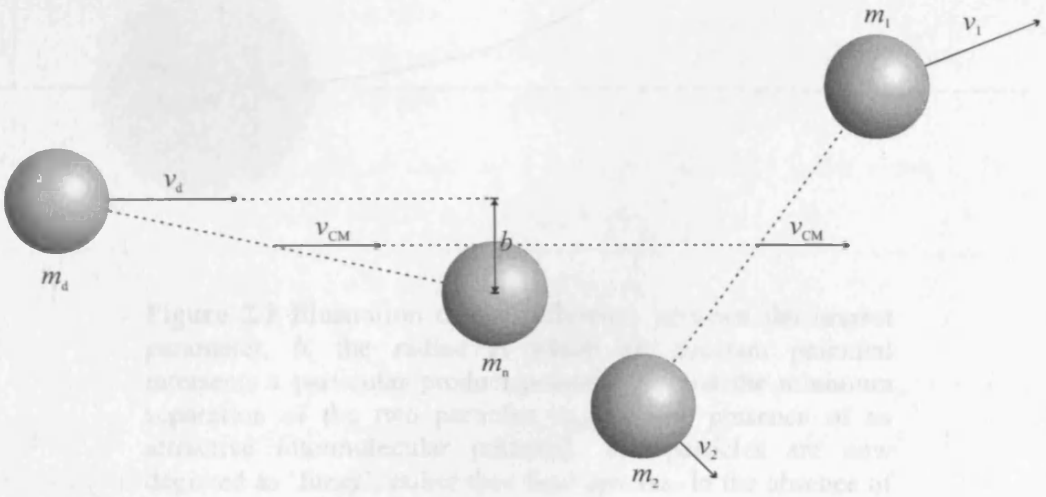

Figure 2.2 A 'hard spheres' picture of a moving particle colliding with a stationary partner of approximately equal mass in the LAB frame.

It is immediately clear that none of these conclusions drawn by recourse to the hard spheres model will actually hold for real atoms and molecules. The hard spheres model treats the area 'inside' a particle as having infinite potential energy and 'outside' as having zero potential energy. In fact, the potential energy of a particle changes over a finite distance and may be attractive or repulsive. The potential energy surface that

represents a collision system as a whole, the intermolecular potential, is not flat and consequently affects the motion of the component particles.

In the case of a dication-neutral collision system, the intermolecular potential is attractive at long range because of the induced dipole in the neutral species. This means that the maximum value of the impact parameter for which a collision can occur is actually larger than the hard spheres model predicts.

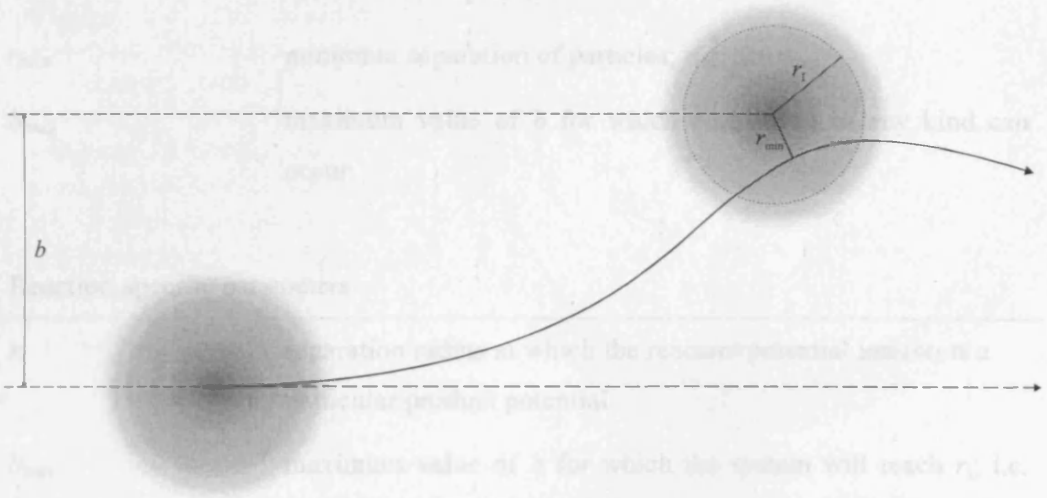

Figure 2.3 Illustration of the difference between the impact parameter, b, the radius at which the reactant potential intersects a particular product potential, r_1, and the minimum separation of the two particles, r_{min}, in the presence of an attractive intermolecular potential. The particles are now depicted as 'fuzzy', rather than hard spheres. In the absence of an intermolecular potential the trajectory of the incident particle is unperturbed (dashed arrow).

As indicated in Figure 2.3, the impact parameter is subtly different to the minimum interspecies separation, r_{min}, of a given trajectory because of the attractive nature of the intermolecular potential of a dication-neutral pair at long distances. If the two reactant particles are considered to be hard spheres then the intermolecular potential is flat and the motion of the dication is unaffected by the presence of the neutral reactant. In this case we have $b = r_{min}$. In reality, the two reactants attract each other and the trajectory of the incident dication curves towards the neutral reactant. The minimum

separation between the two particles, r_{min}, is thus less than the impact parameter. The difference between r_{min} and b depends upon the strength of interspecies attraction and the relative velocity of the dication with respect to the neutral reactant.

Collision parameters	
b (impact parameter)	minimum separation of particles in the absence of an intermolecular potential
r_{min}	minimum separation of particles; $r_{min} \leq b$
b_{max}	maximum value of b for which a collision of any kind can occur
Reaction-specific parameters	
r_1	separation radius at which the reactant potential intersects a particular product potential
b_{max}	maximum value of b for which the system will reach r_1; i.e. value of b for which $r_{min} = r_1$

Table 2.1 Definitions of geometrical parameters used in the text.

The angle at which the product derived from the dication (i.e. the singly charged equivalent of the dication reactant) is scattered relative to its incoming trajectory depends on the minimum interspecies separation during the collision, r_{min}. This minimum separation depends on the exact shape of the interspecies potential, but more importantly on the relative tangential velocity, which in turn depends on the collision energy (for species of a given mass) and, more subtly, on the impact parameter.

A collision cross-section is simply a measure of the number of collision trajectories that have an impact parameter of less than or equal to b_{max}, where b_{max} is the maximum impact parameter for which a reaction of any kind can occur between the two particles. Figure 2.4 shows that this number is proportional to b, so the likelihood of a collision with $b = 0$ is effectively zero. This is important to remember since $b = 0$ collisions are the easiest to visualize, and diagrams of 2D potential energy curves are usually implicitly depicted at $b = 0$. It is also assumed that reactant and product potentials are

angularly symmetric, in other words that the alignment of molecules does not affect the intermolecular potential. In the case of non-atomic species, this is clearly a simplification, but is reasonable for small molecules where steric factors are minimal.

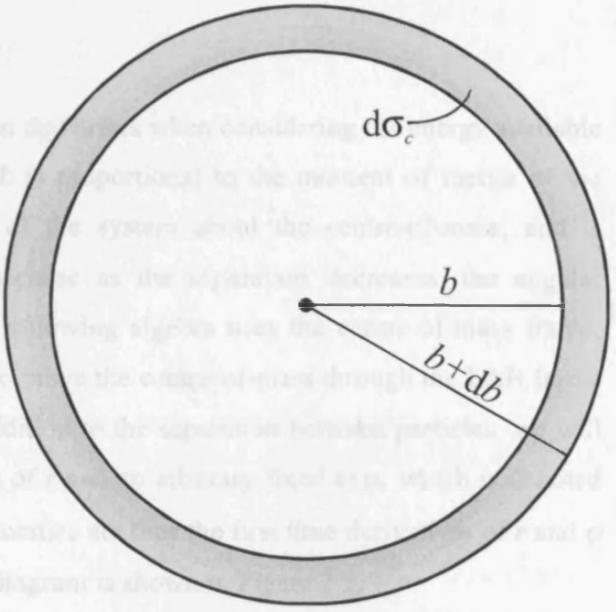

Figure 2.4 The number of collisions with impact parameter b, increases with b up to the maximum value for which a collision can still occur. The area, $d\sigma_c$, of an annulus of width db is approximately $2\pi b\ db$, in the limit that $\pi b \approx \pi(b+db)$.

The number of trajectories that pass though an annulus of radius b and width db is:

$$d\sigma_c = 2\pi b\ db \tag{2.10}$$

Integrating Equation 2.10 over all values of b that result in collision results in the collision cross-section:

$$\sigma_c = \left[\pi b^2\right]_0^{b_{max}} = \pi b_{max}^2 \tag{2.11}$$

Note that the reaction cross-section for a particular reaction channel, σ_r, is calculated in a similar way but must include the probability associated with that channel (i.e. the branching ratio), which is itself usually a function of b. In terms of a specific reaction channel, b_{max} is the maximum impact parameter for which the system will reach a minimum separation of less than or equal to r_1, where r_1 is the radius at which the reactant and product potentials intersect. The sum of the reaction cross-sections for all

possible reaction channels must equal the collision cross-section. The Reaction Window model, described in Section 2.7, is a method of deriving theoretical reaction cross-sections for single electron transfer in doubly charged systems.

2.4. The centrifugal barrier

There is a further complication that arises when considering the energy available in a collision. Angular momentum L is proportional to the moment of inertia of the system I and the angular velocity of the system about the centre-of-mass, and is conserved throughout a collision because as the separation decreases, the angular velocity increases accordingly. The following algebra uses the centre-of-mass frame, because the kinetic energy required to move the centre-of-mass through the LAB frame is not available to the reaction. In addition to the separation between particles, we will need the angle between the direction of r and an arbitrary fixed axis, which is denoted φ. The relative radial and angular velocities are thus the first time derivatives of r and φ respectively. An explanatory vector diagram is shown in Figure 2.5.

$$\begin{aligned} L &= I\dot{\varphi} \\ &= (m_{\mathrm{d}} r_{\mathrm{d}}^2 + m_{\mathrm{n}} r_{\mathrm{n}}^2)\dot{\varphi} \\ &= \mu r^2 \dot{\varphi} \end{aligned} \tag{2.12}$$

where r_{d} and r_{n} are the distances of the dication and neutral respectively from the centre-of-mass.

However, rotational kinetic energy is proportional to the square of the angular velocity of the system about the centre-of-mass. Thus, as the incident dication approaches the neutral target, an increasing proportion of its linear kinetic energy is converted into rotational kinetic energy. This rotational energy is not available for chemical reaction and consequently the effective energy of the collision is reduced.

$$\begin{aligned} KE_{\mathrm{rot}} &= \tfrac{1}{2} I\dot{\varphi}^2 \\ &= \tfrac{1}{2} \mu r^2 \dot{\varphi}^2 \end{aligned} \tag{2.13}$$

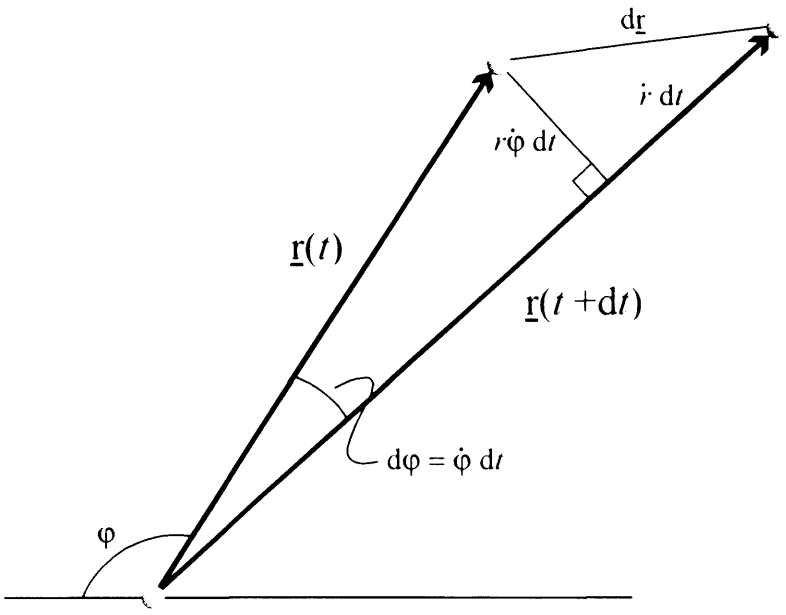

Figure 2.5 Vector diagram showing how the radial and angular velocities of a particle relative to a fixed point are related to the change in the separation vector r in a time interval dt.

At $b = 0$, the relative velocity is entirely radial, so there is no angular component to the dication velocity and hence $KE_{rot} = 0$. However, the larger the impact parameter of the collision, the greater the dication angular velocity for a given collision energy and the greater the proportion of the collision energy that is in rotational, rather than translational form. There are a number of equivalent ways of reasoning to rationalise this effect, known as the centrifugal barrier.[1] The first is to consider that the particles are colliding on the real potential surface, $V(r)$, but that the effective kinetic energy of the collision T_{eff} is reduced for large impact parameters. The second is to consider that the total kinetic energy of the system is made available in the collision, but that the collision occurs on an effective potential surface, $V_{eff}(r)$. Both of these equivalent viewpoints are outlined below.

The total kinetic energy of the system T is the combined translational energy (Equation 2.5) and rotational energy (Equation 2.13):

$$T = \tfrac{1}{2}\mu\dot{r}^2 + \tfrac{1}{2}\mu r^2\dot{\varphi}^2 \qquad (2.14)$$

The total energy of the system is the sum of the rotational energy, the translational energy and the potential energy, which, assuming that initially (i.e. at effectively infinite separation) $V(r_\infty) = 0$ and $\mathrm{d}\varphi\,\mathrm{d}r\,(r_\infty) = 0$ is:

$$E_{\text{total}} = \tfrac{1}{2}\mu\dot{r}^2 + \tfrac{1}{2}\mu r^2\dot{\varphi}^2 + V(r) = \tfrac{1}{2}\mu\dot{r}_\infty^2 \tag{2.15}$$

where $\dot{r}_\infty$ is the initial relative velocity of the particles. Note that E_{total} remains constant throughout the course of a collision, although its translational, rotational and potential components do not; at infinite separation E_{total} is entirely translational.

The angular momentum before the collision may be expressed as the cross-product of the momentum and separation vectors:

$$\begin{aligned} \mathbf{L} &= \mathbf{r}\times\mathbf{p} \\ &= rp\sin\theta \\ &= r\mu\dot{r}_\infty\left(\frac{b}{r}\right) \end{aligned} \tag{2.16}$$

where θ is the angle between the initial separation vector and the motion of the centre-of-mass. The approximation $\sin\theta = b/r$ holds for small values of θ (i.e. large values of r). Now by equating the angular momentum of the system during and before the collision:

$$(\mu r\dot{\varphi})^2 = \left(\mu\frac{b\dot{r}_\infty}{r}\right)^2 \tag{2.17}$$

we find that:

$$\dot{\varphi}^2 = \left(\frac{b\dot{r}_\infty}{r^2}\right)^2 \tag{2.18}$$

so, by substitution, Equation 2.14 becomes:

$$T = \tfrac{1}{2}\mu\dot{r}^2 + \tfrac{1}{2}\mu r^2 \frac{b^2 \dot{r}_\infty^2}{r^4}$$
$$= \tfrac{1}{2}\mu\dot{r}^2 + E_{\text{total}} \frac{b^2}{r^2} \qquad (2.19)$$

The effective (or available) kinetic energy of the collision at separation r is the translational component of the kinetic energy:

$$T_{\text{eff}} = \tfrac{1}{2}\mu\dot{r}^2$$
$$= E_{\text{total}} - E_{\text{total}} \frac{b^2}{r^2} - V(r)$$
$$= E_{\text{total}} \left(1 - \frac{b^2}{r^2}\right) - V(r) \qquad (2.20)$$

Equation 2.20 describes the collision of dication with a neutral as the motion of a single particle of mass μ in a potential $V(r)$ with translational energy T_{eff}. The factor $(1 - b^2/r^2)$ in Equation 2.20 is the centrifugal term and it can be seen that for non-zero values of the impact parameter the effective collision energy is reduced as the particles approach, the effect being greater at larger impact parameters, see Figure 2.6.

A perfectly valid alternative is to treat the centrifugal energy as a modification of the potential energy surface rather than a modification of the kinetic energy. In this way, the kinetic energy available remains unchanged throughout, but the collision takes place on a modified potential $V_{\text{eff}}(r)$.

$$V_{\text{eff}}(r) = V(r) + E_{\text{total}} \left(\frac{b^2}{r^2}\right) \qquad (2.21)$$

Now, instead of the effective kinetic energy decreasing as the collision partners approach, the effective potential increases by the same amount. In this rationalization, the energy of rotation contributes repulsively to $V(r)$, preventing the close convergence of the collision partners (hence the term 'centrifugal barrier').

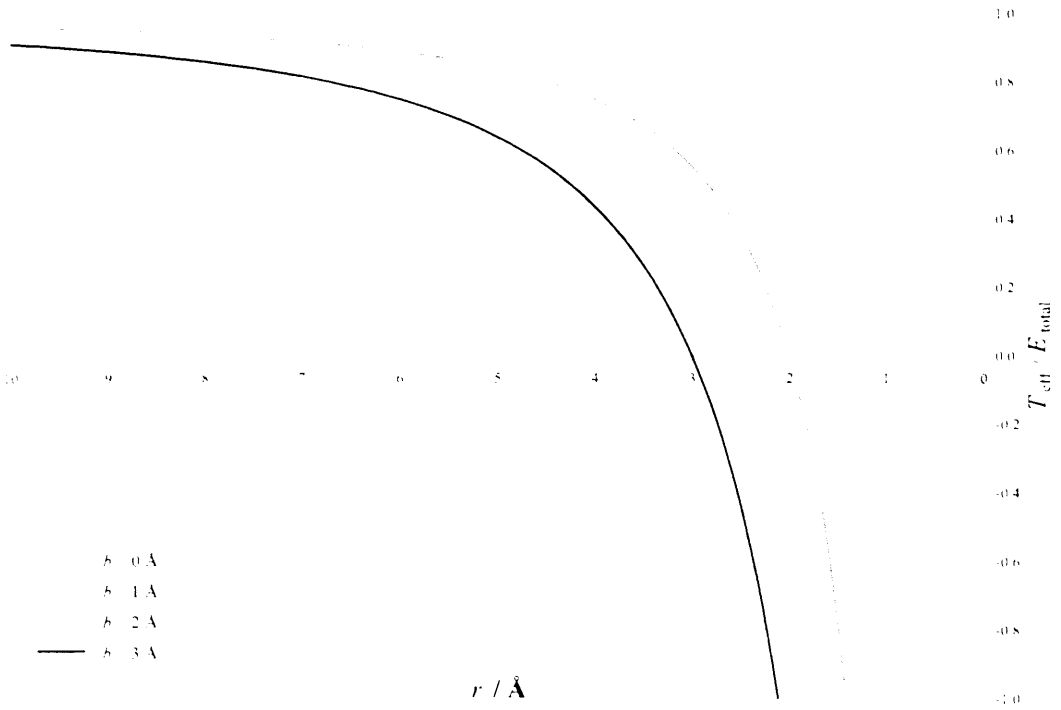

Figure 2.6 The centrifugal component decreases the effective kinetic energy as the collision partners approach. This effect increases with the impact parameter.

The Reaction Window model (see Section 2.7) accounts for the centrifugal barrier by using only the radial component of the velocity of the incident dication. The validity of this can be qualitatively seen by considering collisions with extreme values of the impact parameter. In the (unlikely) case where $b = 0$, the approach velocity of the dication is entirely radial with respect to the neutral target. However, as b increases, so the radial component decreases until, when $b = b_{max}$ (i.e. the dication only just reaches the intersection radius), the velocity is entirely tangential.

2.5. Cross-sections vs. rate constants

In the preceding sections, indeed throughout this thesis, emphasis is placed on obtaining the cross-section of a reaction. This contrasts with many fields of chemistry, which seek to obtain rate constants. Rate constants, as normally defined depend on the concentration and temperature of a sample. Take, for example the elementary reaction:

$$lX + mY \rightarrow nZ \tag{2.22}$$

where l, m, n are stoichiometric numbers. The rate constant of the reaction is a measure of the rate at which the reactants are depleted (or the products are generated) and depends on the concentrations of the reactants and the orders of the reaction, α and β.

$$k(T)[X]^{\alpha}[Y]^{\beta} = -\frac{1}{l}\frac{d[X]}{dt} = -\frac{1}{m}\frac{d[Y]}{dt} = \frac{1}{n}\frac{d[Z]}{dt} \tag{2.23}$$

The failing of such measures when applied to gas-phase dynamics work is that the rate constant defined above relies on large scale (macroscopic) attributes (i.e. temperature and concentration) that have no meaning when applied on an event-wise basis. Remember that temperature is defined for an ensemble of species (a distribution); of much more relevance to event-wise collisions is the velocity of the individual reactants. As a result, it is standard practice to measure the 'likelihood of reaction' using the reaction cross-section when dealing with gas-phase dynamics experiments. However, it is straightforward to convert a cross-section into a rate constant, albeit a velocity dependent rather than a temperature dependent one:[1]

$$k(v) = v_{rel}\sigma_r \tag{2.24}$$

where v_{rel} is the relative velocity of the two particles in collision. Integrating $k(v)$ with respect to velocity returns us to the more familiar $k(T)$.

$$k(T) = \int_0^{\infty} v_{rel}\sigma_r dv \tag{2.25}$$

2.6. Product velocities

Another important requirement of dynamics modelling of bimolecular reactions is a good estimate of the velocities of products following a collision. In some cases, where position sensitive detection is employed, these velocities can be derived from experimental measurements. However, they can also be calculated using simple

mechanics, providing that the velocities and masses of the reactants and the additional kinetic energy released by the reaction are all known. In crossed-beam experiments, the velocity of the charged reactant is known from the beam energy:

$$E_{\text{beam}} = Ze\Delta V \tag{2.26}$$

where Z is the charge of the species in multiples of the elementary charge e, and ΔV is the potential difference used to accelerate the beam. The neutral reactant, introduced into the reaction chamber as a thermalized effusive jet is usually deemed to have negligible velocity. The validity of this assumption can easily be demonstrated, for instance in the case of Ar^{2+} colliding with Ar at a LAB frame energy of 5 V (10 eV):

$$v_{Ar^{2+}} = \sqrt{\frac{E_{\text{beam}}}{m_{Ar}}} = \sqrt{\frac{2\times 5e}{40u}} \approx 5000\ \text{m s}^{-1} \tag{2.27}$$

$$\bar{v}_{Ar\,(\text{thermal})} = \sqrt{\frac{8kT}{\pi m_{Ar}}} = \sqrt{\frac{8\times 298k}{\pi\times 40u}} \approx 400\ \text{m s}^{-1} \tag{2.28}$$

Clearly, the velocity of the neutral reactant is far less than the velocity of reactants in the ion beam. However, the non-zero velocity of the neutral reactant does introduce inaccuracy into calculations (and broadening of peaks in the time-of-flight spectrum), even exceeding 10% at low collision energies.

The energy released in a reaction is discussed towards the end of this section, but it is this energy that must be shared out between the products in such a way as to conserve total linear momentum. Consider a dication of mass m_d and CM frame velocity w_d, colliding with a neutral molecule of mass m_n and velocity w_n. Two products are formed, one scattered principally in the same direction as the incident dication (mass m_1 and velocity w_1) and one scattered principally in the direction of the incident neutral (mass m_2 and velocity w_2). In an atomic system or for a charge transfer reaction, the masses m_1 and m_2 evidently equal m_d and m_n respectively, but this need not necessarily be the case. The collision energy of the reactants (R) in the CM frame is:

$$T_R = \tfrac{1}{2}\mu_R v_{\text{rel(R)}}^2 \tag{2.29}$$

The post-collision kinetic energy of the system is equal to the pre-collision kinetic energy *plus* the exothermicity associated with the reaction.

$$T_P = T_R + \Delta E \tag{2.30}$$

The energy released in a collision is divided between the two product particles in such a way as to conserve linear momentum. Considered in the CM frame, linear momentum is zero prior to collision and hence to be conserved must also be zero after the collision.

$$m_d w_d = m_n w_n \Rightarrow m_1 w_1 = m_2 w_2 \Rightarrow w_2 = -\frac{m_1}{m_2} w_1 \tag{2.31}$$

After the collision, the CM frame kinetic energy of the products is given by:

$$T_P = \tfrac{1}{2}\mu_P v_{rel(P)}^2 = \tfrac{1}{2}\mu_P (w_1 - w_2)^2 = \tfrac{1}{2}\mu_P \left(w_1^2 + w_2^2 - 2w_1 w_2\right) \tag{2.32}$$

and we can substitute for w_2 using Equation 2.31:

$$T_P = \tfrac{1}{2}\left(\frac{m_1^2}{m_2^2} + 2\frac{m_1}{m_2} + 1\right)\mu_P w_1^2 \tag{2.33}$$

And we can simplify this further:

$$\begin{aligned} T_P &= \tfrac{1}{2}\left(\frac{m_1^3}{m_2(m_1+m_2)} + \frac{2m_1^2}{m_1+m_2} + \frac{m_1 m_2}{m_1+m_2}\right) w_1^2 \\ &= \tfrac{1}{2}\left(\frac{m_1^3 + 2m_1^2 m_2 + m_1 m_2^2}{m_2(m_1+m_2)}\right) w_1^2 \\ &= \tfrac{1}{2}\left(\frac{m_1^2(m_1+m_2)^2}{m_2(m_1+m_2)}\right) w_1^2 \\ &= \tfrac{1}{2}\left(\frac{m_1^2}{m_2} + m_1\right) w_1^2 \end{aligned} \tag{2.34}$$

Hence:

$$w_1 = \pm\sqrt{\frac{2T_P}{(k_1 + m_1)}} = \pm\sqrt{\frac{2(T_R + \Delta E)}{(k_1 + m_1)}} \quad \text{where } k_1 = \frac{m_1^2}{m_2} \tag{2.35}$$

Similarly:

$$w_2 = \mp\sqrt{\frac{2(T_R + \Delta E)}{(k_2 + m_2)}} \quad \text{where } k_2 = \frac{m_2^2}{m_1} \tag{2.36}$$

We here define the exothermicity ΔE as the *electronic* state-to-state energy difference between the reactants and products. It is convenient to ignore the possibility of vibrational excitation, so that the exothermicity is identical to the exoergicity ΔT, i.e. the energy realised as translation in the course of the reaction *in addition* to the kinetic energy of the reactants (Figure 2.7). Using these definitions, we can link the exothermicity to the kinetic energy of the reactants T_R and of the products T_P and the difference between the vibrational energies of the reactants and products.

$$\Delta T = T_P - T_R \tag{2.37}$$

$$\Delta E = \Delta T + \Delta E_{vib} \tag{2.38}$$

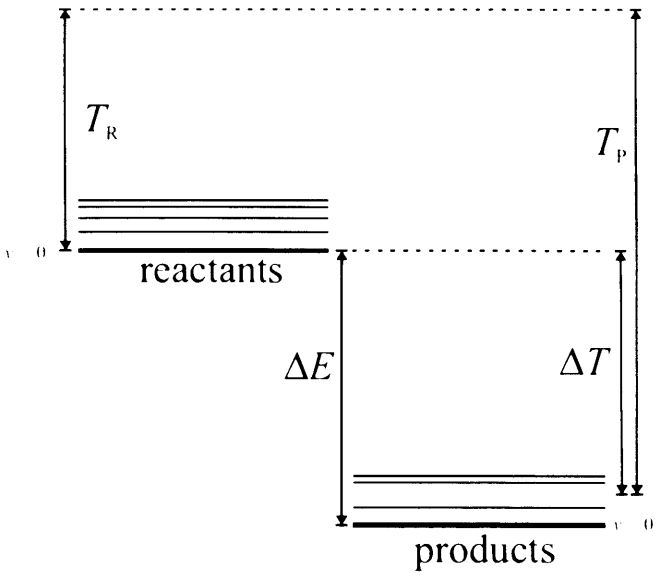

Figure 2.7 Illustration of energy terminology for a transition from the ground vibrational state of the reactants to an excited vibrational state of the products (grey line). The exothermicity ΔE is defined as the difference in electronic energy between the reactants and products. If the products are vibrationally excited, then some of the exothermicity is used in this excitation and as a result the exoergicity ΔT will be correspondingly less than ΔE.

In reality, as the collision energy of a system increases excited vibrational states of the product species will become accessible and a fraction of ΔE will be converted to vibrational energy rather than translational energy, so the exoergicity will be less than the exothermicity. However, for convenience in calculating product velocities, it may be assumed that ΔE is the exothermicity of a transition between vibrational ground states and that any increase in collision energy is approximately matched by the increase in internal energy of the product states populated so that ΔT remains roughly the same. Reaction Window theory (see Section 2.7) predicts that for single electron transfer reactions, only transitions having an exothermicity close to 3.5 – 4.5 eV can proceed efficiently. We can therefore make the approximation that the kinetic energy of the products T_P equals the kinetic energy of the reactants T_R plus roughly 4 eV.

The momentum and energy arguments called upon above, dictate unique values of the speeds of the product ions. Of course in three-dimensional reality the product velocities may be orientated in any direction, providing they are mutually co-linear to maintain zero overall momentum. If a singly charged product of a reaction goes on to dissociate, it is usually assumed that the kinetic energy change caused by this dissociation is negligible, as it will be far smaller than that associated with charge separation processes. Hence, the velocities of fragments of product ions are deemed to be unchanged by the fragmentation process.

2.7. The Reaction Window (RW) model

The RW model[3] is a formulation of Landau-Zener theory[4,5] applied to electron transfer reactions in dication/neutral collision systems. Landau-Zener theory is a semi-classical description of the probability of crossing from one potential surface to another at an intersection.

In a simple triatomic system the reactant potential (XY^{2+} + Z) is modelled as being purely attractive (polarization interactions). Clearly, this approximation is only valid at interspecies separations greater than the position of the bound minimum (XYZ^{2+}), below which repulsive forces begin to dominate the real interactions. Similarly the potential surface of the products of electron transfer (XY^{+} + Z^{+}) is modelled as being purely repulsive (Coulombic interactions). The reactant and product potentials intersect at a certain radius, r_I. The surfaces are assumed to be spherically

symmetric so that r_l has no angular dependence. Landau-Zener theory provides a means of calculating the probability δ of the system remaining on one diabatic potential surface as it passes through an intersection with the other surface.

$$\delta = \exp\left[-\frac{\pi|H_{RP}|^2}{2\hbar\left|V_R' - V_P'\right| v_{rad}(b)}\right] \tag{2.39}$$

In Equation 2.39, V' is the gradient of the reactant and product potentials at the intersection radius and $v_{rad}(b)$ is the radial velocity at the intersection radius, which depends on the impact parameter, b. H_{RP} is the electronic coupling matrix element, a measure of the strength of the electronic coupling between the reactant and product potentials, which can be calculated from the ionization potentials of the reactants and the intersection radius using the semi-empirical formula of Olson et al:[6]

$$|H_{RP}|^2 = \tfrac{1}{2}(I_A I_B)(\sqrt{I_A} + \sqrt{I_B})r_l \exp\left(-1.72 r_l \sqrt{\tfrac{1}{2}I_A + \tfrac{1}{2}I_B}\right) \tag{2.40}$$

The reactant (polarization) potential, V_R, is approximated using:

$$V_R = -\frac{(Ze)^2\alpha}{2r^4} + \Delta E \tag{2.41}$$

where Z is the number of elementary charges, e, on the ion (i.e. in the case of dications $Z = 2$); α is the polarizability of the neutral collision partner; r is the interspecies separation between the dication and neutral; and ΔE is the exothermicity between the asymptotic energies of the reactants and products.

The product (Coulombic) potential, V_P, is approximated using:

$$V_P = \frac{e^2}{r} \tag{2.42}$$

The intersection radius r_l is the value of r for which $V_R = V_P$ and for each potential $V' = dV/dr$.

In the course of a collision, considering only a single reactant surface and a single product surface, then providing the distance of closest approach is less than r_I the system must pass through the intersection twice: once on approach (as r decreases) and again on separation (as r increases). For the net result of the collision to be single electron transfer, the system must cross from one surface to the other only once during the collision. The model assumes that the probability of crossing from the reactant potential to the product potential is the same as crossing from the product potential back to the reactant potential. Hence, the probability of electron transfer is:

$$P_{SET} = \delta(1-\delta) + (1-\delta)\delta = 2\delta(1-\delta) \qquad (2.43)$$

The first term in Equation 2.43 corresponds to surface crossing occurring on the first pass through the intersection ('early' SET) and the second term to crossing on the second pass ('late' SET). These different pathways can be visualized as shown in Figure 2.8.

For any particular value of the impact parameter, transfer to the repulsive potential surface associated with a monocation pair early (in the entrance channel) results in a larger scattering angle than transfer in the exit channel. However, given the bias of collisions towards larger impact parameters and the headlight effect, electron transfer reactions show strong asymmetry in their angular distributions dominated by only small deviations in the LAB frame direction of the incident dications. Such angular distributions have been measured by Harper et al., and typically peak at approximately 10°.

From Equation 2.43, the probability of electron transfer can be seen to be maximized when δ = 0.5. Since the electronic coupling between the reactant and product potentials is weak at large interspecies separations but becomes increasingly strong as the separation decreases, this optimum value of δ must occur at some intermediate value of r. In practice, the optimum value of r is in the region of 3-4 Å, and the region around this point where electron transfer is most efficient is termed the 'reaction window'. If the point of intersection, r_I, for a system lies within the reaction window then significant electron transfer can be expected, however, if r_I is either much smaller or much larger than $r(\delta = 0.5)$ then electron transfer will be inefficient.

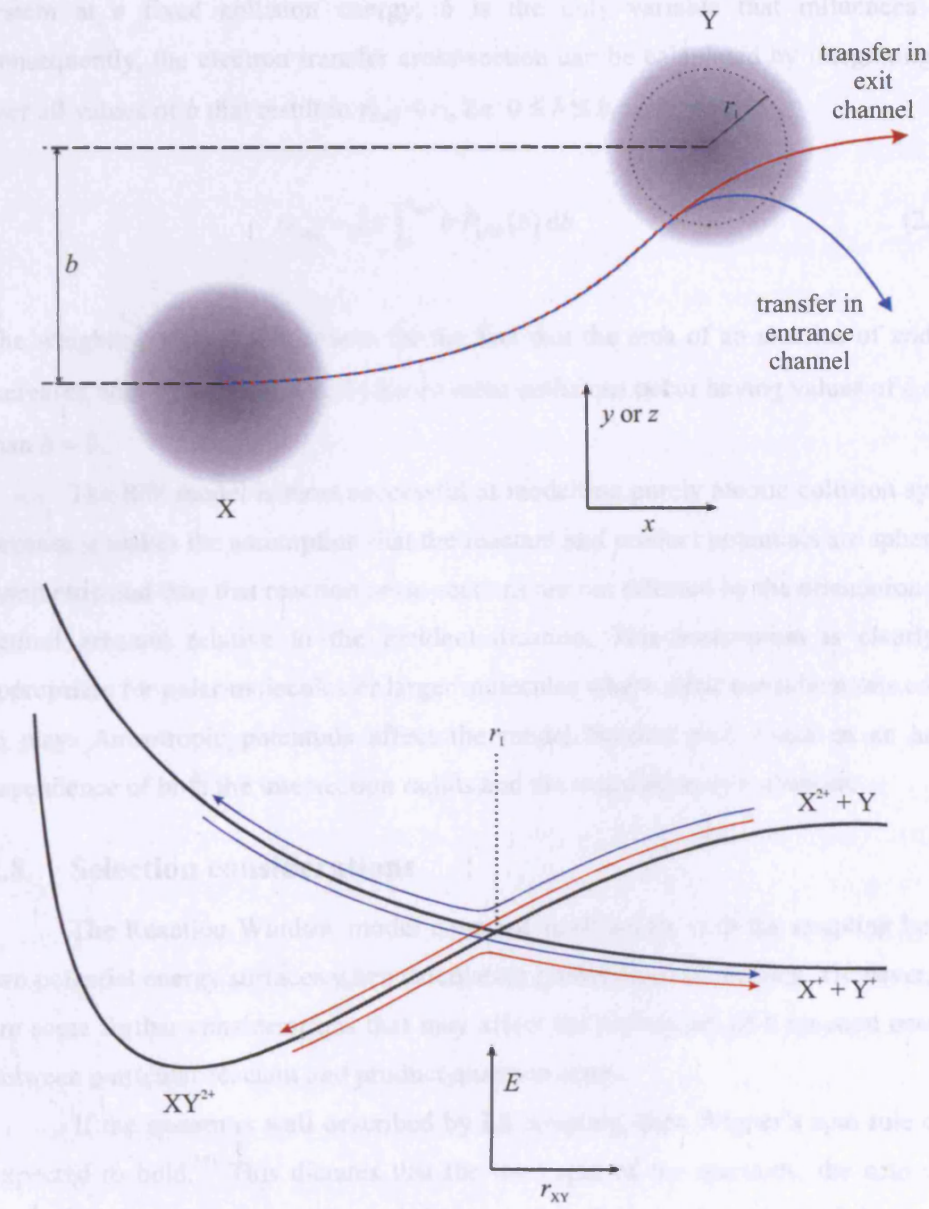

Figure 2.8 Comparison of early (blue) and late (red) single electron transfer from a geometrical perspective (top) and a potential energy perspective (bottom). Notice that the potential energy curves represent a cross-section through the 3D surfaces for $b = 0$.

The value of δ, as shown in Equation 2.39, is a function of the radial collision velocity, which in turn is a function of the impact parameter b. For any given collision system at a fixed collision energy, b is the only variable that influences P_{SET}. Consequently, the electron transfer cross-section can be calculated by integrating P_{SET} over all values of b that result in $r_{min} < r_I$, *i.e.* $0 \leq b \leq b_{max}$.

$$\sigma_{calc} = 2\pi \int_0^{b_{max}} b\, P_{SET}(b)\, db \qquad (2.44)$$

The weighting term $2\pi b$ accounts for the fact that the area of an annulus of width db increases with b (see Section 2.3) hence more collisions occur having values of $b \approx b_{max}$ than $b \approx 0$.

The RW model is most successful at modelling purely atomic collision systems because it makes the assumption that the reactant and product potentials are spherically symmetric and thus that reaction cross-sections are not affected by the orientation of the neutral reactant relative to the incident dication. This assumption is clearly less appropriate for polar molecules or larger molecules where steric considerations come in to play. Anisotropic potentials affect the model because they result in an angular dependence of both the intersection radius and the coupling matrix element.

2.8. Selection considerations

The Reaction Window model concerns itself solely with the coupling between two potential energy surfaces when calculating probabilities of reaction. However, there are some further considerations that may affect the probability of a reaction occurring between particular reactant and product quantum states.

If the system is well described by LS coupling, then Wigner's spin rule can be expected to hold.[7] This dictates that the total spin of the reactants, the spin of any intermediate collision complex, and the total spin of the products must all be equal. In multi-particle systems, Wigner's rule is often not very restrictive, since many different electronic states of the different particles may be possible, whilst still combining to give the appropriate overall spin. Additionally, experimental investigations have shown that Wigner's spin rule may be violated in two cases:

i) Heavy collision partners (>100u): Spin need only be conserved in a collision if the coupling between spin and orbital angular momentum is weak. In heavy atoms spin-orbit coupling is much stronger and a change in spin can occur accompanied by a countering change in orbital angular momentum.

ii) Small impact parameters (<1Å): Myers et al. have shown that the electric field of a doubly charged ion can generate sufficient torque impulse during a collision to bring about a spin flip in an electron only at small values of the impact parameter.

In most collisions, even at the relatively low energies with which this thesis is concerned, the interaction time between the collision partners in the case of electron transfer reactions (see Section 2.9) is so short that multiple electron transfer is extremely inefficient.[8-10] As soon as one electron has been transferred between the colliding particles, the repulsive Coulombic force generated rapidly separates the product ions, making further electronic transitions very unlikely.

An effect related to the dominance of single electron transitions is the conservation of the core electron configuration between reactants and products. For instance should N^{2+} ($1s^2 2s^2 2p^1$) undergo electron transfer in a collision, the N^+ product may be in its ground state ($1s^2 2s^2 2p_x^1 2p_y^1$) or a higher energy state involving the excitation of a valence electron (e.g. $1s^2 2s^2 2p_x^2$ or $1s^2 2s^2 2p^1 3s^1$) providing sufficient energy is available, but is unlikely to have an excited core electron (e.g. $1s^2\ 2s^1\ 2p^3$). Consequently, products are rarely highly excited (either core or multiple excitation) since the reactants are not expected to be so. Core conservation may be violated at small impact parameters[11], if the collision has sufficient energy to bring the particles close enough together for core disturbance to occur; however, as has been shown, small impact parameter collisions represent only a small fraction of the total.

2.9. Reaction mechanisms

In general the reactions between dications and neutral species occur via one of two mechanistic pathways: direct reaction or complex formation. Different reaction mechanisms can be identified by differences in the angular scattering distributions of

the product ions, which can be determined by experiment. It is important to remember that time-of-flight experiments, in most cases, only detect ionic species but that momentum and energy arguments can be used to derive the properties of an additional undetected species. Hence, for a reaction forming two products only one needs to be detected for the properties of the other to be derived. However, for a reaction with three products (assuming the double charge has separated, this means two monocations and a neutral species) both ionic products must be detected in co-incidence for the full dynamics of the system to be obtained. Unfortunately, since in doubly charged systems the maximum number of charged products is two, should a reaction yield four or more products (i.e. two or more neutral species) then the dynamics of the system is not experimentally accessible.

Direct reactions involve minimal interaction between the two species, sometimes called a 'fly-by'. This pathway is most applicable to electron transfer reactions, which occur at relatively large interspecies separations (compared to typical bond lengths). Hydride transfer (and similarly proton transfer), although involving the breaking and formation of a chemical bond, is often treated as 'heavy electron' transfer and similarly modelled using a direct reaction mechanism. The interaction time between reactants in an electron transfer collision is extremely short (on the order of femtoseconds, compared to typical rotational periods on the order of picoseconds) and interaction distance is several angstroms (much longer than a typical bond length) so electron transfer causes relatively little perturbation in the trajectory of the incident dication. Consequently, the angular scattering distributions of reactions occurring via a direct mechanism exhibit strong asymmetry[2], with the product ion derived from the incident dication peaking at scattering angles of 0° – 15° relative to the direction of motion of the centre-of-mass and the product ion derived from the neutral reactant peaking at around 165° – 180°.

In contrast, the angular scattering distributions of reactions that involve the formation of new chemical bonds between heavy atoms (i.e. not hydrogen) are much more symmetric than those for transfer reactions.[2] Bond-forming reactions are modelled as occurring via an intermediate collision complex, a hypothesis that is supported by experimental results[1,2] using position-sensitive detection. A collision complex may also be pictured as the two reactants interacting at a shorter interspecies separation and on a longer timescale than in the case of a direct reaction. If the period of

interaction is on the order of the rotational period of the complex then the angular scattering will become much more symmetric because the complex has time to rotate significantly between forming and breaking apart. This means that most complexes fragment on a timescale greater than their period of rotation, breaking the coupling between the orientation of the velocities of the reactants and products. The degree of symmetry in the angular distributions of products formed via a collision complex depends on the ratio of the lifetime of the complex to its rotational period. Experiments indicate that the angular momentum imparted to the collision complex in crossed-beam experiments results in significantly shorter rotational periods than associated with thermal molecules. Nonetheless, many collision complexes have sufficiently long lifetimes to be indirectly observed in angularly resolved experiments

A collision complex, which in the context of this thesis shall be assumed to be doubly charged, may fragment one of two ways, which can also be distinguished by measurement of product angular scattering distributions. The first pathway (Equation 2.45) involves the concerted dissociation of the complex into a pair of monocations, often accompanied by a neutral species. The second pathway (Equation 2.46) involves ejection of an ion from the collision complex prior to dissociation of the remaining singly charged ion.

$$A^{2+} + B \rightarrow [complex]^{2+} \rightarrow C^{+} + D^{+} + E \qquad (2.45)$$

$$A^{2+} + B \rightarrow [complex]^{2+} \rightarrow [complex]^{+} + C^{+} \qquad (2.46)$$

$$\downarrow$$

$$D^{+} + E$$

In the case of the concerted pathway, the scattering angles of the products will be symmetric relative the motion of the centre-of-mass, but fixed with respect to the motion of each other. However, in the case of the sequential pathway, the scattering angle of the ejected ion will be uncoupled both to the motion of the centre-of-mass and the other products, while the remaining two products, although scattered symmetrically relative to the centre-of-mass motion will be scattered at a fixed angle relative to each other.

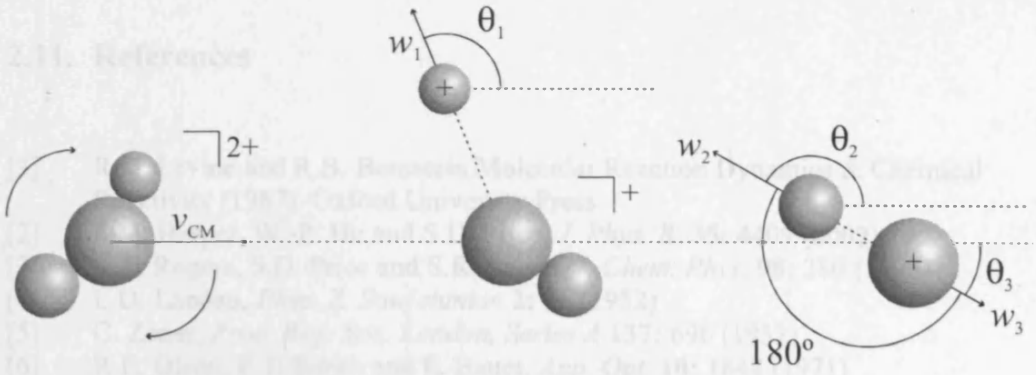

Figure 2.9 Schematic showing the sequential decay of a collision complex. The angles θ_1, θ_2 and θ_3 are all uncoupled to the centre-of-mass motion. However, while the mutual angles (angles between the appropriate CM frame velocities) θ_{12} and θ_{23} are also uncoupled, the mutual angle θ_{23} is fixed at 180°.

2.10. Summary

The principles discussed in this chapter are crucial for understanding dication-neutral collision systems. The analysis of experimental data, detailed in later chapters, relies heavily on a sound model of the mechanics of dication-neutral collisions to obtain experimental values of reaction cross-sections and also on the Reaction Window model to derive calculated values of state-specific reaction cross-sections for comparison with the experimental results.

2.11. References

[1] R.D. Levine and R.B. Bernstein Molecular Reaction Dynamics & Chemical Reactivity (1987). Oxford University Press

[2] S.M. Harper, W.-P. Hu and S.D. Price, *J. Phys. B.* **35:** 4409 (2002)

[3] S.A. Rogers, S.D. Price and S.R. Leone, *J. Chem. Phys.* **98:** 280 (1993)

[4] L.D. Landau, *Phys. Z. Sowjetunion* **2:** 46 (1932)

[5] C. Zener, *Proc. Roy. Soc. London, Series A* **137:** 696 (1932)

[6] R.E. Olson, F.T. Smith and E. Bauer, *App. Opt.* **10:** 1848 (1971)

[7] E. Wigner, *Nachr. Akad. Wiss. Gottingen, Math.-Physik* **K1:** 375 (1927)

[8] D.H. Crandall, R.E. Olson, E.J. Shipsey and J.C. Browne, *Phys. Rev. Lett.* **36:** 858 (1976)

[9] E. Rille and H. Winter, *J. Phys. B* **13:** L531 (1980)

[10] W. Groh, A.S. Schlachter, A. Muller and E. Salzborn, *J. Phys. B.* **15:** L207 (1982)

[11] G.E. Ice and R.E. Olson, *Phys. Rev. A* **11:** 111 (1975)

[12] S.M. Harper, W.-P. Hu and S.D. Price, *J. Chem. Phys.* **120:** 7245 (2004)

Chapter 3: Experimental Details

3.1 Introduction

The experiments reported later in the thesis were carried out using a crossed-beam time-of-flight mass spectrometer[1,2] (Figure 3.1). An electron beam is used to ionize a suitable precursor gas, and the charged fragments are then mass selected and collimated to produce an ion beam. The ion beam is decelerated to the desired collision energy before intersecting an effusive jet of some neutral reactant in the source region of the mass spectrometer. Ions are extracted from this source region by application of a pulsed repelling voltage and are ultimately detected by a multichannel plate detector from which signals are processed and finally passed to a PC for analysis.

This chapter will describe the details of the experimental apparatus in three sections:

i) dication beam generation;

ii) the mass spectrometer;

iii) data collection.

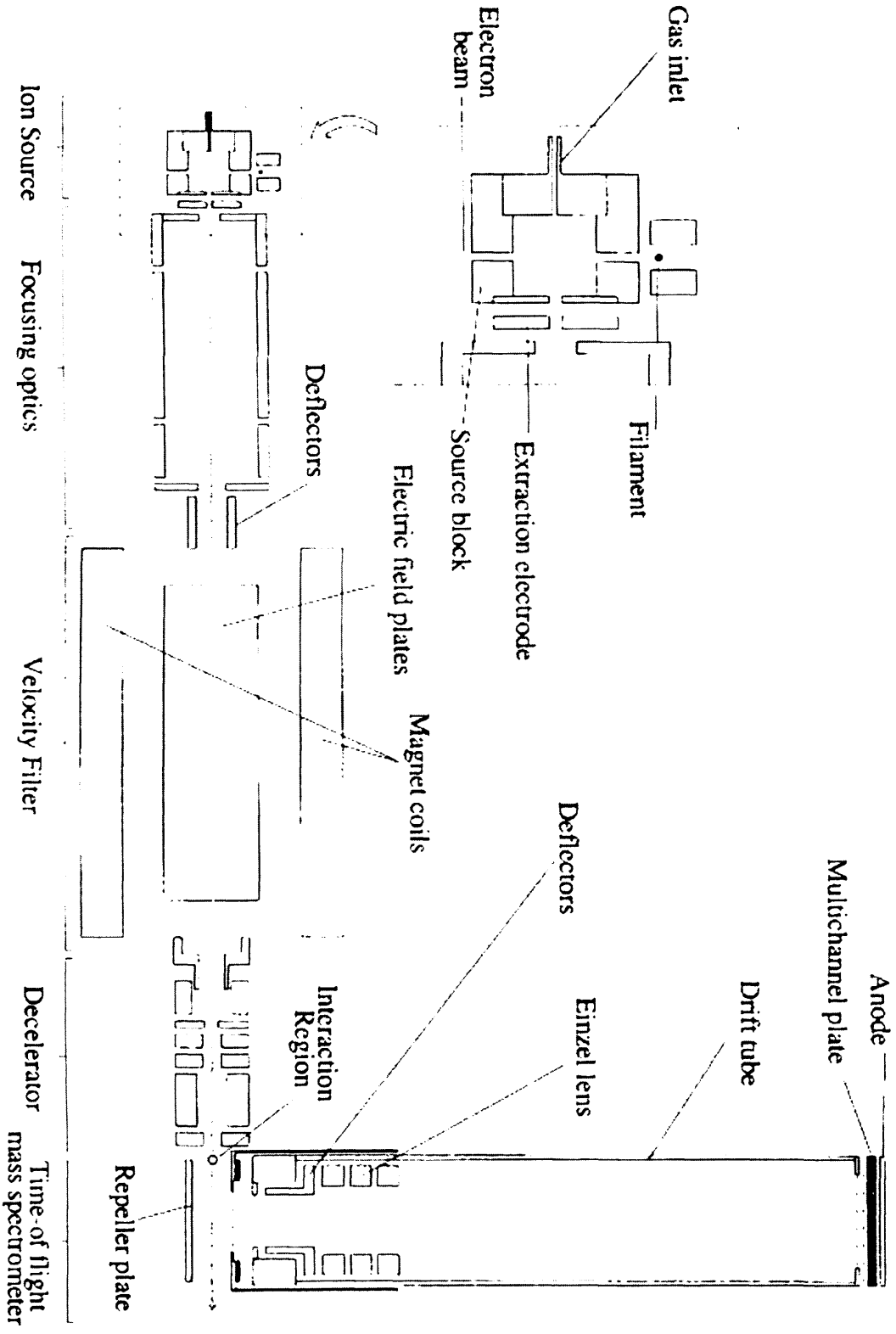

Figure 3.1 Layout of the crossed-beam apparatus.

3.2 Dication beam generation

3.2.1 Ion source

The molecular dications required for an experiment are generated, indiscriminately with other ionization products, from a suitable precursor gas. This is done by perpendicularly intersecting a focussed electron beam with a jet of the precursor gas. The electrons are ejected from a thermionic tungsten filament by application of a variable current (~ 4 A) to produce a constant electron current. The electron current is usually set at 20 μA but is sometimes increased to 50 μA if the signal of the desired dication is low. Increasing the electron current increases rate of ionization but reduces the life of the filament. The energy of the electrons may be adjusted to maximise the ion yield, but is typically 100-200 eV.

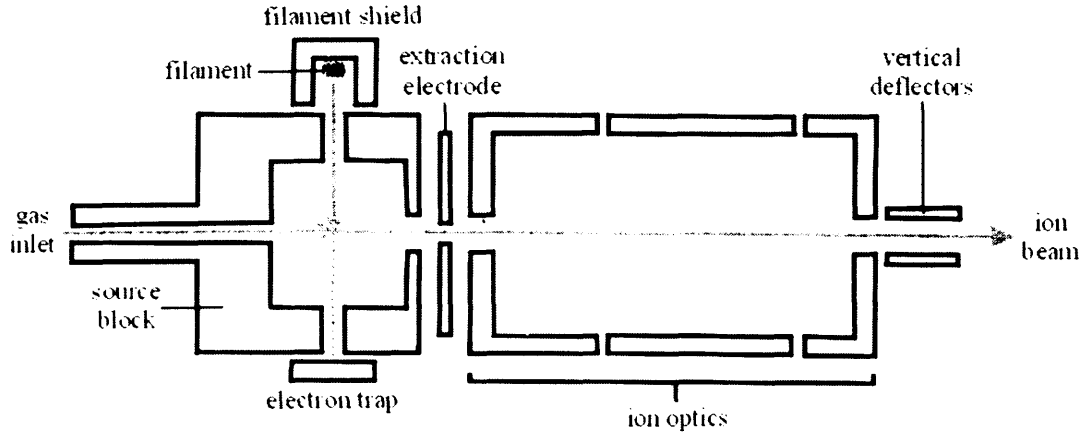

Figure 3.2 Layout of the ion source.

A schematic diagram of the source block and subsequent ion optics is shown in Figure 3.2. The source block is basically cubic and constructed from stainless steel in order to withstand the ionization plasma. In addition to the filament and gas inlet, the source block includes an electron trap to measure the electron current and an electrode to extract all ions from the source region. The ion beam produced by the source is continuous and orientated along the same axis as the gas inlet, i.e. perpendicular to the direction of the electron beam.

The ambient pressure in the ion source is kept low using a dedicated diffusion pump, in order to reduce collisions between ions and background molecules or

precursor gas molecules. Dications undergo charge transfer (Equation 3.1) and charge separation (Equation 3.2) reactions with neutral species very readily, and increasing the flow of the precursor gas beyond its optimal value, despite increasing the number of dications formed, actually decreases the number reaching the reaction chamber.

$$AB^{2+} + M \rightarrow AB^{+} + M^{+} \quad (3.1)$$

$$AB^{2+} + M \rightarrow A^{+} + B^{+} + M \quad (3.2)$$

The incident electron beam has a diameter of approximately 2 mm, dictated by the narrow aperture between the filament and the ionization region, which ensures that ions are only formed in a very small volume within the source block. Hence all ions experience the same electric field and are accelerated to the same kinetic energy as they exit the ion source, this energy being determined solely by the voltages applied to the source block. This uniformity of energy means that the ions can be mass selected simply by passing through a velocity filter. All the fragment ions formed by ionization of the precursor gas are extracted from the ion source and collimated into a beam using a series of ion optics, before entering the velocity filter. The collimating ion optics also further accelerate the ions (to $200q$ eV) so that they reach the reaction chamber as soon as possible, minimising the amount of unimolecular decay of metastable species.

3.2.2 Velocity filter

The velocity filter employed is a commercial Colutron model[3], based on the Wien velocity filter[4-6]. This consists of an electromagnet and a pair of electrostatic plates, mounted so as to produce mutually perpendicular electric and magnetic fields. The layout of the velocity filter is shown in Figure 3.3.

A particle of charge q moving with velocity v through a magnetic field of magnitude B experiences a force F_B, given by:

$$F_B = qBv \quad (3.3)$$

Similarly, the same particle moving through an electric field of magnitude E experiences a force F_E, given by:

$$F_E = qE \tag{3.4}$$

The forces F_B and F_E act in opposing directions so that an ion can only pass through the velocity filter undeflected if the two forces are equal in magnitude:

$$F_E = F_B \tag{3.5}$$

which results in the condition:

$$v = \frac{E}{B} \tag{3.6}$$

As mentioned before, all ions reach the velocity filter with the same kinetic energy KE, depending on the accelerating potential, V:

$$KE = qV \tag{3.7}$$

Therefore:

$$\sqrt{\frac{2KE}{m}} = \frac{E}{B} \tag{3.8}$$

Thus for fixed values of E, B and KE the trajectory of a particle through the velocity filter depends solely upon its mass. In other words, mass selection of an ion of mass m_i can be achieved by adjusting electric field E until the following condition is met:

$$E = B\sqrt{\frac{2KE}{m_i}} \tag{3.9}$$

The velocity filter is tuned by adjusting the electric field, rather than the magnetic flux density, to minimise the detrimental effects of hysteresis losses caused by the heating or cooling of the electromagnet associated with adjusting the applied current.

An unwanted side-effect of the velocity filter is that it focuses ions that are not moving exactly along the centre of the ion beam.[7] This is corrected by including a series of shim plates between the electrostatic plates. The shim plates can be individually finely biased to alter the electric field between the plates. This produces an electric field shape that compensates for the inherent focussing effect of the filter.

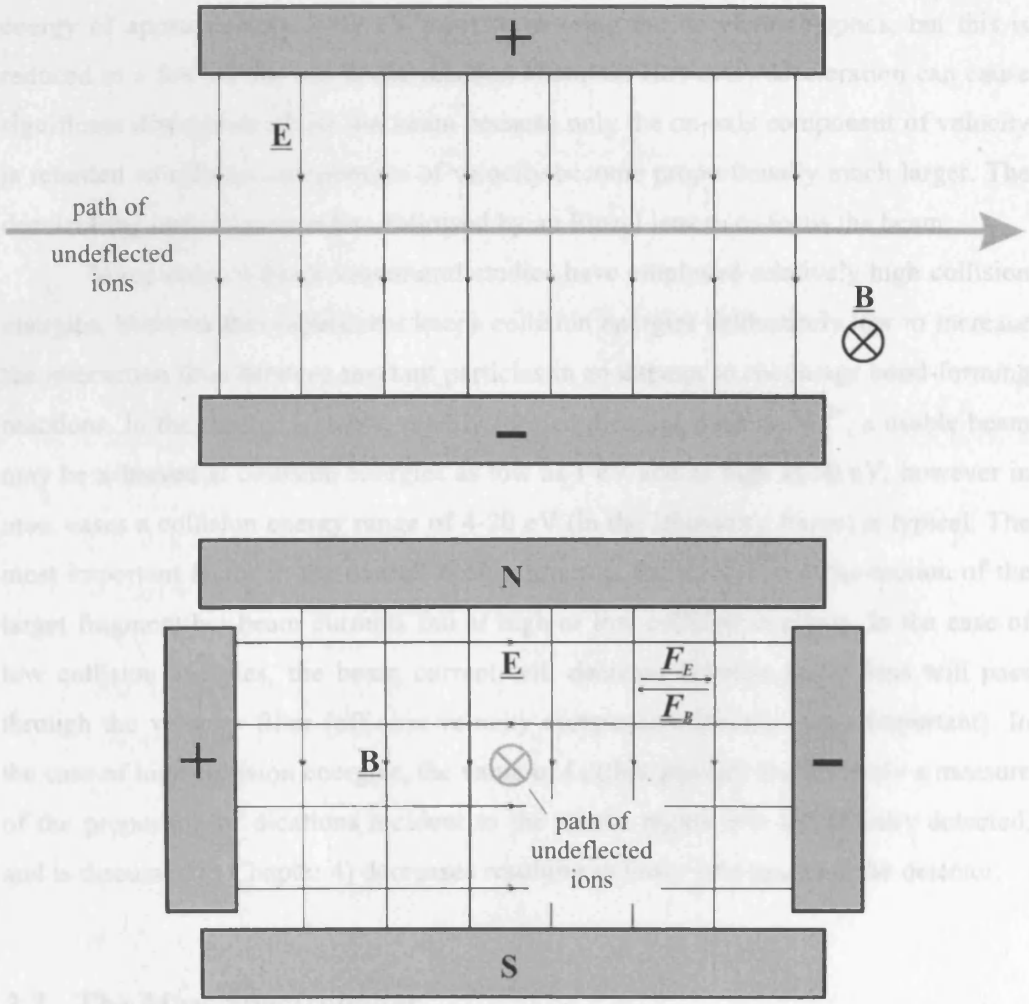

Figure 3.3 Arrangement of the velocity filter viewed along the magnetic field lines (top) and the undeflected beam direction (bottom). If all ions enter the filter with the same kinetic energy, only ions of a single mass:charge ratio will be undeflected. Ions of lower *m/z* (higher velocity) will experience a magnetic force greater than the electrostatic force and be deflected to the left in the bottom diagram, while for ions of higher *m/z* (lower velocity) the reverse is true and they are deflected to the right.

3.2.3 Decelerator

As stated above, ions are accelerated upon leaving the ion source to reduce the transit time to the reaction chamber so that losses of dicationic species through unimolecular decay are minimized. Consequently the mass-selected ion beam must be substantially decelerated prior to use. The decelerator uses retarding electric fields to slow the ions in the beam to the desired collision energy. The dication beam has an energy of approximately $200q$ eV prior to entering the decelerator optics, but this is reduced to a few eV for use in the reaction chamber. However, deceleration can cause significant divergence of the ion beam because only the on-axis component of velocity is retarded so off-axis components of velocity become proportionally much larger. The decelerating optics are therefore followed by an Einzel lens to re-focus the beam.

Many crossed-beam ion-neutral studies have employed relatively high collision energies, however this experiment keeps collision energies deliberately low to increase the interaction time between reactant particles in an attempt to encourage bond-forming reactions. In the case of a stable, readily formed dication, such as Ne^{2+}, a usable beam may be achieved at collision energies as low as 1 eV and as high as 50 eV, however in most cases a collision energy range of 4-20 eV (in the laboratory frame) is typical. The most important factor in the overall beam current is the ionization cross-section of the target fragment but beam currents fall at high or low collision energies. In the case of low collision energies, the beam current will decrease because fewer ions will pass through the velocity filter (off-axis velocity components become more important). In the case of high collision energies, the value of L_d (this quantity is effectively a measure of the proportion of dications incident to the source region that are actually detected, and is discussed in Chapter 4) decreases resulting in fewer ions reaching the detector.

3.3 The Mass Spectrometer

The collimated, mass-selected dication beam is introduced into the reaction chamber where it intersects an effusive jet of a neutral gas in the source region of a Wiley-McLaren type time-of-flight mass spectrometer (Figure 3.4). The geometrical parameters and electrode voltages of the spectrometer are detailed in Table 3.1.

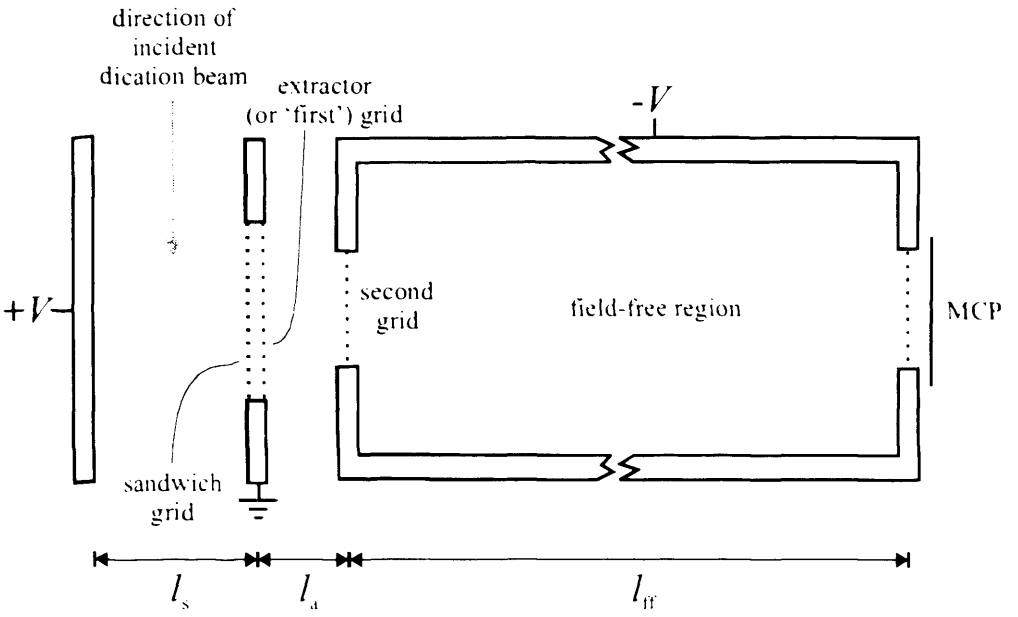

Figure 3.4 Schematic layout of the time-of-flight mass spectrometer.

parameter	setting
collision energy (LAB frame)	4-20 eV
neutral target pressure	6 x 10^{-6} Torr
repeller plate frequency	50 kHz
repeller plate voltage (OFF)	0 V
repeller plate voltage (ON)	+400 V
extractor grid voltage	0 V
drift tube voltage	-1225 V
MCP voltage (front plate)	-2040 V
MCP voltage (back plate)	-40 V
length of source field (l_s)	20 mm
length of acceleration field (l_a)	10 mm
length of drift tube (l_{ff})	280 mm
detector diameter	35 mm

Table 3.1 Experimental parameters under normal operating conditions.

The source optics give first-order space-focussing (see Chapter 1) but do not correct for the distribution in z-velocities of ions in the source. The mass spectrometer is aligned orthogonally to the dication beam to reduce the z-velocity distribution of product ions, since scattering occurs primarily over small angles in the laboratory frame, i.e. the most significant velocity components of products are in the x-direction. This arrangement minimises the effect that scattering has on the mass resolution of the spectrometer, but equally prevents any information about scattering from being directly obtained. For more details on the capabilities and restrictions on Wiley-McLaren optics[8], refer back to Chapter 1.

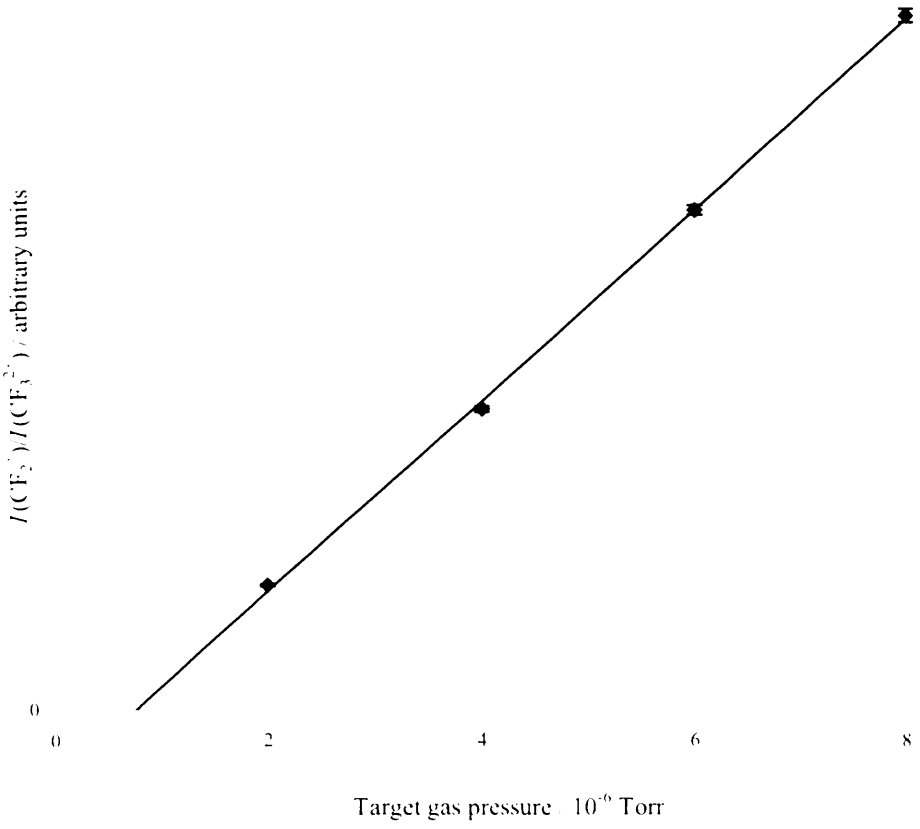

Figure 3.5 Demonstration of the linear relationship between target gas pressure and relative product ion intensity, using the $CF_3^{2+} + H_2O$ system for calibration.[9] Note that for practical reasons, the target gas pressure is not measured at the gas inlet and so the linear fit does not occur at zero.

The pressure in the source region is kept low to ensure single-collision conditions[9-11]. This means that any products of a collision will not be able to react with another neutral molecule; secondary reactions would severely complicate the interpretation of the mass spectrum. Under a single-collision regime, the intensity of a product ion has a linear relationship to the pressure of the neutral reactant; if multiple collisions are occurring this becomes a power relationship.[11,12] Experiments performed during the commissioning of the apparatus confirmed that single-collision conditions do indeed apply at the pressure at which we operate.

The repeller plate at the rear of the source region is pulsed at a frequency of 50 kHz for a duration of 10 μs, equivalent to 10 μs on and 10 μs off. Although the ion source is continuous, the dication beam is deflected by the application of the repeller plate voltage, and only ions already in the source region of the TOF-MS when the pulse begins can reach the detector. Of course, all ions are extracted from the source region, both reaction products and unreacted dications. The extraction electrode is preceded by a sandwich grid, which has a small positive bias to prevent stray ions from entering the acceleration region before the repeller plate pulse is applied.

The time-of-flight of an ion can be readily calculated using classical mechanics and, for fixed experimental parameters, depends only upon an ion's mass-to-charge ratio, m/z, it's initial position along the TOF axis, $s_i(z)$, and it's initial component of velocity along the TOF axis, $v_i(z)$. Note that the components of velocity and position in the dication beam direction (the x-axis) do not affect the TOF of an ion, but do determine whether an ion reaches the detector or hits the wall of the spectrometer and is thus vital for understanding what proportion of a given species is actually detected, as discussed in Chapter 4.

In the following algebra, the subscripts 's', 'a' and 'ff' refer to the source, acceleration and field-free regions respectively. The subscripts 'R', '1' and '2' refer to the repeller plate and the first and second grid electrodes respectively.

The acceleration experienced by an ion of mass m and z multiples of unitary charge in an electric field is given by:

$$a = \frac{F}{m} = \frac{qE}{m} = \frac{ze}{m}\frac{\Delta V}{l} \tag{3.9}$$

The relevant velocities and flight times of such an ion, with an initial z-component of velocity $v_i(z)$, can then be calculated using standard Newtonian equations of motion:

$$v_1(z) = \sqrt{v_i(z)^2 + 2a_s\left(\tfrac{1}{2}l_s - s_i(z)\right)} \tag{3.10}$$

$$t_s = \frac{v_1(z) - v_i(z)}{a_s} \tag{3.11}$$

$$v_2(z) = \sqrt{v_1(z)^2 + 2a_a l_a} \tag{3.12}$$

$$t_a = \frac{v_2(z) - v_1(z)}{a_a} \tag{3.13}$$

$$t_{ff} = \frac{l_{ff}}{v_2} \tag{3.14}$$

$$t = t_s + t_a + t_{ff} \tag{3.15}$$

If the displacement from the centre of the source $s_i(z)$ and the initial velocity $v_i(z)$ are both zero we have the thermal TOF, t_0.

Since the velocities of an ion of any given mass are dependent only on the experimental parameters (the internal dimensions of the spectrometer and the magnitude of the electric fields), all these parameters can be consolidated into a single empirical constant, k:

$$t = k\sqrt{\frac{m}{z}} \tag{3.16}$$

The short flight times in most time-of-flight mass spectrometers allow rapidly pulsed sources to be used and hence minimize collection times. In this experiment the repeller plate is pulsed at 50 kHz (every 20 μs) whereas the flight time of a 100 amu ion is less than 7 μs. Additionally, the simple design of a linear mass spectrometer is straightforward to construct and maintain.

3.4 Detection

Ions are detected using a chevron pair of microchannel plates (MCPs). A large negative potential is applied to the front MCP to accelerate incoming ions into the plate and a grid is positioned 2 mm in front of the MCPs to prevent field penetration into the drift region. Between its threshold for detection and maximum detection efficiency, the detection efficiency of an MCP is linearly proportional to the momenta of incident ions; however, once the maximum detection efficiency is reached, this becomes independent of momentum. The high field in front of the detector ensures that the detection efficiency does not depend on the momentum of incident ions and so all ions are detected with equal efficiency. The rear MCP is held at a potential close to zero to draw the electrons generated by an ion impact through the channels of the plates. Each MCP typically produces $10^{4\text{-}6}$ electrons for each ion impact and hence an amplification of charge by the same factor.

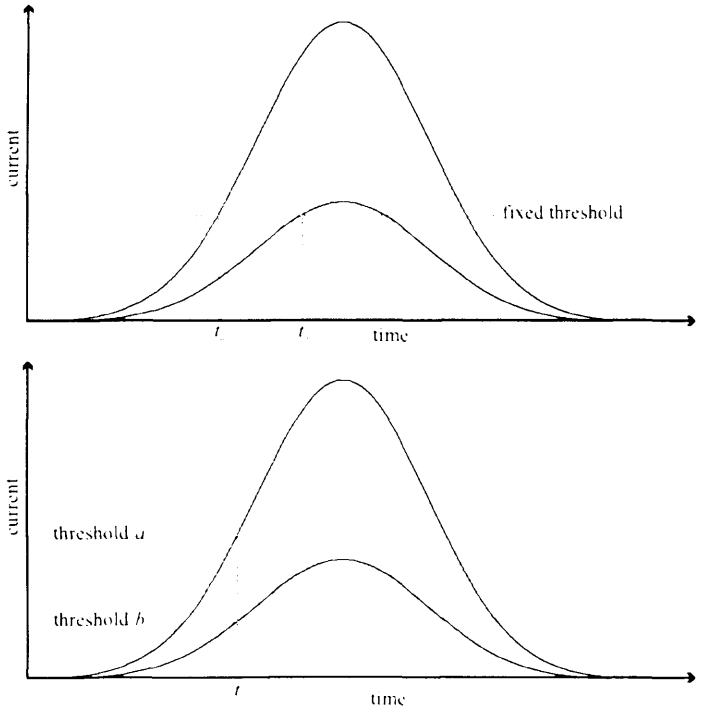

Figure 3.6 Comparison of fixed threshold (top) and constant fraction (bottom) discrimination. By varying the threshold for peaks of different heights, CFD records a single time for all co-incident peaks.

The current pulse generated by the MCPs following an ion arrival is passed to a constant-fraction discriminator (CFD) that monitors pulses caused by ion impacts. A CFD, unlike a simple threshold discriminator, outputs identical arrival times for pulses of different intensities but the same peak position (Figure 3.6), thus minimising timing errors. The CFD also applies threshold discrimination to remove weak noise signals. Output pulses from the CFD are passed to a time-to-digital converter and end the timing cycle, as described below.

The timing cycle is dictated by a pulse generator and monitored by a LeCroy time-to-digital converter (TDC). The pulse generator delivers a voltage pulse to the repeller plate of the mass-spectrometer and then sends a START signal to the TDC. The START signal is generated as a NIM pulse, but is converted into an ECL pulse by a CFD before being passed to the TDC. The TDC commences timing after a short delay so that RF noise produced by the repeller plate pulse is not recorded. An ion impact at the detector generates a STOP signal, which, as detailed above is amplified and discriminated before reaching the TDC, which stops timing.

The delays associated with the detection electronics add a second experimental constant to the time-of-flight equation:

$$t = k\sqrt{\frac{m}{z}} + c \tag{3.16}$$

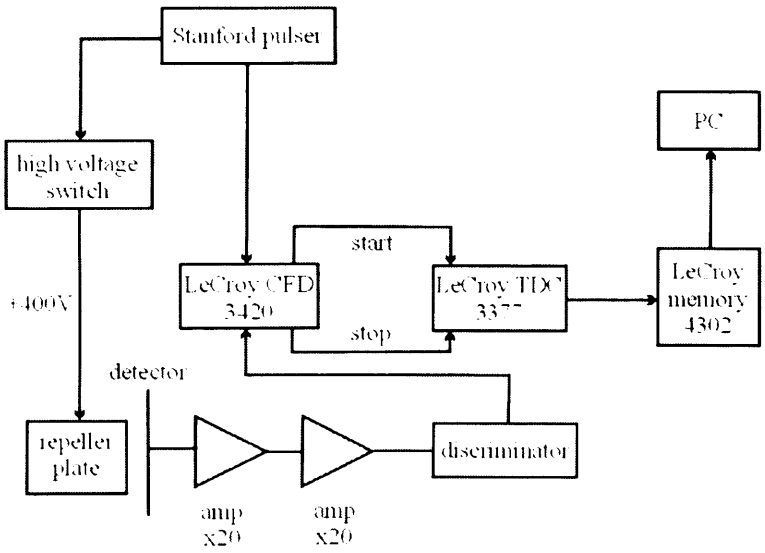

Figure 3.7 Schematic layout of the detection and timing electronics.

Note that while times-of-flight can be calculated absolutely using all the experimental parameters, the constants k and c can be ascertained from any mass spectrum for which the masses of two peaks are known and these constants will not change providing the experimental conditions remain fixed.

Spectra are recorded for a fixed number of cycles, so the recording time is proportional to the dication beam current. A single cycle comprises 512 kb of data, and spectra are usually run for 5000 cycles, which can take between 10 min and 2 hr to collect. Flight times are passed to a PC where they are compiled into a histogram. These time spectra can be readily converted into mass spectra using Equation 3.16, however, reaction cross-sections are not directly proportional to intensities in the mass spectra. The following chapter describes how 'real' product intensities are extracted from mass spectra and the method previously used to turn those intensities into reaction cross-sections. As will be shown, this method makes a number of assumptions that are only valid for certain product ions and so a new, more rigorous treatment that is more generally applicable is introduced.

3.5 References

[1] S.D. Price, *J. Chem. Soc., Faraday Trans.* **93:** 2451 (1997)
[2] P.W. Burnside and S.D. Price, *Int. J. Mass Spectrom.* **249:** 279 (2006)
[3] L. Wahlin, *Nuc. Instrum. & Methods* **27:** 55 (1964)
[4] W. Wien, *Ann. Physik.* **65:** 440 (1898)
[5] M.L. Oliphant, E.S. Shire and B.M. Crowther, *Proc. Royal Soc.* **A146:** 922 (1934)
[6] W. Aberth and H. Wollnik, *Mass Spec. Rev.* **9:** 383 (2005)
[7] A.R. Kip (1969) Fundamentals of Electricity and Magnetism. McGraw-Hill, Singapore
[8] W.C. Wiley and I.H. McLaren, *Rev. Sci. Instrum.* **26:** 1150 (1955)
[9] N. Tafadar (2001) PhD thesis, UCL
[10] N. Lambert, D. Kearney, N. Kaltsoyannis and S.D. Price, *J. Am. Chem. Soc.* **126:** 3658 (2004)
[11] D. Kearney (2005) PhD thesis, UCL
[12] K. Yamasaki and S.R. Leone, *J. Chem. Phys.* **90:** 964 (1989)

Chapter 4: Data Analysis

4.1. Introduction

This chapter describes how ion counts recorded by the detector are processed, first to give intensities of ion signals and ultimately produce reaction cross-sections for all ionic products. The model used to extract cross-sections from experimental data has been redeveloped from first principles, and so this chapter includes both a description of the previous methodology and a thorough explanation of the extensive new model. The work done on improving this process of analysis has resulted in the ability to extract cross-sections of all ionic products from electron transfer reactions and bond-forming reactions for the first time and the new methodology is applied to experimental results in the following two chapters where it is seen to dramatically outperform the previous method of analysis.

4.2. Data collection

As discussed in the previous chapter, flight times of ions are measured using a time-of-flight mass spectrometer and transferred to a PC. Each count is assigned to a channel depending on its flight time, typically the time window that is monitored is

divided into 1000 channels. The completed histogram represents a time-of-flight spectrum and can be calibrated to a mass spectrum using the relationship:

$$t = k\sqrt{\frac{m}{z}} + c \tag{4.1}$$

Identifying the mass of two peaks in the time-of-flight spectrum yields a pair of simultaneous equations that can be solved to give the constants k and c, which are dependent on the operational parameters and the detection electronics respectively. This empirical calibration is easy to employ in simple systems, as are dealt with in this thesis.

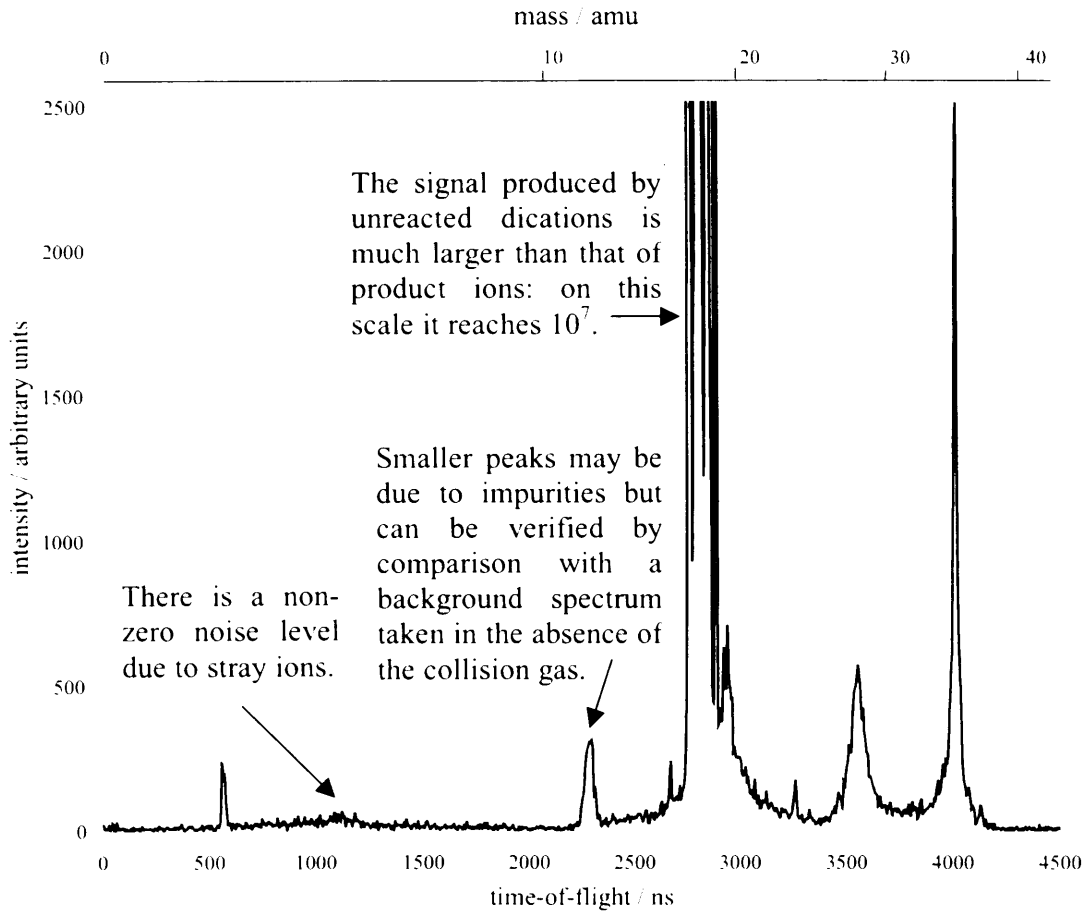

Figure 4.1 An example of experimental data from a bimolecular collision (Cl^{2+} + CO). The spectrum is scaled linearly in time (bottom scale), which is equivalent to a non-linear mass scale (top scale). To show product peaks, the y-axis has been curtailed; on this intensity scale, the dication signal reaches 10^7.

Notice that the dependency of the time-of-flight on the square root of mass means that consecutive masses appear closer together at higher masses, giving time-of-flight spectra an increasingly temporally 'squashed' appearance at higher masses (Figure 4.1). Consequently a spectrometer's resolution only becomes an issue when dealing with large molecules. The mass spectrometer employed in these experiments has rather low resolving power, but since it is primarily used to study species of less than 100 amu, this does not become a problem.

4.2.1. Raw intensities

Spectra are taken in pairs, each comprising the same number of cycles, the first recorded with the neutral collision gas absent ('background') and the second with the collision gas present ('reaction'). A 'peak' is manually identified and allocated a 'start channel' and a 'stop channel'; this is done by eye, as algorithmic delineation of peaks is sometimes unreliable, particularly for weak signals. The total number of counts in the peak is then the sum of counts in the channels between, and including, the start and stop channels. Note, that if the spectrum were continuous rather than discrete, complicated numerical integration would be required rather than a simple summation.

The number of 'real' counts, i.e. the number of counts in the peak that are actually due to ions of the mass associated with that peak, is the total number of counts minus the number of counts due to stray ions (Figure 4.2). Stray ions are those that do not originate from the reaction region of the mass spectrometer and hence have no correlation between their mass and their recorded flight time. Such ions are largely responsible for the experimental noise (a non-zero baseline) in time-of-flight spectra. An estimate of the contribution of stray ions to a spectral peak is obtained by estimating the level of noise at the start channel and at the stop channel and calculating the area beneath. The noise level is usually taken to be the approximate level of the baseline of the spectrum directly before and directly after the peak of interest. However, if the peak is close to another signal, particularly that of the dication beam, the contribution of stray ions becomes a little harder to estimate. Clearly, the larger the proportion of total counts in a peak constituted by stray ions, the more important the accuracy of this estimation becomes. In cases where the signal is particularly weak ($< 10^{-5}$ relative to the intensity of the dication signal), small changes in the estimate of the contribution of stray ions can have a significant effect on the calculated 'real' intensity.

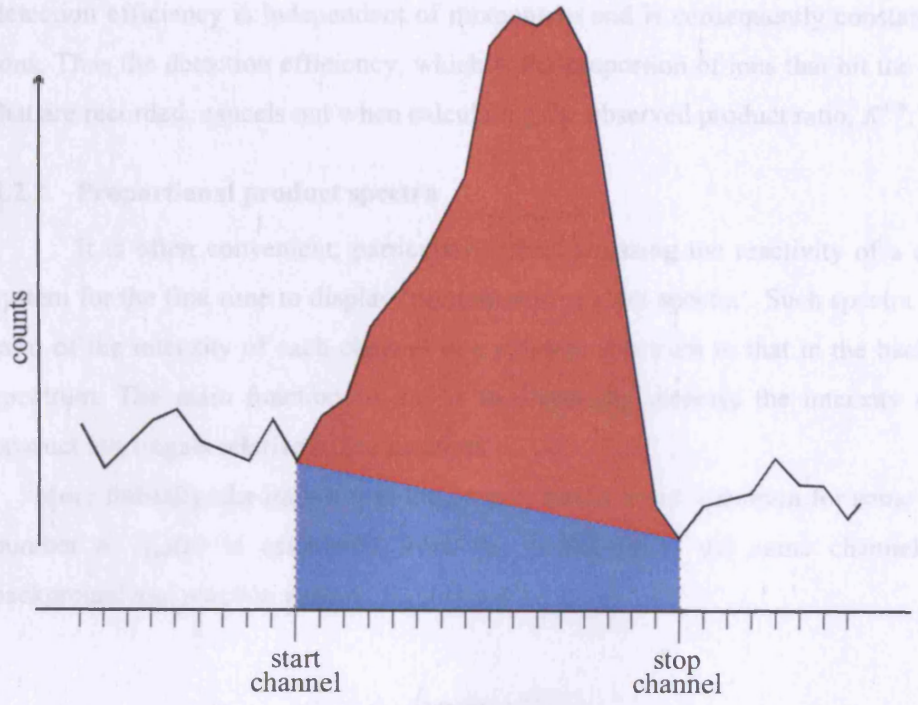

Figure 4.2 An example section of a typical spectrum including a single peak. The start channel and stop channel are chosen by inspection. The real counts (shaded red) are obtained by subtracting the noise counts (shaded blue) from the sum total of counts in all channels in the peak.

The number of 'real' counts in a peak is thus the total number of counts minus the estimated number of noise counts. The difference between the number of real counts in a peak in a reaction spectrum and the number of real counts in the corresponding peak in a background spectrum is the number of counts of the particular ion resulting from bimolecular reactions. This number (I_j) is normalized relative to the intensity of the dication peak in a background spectrum (I_d), to provide consistency between different spectra, and the result is termed the 'observed product ratio', R^{obs}, for the product ion m_j associated with the peak in question.

$$R^{obs} = \frac{I_j}{I_d} \tag{4.2}$$

The use of product ratios circumvents any need to establish the detection efficiency of the detector. At the energy range over which ions hit the detector, the detection efficiency is independent of momentum and is consequently constant for all ions. Thus the detection efficiency, which is the proportion of ions that hit the detector that are recorded, cancels out when calculating the observed product ratio, R^{obs}.

4.2.2. Proportional product spectra

It is often convenient, particularly when assessing the reactivity of a collision system for the first time to display 'proportional product spectra'. Such spectra take the ratio of the intensity of each channel in a reaction spectrum to that in the background spectrum. The main function of this is to drastically increase the intensity of weak product ion singals relative to the dication.

More formally, the intensity in the proportional product spectrum for some channel number n, $I_{ppd}(n)$ is calculated from the intensities of the same channel in the background and reaction spectra, $I_{back}(n)$ and $I_{reaction}(n)$:

$$I_{ppd}(n) = \frac{I_{reaction}(n) + \Delta}{I_{back}(n) + \Delta} \tag{4.3}$$

where Δ is an optional constant (>1) to reduce the noisiness of the proportional product spectrum associated with regions of low counts.

Clearly the use of proportional product spectra is inappropriate for quantitative analysis because the intensity scale becomes non-linear, however it readily identifies all products of a collision, regardless of cross-section, on a similar 'intensity' scale.

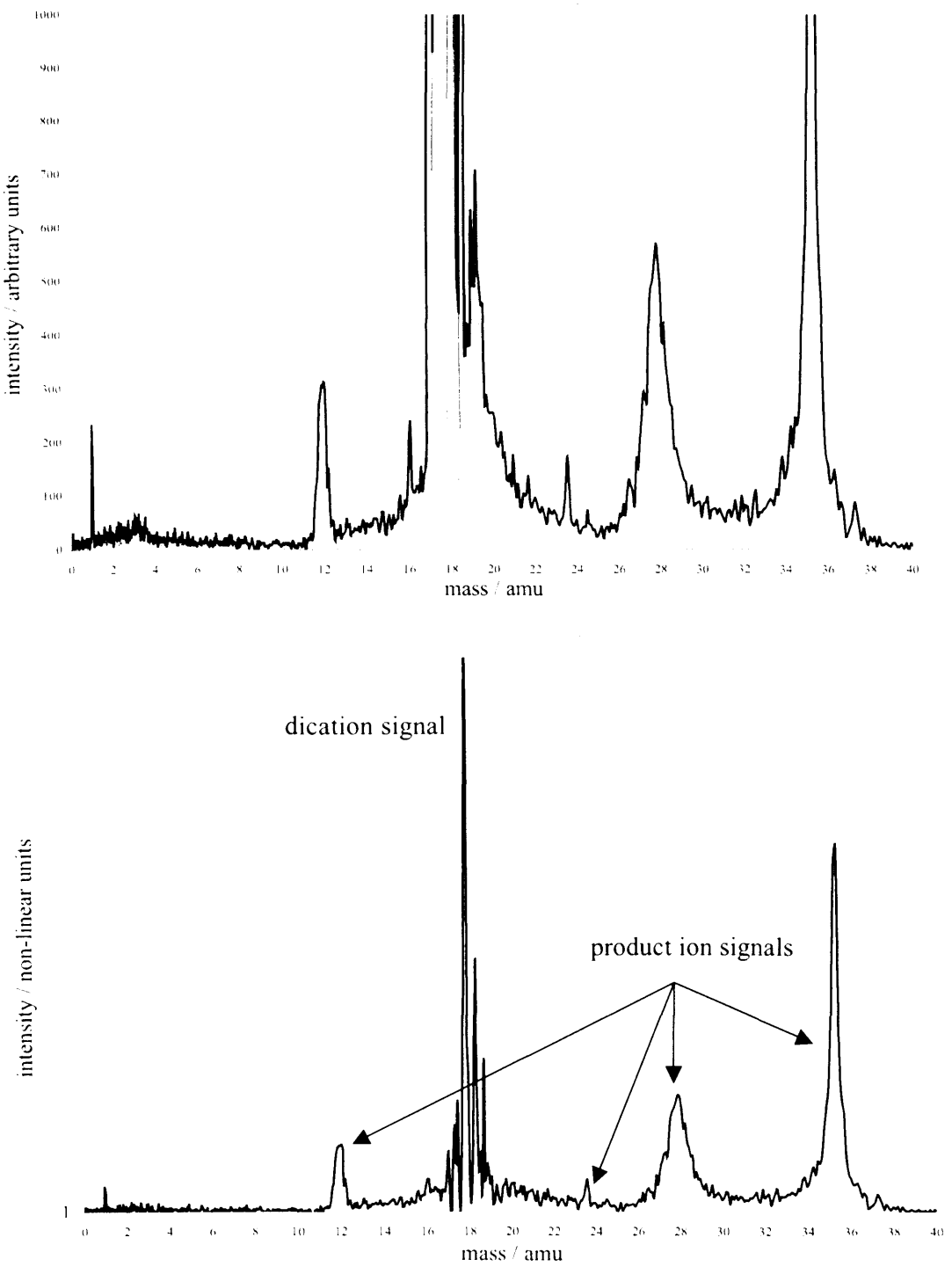

Figure 4.3 Top: the same data as Figure 4.1, but on a linear mass scale and with a background spectrum superimposed (thin line). Bottom: the corresponding proportional product spectrum. Notice that the dication signal is greatly reduced in the proportional product spectrum.

4.2.3. Counting effects

R^{obs} is the ratio of a particular product intensity to the dication intensity. However, the measured dication intensity may underestimate the number of dications that actually hit the detector. This uncertainty is due to the deadtime of the detector, which means that if two ions hit the detector within 32 ns of each other, only the first will be detected. The dication beam current is always kept below an average of 1 ion per pulse, but the closer the current is to 1 ion per pulse, the more likely it is that two dications will be extracted in any single pulse. Since the dications have the same mass, the focussing properties of the mass spectrometer means that they will hit the detector within 32 ns of each other and hence only one count will be recorded. This is purely a statistical problem and is corrected empirically as previous calibration experiments have shown that the following relationship exists between the observed and the true product ratios:

$$R^{obs} = k\ R^{true} \tag{4.4}$$

where k is:

$$k = \frac{a}{t^b} + 1 \tag{4.5}$$

In Equation 4.5, t is the time taken to collect the data for a spectrum, which, subject to the collection time being determined by a fixed total amount of data, is inversely proportional to the dication beam current. Moreover, the constants a and b have been found to be independent of the collision system and equal to 1.4 x 10^{13} and 5.94 respectively.[1,2] At lower values of t, the true value of the dication intensity is increasingly underestimated and hence the true value of each product ratio is overestimated. However, a plot of k against t (Figure 4.4) shows that the value of k only becomes greater than 1.1 at collection times of below 240 s (4 min), and most spectra have considerably longer collection times than this.

The counting effects described above only affect the collection of unreacted dications and not product ions, because product ion intensities are typically more than 1000 times weaker than the parent dication intensity and consequently the probability of

two product ions of the same mass hitting the detector following the same repeller plate pulse is negligible.

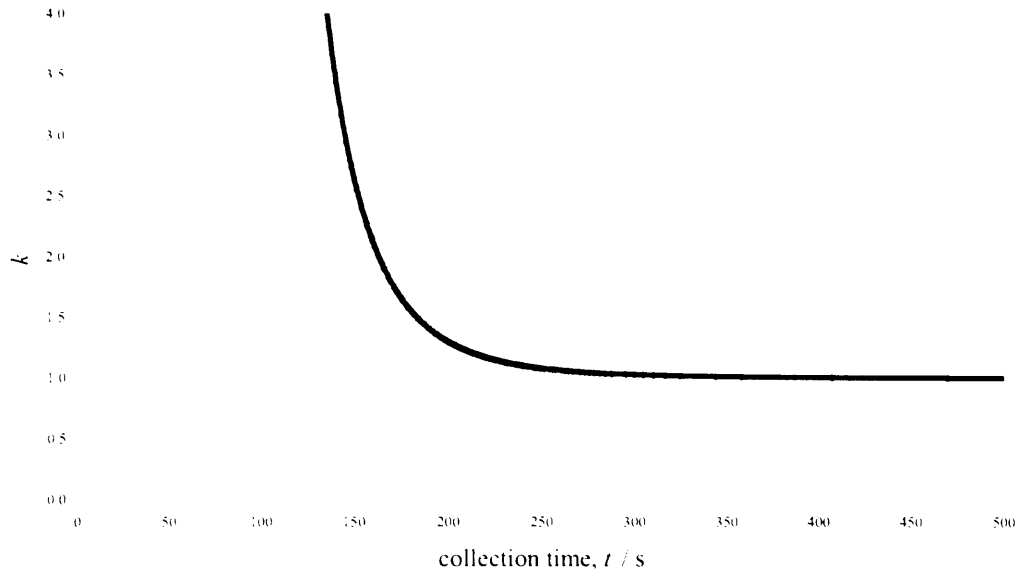

Figure 4.4 A plot of the counting factor k against collection time. This becomes appreciably greater than unity only for short collection times (< 250 s).

4.3. Calculating ion trajectories

It is of crucial importance when interpreting the experimental data to be able to calculate whether an ion of a particular mass, velocity and position when the repeller plate pulse is applied will go on to hit the detector. After all, as far as the experiment is concerned, any ions that do not reach the detector may as well not exist. Fortunately, since only linear electric fields are employed, the trajectories of ions can be simply calculated by application of basic electrostatic laws. For the purpose of computing ion motion, all trajectories are considered to lie in the xz-plane, since the y-component of velocity will not affect the time-of-flight of an ion, and is extremely unlikely to be large enough to cause sufficient deviation from the time-of-flight axis for an ion to miss the detector. The initial z-component of velocity may also be ignored, because this will always be very small compared to the z-velocity after extraction and hence make a negligible difference to the time-of-flight. The important calculation to be made is the x-

position of an ion as a function of the z-position; if these co-ordinates are then compared with the physical size of the inside of the mass spectrometer it can be determined whether an ion will reach the detector.

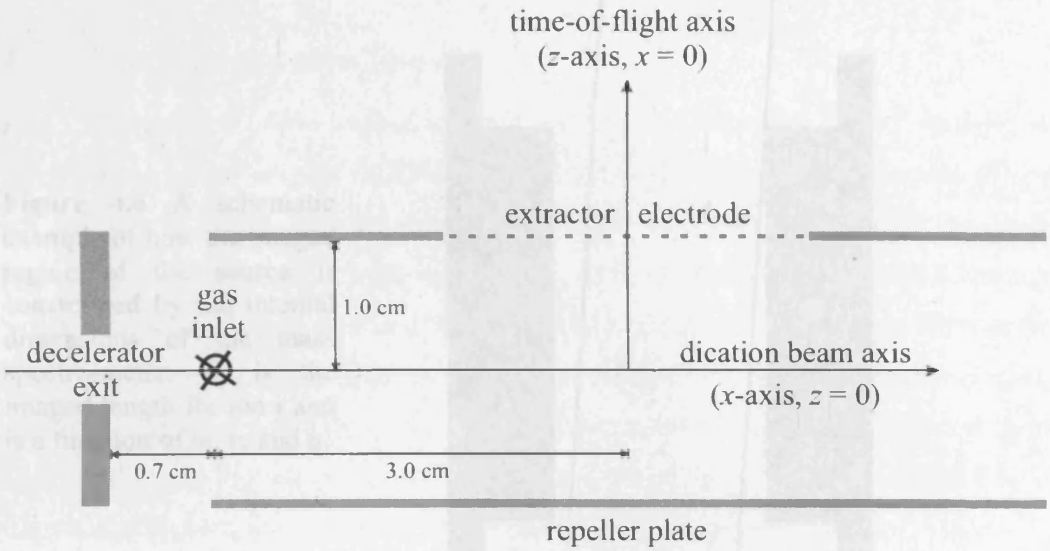

Figure 4.5 Scale diagram of the source region of the mass spectrometer.

The limiting values of x, as the repeller plate pulse is applied ($z = 0$), for an ion to pass through an aperture of diameter Ø at some position along the time-of-flight axis z, are:

$$x_{\text{min}}^{\text{max}}(z=0) = \pm\tfrac{1}{2}\text{Ø}_z - v_j t_z \qquad (4.6)$$

where t_z is the flight time of the ion up to the given value of z and v_x is the initial value of the x-component of the LAB frame velocity (this can be positive or negative). Note that in this section, the term 'initial' refers to the time when the repeller plate pulse is applied. This is different to the time when the ion is 'born', an important distinction that is introduced into the analysis at a later stage.

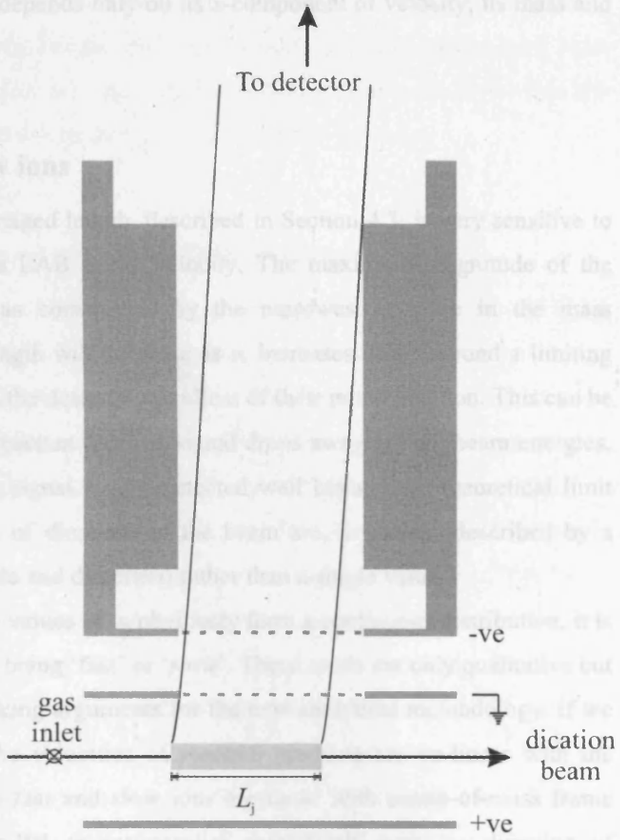

Figure 4.6 A schematic example of how the imaged region of the source is constrained by the internal dimensions of the mass spectro-meter. L_j is the imaged length for ion j and is a function of m, v_x and q.

In fact, rather than calculating limiting values of x for all values of z, we need only consider three: the extraction electrode (z = 1.0 cm, Ø = 3.0 cm), the exit of a series of ion optics (which are no longer used) in the field-free region (z = 9.0 cm, Ø = 2.6 cm) and the detector (z = 31.5 cm, Ø = 4.0 cm). An ion must pass within all three of these apertures in order to hit the detector, for which there will be a single value of x_{max} and a single value of x_{min}. The length between these two limiting values is termed the 'imaged length', L; only ions located within the imaged length when the repeller plate pulse is applied will reach the detector. Note that although the term imaged length is used, strictly what we are defining is an imaged *volume*, of length L and a cross-sectional area equal to that of the dication beam. However, due to the space-focussing properties of the mass spectrometer, small deviations in the initial z-position

of an ion has a negligible effect on its velocity. For fixed experimental parameters, the imaged length of some ion j depends only on its x-component of velocity, its mass and its charge.

4.4. Fast ions and slow ions

The position of the imaged length, described in Section 4.3, is very sensitive to the x-component of an ion's LAB frame velocity. The maximum magnitude of the imaged length is 2.6 cm, as constrained by the narrowest aperture in the mass spectrometer. The imaged length will decrease as v_x increases until, beyond a limiting value of v_x, no ions can reach the detector regardless of their initial position. This can be seen experimentally, as the reactant dication signal drops away at high beam energies, although in practice a small signal is still detected well beyond the theoretical limit because the velocity vectors of dications in the beam are, in reality, described by a distribution (in both magnitude and direction) rather than a single value.

Although the possible values of v_x obviously form a continuous distribution, it is convenient to refer to ions as being 'fast' or 'slow'. These terms are only qualitative but will be useful later when making arguments for the new analytical methodology. If we make the assumption that the velocities of reaction products are co-linear with the incident dication beam, then fast and slow ions are those with centre-of-mass frame velocity vectors aligned parallel or anti-parallel respectively with the direction of motion of the centre-of-mass. Put another way, fast ions have LAB frame velocities greater than the velocity of the centre-of-mass; slow ions have LAB frame velocities less than the velocity of the centre-of-mass.

At high collision energies, the distinction between fast and slow ions is of little importance. However, at the low collision energies employed in this experiment, the change in velocities brought about by the energy released in a charge separation reaction is large relative to the velocities of the reactants. This means that slow ions usually have LAB frame velocities of less than 0.1 cm μs^{-1}, and may even be scattered backwards in the LAB frame.

The important difference between fast and slow ions is the location and size of the imaged length. For fast ions, the imaged length will be centred at a negative values of x, in the proximity of the gas inlet (at $x \approx -3.0$ cm; the gas inlet so located for this

reason), and be relatively short. In contrast, the imaged length for slow ions will be centred somewhere close to the centre of the source region, where the number density of the collision gas is much lower, and be relatively long. This result explains, at a basic level, why the intensities of slow ions are usually measured to be much lower than the intensities of the fast ions with which they are concomitantly formed.

4.5. Extraction of cross-sections (original method)

The rest of this chapter deals with the conversion of intensities measured by experiment into reaction cross-sections. This process is not as straightforward as it may at first appear, because spectral intensities in time-of-flight experiments are a measure of number densities in the source region, whereas reaction cross-sections are related fluxes through the source region. This section describes how reaction cross-sections, in arbitrary units, have previously been obtained from product ratios, R^{true}. This method is neither time-dependent nor does it include pressure variations or angular distributions. It has been shown to produce adequate results for fast ions but breaks down badly for slow ions, which have not been analyzed in previous reports regarding this experiment[1,3-12]. A new method of analysis has been developed, which works for both fast and slow ions, is detailed later in Section 4.6.

The experimental data from which we begin records intensities, which are measures of number densities in the source region of the spectrometer. However, reaction cross-sections are proportional to the *flux* of each product across the source region, so simply comparing different product peaks in a time-of-flight spectrum does not give a direct indication of the relative reaction cross-sections for forming the different products.

The flux of a reaction product, F_j, can be related to the flux of incident dications, F_d, by:

$$F_j = \sigma_j N_n L_0 F_d \tag{4.7}$$

where σ_j is the absolute reaction cross-section for forming species j, N_n is the number density of the neutral collision gas per unit volume and L_0 is the length over which the

dication beam is attenuated by the neutral reactant, hence $N_n L_0$ is the column density of the neutral collision species.

The detected intensity, assuming a detection efficiency of 100%, is the number of ions in the imaged volume, of length L and area A, the cross-sectional area of the dication beam.

$$I = NLA \tag{4.8}$$

The number density per unit volume of an ion is related to its flux per unit area and speed in the direction of the dication beam.

$$N = \frac{F}{v} \tag{4.9}$$

Consequently, the flux of a species across the source region can be directly related to its intensity:

$$I = \frac{F}{v} LA \tag{4.10}$$

Using Equation 4.10 to express the fluxes in Equation 4.7 for some product species j and the parent dication d we have:

$$\frac{I_j v_j}{L_j A} = \sigma_j N_n L_0 \frac{I_d v_d}{L_d A} \tag{4.11}$$

By making the considerable assumption that N_n, L_0 and A are all constant for a particular collision system, we define:

$$\sigma_j' = \frac{\sigma_j}{N_n L_0} \tag{4.12}$$

as the absolute cross-section in arbitrary units, which yields:

$$\sigma_j = \frac{v_j}{v_d}\frac{L_d}{L_j}\frac{I_j}{I_d} = \frac{v_j}{v_d}\frac{L_d}{L_j}R^{true} \qquad (4.13)$$

The dication velocity v_d is known from the beam energy and, as described in Section 2.6, the product velocity v_j can be estimated using momentum and energy arguments.

Inspection of Equation 4.13 immediately poses problems when considering its behaviour towards limits of v_j. As v_j decreases, L_j increases but is subject to a maximum value of 2.6 cm (see Section 4.3). Thus in the case where $v_j = 0$ (which is perfectly possible, given the operating conditions, albeit practically unlikely), the resultant reaction cross-section of product j will also be zero, which is clearly not true. This inconistency can be removed by considering L_j/v_j as a single quantity, representing the residence time τ of ion j in the cylindrical imaged volume. As $v_j \rightarrow 0$, in the absence of stray fields, the residence time would tend to very large values, but in practice is subject to a maximum imposed by the pulsed nature of the experiment. The repeller plate is pulsed at a fixed frequency of 50 kHz (= every 20 μs) and, although the pulse duration can be altered (for instance, extended to allow detection of particularly heavy ions), it is typically set at 10 μs. This gives a maximum residence time of 10 μs, this time being the period that the source region is free of electric fields. Equation 4.13 can now be re-written in terms of residence times:

$$\sigma_j = \frac{\tau_d}{\tau_j}R^{true} \qquad (4.14)$$

subject to $\tau \leq 10$ μs.

The methodology described above, which was employed until recently, obtains reaction cross-sections using what might be termed the 'cell approach', whereby for each reaction product a region of the source of fixed length (L_j, or L_0 in the case of the parent dications) and uniform collision gas number density (N_n) was defined and treated as a reaction cell to which the Beer-Lambert law could be applied. There are no physical boundaries to such a cell, but its dimensions are defined by the limiting

trajectories for which ions of a certain mass and velocity are calculated to reach the detector.

In reality, however, since the neutral reactant is introduced as an effusive jet, the neutral number density varies a great deal across the source region and the cell approximation only holds for ions formed in the 'high' pressure region close to the gas inlet. Indeed, most fast ions that go on to be detected are formed close to the gas inlet, which is why the above method works well. However, only slow ions formed far from the gas inlet (in 'low' pressure conditions) have appropriate trajectories to reach the detector but the 'cell' approximation does not allow for the formation of such ions.

The cell approach also neglects the angular distribution of product ions and the motion of both parent dications and product ions during the period that the repeller plate voltage is off and reactions can take place. All these problems have been tackled in the development of a new method of analysis that explicitly accounts for:

i) the number density distribution of the neutral collision gas along the line of the dication beam (x-axis),

ii) the variation of the dimensions of the notional reaction cell with time,

iii) the angular distribution of product ions,

iv) the finite time required for the dication beam to propagate across the source region.

4.6. Incorporation of time-, pressure-, and angular-dependences into the analysis of mass spectra

This section is devoted to a thorough explanation of the new analytical model for the first time. In attempting to develop a more general methodology for the analysis of our experimental data, we can begin by considering how the detection of fast and slow ions differs. As described in Section 4.4, product ions with a lab frame velocity, immediately following a collision, in the beam direction *greater* than the velocity of the centre-of-mass are termed 'fast' and those with such a velocity *less* than the velocity of the centre-of-mass are termed 'slow'. In SET events, the angular scattering of incident dications is strongly biased towards small scattering angles because electron transfer occurs at large separations (> 2 Å), so in an SET event between a dication, X^{2+}, and a neutral collision partner Y, X^{+} would in most cases be the fast ion and Y^{+} the slow ion.

$$X^{2+} + Y \rightarrow X^{+} + Y^{+} \qquad (4.15)$$

Crucially, since we operate at low collision energies, the velocity of the centre-of-mass is relatively low (typically in the range 2-6 cm μs^{-1}), and as a result slow ions often have very low or even negative lab frame velocities. In previous experimental work with this apparatus, slow product ions were not included in the analysis. This was because those slow ions that reach the detector are formed in a spatially distinct portion of the source region to fast ions. For instance, in the SET reaction above, each reactive event forms a $X^{+} + Y^{+}$ pair. However, despite not directly measuring co-incidences, due to the orthogonal arrangement of the TOF-MS we know with certainty that none of the *detected* X^{+} ions were formed in co-incidence with any of the detected Y^{+} ions; in each case the partner ion goes undetected. Detected fast ions are formed near the neutral gas inlet, across a small spatial region over which the neutral gas pressure is relatively high and does not change significantly. Previous comparison with other published work has shown that the calculated relative reaction cross-sections (using the methodology outlined in Section 4.5) for such fast ions across our collision energy range are valid.[4,7,13] However, detected slow ions are formed much further away from the neutral gas inlet and over a much larger portion of the source region. The neutral gas pressure will be much lower in this sample space and will change considerably across it. Hence, measured intensities of slow ions will require considerable correction to compensate for the nature of the sample space and so to place their reaction cross-sections on the same scale as those of fast ions. The following section details a more general analysis of our data, which may be applied to all product ions.

The repeller plate is pulsed at a frequency of 50 kHz, and each pulsing cycle, though adjustable, typically comprises 10 μs with the voltage applied and 10 μs with the voltage removed. The dication beam is deflected for the duration of the repeller plate pulse, but propagates across the source in the positive x-direction with velocity v_d from the time at which the repeller plate voltage is removed (t=0) until the voltage is re-applied (t=T). Note that these times relate only to the pulse cycle and have no connection with times-of-flight. This time window ($0 < t < T$) is the period in which observable reactions may occur. In order for a product ion, j, to hit the MCP detector, it must be located in some cylindrical volume, of length L_j and cross-sectional area A (see Section 4.3), at time T. The limits of this length along the dication beam axis are $x_{j1}(T)$

and $x_{j2}(T)$, which are determined by the internal dimensions and electric fields of the mass spectrometer, the velocity of the ion, v_j, and the *m/z* ratio of the ion, similarly to that described in Section 4.5. However, while detected product ions may be formed in $L_j(T)$ at time T, they can also be formed in a different region at an earlier time, provided they reach $L_j(T)$ when the repeller plate pulse is applied. In other words, for a product ion to reach the detector it must be formed in a time-dependent region of the source, $L_j(t)$ where $0 < t < T$ (Figure 4.7).

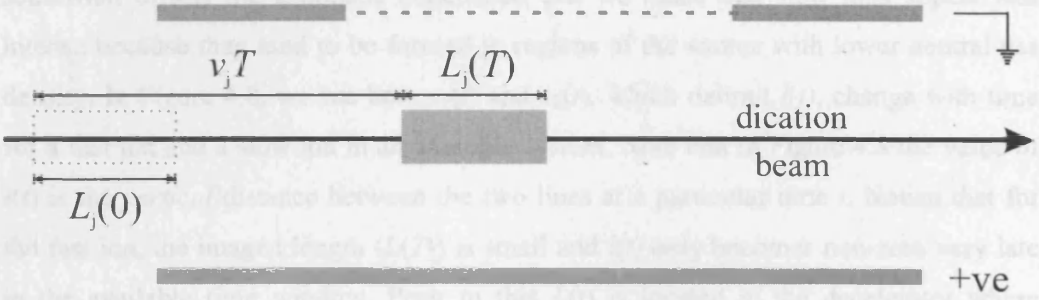

Figure 4.7 In principle, the length $L_j(0)$ propagates across the source with velocity v_j. In practice, however, the internal dimensions of the spectrometer or the propagation of the dication beam may mean that the real region over which observable reactions are actually occurring is less than $L_j(t)$, so limiting values of x must be calculated for all values of t.

Both the position and magnitude of L_j can change with time and its limits are denoted as $x_{j1}(t)$ and $x_{j2}(t)$. In principle, the points $x_{j1}(0)$ and $x_{j2}(0)$ are given by:

$$x_{jn}(0) = x_{jn}(T) - v_{jn}T \qquad n = 1,2 \tag{4.16}$$

Points x_1 and x_2, the limits of $L_j(t)$, move across the source region with velocity, v_j.

$$x_{jn}(t) = x_{jn}(0) + v_{jn}t \qquad n = 1,2 \tag{4.17}$$

However, when considering the actual region in which observable product ions are being formed at any given time, one must also consider firstly whether the calculated value of $L_j(t)$ lies partly or wholly physically outside the source region of the mass

spectrometer and secondly whether it is encompassed by the dication beam. In other words, the above definition of $L_j(t)$ (delimited by Equation 4.17) may include points at which observable ions cannot possibly be formed, such as in the decelerator, or ahead of the dication beam, which takes a finite time after $t = 0$ to propagate across the source region. Thus the length of the volume in which observable reactions are occurring at time t is defined by another length $l_j(t)$ where $0 \leq l_j(t) \leq L(t)$.

The evolution of l with time can often be quite complicated and difficult to predict intuitively. An interesting competition arises between $l(t)$ and N_n, which somewhat offsets the simplistic conclusion that we made that slow ions appear less intense because they tend to be formed in regions of the source with lower neutral gas density. In Figure 4.8, we see how $x_1(t)$ and $x_2(t)$, which delimit $l(t)$, change with time for a fast ion and a slow ion in an example system. Note that in Figure 4.8 the value of $l(t)$ is the *vertical* distance between the two lines at a particular time t. Notice that for the fast ion, the imaged length ($L(T)$) is small and $l(t)$ only becomes non-zero very late in the available time window. Prior to this $L(t)$ is located in the decelerator where observable ions are unlikely to be formed, because of the aperture that separates the decelerator from the source region of the mass spectrometer. In the case of the slow ion, the dication beam must propagate across the source until it overlaps $L(t)$ at which point $l(t)$ starts to increase from zero until it reaches its maximum value. The results of this is that observable slow ions, while being formed in regions of lower neutral number density compared to the fast ions, are being formed for a larger proportion of the 10 μs window. Figure 4.9 shows the number of neutral molecules in a volume of length $l(t)$ and unit area as a function of time (how the neutral number density is estimated is dealt with in Section 4.6.1). Integrating such a curve gives a quantity that is proportional to the intensity of a product ion (the constant of proportionality being σ_j). Hence, Figure 4.9 shows that in this example (where both products have the same reaction cross-section) the difference in neutral number density wins out and the fast product ion will appear more intense than the slow product ion.

The types of diagram described here will be employed in Chapters 5 and 6. It is important to remember that the vertical distance between the two lines in Figure 4.8 shows the region where observable ions are being formed and that the area under the curve in Figure 4.9 is an indication of the predicted intensity of the subject ion.

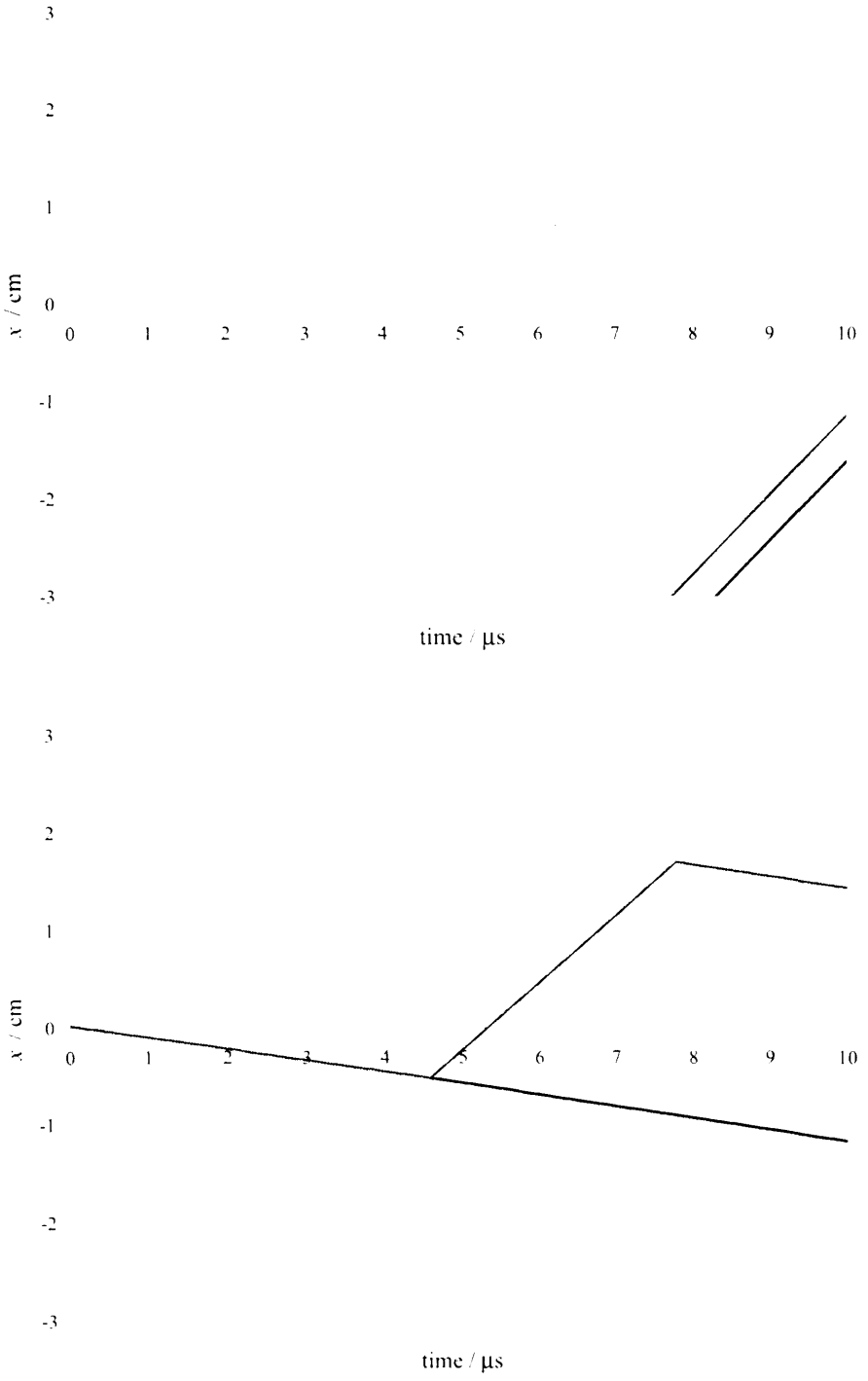

Figure 4.8 The limiting values of l_j (x_{j1} and x_{j2}) plotted as a function of time. In this example, the collision is between Ar^{2+} + Ar at a lab frame collision energy of 10 eV, with a reaction exothermicity of 4 eV, forming a pair of Ar^+ ions. The fast ion (top diagram) is scattered at 0°, the slow ion (bottom diagram) is scattered at 180°.

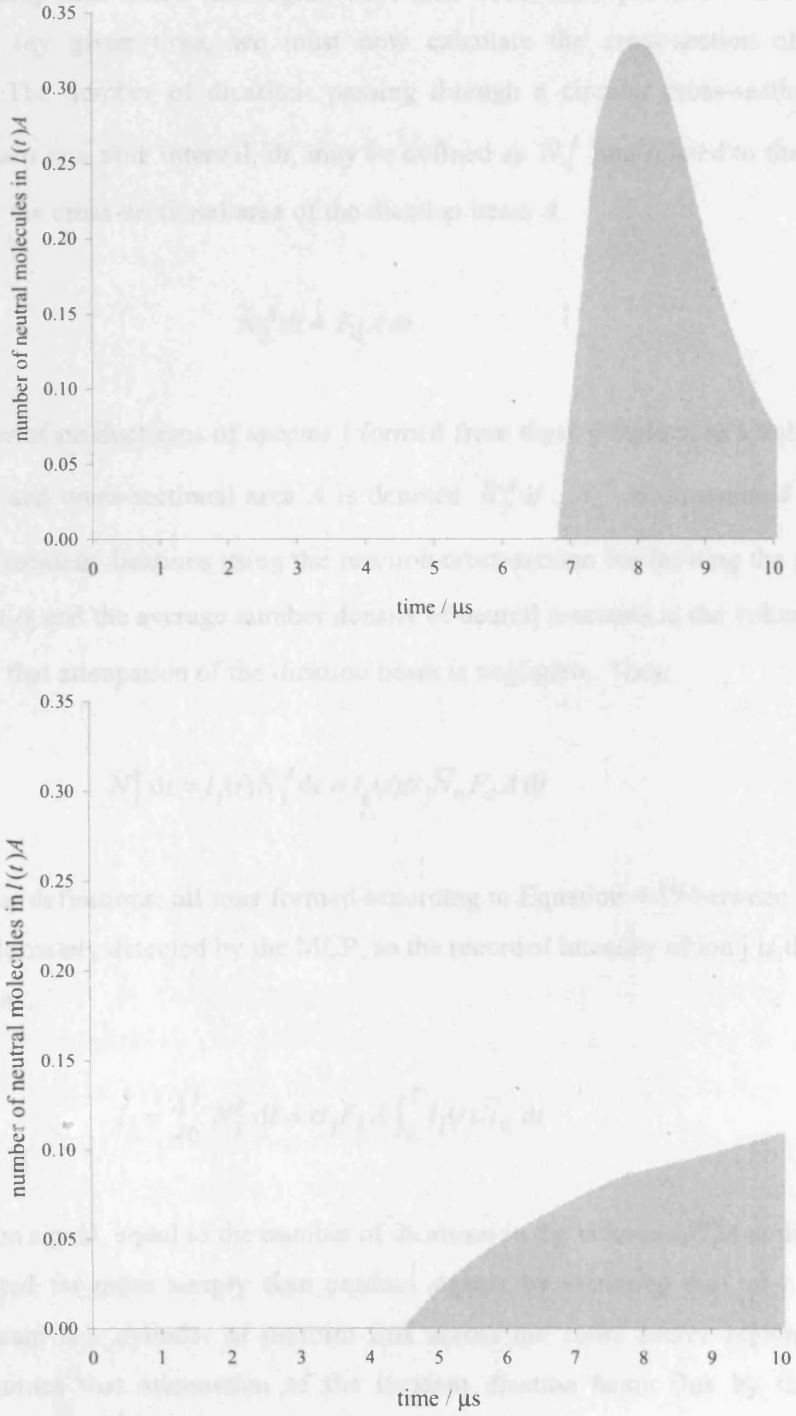

Figure 4.9 The number of neutral gas molecules in the volume $l(t)A$ for the fast and slow ions of Figure 4.8. The lines are not completely smooth because the calculations have been performed at discrete time intervals.

Having established the region in which observable product ions are being formed at any given time, we must now calculate the cross-section of product formation. The number of dications passing through a circular cross-section of the dication beam in a time interval, dt, may be defined as $\dot{N}_{\mathrm{d}}^{A}$ and related to the dication flux F_{d} and the cross-sectional area of the dication beam A.

$$\dot{N}_{\mathrm{d}}^{A} dt = F_{\mathrm{d}} A \, \mathrm{d}t \tag{4.18}$$

The number of product ions of species j formed from these dications in a volume V of length $l_{\mathrm{j}}(t)$ and cross-sectional area A is denoted $\dot{N}_{\mathrm{j}}^{A}\mathrm{d}t$. $\dot{N}_{\mathrm{j}}^{A}$ is determined from the number of incident dications using the reaction cross-section for forming the particular product ion σ_{j} and the average number density of neutral reactants in the volume $\overline{N}_{\mathrm{n}}$. It is assumed that attenuation of the dication beam is negligible. Thus:

$$\dot{N}_{\mathrm{j}}^{V} \mathrm{d}t = l_{\mathrm{j}}(t)\dot{N}_{\mathrm{j}}^{A}\mathrm{d}t = l_{\mathrm{j}}(t)\sigma_{\mathrm{j}}\overline{N}_{\mathrm{n}}F_{\mathrm{d}}A \, \mathrm{d}t \tag{4.19}$$

Now, by our definitions, all ions formed according to Equation 4.19 between $t = 0$ and $t = T$ are ultimately detected by the MCP, so the recorded intensity of ion j is the sum of all these ions:

$$I_{\mathrm{j}} = \int_0^T \dot{N}_{\mathrm{j}}^{V} \mathrm{d}t = \sigma_{\mathrm{j}} F_{\mathrm{d}} A \int_0^T l_{\mathrm{j}}(t)\overline{N}_{\mathrm{n}} \, \mathrm{d}t \tag{4.20}$$

The dication signal, equal to the number of dications in the volume $l_{\mathrm{d}}(T)A$ at time T, can be calculated far more simply than product signals by assuming that, at $t = T$, the dication beam is a cylinder of uniform flux across the entire source region. This of course assumes that attenuation of the incident dication beam flux by the neutral collision gas is insignificant, but this can be seen to be justified by comparing the total product signal to that of the dication reactant, which indicates attenuation of $< 1\%$. The number of dications per unit volume N_{d} is thus:

$$N_d = \frac{F_d}{v_d} \tag{4.21}$$

Therefore, the number of dications in the volume $l_d(T)A$, equivalent to the dication intensity I_d is:

$$I_d = \frac{F_d l_d(T) A}{v_d} \tag{4.22}$$

Hence the observed product ratio for ion j is:

$$R^{true} = \frac{I_j}{I_d} = \frac{\sigma_j F_d A v_d}{F_d L_d A} \int_0^T \bar{N}_n l_j(t)\,dt \tag{4.23}$$

which, by re-arrangement, gives the partial reaction cross-section, σ_j:

$$\sigma_j = \frac{R_j^{true} l_d(T)}{v_d \int_0^T \bar{N}_n l_j(t)\,dt} \tag{4.24}$$

Equation 4.24 does not include angular scattering, assuming that all velocities are either parallel or anti-parallel to the dication beam direction (x-axis). This is a reasonable approximation in the case of SET, but the time-dependent model can be further refined to incorporate the angular distribution of j; such distributions for SET products have been characterized using angularly resolved scattering.[14] Since allowing an off-axis component of velocity reduces the on-axis component of velocity (which dictates an ion's trajectory) we find that l_j becomes a function of θ as well as t. If the angular distribution of j is described by some function, $f(\theta)$ then Equation 4.24 becomes:

$$\sigma_j = \frac{R_j^{true} l_d(T)}{v_d \int_0^{180} f(\theta) \int_0^T \bar{N}_n l_j(t,\theta)\,dt\,d\theta} \tag{4.25}$$

Note that although θ is the scattering angle in the COM frame, $I(t,\theta)$ is a LAB frame property. For a discussion of the form of $f(\theta)$ see Section 4.6.2.

In principle, this analysis allows calculations of absolute cross-sections, but the task of accurately determining the number density distribution of the neutral gas across the source region in absolute terms makes this impractical. Indeed, even estimating the functional form of the number density distribution is difficult, given the presence of multiple diffusion pumps and many irregular surfaces. Uncertainty in the neutral number density is the biggest problem in reconciling the analysis of fast and slow ions.

4.6.1. Neutral number density distributions

The ion source and mass spectrometer form a contiguous space, which is pumped at three different places. Moreover, the source region of the spectrometer is a cluttered space of irregular shape and many surfaces. In light of this situation it is unrealistic to attempt to make anything more than an approximation of the number density distribution of the neutral collision gas. However, the simplest way to make an estimate is to treat the gas inlet as an unconfined effusive source.

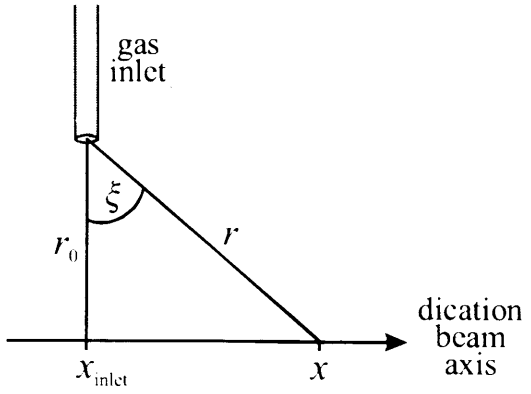

Figure 4.10 Geometrical definition of the variables used in estimating the neutral reactant number density N_n.

The angular dependence of such a source is known to be a cosine distribution, while the radial dependence follows the inverse-square law.[116] Hence, we can model the neutral number density using the functional form:

$$N_n = \frac{1}{r^2}\cos\xi \tag{4.26}$$

The line described by the dication beam varies in both r and ξ, with the point of closest approach occurring when $r = r_0$ and $\xi = 0$. Simple geometrical arguments give the relationships of r and ξ to the more useful quantities, x and r_0:

$$r^2 = r_0^2 + x^2 \tag{4.27}$$

$$\tan\xi = \frac{x}{r_0} \tag{4.28}$$

so by making the appropriate substitutions we find:

$$N_n = \frac{1}{r_0^2 + x^2}\cos\left[\arctan\left(\frac{x}{r_0}\right)\right] \tag{4.29}$$

Equation 4.30 assumes that $x = 0$ occurs at the closest point of approach between the dication beam and the gas inlet, however it is generally more convenient to set $x = 0$ as the centre of the source region of the mass spectrometer. This simply means that values of x must be offset by the x-position of the gas inlet so that the distribution N_n is centred at the gas inlet.

$$N_n = \frac{1}{r_0^2 + (x - x_{inlet})^2}\cos\left[\arctan\left(\frac{x - x_{inlet}}{r_0}\right)\right] \tag{4.30}$$

Equation 4.30 is only a functional form and is not intended to be a measure of the absolute number density of neutral reactant molecules, but allows positions with different neutral number densities in the source region to be relatively compared.

N_n is in arbitrary units, but will be proportional to the absolute number density; moreover the arbitrary units will depend on the square root of molecular mass, as dictated by Graham's law of effusion:

$$\frac{\text{effusive rate of } m_1}{\text{effusive rate of } m_2} = \sqrt{\frac{m_2}{m_1}} \tag{4.31}$$

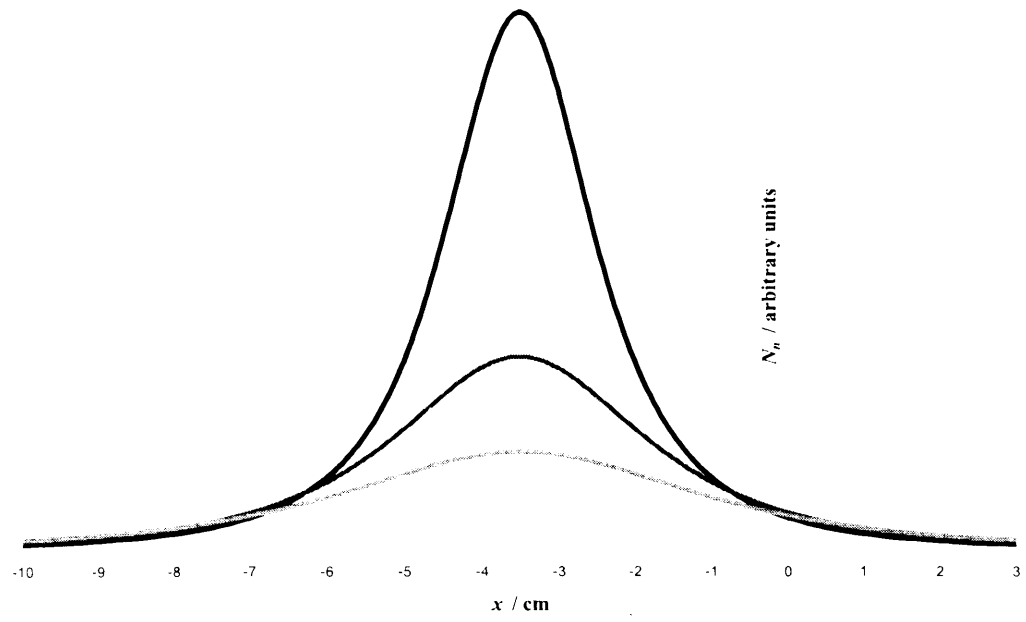

Figure 4.11 This modelled distribution of the neutral number density along the x-axis. The distribution is very sensitive to the distance of closest approach between the dication beam and the gas inlet (r_0) but only close to the gas inlet. The diagram includes three different values of r_0: 1.5 cm (black line), 2.5 cm (dark grey line) and 3.5 cm (light grey line).

This model is used to estimate the relative neutral number density at different positions in the source region, which cannot be accurately experimentally measured. The values of r_0 and x_{inlet} have been adjusted to produce a reasonable agreement with experimental data gathered on the Ar^{2+} + Ne collision system by Harper *et al.*[14] This system, being diatomic, has only two products of SET, making it a good system for calibrating the model. Therefore, the parameters r_0 and x_{inlet}, which are not known exactly can be fine-tuned so that the calculated cross-sections of Ar^+ and Ne^+ are approximately equal across a range of collision energies.

The simplifications made in calculating the neutral number density distribution will inevitably result in a degree of error, and it is likely that inaccuracy in values of the neutral number density is a major contributing factor towards overall errors in the extraction of cross-sections.

4.6.2. Angular distributions

The angular distributions used in the analysis are simply fits of those typically observed using the position sensitive apparatus also operating in this department.[114] The angular distributions observed in electron transfer are, in most cases, very similar. A sharp peak is observed at small scattering angles, but the distribution is very broad with some counts at all scattering angles.

Empirically, a Lorentzian function provides a good match for typical angular distribution. This has the functional form:

$$f(\theta) = \frac{1}{a\pi\left[1+\left(\frac{\theta-\theta_0}{a}\right)^2\right]} \qquad (4.32)$$

In Equation 4.32, the constant a determines the amplitude of the distribution and θ_0 is the centre of the distribution. The effect of a on the width of the distribution is shown in Figure 4.12.

The primary consequence of allowing off-axis scattering in the model is that it gives a spread in x-velocities of collision products. The small difference that non-zero z-velocities will have on times-of-flight is ignored, being a matter of a few nanoseconds. Scattering is also assumed to be entirely co-planar with the dication beam axis (x) and the time-of-flight axis (z), and as such is defined by a single angle θ.

Although the shape of the angular scattering function can be estimated quite well for SET products, since most systems show similar scattering behaviour for such reactions, it is much more uncertain for products formed via a collision complex. Perhaps the best way to estimate $f(\theta)$ in these cases is to assume that the collision complex is sufficiently long-lived for the angular distribution to be fully symmetric.

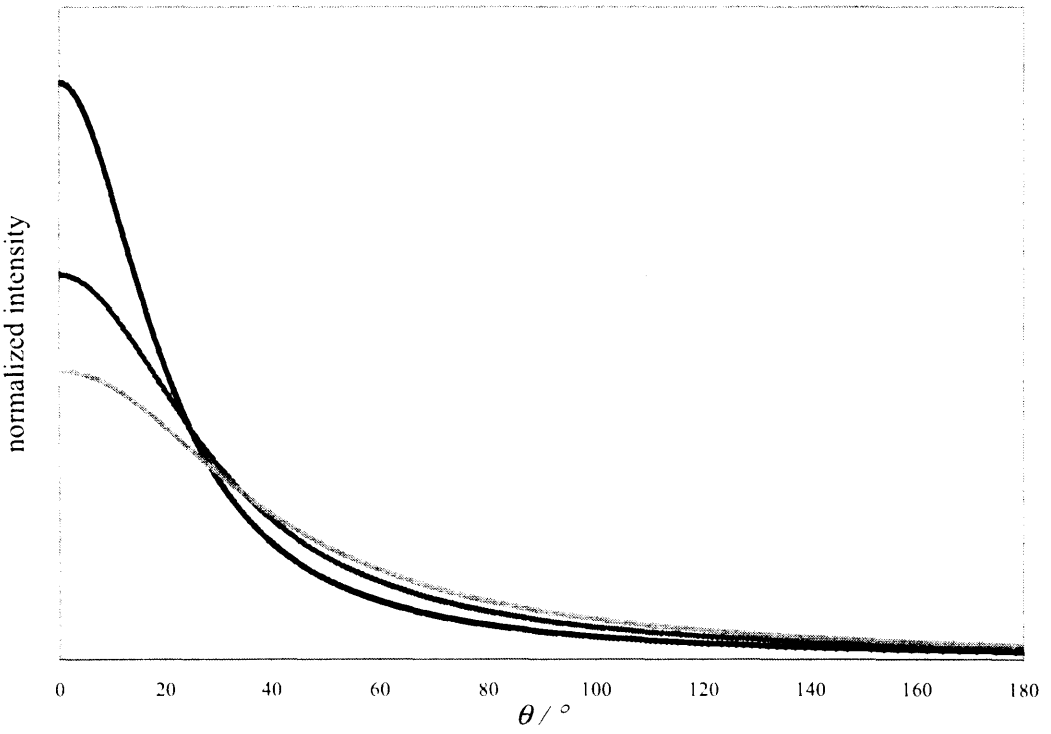

Figure 4.12 The effect of a on a Lorentzian profile: $a = 20$ (black line), $a = 30$ (dark grey line), $a = 40$ (light grey line).

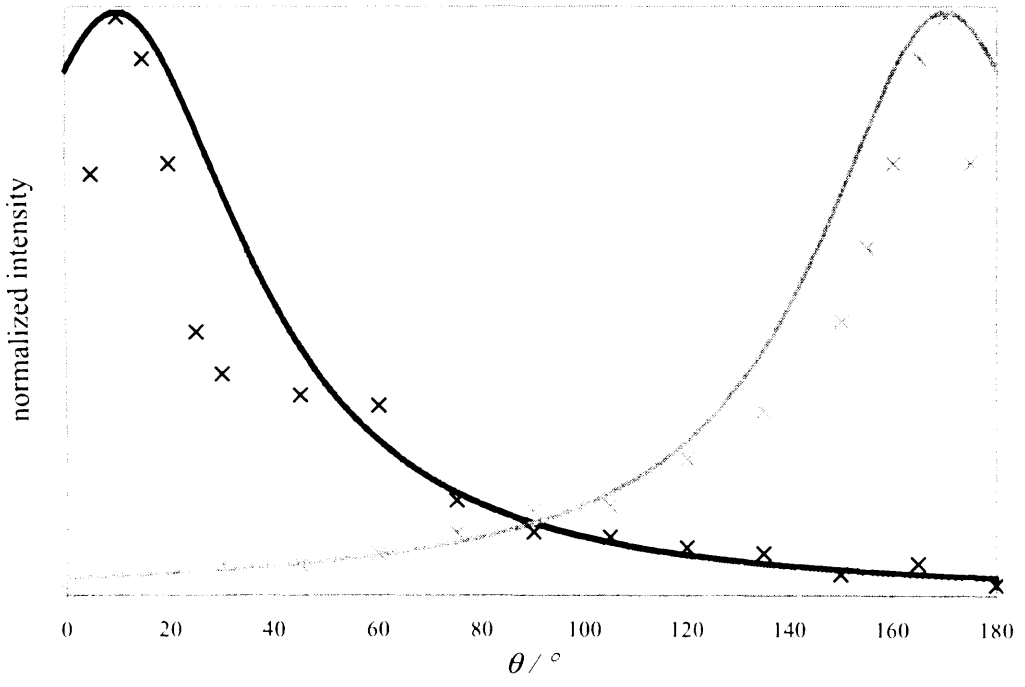

Figure 4.13 Comparison of the angular distribution for a pair of SET products using experimental data[114] (points) and Lorentzian profiles (lines).

4.7. Conclusions

The newly developed method of analysis incorporates time-, number- and angular dependences to create a far more detailed model of the experiment than has been previously employed. While inevitable simplifications, particularly in estimating the neutral number density, may introduce sizeable errors when putting the model into practice, the model is mathematically tractable and is capable of succeeding in its aim of allowing the calculation of reaction cross-sections, in arbitrary units, for all product ions associated with a collision system. Another important feature is that these units, while not known absolutely should stay approximately the same between collision systems, allowing inter-comparison of the cross-sections measured for different systems using this apparatus. This can be seen by inspection of Equation 4.25, from which we can see that the only variable for which we do not have absolute units is $\overline{N}_n$, and the relative value of this will change between collision systems only due to differences in the effusive properties of the neutral reactant. Consequently, when using neutral reactants of similar mass, inter-comparison of results is valid.

As a result of the work outlined in this chapter, we now have a far greater understanding of the dynamics of the reaction region of the spectrometer and are able to fully model observed reactions. The following two chapters demonstrate the application of this new model to experimental data, where it is seen to dramatically outperform the pre-existing methodology for extracting cross-sections, particularly when applied to slow ions.

4.8. References

[1] N. Lambert, D. Kearney, N. Kaltsoyannis and S.D. Price, *J. Am. Chem. Soc.* **126:** 3658 (2004)

[2] D. Kearney (2005) PhD thesis, UCL

[3] N. Tafadar and S.D. Price, *Int. J. Mass Spectrom.* **223-224:** 547 (2003)

[4] N. Tafadar, D. Kearney and S.D. Price, *J. Chem. Phys.* **115:** 8819 (2001)

[5] N. Tafadar, N. Kaltsoyannis and S.D. Price, *Int. J. Mass Spectrom.* **192:** 205 (1999)

[6] S.D. Price, *J. Chem. Soc., Faraday Trans.* **93:** 2451 (1997)

[7] K.A. Newson and S.D. Price, *Chem. Phys. Lett.* **269:** 93 (1997)

[8] K.A. Newson and S.D. Price, *Chem. Phys. Lett.* **294:** 223 (1998)

[9] K.A. Newson, N. Tafadar and S.D. Price, *J. Chem. Soc.-Faraday Trans.* **94:** 2735 (1998)

[10] N. Lambert, N. Kaltsoyannis, S.D. Price, J. Zabka and Z. Herman, *J. Phys. Chem. A* **110:** 2898 (2005)

[11] N. Lambert, N. Kaltsoyannis and S.D. Price, *J. Chem. Phys.* **119:** 1421 (2003)

[12] D. Kearney and S.D. Price, *Phys. Chem. Chem. Phys.* **5:** 1575 (2003)

[13] Z. Dolejsek, M. Farnik and Z. Herman, *Chem. Phys. Lett.* **235:** 99 (1995)

[14] S.M. Harper, W.-P. Hu and S.D. Price, *J. Phys. B.* **35:** 4409 (2002)

[15] Z. Herman, J. Zabka, Z. Dolejsek and M. Farnik, *Int. J. Mass Spectrom.* **192:** 191 (1999)

[16] R.D. Levine and R.B. Bernstein Molecular Reaction Dynamics & Chemical Reactivity (1987). Oxford University Press

Chapter 5: The SF^{2+} + Ar Collision System

5.1. Introduction

The SF^{2+} dication is one of a number of doubly charged fragments that result from electron ionization of SF_6. Numerous studies have been conducted on this precursor molecule, including several that have determined partial ionization cross-sections for electron ionization[1-6]. Nagesha et. al. have calculated theoretical potential energy curves for low-lying states of SF^{2+}[7] and more recently, in this department, Lambert has calculated potential energy curves for a number of electronic states of SF_2^{2+} and SF^{2+}[8]. However, no records exist in the literature of crossed-beam experiments involving doubly charged fragments of SF_6, although unpublished experiments using our apparatus have been conducted with SF_4^{2+}, SF_2^{2+} and SF^{2+}, mostly by this author. The reactivity of SF_n^{2+} appears to bear certain similarities to that of CF_n^{2+}, which has been extensively studied. Indeed, if anything, the flexible valency of S results in a richer chemistry. Earlier unpublished work by this author has shown that both SF^{2+} and SF_2^{2+} form metastable complexes with hydrogenated neutral molecules such as water and ammonia.

Singly charged ions	Partial ionization cross-section	Doubly charged ions	Partial ionization cross-section
SF_5^+	1000		
SF_4^+	93	SF_4^{2+}	68
SF_3^+	313	SF_3^{2+}	8
SF_2^+	92	SF_2^{2+}	50
SF^+	167	SF^{2+}	9
S^+	131		
F^+	240		

Table 5.1 Relative partial ionization cross-sections for products of electron impact ionization of SF_6, at an electron energy of 150 eV[6]. Values are relative to the dominant ion, SF_5^+, which is assigned an arbitrary cross-section of 1000. Note that due to an unfavourable Frank-Condon factor, the parent molecular ion, SF_6^+, is not observed.

5.2. Results

Mass spectra were recorded, as described above, at collision energies from 6.0 eV to 14.0 eV in the LAB frame corresponding to 2.6 eV to 6.2 eV in the centre-of-mass frame. Comparison of the reaction and background mass spectra (Figure 5.1) clearly indicates the formation of S^+, SF^+, Ar^+ and ArS^{2+} ions. However, F^+ is not detected from bimolecular collisions. The absence of F^+ signals following bimolecular reactions has also been reported following collisions of other fluorinated dications. Additionally, no Ar^{2+} signal is observed, an ion which would be produced by double electron transfer processes. Given the absence of any product F^+ ion signals it is clear that only two electron transfer reactions are occurring in the SF^{2+} + Ar collisions, along with a bond-forming reaction generating ArS^{2+}:

$$SF^{2+} + Ar \rightarrow SF^+ + Ar^+ \quad (5.1)$$

$$SF^{2+} + Ar \rightarrow S^+ + F + Ar^+ \quad (5.2)$$

$$SF^{2+} + Ar \rightarrow ArS^{2+} + F \quad (5.3)$$

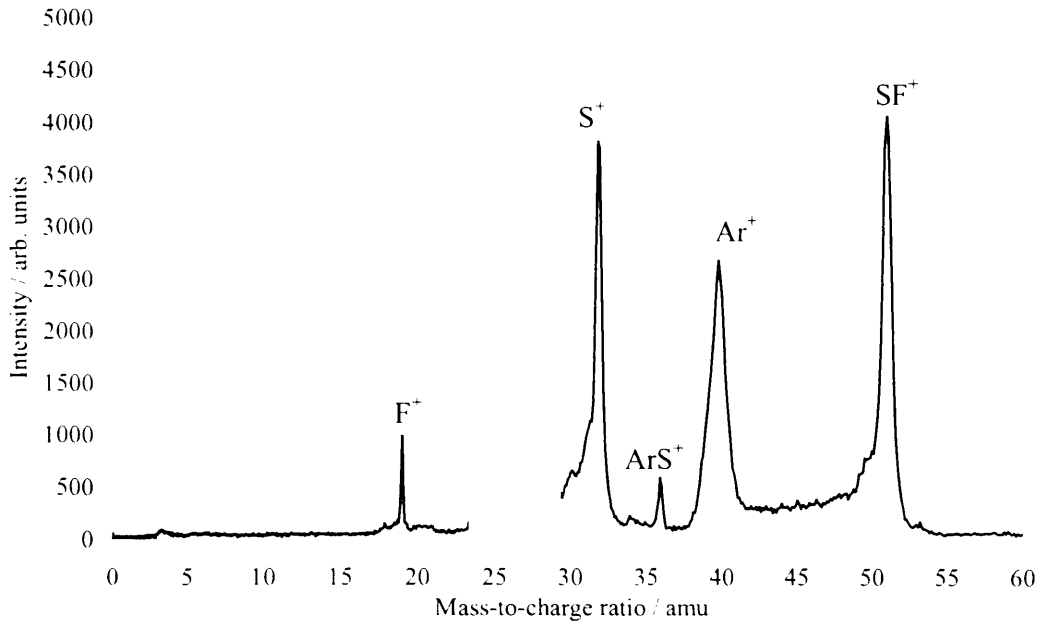

Figure 5.1 Representative reaction (thick line) and background (thin line) mass spectra for SF^{2+} + Ar. The large dication beam signal has been removed. The F^+ signal is due entirely to contamination in the dication beam.

For the products of the SET reactions, the relevant ion intensities (Table 5.2) in the mass spectra were processed, as described in the previous chapter, to yield values of σ'_j for these product ions as a function of collision energy. The angular distribution of SET products was modelled using a Lorentzian function (see Section 4.6.2), while the angular distribution of ArS^{2+} was assumed to be symmetric. The product ion velocities were calculated using the method described in Section 2.6. Note that for the formation of the S^+ ion it has been assumed, as has been determined experimentally for similar collision systems, that the energy release (ΔT) upon dissociation of the excited electronic states of SF^+ to form S^+ is negligible in comparison to the energy release involved in charge separation. We know that efficient electron transfer occurs with an exothermicity in the region of 4 eV, while the bond energy of most excited states of SF^+ is < 1 eV[18]. Thus, the velocity of the S^+ ion across the source region is assumed to be approximately the same as the velocity of the parent SF^+ ion. The extraction of the cross-section for the formation of the ArS^{2+} ion is discussed in more detail later in the chapter.

E_{lab} / eV	E_{com} / eV	average R^{true}			
		SF^+	S^+	Ar^+	ArS^{2+}
6	2.6	1.26×10^{-3}	5.52×10^{-4}	5.38×10^{-4}	6.31×10^{-6}
7	3.1	1.35×10^{-3}	8.36×10^{-4}	5.77×10^{-4}	1.51×10^{-5}
8	3.5	1.15×10^{-3}	7.70×10^{-4}	7.91×10^{-4}	3.64×10^{-5}
9	4.0	8.00×10^{-4}	5.67×10^{-4}	5.28×10^{-4}	2.51×10^{-5}
10	4.4	7.92×10^{-4}	5.73×10^{-4}	5.61×10^{-4}	3.40×10^{-5}
11	4.8	7.92×10^{-4}	5.71×10^{-4}	5.93×10^{-4}	3.20×10^{-5}
12	5.3	8.21×10^{-4}	6.22×10^{-4}	6.86×10^{-4}	3.64×10^{-5}
13	5.7	8.76×10^{-4}	6.51×10^{-4}	7.97×10^{-4}	3.44×10^{-5}
14	6.2	8.15×10^{-4}	7.52×10^{-4}	8.76×10^{-4}	4.51×10^{-5}

Table 5.2 Corrected product ratios for all products observed in the SF^{2+} + Ar collision system at each collision energy. Note that for all data collected on this system $k \approx 1$ so $R^{true} \approx R^{obs}$.

5.3. Electron Transfer

Figure 5.2 and Figure 5.3 plot calculated values of I and N^I/A as functions of time for the non-dissociative SET products SF^+ and Ar^+ (this type of plot was introduced in Chapter 4). The equivalent plot for S^+ would be very similar to that of SF^+, since the velocity of S^+ across the source, v_x, is assumed to be the same as that for SF^+, although upon application of the repeller plate pulse S^+ and SF^+ would follow slightly different trajectories due to the difference in their kinetic energies.

Before attempting to interpret these plots, we must remember three important points:

i) $I_j(t)$ is the vertical distance between x_{j1} and x_{j2} at time t;

ii) the shaded area is directly proportional to intensity;

iii) each plot is calculated at a single scattering angle, hence all SF^+ ions are deemed to be scattered at 0° (so they are 'fast') and all Ar^+ ions are deemed to be scattered at 180° (so they are 'slow').

The plots in Figure 5.2 predict that the SF^+ signal will weaken significantly as collision energy increases, firstly because the imaged length, $L_{SF^+}(T)$, decreases as the LAB frame x-velocity of SF^+ increases and secondly because $l_{SF^+}(t)$ is shifted upstream as the LAB frame velocity of SF^+ increases and consequently only enters the source region of the spectrometer later in the time period for which the repeller plate voltage is switched off. Experimentally, the intensity of SF^+ is indeed seen to drop as collision energy is increased (Table 5.2), but the effect is moderated by off-axis scattering of SF^+ (i.e. in reality not all SF^+ ions are scattered at 0°).

The plots in Figure 5.3 predict that the Ar^+ signal will intensify slightly as collision energy is increased, because the dication beam takes longer to reach $L_{Ar^+}(t)$ and $l_{Ar^+}(t)$ only becomes non-zero when there is some overlap between $L_{Ar^+}(t)$ and the dication beam. The LAB frame x-velocity of Ar^+ is negative (i.e. directed upstream, as shown by the negative gradients in Figure 5.3) so its *speed decreases* as the collision energy *increases*, which, on its own, would delay the time it takes for the propagating dication beam to begin to overlap $L_{Ar^+}(t)$. This effect, however, is outweighed by the increase in the velocity of the dication beam with collision energy, and consequently $l_{Ar^+}(t)$ becomes non-zero earlier at higher collision energies.

Figure 5.2 (overleaf) Plot of x_1 and x_2 (solid lines, left-hand scale) and N'/A (shaded area, right-hand scale) for SF^+ at LAB frame collision energies of 6 eV (top), 10 eV (middle) and 14 eV (bottom) at a scattering angle of 0°.

Figure 5.3 (page 130) Plot of x_1 and x_2 (solid lines, left-hand scale) and N'/A (shaded area, right-hand scale) for Ar^+ at LAB frame collision energies of 6 eV (top), 10 eV (middle) and 14 eV (bottom) at a scattering angle of 180°.

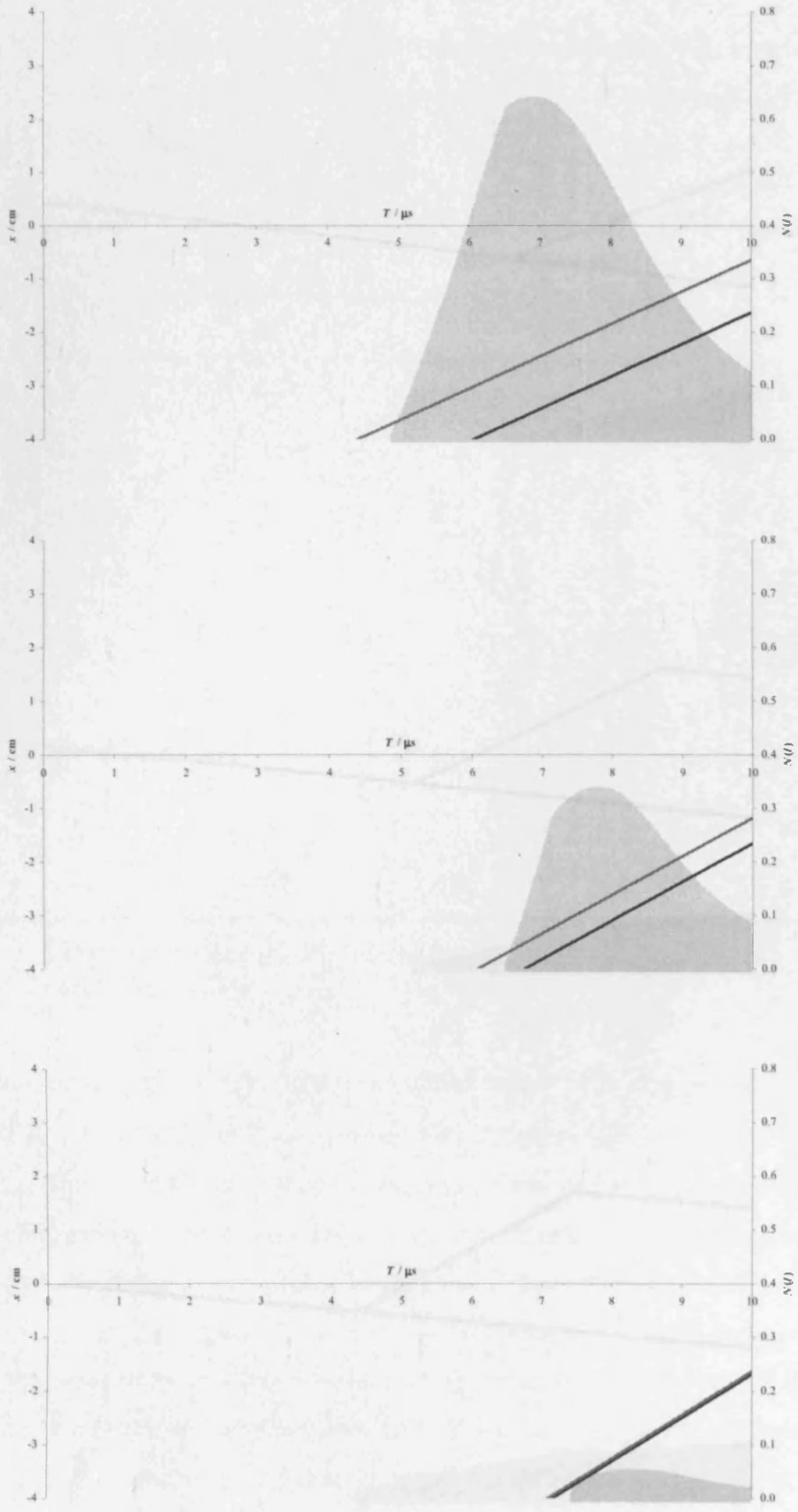
x / cm
T / μs
N(t)

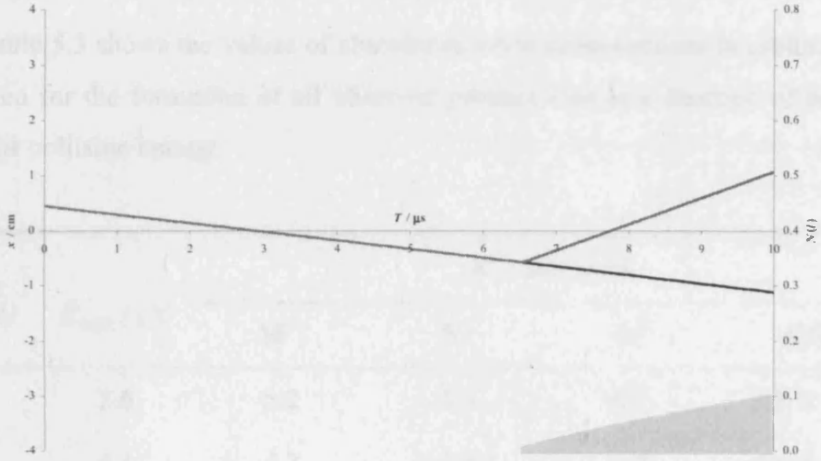
x / cm
T / μs
N(t)

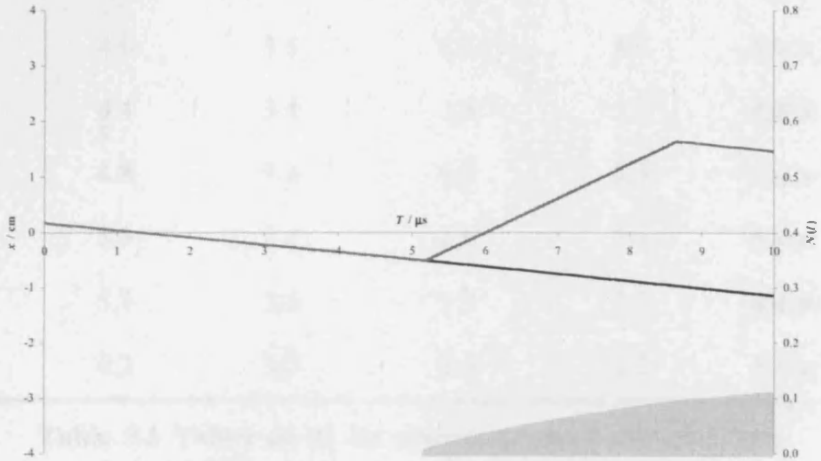
x / cm
T / μs
N(t)

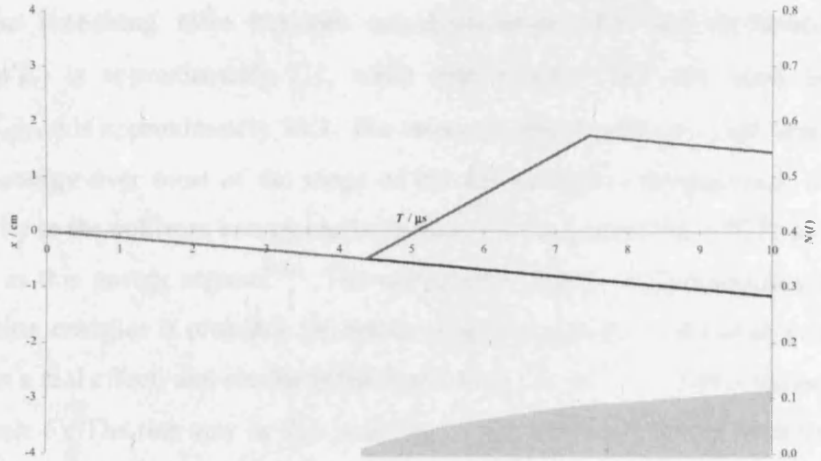
x / cm
T / μs
N(t)

5.3.1. Experimental reaction cross-sections

Table 5.3 shows the values of absolute reaction cross-sections in arbitrary units, σ'_J obtained for the formation of all observed product ions as a function of centre-of-mass frame collision energy.

E_{lab} / eV	E_{com} / eV	σ'_J / arb. units			
		SF^+	S^+	Ar^+	ArS^{2+}
6	2.6	5.2	1.8	6.7	2.7×10^{-2}
7	3.1	4.2	2.2	6.0	3.5×10^{-2}
8	3.5	4.2	2.1	5.6	4.7×10^{-2}
9	4.0	3.5	1.3	4.0	5.0×10^{-2}
10	4.4	3.4	1.6	3.7	6.0×10^{-2}
11	4.8	3.4	1.6	3.3	5.0×10^{-2}
12	5.3	3.4	1.6	3.3	5.1×10^{-2}
13	5.7	3.8	1.7	3.3	4.4×10^{-2}
14	6.2	3.7	1.9	3.2	5.3×10^{-2}

Table 5.3 Values of σ'_J for reaction products obtained from experimental data.

The branching ratio between non-dissociative SET and dissociative SET (σ'_{SF+} : σ'_{S+}) is approximately 2:1, while that between SET and bond formation (σ'_{Ar+} : σ'_{ArS++}) is approximately 90:1. The cross-sections do not vary significantly with collision energy over most of the range of our experimental investigations. A similar insensitivity to the collision energy has been observed for several other SET reactions of dications in this energy regime[9-11]. The unexpected increase in cross-sections at very low collision energies is probably the result of approximations in the analytical model rather than a real effect, and similar behaviour is seen for the Cl^{2+} + CO collision system (see Chapter 6). The rise may be due to an effect that has been omitted from the model or an effect that is modelled poorly at low collision energies. It is possible that deviations from uniformity in the source electric fields has an effect on that becomes

noticeable for low-energy ions. Additionally, the estimated energy release (and consequently the calculated velocity of product ions) may be slightly out (since ΔT will, of course, be a distribution across the Reaction Window depending on where each product state lies, not exactly 4 eV), and this would be proportionally more significant at lower collision energies. The latter possibility is supported by the fact that no such rise is seen in the intensity of ArS^{2+} (or CCl^{2+} in the following chapter) for which the energy release is much smaller.

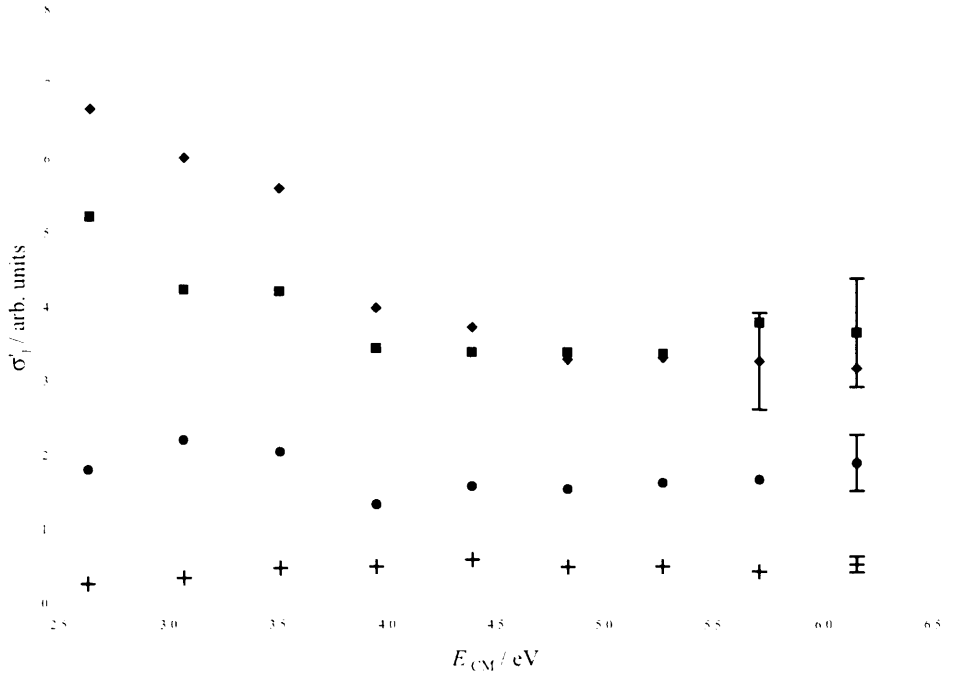

Figure 5.4 Plot of the data in Table 5.3: σ'_{Ar+} (◆), σ'_{SF+} (▪), σ'_{S+} (●), $\sigma'_{ArS++} \times 10$ (+); the representative error bars are ±25%, but it is difficult to estimate the error associated with the model.

A benefit of the simplicity of this collision system is that the accuracy of the analytical model is easy to test. From the reactions occurring in the system, it is easy to recognize that each Ar^+ ion must be formed concomitantly with either an SF^+ ion or an S^+ ion. Consequently, the reaction cross-section for forming Ar^+ should always equal the sum of those for forming SF^+ and S^+. The model performs reasonably well when judged by this criterion, although the ratio $\sigma'_{Ar+} : (\sigma'_{SF+}+\sigma'_{S+})$ falls from just under unity to 0.6 across the energy range. However, this is a dramatic improvement on attempts to

incorporate slow ions using the previous method of analysis that was detailed in Chapter 4. Figure 5.5 demonstrates the results of applying the previous method of analysis to the same experimental data. The cross-section of Ar^+ is severely underestimated, indeed the ratio $\sigma'_{Ar+} : (\sigma'_{SF+}+\sigma'_{S+})$ at no point exceeds 0.1.

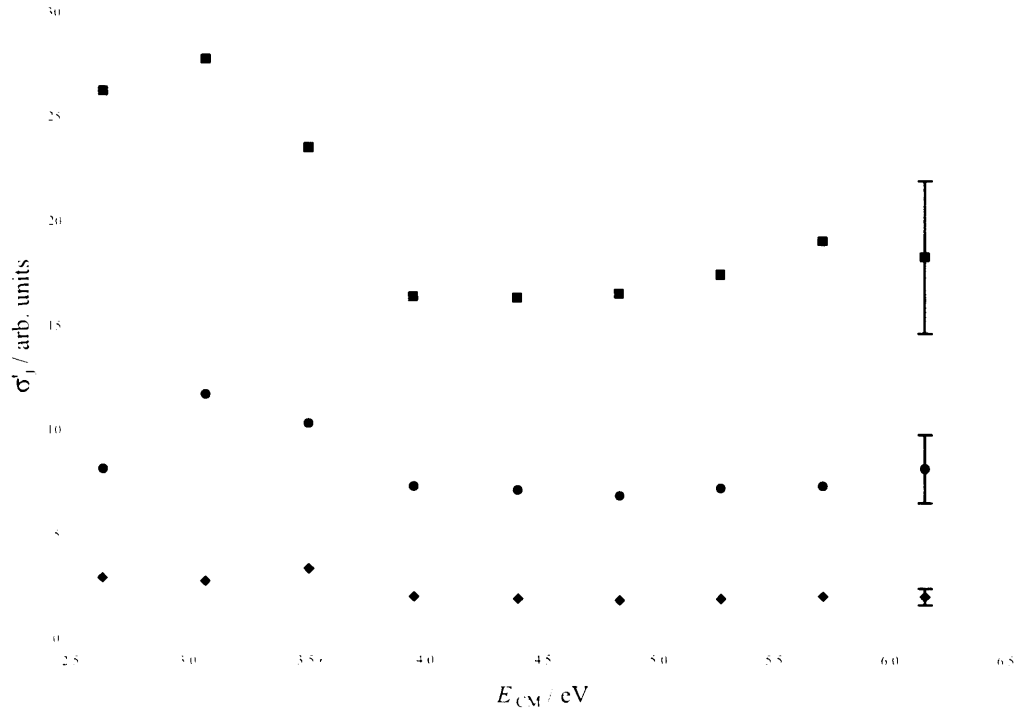

Figure 5.5 Results of applying the previous method of analysis to the same experimental data as in Figure 5.4: σ'_{Ar+} (◆), σ'_{SF+} (▪), σ'_{S+} (●). For clarity the data for ArS^{2+} is omitted, although the results obtained are, relative to SF^+, similar to the new method.

Given the number of approximations inherent in the new method of analysis, it appears to very satisfactorily reconcile the differences between fast and slow ions in this collision system. These results represent the first time that reaction cross-sections for all products of a collision system have been extracted from experimental data using this apparatus.

5.3.2. Reaction Window calculations

To perform the Reaction Window calculations, outlined in Chapter 2, to attempt to account for the relative intensities of SF^+ and S^+ that are observed, requires knowledge of the relative energies of the relevant electronic states of SF^{2+} and SF^+. Little experimental information is available on the relative energetics of the monocationic and dicationic states of SF^+, therefore these energies have been determined theoretically using a quantum chemical approach. The detailed results of these quantum chemical investigations into the potential energy curves of SF^{2+} and SF^+ have been reported in detail elsewhere[8], and were not conducted by the author. Briefly, the computational approach involved generating potential energy curves for electronic states of SF^+ and SF^{2+} by performing single-point energy calculations at 0.05 Å intervals using the state-averaged AQCC method with a full valence active space, coupled with an uncontracted basis set as implemented in Molpro v.2002.3[12] consisting of 16s11p3d2f1g functions for S atoms and 12s6p3d2f1g functions for F atoms.

The results from the computational work show that the ground dication state of SF^{2+} ($X\ ^2\Pi$) is metastable, as it possesses a significant barrier (~ 4.5 eV) to charge separation. The first SF^{2+} excited state ($A\ ^2\Pi$) is also metastable, possessing a barrier of ~ 2.5 eV to charge separation, and lies 4.0 eV above the ground state. A further six metastable dication states lie within 6.0 eV of the ground state, but these are all much more weakly bound (< 1 eV). Thus the dication beam may be expected to be predominantly composed of SF^{2+} ions in either the ground or first excited electronic state. With regard to the monocations, the first three electronic states of SF^+ ($X\ ^3\Sigma^-$, $a\ ^1\Delta$, $b\ ^1\Sigma^+$) are all predicted to be bound; the first dissociative state ($A\ ^3\Pi$) lies 5.7 eV above the ground state of SF^+ and the higher electronic states of SF^+ are also calculated to be dissociative. The adiabatic ionization energy of SF^+ is calculated to be 21.3 eV[13] and the first ionization energy of SF is experimentally established as 10.1 eV, a value in good agreement with our calculations. The ionization energy for populating the $3p^{-1}$ (^2P) electronic state of Ar^+ is well known[13], and hence the exothermicities for populating the accessible $SF^+ + Ar^+$ product asymptotes may be evaluated; these are listed in Table 5.4.

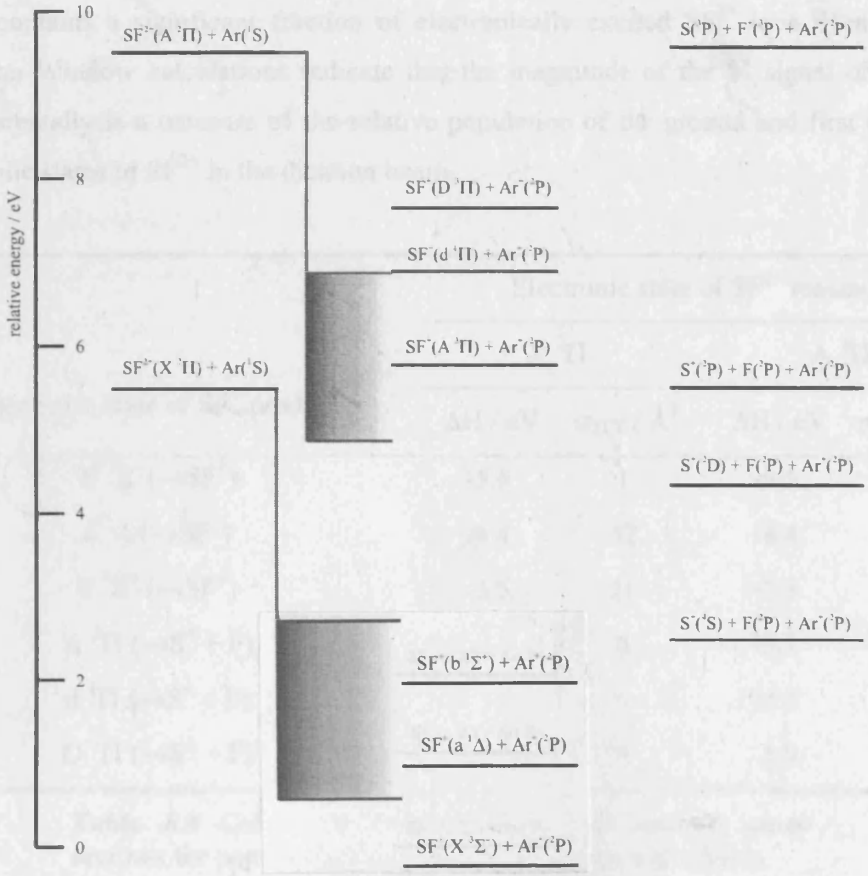

Figure 5.6 Composite energy level diagram for SET asymptotes. Shaded areas indicate the approximate position of the Reaction Window. SET from the ground state of SF^+ only populates product states lying below the first dissociative asymptote, indicating that all S^+ that is observed originates from electronically excited dications.

Note that SET reactions involving the population of higher electronic states of Ar^+, for example the $3s^{-1}(^2S_{1/2})$ state, are endothermic and thus are not expected to occur, as has been confirmed experimentally for other collision systems[14,15].

Table 5.4 shows calculated SET cross-sections for populating the various electronic states of SF^+, formed together with $Ar^+(^2P)$, from the two electronic metastable states of SF^{2+}. It can be seen from Table 5.4 that the probability of the SET reaction populating dissociative electronic states of SF^+ is negligible unless the SF^{2+} is electronically excited. This implies that the S^+ signal observed in the mass spectra must result from the population of the dissociative higher lying states of SF^+ by the SET reactions of the first excited state of SF^{2+}, supporting the expectation that the dication

beam contains a significant fraction of electronically excited SF^{2+} ions. Hence, the Reaction Window calculations indicate that the magnitude of the S^+ signal observed experimentally is a measure of the relative population of the ground and first excited electronic states of SF^{2+} in the dication beam.

Electronic state of SF^+ product	Electronic state of SF^{2+} reactant			
	$X\ ^2\Pi$		$A\ ^2\Pi$	
	ΔH / eV	σ_{SET} / Å^2	ΔH / eV	σ_{SET} / Å^2
$X\ ^3\Sigma^-$ ($\rightarrow SF^+$)	-5.5	1	-9.5	0
$a\ ^1\Delta$ ($\rightarrow SF^+$)	-4.4	12	-8.4	0
$b\ ^1\Sigma^+$ ($\rightarrow SF^+$)	-3.5	21	-7.5	0
$A\ ^3\Pi$ ($\rightarrow S^+ + F$)	+0.3	0	-3.7	23
$d\ ^1\Pi$ ($\rightarrow S^+ + F$)	+1.4	0	-2.7	3
$D\ ^3\Pi$ ($\rightarrow S^+ + F$)	+2.2	0	-1.9	0

Table 5.4 Calculated exothermicities and reaction cross-sections for populating accessible SET product asymptotes.

Given the cross-sections listed in Table 5.3, and the observed ratio of S^+ to SF^+, it is clear that there must be a significant population of the $SF^{2+}(A)$ state in the dication beam; approximately half as many dications in the first excited electronic state as dications in the ground electronic state.

5.4. Bond-formation

As discussed above, the peak observed in the in the mass spectrum at m/z = 36 (Figure 5.1) is assigned to ArS^{2+}, clearly indicating the occurrence of Reaction (5.3). Table 5.3 shows the reaction cross-section, again in arbitrary units, for the formation of ArS^{2+} as a function of collision energy. The formation of ArS^{2+} is thought to proceed via the formation of an $ArSF^{2+}$ collision complex. Hence, the extraction of the cross-sections for ArS^{2+} assumes that the kinetic energy release accompanying the dissociation of the collision complex is negligible, since it is not accompanied by charge separation, and hence the LAB frame velocity of ArS^{2+} is assumed to be equal to the

velocity of the centre-of-mass of the collision system. It is also assumed that the complex lives for considerably longer than its rotational period so that the angular distributions of ArS^{2+} and F are symmetric.

It appears from Table 5.3 that the cross-section for this bond forming reaction rises from a threshold somewhere below a centre-of-mass collision energy of 2.5 eV. A more accurate determination of this threshold is not possible in our experiments due to the weakness of the ArS^{2+} signal and the low flux of SF^{2+} in these experiments. Note that in Figure 5.4 the cross-section for forming ArS^{2+} is multiplied by a factor of 10.

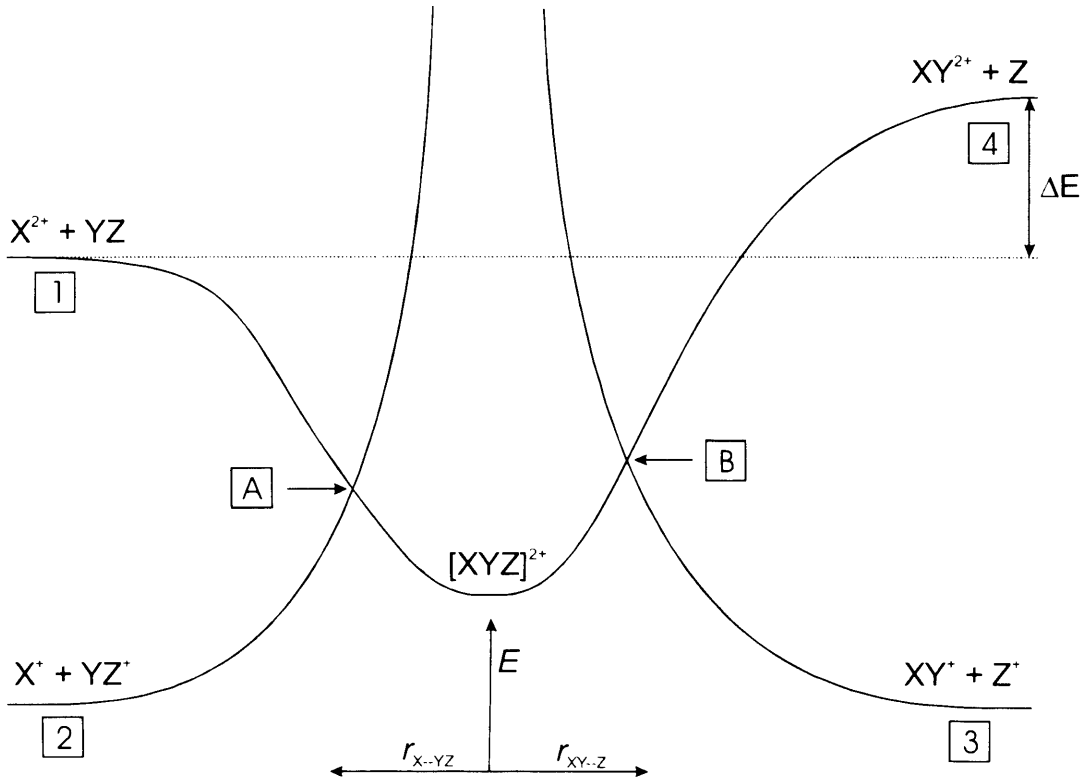

Figure 5.7 Schematic illustration of the pathways open to a dication and neutral molecule in collision. Note that excited levels are ignored, which in reality lead to many curve intersections on both sides of the diagram. The energy gaps between different asymptotes is, of course, species specific and can vary greatly.

As discussed above, the observation of a doubly charged molecular product from the reaction of a small molecular dication with a rare gas atom is rather unusual[116-

[19]. A schematic model proposed to rationalize the observations of reactions that generate dicationic products has been presented before[20], and is illustrated in Figure 5.7. The diagram represents the possible products of a basic doubly charged triatomic system. The reactant dication and neutral are at asymptote [1] on the left hand side, while a double-charged product with an accompanying neutral species (in this case ArS^{2+} + F) corresponds to asymptote [4]. However, for the reactants to achieve the intimate contact required to form new chemical bonds, the collision system must successfully pass through the intersection that leads to SET (Point [A], Figure 5.7) without crossing between curves. If the collision system passes through Point [A] then a collision complex can be formed and the necessary chemistry may occur. The collision complex may separate along its newly formed bond, thus returning to the LHS of the diagram, or along the original bond, and exiting towards the RHS of the diagram. In the latter case, the separating products must pass through another intersection (Point [B], Figure 5.7), where a change of potential surfaces will result in the formation of a pair of monocations. Indeed, bond-forming reactions forming pairs of monocations are often observed following collisions of dications with neutrals[21]. Even if the collision system successfully negotiates this second region of intersections, it must possess sufficient kinetic energy ΔE to reach the asymptotic limit corresponding to ArS^{2+} + F. Of course, in addition to these energetic and dynamic considerations, the doubly charged product must be formed in a non-dissociative state in order to be detected.

Figure 5.8 shows the relative energetics of the various critical points in the reaction mechanism forming ArS^{2+} for our collision system. All of the product asymptotes in Figure 5.8 can be reached in a spin allowed fashion from the ground state of SF^{2+} and, hence, other factors must account for the propensity for forming ArS^{2+} in this collision system. To derive the energetics shown in Figure 5.8, additional quantum chemical calculations were performed in order to determine the energies and geometries of species containing an Ar–S bond. These calculations were performed using Gaussian98[22] implemented on a Linux workstation. Optimised geometries (see Table 5.5) were determined using an MP2 algorithm with a cc-VQZ basis set and the energies of these geometries (relative to Ar^+ + F^+ + S) were then evaluated using a coupled cluster [CCSD(T)] algorithm.

	r(Ar-S) / Å	r(F-S) / Å	∠(Ar-S-F) / °	Relative energy / eV
$^2ArSF^{2+}$	2.14	2.05	167.5	0.0
$^2ArS^+$	2.13	-	-	-0.1
$^3ArS^{2+}$	2.06	-	-	0.7
$^1ArS^{2+}$	2.02	-	-	2.2

Table 5.5 Optimised geometries and relative energies calculated for species containing an Ar–S bond. Note that the ground doublet state of the collision complex $ArSF^{2+}$ is calculated to be bound (i.e. it is not just a transition state).

As described in section 5.3.2, the ionization energy of SF^+ that was given earlier was calculated via a different methodology as part of a different investigation[8]. However, since the ionization energy and heat of formation of SF are known experimentally[13], the relative energy of the reactant asymptote can be determined appropriately in Figure 5.8.

In the present experiment the collision system readily crosses at the first curve intersection, (Point A, Figure 5.7) as strong signals of SF^+ (and S^+) and Ar^+ are observed. However, for the equilibrium geometries of ArS^{2+} and ArS^+, the asymptote corresponding to $ArS^+ + F^+$ lies just 0.8 eV below the asymptote corresponding to $^3ArS^{2+}$ + F and 2.3 eV below that corresponding to $^1ArS^{2+}$ + F (Figure 5.8). These small energy differences between these asymptotes means that the critical intersections between potential curves in the exit channel towards ArS^{2+} + F (Point B, Figure 5.7) occur at large interspecies separations. Hence, the probability of crossing between surfaces at Point B will be small. This energetic argument clearly explains why no ArS^+ signal is observed in this collision system, even though the observation of ArS^{2+} indicates that there must be a product flux through the intersection in the exit channel.

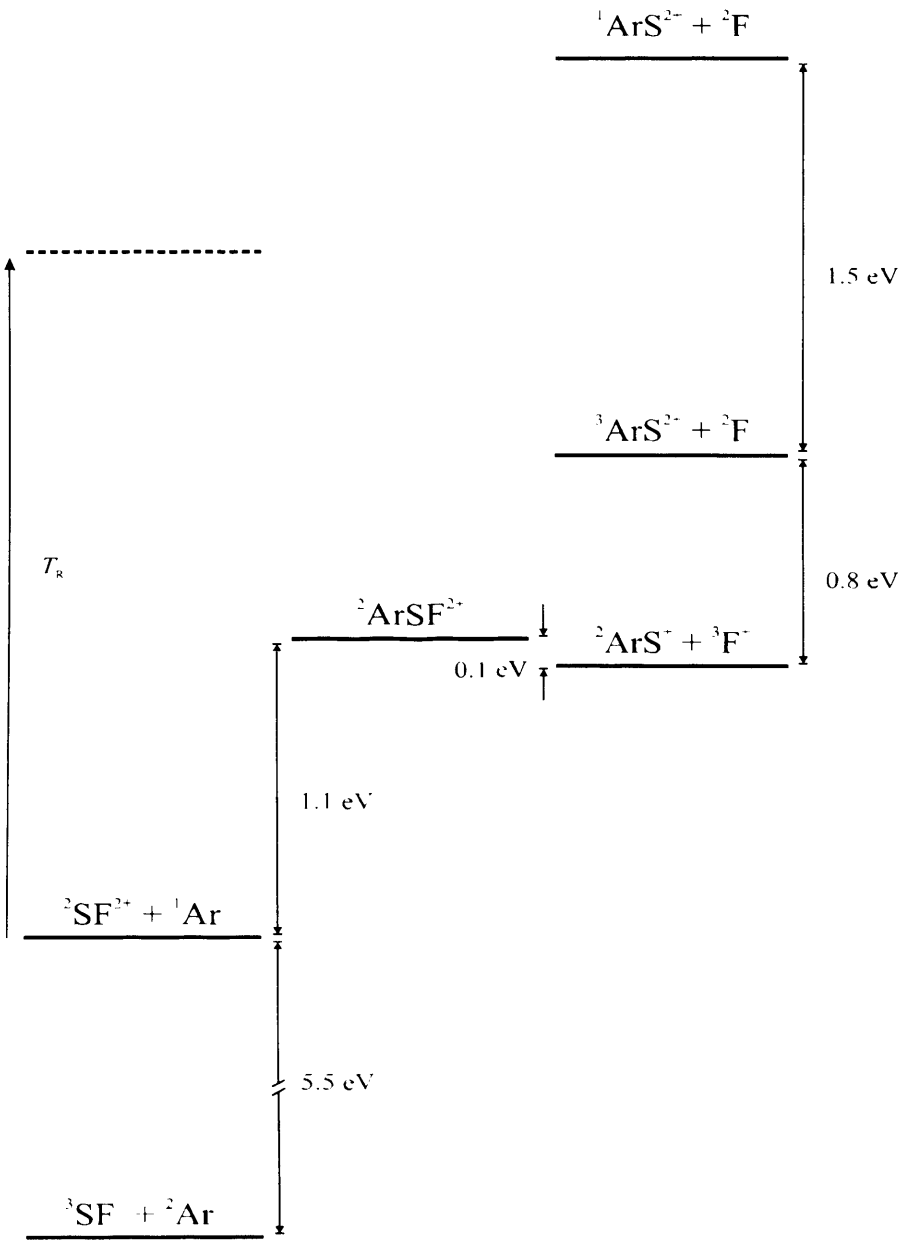

Figure 5.8 Composite energy level diagram for SF^{2+} + Ar. The dashed line indicates the centre-of-mass frame collision energy available in the lowest energy collision (i.e. 2.6.eV).

Note that the calculated energetics (Figure 5.8) show that the excited (singlet) state of ArS^{2+} lies 1.5 eV above the ground (triplet) state of this dication and that accessing the singlet and triplet asymptotes from the ground state reactants requires the centre-of-mass kinetic energy to exceed 1.8 eV and 3.6 eV respectively. The lower of these thresholds is below the lower extreme of the experimental collision energy range

(indicated by the dashed line in Figure 5.8). However, in Figure 5.4 the cross-section for forming ArS^{2+} does begin to fall off below 3.5 eV, in accordance with the higher threshold predicted from our energetic data. Thus our experimental data suggests that both the singlet and triplet states of the ArS^{2+} dicationic product are populated in this reaction, however the contribution of excited SF^{2+} reactant ions to the reaction cannot be confidently ascertained from this data.

It is likely that at higher collision energies than were reached in the experiment, the cross-section for forming ArS^{2+} will begin to fall off, as has been observed for the formation of ArC^{2+}, as the increase in the internal energy of the collision system results in the population of dissociative excited states of ArS^{2+}.

5.5. Conclusions

The formation of S^+ and SF^+ in SET reactions between SF^{2+} and Ar has been detected and the cross-sections, in arbitrary units, for forming these species have been evaluated as a function of collision energy from 2.6 eV to 6.2 eV in the centre-of-mass frame. The form of this SET reactivity has been rationalized by Landau-Zener calculations, which indicate that the S^+ product results from the dissociation of excited electronic states of SF^+ populated by the reaction of the first excited electronic state of SF^{2+}. The calculations also indicate that the stable SF^+ ions detected result from the SET reactions of the ground state of SF^{2+}. The reactivity of this collision system also involves an unusual bond-forming reaction, which generates ArS^{2+}. Quantum chemical calculations of the relevant energetics show that the lowest lying singlet and triplet states of ArS^{2+} are bound and are energetically accessible for this collision system at the above collisions energies. The observation of ArS^{2+} has been rationalized in terms of the relative energetics of the competing chemical and electron transfer reactions. This analysis shows that electron transfer in the exit channel between the separating ArS^{2+} and F atom is likely to be inefficient, explaining the observation of a doubly charged product and not a pair of monocations.

The newly developed methodology for extracting reaction cross-sections from measured ion intensities has been implemented for the first time and demonstrated to significantly outperform the previous model. This allowed good estimates of the cross-sections of all product ions of this collision system to be successfully obtained.

5.6. References

[1] T. Stanski and B. Adamczyk, *Int. J. Mass Spectrom. Ion Process.* **46:** 31 (1983)

[2] R.K. Singh, R. Hippler and R. Shanker, *Phys. Rev. A* **67:** (2003)

[3] R. Rejoub, D.R. Sieglaff, B.G. Lindsay and R.F. Stebbings, *J. Phys. B* **34:** 1289 (2001)

[4] M.V.V.S. Rao and S.K. Srivastava, Proceedings of the XXth international conference on the physics of electronic and atomic collisions, scientific programs and abstracts of contributed papers, Vienna, Austria (1997)

[5] D. Margreiter, G. Walder, H. Deutsch, H.U. Poll, C. Winkler, K. Stephan and T.D. Mark, *Int. J. Mass Spectrom. Ion Process.* **100:** 143 (1990)

[6] N. Love (2006) PhD thesis, UCL

[7] K. Nagesha, V.R. Marathe and D. Mathur, *Chem. Phys.* **154:** 125 (1991)

[8] N. Lambert (2005) PhD thesis, UCL

[9] S.D. Price, S.A. Rogers and S.R. Leone, *J. Chem. Phys.* **98:** 9455 (1993)

[10] N. Tafadar, N. Kaltsoyannis and S.D. Price, *Int. J. Mass Spectrom.* **192:** 205 (1999)

[11] D. Kearney and S.D. Price, *Phys. Chem. Chem. Phys.* **5:** 1575 (2003)

[12] Molpro is a package of ab initio programs written by H. J. Werner and P. J. Knowles, with contributions from R. D. Amos, A. Bernhardsson, A. Berning, P. Celani, D. L. Cooper, M. J. O. Deegan, A. J. Dobbyn, F. Eckert, C. Hampel, G. Hetzer, T. Korona, R. Lindh, A. W. Lloyd, S. J. McNicholas, F. R. Manby, W. Meyer, M. E. Mura, A. Nicklass, P. Palmieri, R. Pitzer, G. Rauhut, M. Sch'utz, H. Stoll, A. J. Stone, R. Tarroni, T. Thorsteinsson

[13] NIST Chemistry WebBook www.nist.gov

[14] N. Lambert, D. Kearney, N. Kaltsoyannis and S.D. Price, *J. Am. Chem. Soc.* **126:** 3658 (2004)

[15] W.-P. Hu, S.M. Harper and S.D. Price, *Mol. Phys.* **103:** 1809 (2005)

[16] D. Ascenzi, P. Franceschi, P. Tosi, D. Bassi, M. Kaczorowska and J.N. Harvey, *J. Chem. Phys.* **118:** 2159 (2003)

[17] W.Y. Lu, P. Tosi and D. Bassi, *J. Chem. Phys.* **112:** 4648 (2000)

[18] P. Tosi, R. Correale, W.Y. Lu, S. Falcinelli and D. Bassi, *Phys. Rev. Lett.* **82:** 450 (1999)

[19] P. Tosi, W.Y. Lu, R. Correale and D. Bassi, *Chem. Phys. Lett.* **310:** 180 (1999)

[20] Z. Herman, *Int. Rev. Phys. Chem.* **15:** 299 (1996)

[21] S.D. Price, *Phys. Chem. Chem. Phys.* **5:** 1717 (2003)

[22] M.J. Frisch, G.W. Trucks, H.B. Schlegel, G.E. Scuseria, M.A. Robb, J.R. Cheeseman, V.G. Zakrzewski, J.A. Montgomery Jr., R.E. Stratmann, J.C. Burant, S. Dapprich, J.M. Millam, A.D. Daniels, K.N. Kudin, M.C. Strain, O. Farkas, J. Tomasi, V. Barone, M. Cossi, R. Cammi, B. Mennucci, C. Pomelli, C. Adamo, S. Clifford, J. Ochterski, G.A. Petersson, P.Y. Ayala, Q. Cui, K. Morokuma, M.D. K., A.D. Rabuck, K. Raghavachari, J.B. Forseman, J. Cioslowki, J.V. Ortiz, B.B. Stefanov, G. Liu, A. Liashenko, P. Piskorz, I. Komaromi, R. Gomperts, R.L. Martin, D.J. Fox, T. Keith, M.A. Al-Laham, C.Y. Peng, A. Nanayakkara, C. Gonzalez, M. Challacombe, P.M.W. Gill, B. Johnson, W. Chen, M.W. Wong, J.L. Andreas, M. Head-Gordon, E.S. Replogle and J.A. Pople *Gaussian 98, Revision A.3* (1998). Gaussian, Inc., Pittsburgh PA

Chapter 6: The $(H)Cl^{2+}$ + CO Collision System

6.1. Introduction

Although extensive research has been conducted into the properties of the precursor molecule of this system, HCl, no crossed-beam experiments have been performed with doubly charged derivatives. Electron ionization of HCl forms all possible singly and doubly charged fragments in appreciable quantities and partial ionization cross-sections have been determined experimentally.[1-5] Additionally, some spectroscopic experiments have been carried out on both HCl^{2+} and Cl^{2+}.[6-10] Most recently Critchley et al. resolved vibrational levels in two electronic states of HCl^{2+} using TPESCO and performed *ab initio* calculations for comparison[11]. The mass spectrum of ionization products of HCl includes a quartet corresponding to $^{35}Cl^{2+}$, $H^{35}Cl^{2+}$, $^{37}Cl^{2+}$ and $H^{37}Cl^{2+}$ at 0.5 unit intervals on an atomic *m/z* scale. Consequently, $^{35}Cl^{2+}$ is the easiest doubly charged fragment of which to obtain a well-resolved beam because there are no more ion signals nearby on the lower mass side. However, producing such a beam of $H^{35}Cl^{2+}$ is much more problematic as it is difficult to completely filter out the intense signals of $^{35}Cl^{2+}$ and $^{37}Cl^{2+}$ that occur just half an *m/z* unit either side. All the experiments conducted in this chapter involve the Cl-35 isotope and henceforth the atomic mass will not be explicitly labelled.

Singly charged ions	Partial ionization cross-section	Doubly charged ions	Partial ionization cross-section
HCl^+	1000	HCl^{2+}	103
Cl^+	339	Cl^{2+}	67
H^+	373		

Table 6.1 Relative partial ionization cross-sections for products of electron impact ionization of HCl, at an electron energy of 150 eV.[5]

A thorough investigation of the Cl^{2+} collision was conducted but due to the difficulty of obtaining a usable beam of HCl^{2+}, only a limited number of spectra were collected for collisions of that species and so full quantitative analysis was not performed.

6.2. Results

Mass spectra were recorded at collision energies between 5.0-16.0 eV in the LAB frame corresponding to 2.2-7.1 eV in the centre-of-mass frame.

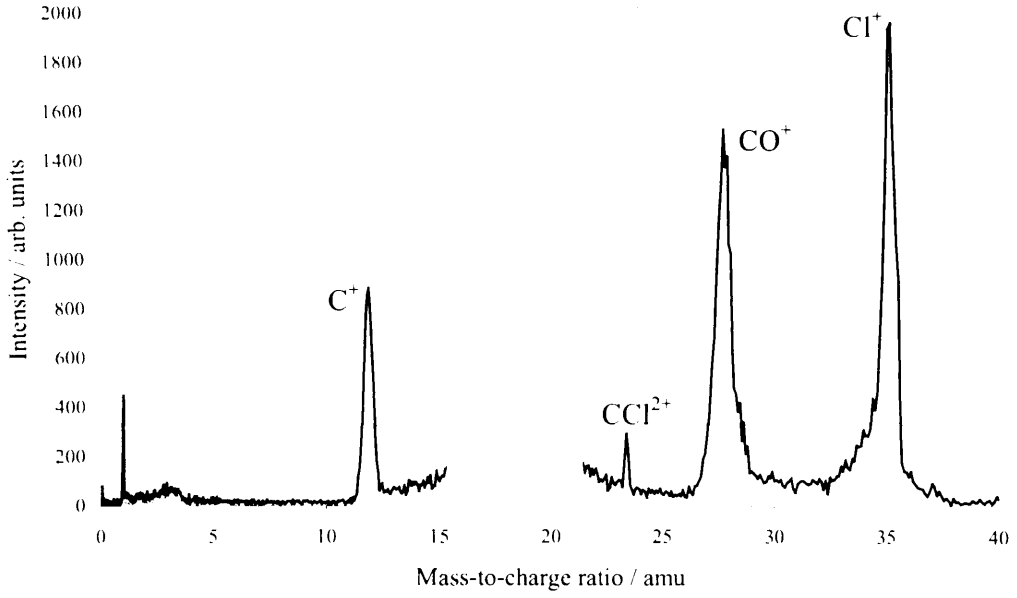

Figure 6.1 Reaction (thick line) and background (thin line) mass spectra for Cl^{2+} + CO. The dication signal has been removed.

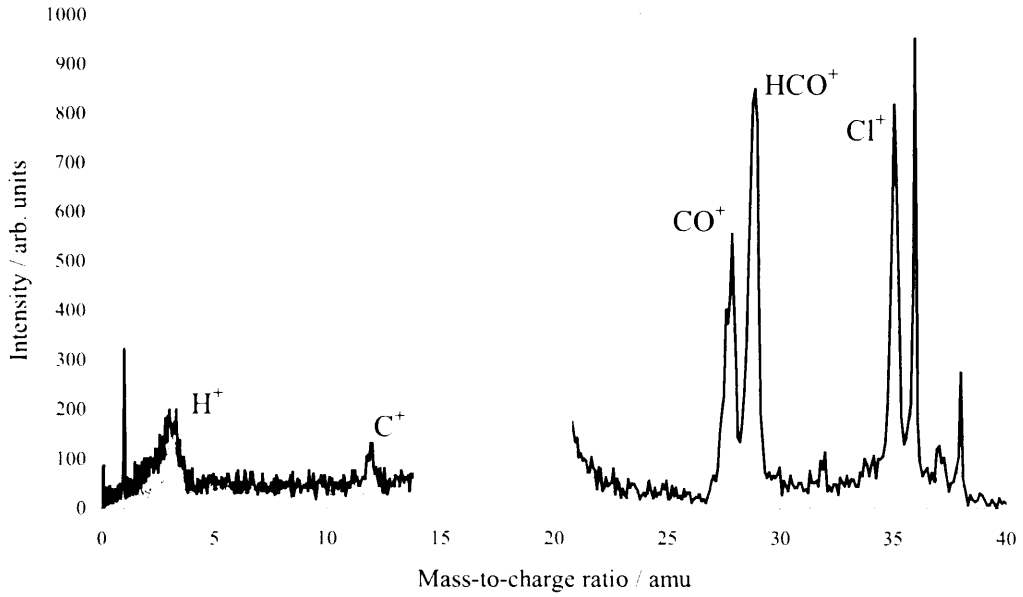

Figure 6.2 As Figure 6.1, but for HCl^{2+} + CO.

Representative mass spectra for collisions of Cl^{2+} and HCl^{2+} with CO are shown in Figure 6.1 and Figure 6.2 respectively. These spectra are discussed below.

6.2.1. Cl^{2+} data

Comparison of the reaction and background spectra reveals that Cl^+ and CO^+ ions are the major products in this collision system. Appreciable quantities of C^+ are also detected, but O^+ is only observed in small amounts. Furthermore, a small signal located at m/z = 23.5 indicates the presence of CCl^{2+}, a doubly charged product of a chemical bond-forming reaction. Additionally, traces of CCl^+ and possibly even OCl^{2+} and OCl^+ are discernible in the spectra but in quantities far too small to reliably quantify. Therefore, the major reaction channels occurring in this collision system appear to be:

$$Cl^{2+} + CO \rightarrow Cl^+ + CO^+ \quad (6.1)$$

$$Cl^{2+} + CO \rightarrow Cl^+ + C^+ + O \quad (6.2)$$

$$Cl^{2+} + CO \rightarrow CCl^{2+} + O \quad (6.3)$$

E_{lab} / eV	average R^{true}			
	Cl^+	CO^+	C^+	CCl^{2+}
5	1.65×10^{-03}	5.43×10^{-04}	1.83×10^{-04}	2.40×10^{-05}
6	1.37×10^{-03}	6.73×10^{-04}	2.34×10^{-04}	3.92×10^{-05}
7	1.48×10^{-03}	7.09×10^{-04}	2.58×10^{-04}	4.28×10^{-05}
8	1.17×10^{-03}	7.15×10^{-04}	2.70×10^{-04}	3.98×10^{-05}
9	1.19×10^{-03}	7.83×10^{-04}	2.92×10^{-04}	4.27×10^{-05}
10	1.21×10^{-03}	7.19×10^{-04}	3.12×10^{-04}	4.60×10^{-05}
11	1.20×10^{-03}	9.16×10^{-04}	4.18×10^{-04}	4.59×10^{-05}
12	1.35×10^{-03}	9.86×10^{-04}	4.69×10^{-04}	4.73×10^{-05}
13	1.26×10^{-03}	1.09×10^{-03}	5.02×10^{-04}	4.74×10^{-05}
14	1.19×10^{-03}	1.11×10^{-03}	5.17×10^{-04}	4.48×10^{-05}
15	1.21×10^{-03}	1.16×10^{-03}	5.65×10^{-04}	4.32×10^{-05}
16	1.27×10^{-03}	1.30×10^{-03}	7.01×10^{-04}	4.36×10^{-05}

Table 6.2 Corrected product ratios for all products observed in the Cl^{2+} + CO collision system at each collision energy. Note that for all data collected on this system $k \approx 1$ so $R^{true} \approx R^{obs}$.

For the products of the reactions 6.1 – 6.3, the relevant ion intensities (Table 6.2) were processed, as described in Chapter 4, to yield the values of σ'_j for these product ions as a function of collision energy. Note that for this purpose it has been assumed that all C^+ ions are formed via dissociative SET, which is treated in the same manner as the case of S^+ in the previous chapter, i.e. the dissociation of CO^+ is assumed to occur with zero energy release and hence the velocity of C^+ is taken to be the same as that calculated for CO^+. However, this is not the only possible source of C^+, as will be discussed later.

6.2.2. HCl^{2+} data

Experiments using HCl^{2+} as the reactant dication produced a full range of electron transfer products: HCl^+, Cl^+, CO^+, C^+ and H^+ were all observed. The molecular product of non-dissociative SET, HCl^+, is observed with a much weaker signal than Cl^+, but far

less C^+ is observed than in the Cl^{2+} + CO system. Additionally a strong proton transfer channel is observed in competition with electron transfer. Collisions using HCl^{2+} did not yield discernible quantities of doubly charged products.

6.3. Electron transfer reactions of Cl^{2+}

Figure 6.3 and Figure 6.4 plot calculated values of l and N^V/A as functions of time for the non-dissociative SET products Cl^+ and CO^+. These plots are very similar in shape to those of SF^+ and Ar^+ respectively, that were discussed in the previous chapter. The very similar ratio of the mass of the neutral molecule to the mass of the dication in each case means that the partitioning of energy released by the separation of charge will be almost identical. The kinetic energy release will also be similar in both systems since this depends primarily on the electrostatic repulsion between charges rather than the identity of the participants. However, Cl^+ is lighter than SF^{2+} so will travel faster at the same kinetic energy; the same goes for CO^+ in comparison with Ar^+. This difference manifests itself as steeper gradients in Figure 6.3 and Figure 6.4 compared to those of SF^+ and Ar^+ at the same collision energy shown in the previous chapter.

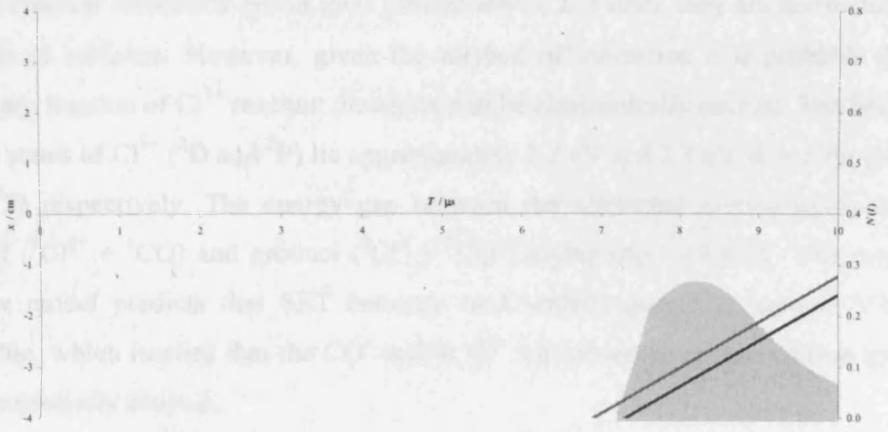

Figure 6.3 Plot of x_1 and x_2 (solid lines, left-hand scale) and N^V/A (shaded area, right-hand scale) for Cl^+ at a LAB frame collision energy of 11 eV at a scattering angle of 0°.

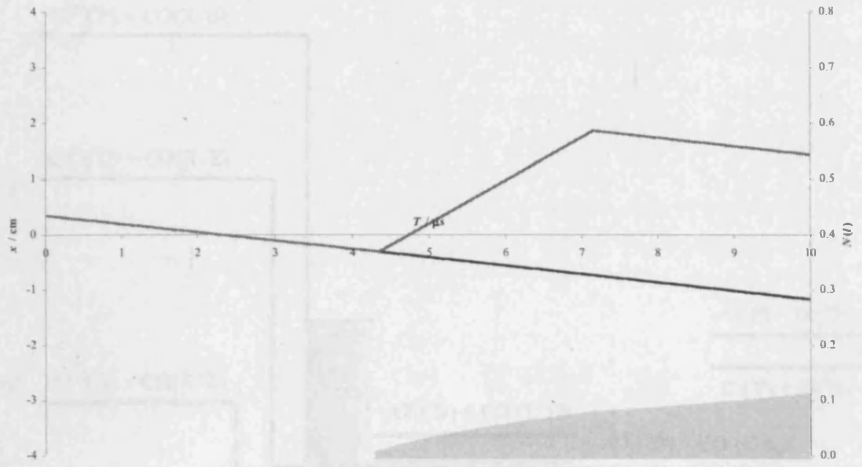

Figure 6.4 Plot of x_1 and x_2 (solid lines, left-hand scale) and N^P/A (shaded area, right-hand scale) for CO^+ at a LAB frame collision energy of 11 eV at a scattering angle of 180°.

The composite energy level diagram for this collision system, demonstrating the possible products of electron transfer, is shown in Figure 6.5. Note that for clarity, only $Cl^+ + CO^+$ states lying below the energy of the ground state reactants are shown. All of the CO reactant molecules are in their ground state ($^1\Sigma^+$) since they are thermalized at the time of collision. However, given the method of ionization it is probable that a significant fraction of Cl^{2+} reactant dications will be electronically excited. The first two excited states of Cl^{2+} (^2D and ^2P) lie approximately 2.2 eV and 3.7 eV above the ground state (^4S) respectively. The energy gap between the electronic ground states of the reactant ($^4Cl^{2+}$ + ^1CO) and product ($^3Cl^+$ + $^2CO^+$) asymptotes is 9.8 eV. The reaction window model predicts that SET between such widely spaced asymptotes will be negligible, which implies that the CO^+ and/or Cl^+ ions observed in the reaction spectra are electronically excited.

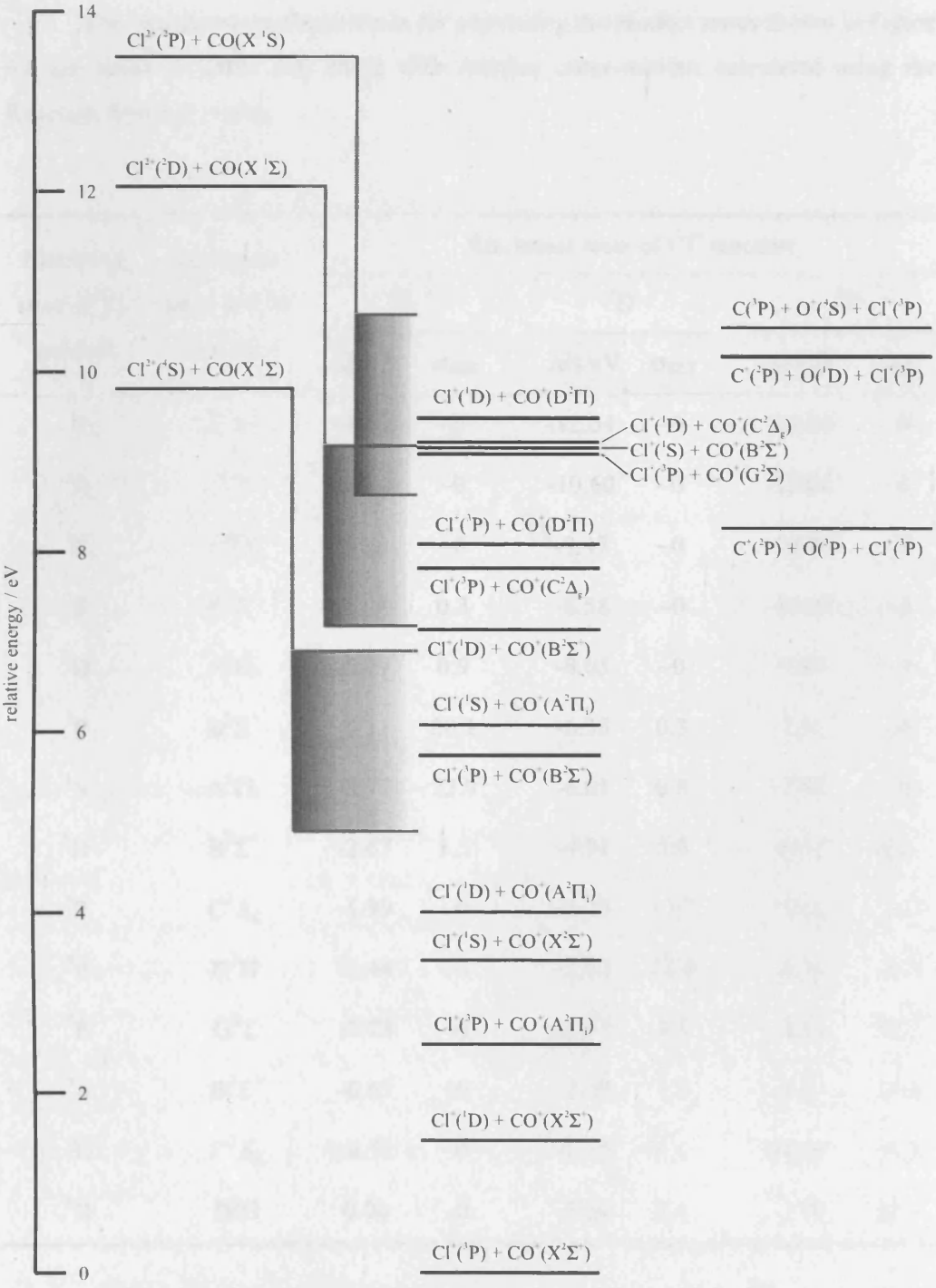

Figure 6.5 Composite energy level diagram for Cl^{2+} + CO. Note that for clarity, only Cl^+ + CO^+ states lying below the energy of the ground state reactants are shown. Shaded areas indicate the approximate position of the Reaction Windows.

The calculated exothermicities for populating the product states shown in Figure 6.5 are listed in Table 6.3, along with reaction cross-sections calculated using the Reaction Window model.

Electronic state of Cl^+ product	Electronic state of CO^+ product	Electronic state of Cl^+ reactant					
		^4S		^2D		^2P	
		ΔH/eV	σ_{SET}	ΔH/eV	σ_{SET}	ΔH/eV	σ_{SET}
^3P	$X^2\Sigma^+$	-9.80	~0	-12.04	~0	-13.50	~0
^1D	$X^2\Sigma^+$	-8.36	~0	-10.60	~0	-12.06	~0
^3P	$A^2\Pi_i$	-7.23	~0	-9.47	~0	-10.93	~0
^1S	$X^2\Sigma^+$	-6.34	0.3	-8.58	~0	-10.04	~0
^1D	$A^2\Pi_i$	-5.79	0.9	-8.03	~0	-9.49	~0
^3P	$B^2\Sigma^+$	-4.11	20.1	-6.35	0.3	-7.81	~0
^1S	$A^2\Pi_i$	-3.77	23.9	-6.01	0.6	-7.47	~0
^1D	$B^2\Sigma^+$	-2.67	3.5	-4.91	5.6	-6.37	0.3
^3P	$C^2\Delta_g$	-1.99	~0	-4.23	17.7	-5.69	1.1
^3P	$D^2\Pi$	-1.44	~0	-3.68	23.8	-5.14	3.7
^3P	$G^2\Sigma$	-0.73	~0	-2.97	9.3	-4.43	13.7
^1S	$B^2\Sigma^+$	-0.65	~0	-2.89	7.5	-4.35	15.3
^1D	$C^2\Delta_g$	-0.55	~0	-2.79	5.4	-4.25	17.3
^1D	$D^2\Pi$	0.00	~0	-2.24	0.4	-3.70	23.9

Table 6.3 Calculated exothermicities and reaction cross-sections for populating SET product asymptotes. These calculations refer to a laboratory frame collision energy of 10 eV, but do not change significantly over our collision energy range. Splitting of product terms has been ignored; in such cases calculations refer to the lowest energy level.

These results indicate that the vast majority of SET processes originating from the ground state of the reactants are as follows:

$$Cl^{2+}(^4S) + CO(X^1\Sigma^+) \rightarrow Cl^+(^3P) + CO^+(B^2\Sigma^+) \quad (6.4)$$

$$Cl^{2+}(^4S) + CO(X^1\Sigma^+) \rightarrow Cl^+(^1S) + CO^+(A^2\Pi_i) \quad (6.5)$$

The product states of CO^+ in both reactions 6.4 and 6.5 are electronically stable, however the latter reaction is spin forbidden and hence the former reaction is likely to be the primary source of CO^+ ions observed in the mass spectrum. In contrast, the first and second excited states of Cl^{2+} can efficiently undergo electron transfer to a number of higher excited CO^+ product states that are either weakly bound or purely repulsive. All the electronic combinations of $Cl^+ + CO^+$ populated from the first excited state of Cl^{2+} with ground state CO lie lower in energy than the $C + O^+$ dissociation asymptote and so would be expected to dissociate only to $C^+ + O$. Most electronic combinations of $Cl^+ + CO^+$ populated from the second excited state of Cl^{2+} with ground state CO also lie lower in energy than the $C + O^+$ dissociation asymptote and one would expect, therefore, dissociative SET to preferentially result in C^+ rather than O^+, as is borne out by the experimental data.

The experimental partial reaction cross-sections, in arbitrary units, of the SET products, Cl^+, CO^+ and C^+, are plotted as a function of collision energy in Figure 6.6. In a striking similarity to the results discussed in the previous chapter, the calculated cross-sections of SET product ions increase slightly at the lower end of the energy range. The reaction cross-section for the formation of Cl^+ is seen to be approximately constant across much of the energy range while the cross-section for the formation of CO^+ drops slightly as the collision energy increases, as might be expected if the proportion that dissociates into $C^+ + O$ increases. The cross-section for forming C^+ does not increase correspondingly, but the calculated cross-section for formation of C^+ assumes that all C^+ observed is the product of dissociative electron transfer, whereas in fact, as described in the following section, it is likely that a proportion of C^+ ions arises from dissociation of CCl^+. C^+ ions generated by these different sources would have different velocities and hence different values of $I(t,\theta)$, thus affecting the analysis. However, the analysis already contains many variables and so introducing another (i.e a branching ratio for the

formation of C^+ through each channel) to back-extrapolate the proportion of C^+ produced by each channel would not result in a meaningful value.

E_{lab} / eV	E_{com} / eV	σ'_j / arb. units			
		Cl^+	CO^+	C^+	CCl^{2+}
5	2.2	6.9	6.5	2.0	5.1×10^{-2}
6	2.7	5.5	6.1	2.0	6.4×10^{-2}
7	3.1	5.9	5.2	1.7	5.9×10^{-2}
8	3.6	4.6	4.2	1.5	5.8×10^{-2}
9	4.0	4.7	4.0	1.4	4.9×10^{-2}
10	4.4	4.8	3.2	1.3	5.2×10^{-2}
11	4.9	4.8	3.3	1.5	5.2×10^{-2}
12	5.3	5.6	3.3	1.4	5.3×10^{-2}
13	5.8	5.3	3.2	1.4	5.5×10^{-2}
14	6.2	5.1	2.9	1.2	5.0×10^{-2}
15	6.7	5.2	2.7	1.2	4.5×10^{-2}
16	7.1	5.5	2.7	1.3	4.9×10^{-2}

Table 6.4 Values of σ'_j for reaction products obtained from experimental data.

If we ignore, for a moment, all reaction channels other than SET, then the reaction cross-section for forming Cl^+ ought to equal the sum of those for forming CO^+ and C^+ since Cl^+ is a product of both dissociative and non-dissociative SET. The new method of analysis puts the ratio $\sigma'_j(Cl^+) : \sigma'_j(CO^+) + \sigma'_j(C^+)$ much closer to its true value (i.e. unity) than was possible with the previous methodology, which, similarly to when applied to the SF^+ + Ar system, underestimates this value by an order of magnitude.

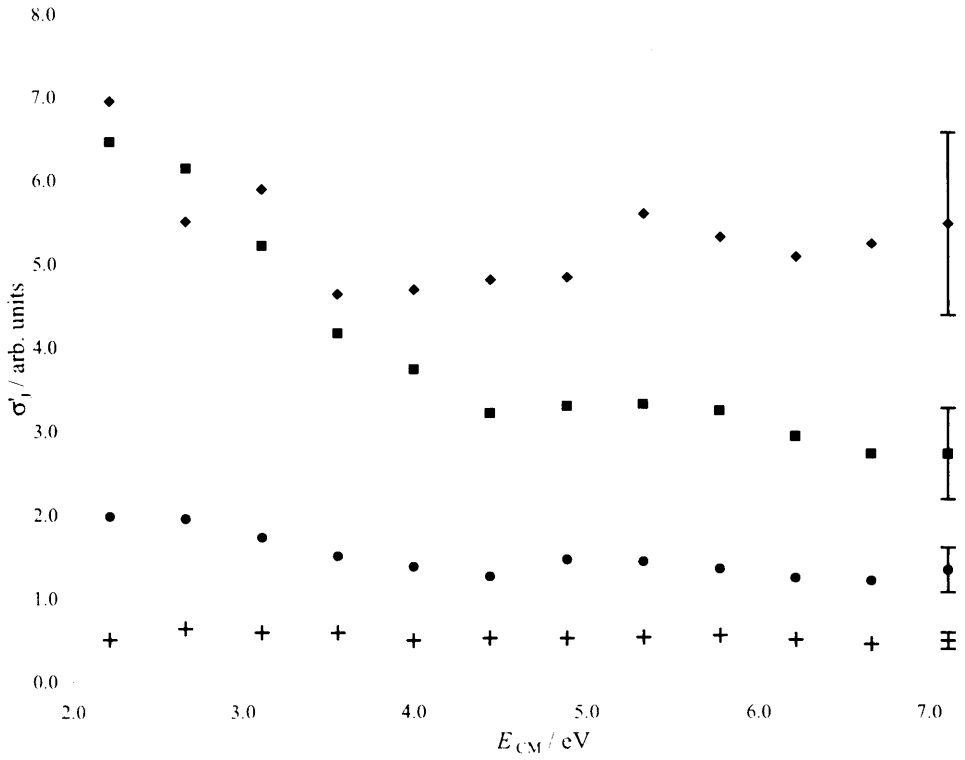

Figure 6.6 Plot of the values of the data in Table 6.4: Cl^+ (◆), CO^+ (▪), C^+ (●) and CCl^{2+} × 10 (+); the representative error bars are ±25%, but it is difficult to estimate the error associated with the model.

In conclusion, the new method of analysis again proves to be a good model for both fast and slow ions, although the two possible sources of C^+ is something of a complication. While CO^+, C^+ and Cl^+ will be readily generated by SET reactions, the small O^+ signal may be due either to excited Cl^{2+} crossing into higher states of Cl^+ + CO^+ or formation of unstable CCl^+:

$$Cl^{2+} + CO \rightarrow CCl^+ + O^+ \rightarrow C^+ + Cl + O^+ \qquad (6.6)$$

The possibility of forming CCl^+ is discussed further below, in relation to the observation of CCl^{2+}.

6.4. Observation of CCl^{2+}

The doubly charged product CCl^{2+} is observed with an approximate reaction cross-section, measured in the same arbitrary units as the other products of the same system, of 5×10^{-2} in the middle of the collision energy range.

In order to rationalise this observation, Gaussian 98[12] was used to determine energies not readily available in the literature, and single-point energy calculations were performed using CCSD(T)-VQZ optimised at geometries obtained using MP2-VQZ (energetics and optimised geometries of species containing a C–Cl bond are shown in Table 6.5 and Table 6.6). The energies of the four non-dissociative ground state asymptotes associated with the system are shown in Figure 6.7. Additionally, a linear collision complex, $OCCl^{2+}$, was found to have a local potential minimum in its doublet ground state.

	r(C–Cl) /Å		Ionization Energy/ eV	
	This Work	Literature	This Work	Literature
^2CCl	1.64	1.65[13]	8.9	9.1[14]
$^1CCl^+$	1.53	1.54[15]	21.6	-
$^2CCl^{2+}$	1.45	-	-	-

Table 6.5 Calculated geometries and energetics for CCl, CCl^+ and CCl^{2+}. Spectroscopic data on CCl and CCl^+ is reviewed in Reference [16].

	r(C–Cl) /Å	r(C–O) /Å	∠(OCCl)	Ionization Energy/ eV
^2OCCl	1.64	1.65	180.0°	0.0
$^2OCCl^{2+}$	1.53	1.54	129.3°	+30.0

Table 6.6 Calculated geometries and energetics for OCCl and $OCCl^{2+}$. Note that the doublet ground state of the collision complex $OCCl^{2+}$ is calculated to be bound.

Inevitably, a significant number of reactions will result in SET without even reaching the collision complex. However, reaction window calculations predict that when $OCCl^{2+}$ separates along the O–C bond it ought readily to cross potential energy

surfaces to form CCl^{+} + O^{+}. The rationale behind this can be seen by returning to the quantity δ, the probability of remaining on a diabatic potential energy curve as it passes through a crossing. In the mechanism for SET described in Chapter 2, it was shown that the probability of exiting a collision on a different potential surface after passing through two curve crossings is δ(1-δ) + (1-δ)δ, while the probability of exiting on the same surface is δδ + (1-δ)(1-δ).

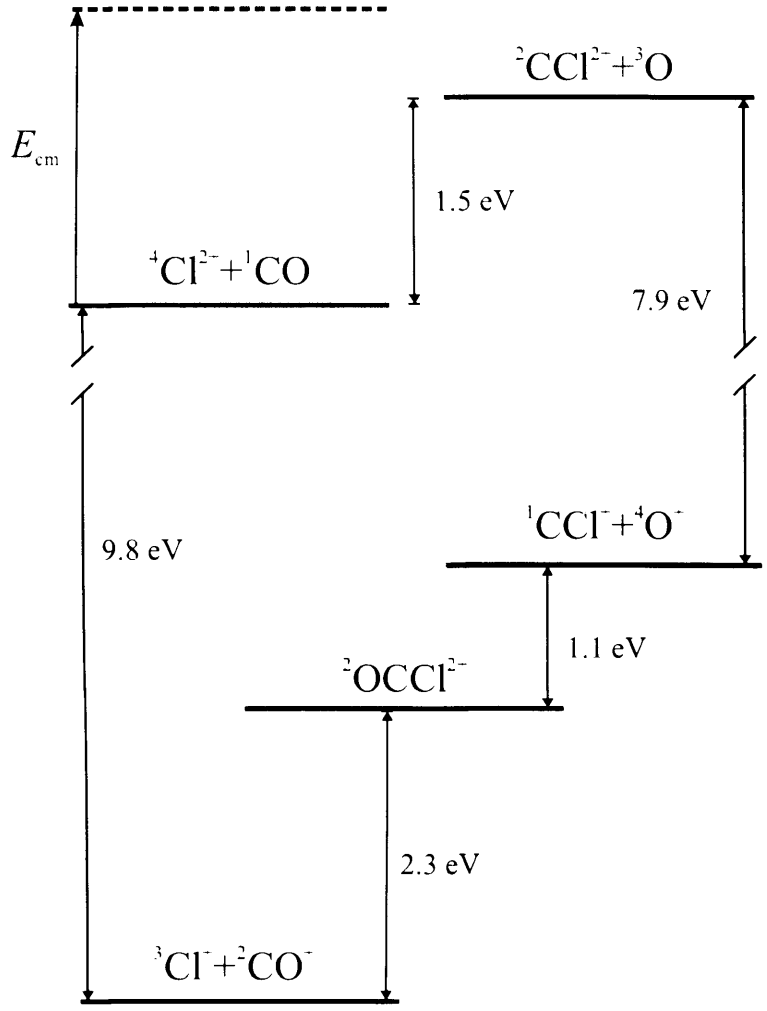

Figure 6.7 Relative energies of non-dissociative ground state asymptotes associated with the Cl^{2+} + CO system.

In contrast to this SET mechanism, upon dissociation $OCCl^{2+}$ will traverse any particular crossing only *once*, and hence the probability of remaining on the same

surface (to form CCl^{2+} + O) is directly proportional to δ, and the probability of changing surfaces (to form CCl^{+} + O^{+}) is (1-δ). The corollary of this is that asymptotes that are widely spaced, so that δ is close to zero, will provide the most efficient crossing between curves. Conversely, asymptotes with a small energy gap will not readily transfer because the crossing radius is large and δ is close to 1. This reasoning has been used to explain the absence of ArS^{+} despite the observation of ArS^{2+} in collisions of SF^{2+} with Ar. In that case, the ground state of ArS^{+} + F^{+} lies only 0.8 eV and 2.3 eV lower in energy than the first two electronic states of ArS^{2+} + F. This small exothermicity strongly disfavours transfer to a pair of monocations, a fact confirmed by the complete absence of F^{+} in the product spectra. However, the energies of the present system are in stark contrast to those of the SF^{2+} + Ar system: the ground electronic state of CCl^{+} + O^{+} lies 7.9 eV below that of CCl^{2+} + O. This means that the argument proposed in Chapter 5 for the absence of ArS^{+} (i.e. the narrow energy gap between the ArS^{+} and ArS^{2+} product asymptotes) does not explain the absence of CCl^{+}. In the present system, the ground state reaction $^{2}OCCl^{2+} \rightarrow {}^{1}CCl^{+} + {}^{4}O^{+}$ is spin-forbidden (the multiplicity of the collision complex also forbids the reaction proceeding from the ground state reactants) and so is not likely to make a significant contribution. Furthermore, when employing the Reaction Window model, only long range interactions are considered (i.e. dication potential energy is purely attractive) and thus the model will always return a crossing radius if the product potential asymptote (cation/cation) lies lower in energy than the reactant potential (dication/neutral), as shown in Figure 6.8. However, in reality, if the product asymptote lies much lower in energy than the reactant asymptote, such as is the case for the ground state reaction: Cl^{2+} + CO → CCl^{+} + O^{+}, then the curves may not intersect at all. Despite these arguments, however, both O^{+} and CCl^{+} have two excited electronic states lying within 5.5 eV of their respective ground states that can combine to give a number of excited states of CCl^{+} + O^{+} with exothermicities associated with crossing radii of 2-4 Å and consequently values of δ close to zero. Analogy between Cl^{2+} + CO and SF^{2+} + Ar does not, therefore, fully explain why CCl^{+} appears to be far less abundant than CCl^{2+}.

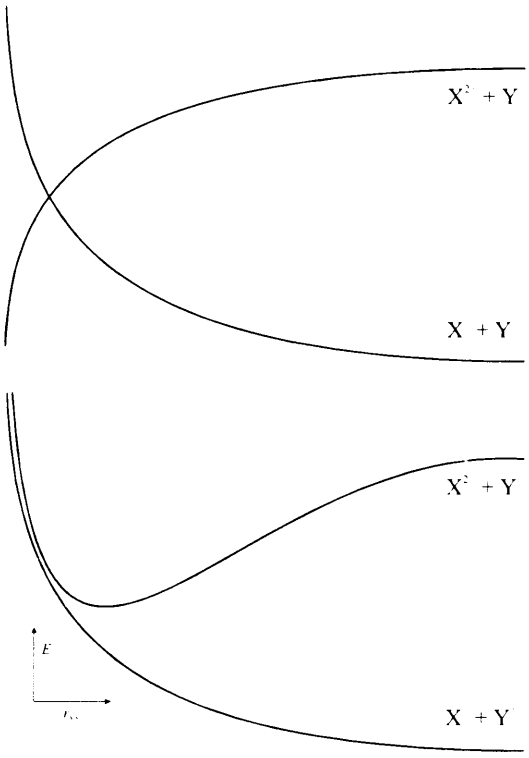

Figure 6.8 Crossing radii are calculated by considering the X^{2+} + Y potential to be purely attractive (top image). This approximation is valid for crossing radii greater than the radius of the bound minimum, but breaks down at short interspecies separation. Hence, the Reaction Window model will always predict a crossing between the two potential surfaces, even if in reality (where repulsive forces dominate at close range) the surfaces do not cross at all.

Intact CCl^+ is observed only in trace quantities and it is probable that most CCl^+ that is formed will dissociate. This is because our calculations indicate that the excited electronic states of CCl^+ are only weakly bound and the internal energy of the system following the collision is likely to cause CCl^+ to dissociate. Any C^+ ions resulting from this reaction pathway would be indistinguishable from those produced by dissociative SET. However, CCl^+ must be formed in coincidence with O^+, but the O^+ signal in our data is smaller than either C^+ or CCl^{2+}. This observation does not necessarily imply that our line of reasoning is incorrect, because it is probable that the collection efficiency of O^+ ions associated with CCl^+ is very low. The orthogonal arrangement of our apparatus is designed to collect ions with low y and z velocities (the x-axis being along the dication beam). However, if $OCCl^{2+}$ lives for at least a significant fraction of a rotational period, the large KER associated with charge separation will expel the products, O^+ and CCl^+, at a wide range of off-axis scattering angles with considerable y,z velocity components. The same reasoning applies to the partner ion CCl^+ or C^+ arising from dissociation of CCl^+. Repeating these experiments using an on-axis spectrometer would resolve this uncertainty over the real abundances of O^+ and CCl^+.

However, despite predictions that transfer at the intersection in the O–C separation co-ordinate (to $O^+ + CCl^+$) is not disfavoured, CCl^{2+} is still observed. The energetics of systems that exhibit dication-forming reactions of this type differ significantly[17-20], from which we conclude that the rarity examples of this class of reaction is not due to the requirement of favourable energetics to allow the system to avoid charge separation. Instead, perhaps, it is the need to populate a doubly charged product state that is sufficiently long-lived for the products to be detected that is the more important factor in determining whether a bond-forming reaction producing a dication-neutral pair is observed.

6.5. Proton transfer

The dominant reaction in collisions of HCl^{2+} with CO is proton transfer, which in fact outweighs the electron transfer channel. A number of electron transfer products are observed, since both HCl^+ and CO^+ formed via SET may or may not dissociate. Qualitatively, most CO^+ remains intact, similarly to the reactions of Cl^+ discussed earlier, while almost all HCl^+ dissociates.

$$HCl^{2+} + CO \rightarrow HCO^+ + Cl^+ \quad (6.7)$$

$$HCl^{2+} + CO \rightarrow HCl^+ (\rightarrow H^+ + Cl) + CO^+ (\rightarrow C^+ + O) \quad (6.8)$$

The reaction cross-section for HCO^+ is difficult to extract because the angular distribution is less well characterized than for electron transfer. Additionally, if encounter times for proton transfer are generally longer than for electron transfer, as suggested by Roithová, we would again have the problem of a Coulombic explosion occurring over a wide range of scattering angles which will significantly impair the collection efficiency. However, at a LAB frame collision energy of 11 eV, we obtain $\sigma'_{CO+} = 6.5$ and $7.0 \leq \sigma'_{HCO+} \leq 10.2$, depending on the degree of angular scattering allowed. This corresponds to a branching ratio for proton transfer of 0.52-0.61.

The dominance of proton transfer over electron transfer is similar to that observed in collisions of $HCCl^{2+}$ with CO by Roithová et al.[21] Roithová calculates the exothermicities of electron and proton transfer in that system to be 3.4 eV and 7.0 eV respectively, and obtains an experimental branching ratio, in a low collision energy regime, of approximately 1.5:1. A clear distinction is seen between the behaviour of

polar and non-polar molecules with respect to electron and proton transfer. In the case of non-polar molecules, electron transfer is inhibited for endothermic or slightly exothermic reaction, but increases rapidly as the exothermicity enters the Reaction Window energy range (< 2 eV), at the expense of proton transfer. There is no such clear pattern evident in the case of polar molecules (such as CO), with the branching ratios for proton transfer being substantial even at large electron transfer exothermicities.

In the HCl^{2+} + CO system, the energetics are rather different: the exothermicity of the electron transfer channel is 8.8 eV[13] and that of the proton transfer channel is 10.7 eV[6,13] for the proton transfer channel. These figures are consistent with Roithová's conclusion that in collisions with polar molecules, proton transfer is not suppressed even for favourable electron transfer exothermicities. The Roithová study encompasses reactions between HCX^{2+}, where X is a halogen, and a range of polar and non-polar molecules. In terms of exothermicities of collisions with polar molecules, HCl^{2+} + CO is closest to HCF^{2+} + H_2O, which has exothermicities of 7.3 eV and 11.2 eV for electron and proton transfer respectively. It is interesting to note that the branching ratio for proton transfer in that system is given as 0.56, which is very similar to the estimated branching ratio in the HCl^{2+} + CO system, given above.

6.6. Conclusions

The implementation of the new methodology for extracting reaction cross-sections from our experimental data has again allowed results for all ionic products, whether 'fast' or 'slow'. The analysis of data from this experiment has now perhaps been taken as far as it will go, and while it constitutes a good physical model of the factors that affect our spectral intensities and is particularly useful for understanding SET reactions, there are simply too many sources of inaccuracy to extract very reliable cross-sections for energetic ions with a broad angular spread.

The formation of Cl^+, CO^+ and C^+ in SET reactions between Cl^{2+} and CO has been detected and the reaction cross-sections, in arbitrary units, for forming these ions have been evaluated as a function of collision energy in the range 2.2-7.1 eV in the centre-of-mass frame. The electronic states populated by SET reactions have been predicted using Landau-Zener calculations. The reactivity of the collision system also includes another example of bond-forming chemistry resulting in a doubly charged product. This product, CCl^{2+} is observed with a greater cross-section than CCl^+, though

this is thought to be due to the propensity of excited states to dissociate and population of the more strongly bound ground state being spin-forbidden, coupled with the high off-axis velocity of CCl^+ resulting from the exoergic dissociation of $OCCl^{2+}$.

6.7. References

[1] R.E. Fox, *J. Chem. Phys.* **32:** 385 (1960)
[2] M.C. Marden and W.R. Snow, *Bull. Am. Phys. Soc.* **21:** 160 (1976)
[3] W.L. Morgan, *Plas. Chem. Plas. Process.* **12:** 449 (1992)
[4] D.G. Thompson and K. Blum, *J. Phys. B* **33:** L773 (2000)
[5] S. Harper, P. Calandra and S.D. Price, *Phys. Chem. Chem. Phys.* **3:** 741 (2001)
[6] A.G. McConkey, G. Dawber, L. Avaldi, M.A. Macdonald, G.C. King and R.I. Hall, *J. Phys. B* **27:** 271 (1994)
[7] F.R. Bennett and I.R. McNab, *Chem. Phys. Lett.* **251:** 405 (1996)
[8] R. Abusen, F.R. Bennett, I.R. McNab, D.N. Sharp, R.C. Shiell and G.A. Woodward, *J. Chem. Phys.* **108:** 1761 (1998)
[9] R. Abusen, F.R. Bennett, S.G. Cox, I.R. McNab, D.N. Sharp, R.C. Shiell, F.E. Smith and J.M. Walley, *Phys. Rev. A* **61:** art. no. (2000)
[10] S.G. Cox, A.D.J. Critchley, P.S. Kreynin, I.R. McNab, R.C. Shiell and F.E. Smith, *Phys. Chem. Chem. Phys.* **5:** 663 (2003)
[11] A.D.J. Critchley, G.C. King, P. Kreynin, M.C.A. Lopes, I.R. McNab and A.J. Yencha, *Chem. Phys. Lett.* **349:** 79 (2001)
[12] M.J. Frisch, G.W. Trucks, H.B. Schlegel, G.E. Scuseria, M.A. Robb, J.R. Cheeseman, V.G. Zakrzewski, J.A. Montgomery Jr., R.E. Stratmann, J.C. Burant, S. Dapprich, J.M. Millam, A.D. Daniels, K.N. Kudin, M.C. Strain, O. Farkas, J. Tomasi, V. Barone, M. Cossi, R. Cammi, B. Mennucci, C. Pomelli, C. Adamo, S. Clifford, J. Ochterski, G.A. Petersson, P.Y. Ayala, Q. Cui, K. Morokuma, M.D. K., A.D. Rabuck, K. Raghavachari, J.B. Forseman, J. Cioslowki, J.V. Ortiz, B.B. Stefanov, G. Liu, A. Liashenko, P. Piskorz, I. Komaromi, R. Gomperts, R.L. Martin, D.J. Fox, T. Keith, M.A. Al-Laham, C.Y. Peng, A. Nanayakkara, C. Gonzalez, M. Challacombe, P.M.W. Gill, B. Johnson, W. Chen, M.W. Wong, J.L. Andreas, M. Head-Gordon, E.S. Replogle and J.A. Pople *Gaussian 98, Revision A.3* (1998). Gaussian, Inc., Pittsburgh PA
[13] NIST Chemistry WebBook www.nist.gov
[14] F. Remy, D. Macauhercot, I. Dubois, H. Bredohl and J. Breton, *J. Mol. Spec.* **159:** 122 (1993)
[15] M. Gruebele, M. Polak, G.A. Blake and R.J. Saykally, *J. Chem. Phys.* **85:** 6276 (1986)
[16] C.J. Reid, *Chem. Phys.* **210:** 501 (1996)
[17] P. Tosi, W.Y. Lu, R. Correale and D. Bassi, *Chem. Phys. Lett.* **310:** 180 (1999)
[18] P. Tosi, R. Correale, W.Y. Lu, S. Falcinelli and D. Bassi, *Phys. Rev. Lett.* **82:** 450 (1999)
[19] W.Y. Lu, P. Tosi and D. Bassi, *J. Chem. Phys.* **112:** 4648 (2000)
[20] D. Ascenzi, P. Franceschi, P. Tosi, D. Bassi, M. Kaczorowska and J.N. Harvey, *J. Chem. Phys.* **118:** 2159 (2003)
[21] J. Roithova, Z. Herman, D. Schroder and H. Schwarz, *Chem. Eur. J.* **12:** 2465 (2006)

Chapter 7: A New Experimental Design

7.1. Introduction

In Chapter 4 we saw that while it is possible to convert observed mass spectral intensities into reaction cross-sections with the present experimental design, doing so requires a considerable amount of mathematical treatment. Furthermore, although the present apparatus has the advantages of short collection times and good sensitivity, which has allowed the observation of a number of weak reaction channels, the amount of dynamical information that it presently yields is rather limited. In this chapter, solutions to the shortcomings of the present experimental design are considered, drawing in particular on the ideas of velocity map imaging (Section 1.4.8), position-sensitive detection (Section 1.4.7), second-order space-focussing (Section 1.5.2) and ion mirrors (Section 1.5.5) that were introduced in Chapter 1. As a result of these considerations, a new experimental design is proposed that, while still based on the principle of time-of-flight mass spectrometry to identify ions, provides improved mass resolution and facilitates the study of metastable fragmentation processes and the measurement of ion translational energies.

7.2. Metastable fragmentation

In the present context, metastable fragmentation may be defined as delayed unimolecular decay of a product of a bimolecular reaction before it reaches the detector. Daughter ions, of mass m, formed by the dissociation of parent ions, of mass M, may be divided into three classes, summarized in Table 7.1. Previous work by this author has observed evidence of the formation of metastable complexes in the collisions of some dications with hydrogenated target molecules. For instance, SF_n^{2+} (n=1,2) + $H_2O/NH_3/CH_4$ all show evidence of metastable complex formation. Attempts to model this behaviour have been made, with some success, by using a Monte-Carlo simulation but the unambiguous identification of the unimolecular decay channels involved proved impossible within the confines of the present apparatus.

	Parent dissociates...	Flight time
Type I	before repeller plate pulse	$t = t_m$
Type II	in source fields	$t_m < t < t_M$
Type III	in drift region	$t = t_M$

Table 7.1 Classification of daughter ions.

The difficulty in identifying metastable decay channels using a linear TOF mass spectrometer lies in the fact that if an ion's mass changes at some point between the source and the detector, the simple relationship between flight time and mass is broken. In a TOF mass spectrometer, ions with masses M and m have corresponding 'expected' flight times t_M and t_m respectively, but in the case of metastable fragmentation a daughter ion of mass m can be detected with a flight time anywhere between t_M and t_m. If fragmentation occurs before the repeller plate pulse is applied then daughter ions are indistinguishable from other ions of mass m, having flight time t_m. Conversely, if the parent ion decays in the drift region then daughter ions are recorded with the same flight time as intact parent ions, t_M (although this peak will be broadened by any kinetic energy release associated with the fragmentation). However, if fragmentation occurs at some point in the source fields of the spectrometer, then daughter ions may arrive at the detector at any time between t_m and t_M. Type II ions form a broad peak starting at t_m and

tailing off towards t_M. The maximum intensity of a Type II peak depends on the lifetime of the parent ion. In a Wiley-McLaren source, most Type II ions originate from dissociation events in the first electric field since ions pass through the short, high-field acceleration region very quickly. In a linear spectrometer, the presence of a metastable species is only particularly noticeable if the lifetime of the species is such that a large number of Type II daughter ions are formed, producing a characteristic broad peak in the spectrum (shown schematically in Figure 7.1; Figure 7.2 shows an observed example).

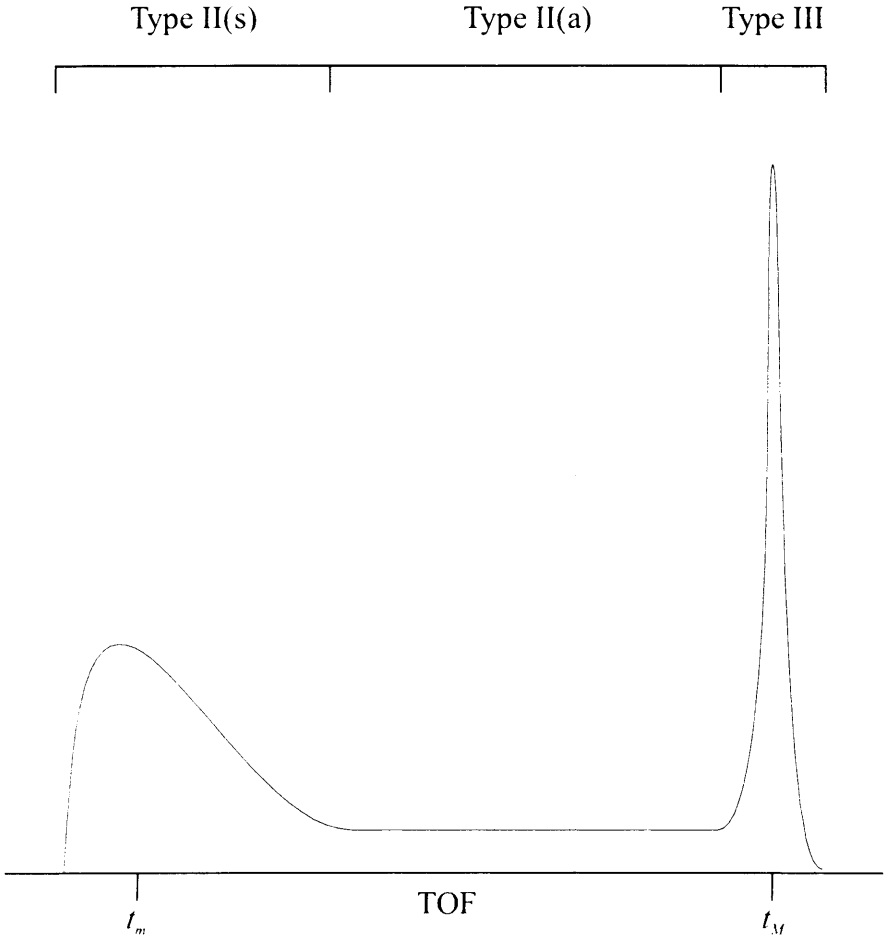

Figure 7.1 Schematic diagram of daughter ion signals resulting from single-step decay in a linear TOF-MS. The labels (s) and (a) refer to Type II ions formed in the source region (first electric field) and the acceleration region (second electric field) respectively. The intensity of the Type III signal relative to the Type II(s) signal increases with the lifetime of the parent ion. In a real spectrum other ion signals would cloud this picture, including parent ions that have not decayed (appearing as a sharp peak at t_M) and Type I daughter ions (appearing as a sharp peak at t_m).

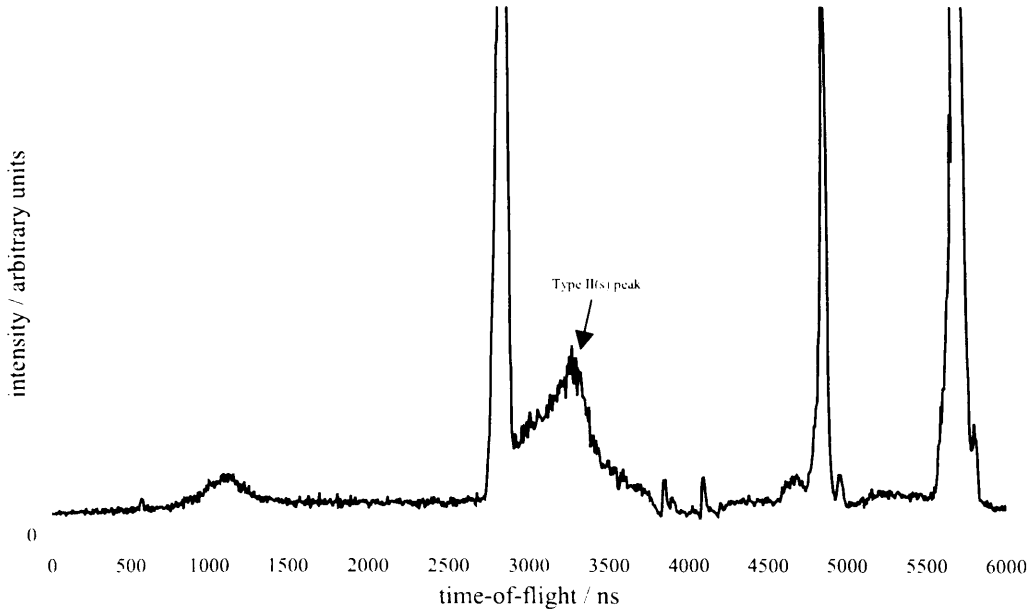

Figure 7.2 Example of an observed metastable feature occurring in the $SF_2^{2+} + H_2O$ collision system.

In most cases, we might expect the metastable parent ion to fragment in a single step, so that the process is appropriately described by simple rate equation:

$$\frac{dN_M}{dt} = -\frac{1}{\tau_M} N_M(t) \tag{7.1}$$

where N_M is the number of metastable parent ions of mass M and τ_M is their characteristic lifetime. In this context, t is the time since the population of parent ions is formed, which for simplicity we may assume to occur at a single time. Assuming that only one decay channel is present, the rate of formation of daughter ions equals the rate of decay of parent ions.

$$\frac{dN_m}{dt} = +\frac{1}{\tau_M} N_M(t) \tag{7.2}$$

The rate equation (7.1) has the solution:

$$N_M(t) = N_M(0)\exp\left(-\frac{t}{\tau_M}\right) \tag{7.3}$$

In the case of a single-step decay, therefore, one would expect the maximum intensity of a Type II peak to occur at t_m, regardless of the lifetime of the species, because the rate of formation of daughter ions (dN_m/dt) is greatest at $t = 0$. However, in collisions between SF_n^{2+} and the hydrogenated species noted above, the maximum intensity occurs at $t > t_m$. This indicates that a multiple step process is occurring, with the daughter ion m being formed via an intermediate species.

$$M \xrightarrow{\tau_1} \text{intermediate} \xrightarrow{\tau_2} m \tag{7.4}$$

Note that since each step involves a change of mass, additional products must be formed at each stage, but since both steps are unimolecular these do not affect rate calculations. If the lifetime associated with the first step is very long in comparison with that of the second step ($\tau_1 >> \tau_2$) then the rate of formation of m will peak rapidly, similarly to the single-step case. However, if the rate-determining step is the fragmentation of the intermediate, there is a delay before dm/dt peaks as the population of the intermediate builds up. This results in a shift in the position of the maximum intensity of the Type II(s) peak away from t_m and towards t_M. Indeed comparison of peaks produced using Monte-Carlo simulations with experimental data for SF_n^{2+} (n=1,2) + $H_2O/NH_3/CH_4$ suggests that a collision complex formed from the two reactants is stabilized by rapid ejection of a proton, thereby delaying its fragmentation to the detected products, although this has not been confirmed.

Identification of metastable decay channels using a normal TOF-MS is, then, at best difficult and at worst not possible. However, there are techniques that may be incorporated into a new design allowing the study of metastable fragmentation.

Type I ions may be distinguished by recording angular information, since if the parent complex lives significantly longer than its rotational period, its direction will not be correlated with that of the centre-of-mass of the system. This approach is used by Price et al. to determine reaction mechanisms.[1,2] Type II and III daughter ions, however, require retarding field analysis[3-6] to be unambiguously identified. Retarding field analysis is a means of mass analyzing products after they have traversed the drift

region, and an ion mirror can be employed to similar effect. A retarding field is positioned between the drift tube and the detector for which the potential difference can be scanned up or down. If the strength of the retarding field is set so high that no ions can reach the detector and then gradually reduced, each type of daughter ion will appear at a different voltage. This is effectively a way of re-mass analyzing products after fragmentation has occurred. Of course, the lifetime of the metastable parent ions must be sufficiently short that most have already decayed before they reach the retarding field. An ion mirror can be used as a retarding field analyzer, with ions being collected at the linear detector, or alternatively if the ions are reflected and collected at the reflectron detector then any peaks due to daughter ions will appear shifted in comparison with spectra taken with the linear instrument.

In a normal linear instrument, as is presently used, metastable decay channels can only be identified by fitting simulated spectra to experimental data. Although this may be feasible for a single-step process, it is of little use for multiple-step processes where there are additional decay lifetimes to be determined and one or more intermediate species that need to be identified. The only way, then, to distinguish fragmentation pathways with some certainty is to employ delayed, secondary, mass analysis, such as could be achieved by introducing an ion mirror into the apparatus.

7.3. Simulations

In order to calculate the appropriate parameters required to achieve second-order space-focussing, in either a linear or reflectron instrument, a *Mathematica*[7] script was developed. An annotated copy of this script is included in Appendix C. This script has been designed to be as flexible as possible, making it a powerful but general tool for determining ion trajectories in electric-field mass spectrometers. All experimental parameters may be user-defined: all electric fields (i.e. the spaces between electrodes and the applied voltages), both field-free regions, the reflection angle and ion properties. While the ultimate purpose of the script is to calculate the space-focussing properties of an experimental arrangement, along the way it also outputs positions, times and velocities at various stages of the spectrometer. This means that distances such as the x-displacement at the detector or the penetration distance into the ion mirror can also be extracted. Providing that any two variables are left undefined, the program searches for

values of these parameters that result in the first and second derivatives of the time-of-flight equations with respect to source position equalling zero at the centre of the source. However, since *Mathematica* calculates derivatives numerically, the large number of parameters that affect the flight time of an ion in a reflectron instrument, means that the programme requires a reasonable 'guess' to use as a starting point if it is to find a suitable solution. The script also includes the reflection angle θ, between the symmetry axes of the first and second drift tubes. This angle is not of great importance when calculating flight times, since the additional distance travelled is a factor of $1/\cos\theta$, which is only 1.004 for $\theta = 5°$. The reflection angle is much more important when calculating transverse displacement because this is proportional to $\sin\theta$, which equals 0.087. Of course, if the reflection angle is neglected then any x-displacement will be due only to the initial x-component of velocity, and the ion mirror reflects ions directly back towards the source.

This script has been used to find the physical dimensions required to produce second-order space-focussing when using linear source fields. The version included in Appendix C calculates such parameters for a reflectron instrument, while a simpler version does the same for a linear instrument. The total drift length can then be divided so that second-order space-focussing is achieved at both the linear detector and the reflectron detector.

The commercial ion optics modelling software *Simion3D*[8] is also useful for simulating ion trajectories, but is cumbersome when adjusting physical dimensions, since the electrode positions must be re-assigned and the electric fields re-evaluated. *Simion3D* was therefore only used as a visualization tool when optimum experimental parameters had been determined using the *Mathematica* program.

7.4. Design considerations

There are a number of aspects of a time-of-flight mass spectrometer that may be considered separately when working towards a modified design.

7.4.1. Reactant injection

At present, the apparatus injects the dication beam orthogonally to the time-of-flight axis and introduces the neutral reactant effusively from a needle mutually

perpendicular to both of these directions (i.e. along the y-axis). This set-up has resulted in the difficulty in comparing spectral intensities between different ions, with which the analysis developed in Chapter 4 has attempted to deal. The two problems with the effusive jet are that product ions are formed across a wide range of source positions (in the x-direction) and that the number density of the neutral reactant varies drastically across this range of positions. The most simple way to reduce the effect of changes in pressure would be to position the gas needle much further downstream so that most reactive events occurred far from the inlet position in a region across which the neutral number density remains roughly constant. This would only be a partial solution, however, and such a large interaction volume would simply not be compatible with velocity imaging. A far more effective solution is to replace the effusive jet with a molecular beam as the means of introducing the neutral reactant. Although the creation of a molecular beam poses more practical difficulties than an effusive jet, it is essential in imaging experiments on bimolecular reactions to minimize the dimensions of the interaction region between the ionic and neutral reactants. Furthermore, it may be necessary to inject the dication beam axially rather than orthogonally to reduce the transverse velocities of product ions, because the long total flight distance of the reflectron means that ions will diverge considerably from the time-of-flight axis and the detector will need to be as large as is practical to ensure good collection of ions. The advantages of axial injection of the dication beam are discussed further in Section 7.4.5.

7.4.2. Source optics

The source optics of the existing experiment may be adjusted by lengthening the acceleration region to provide second-order space-focussing, in accordance with Eland's set of solutions to Wiley-McLaren's equations (see Chapter 1). For instance, using the dimensions of 2.0 cm, 13.0 cm and 32.1 cm for the source, acceleration and field-free regions respectively gives second-order space-focussing (Figure 7.3).

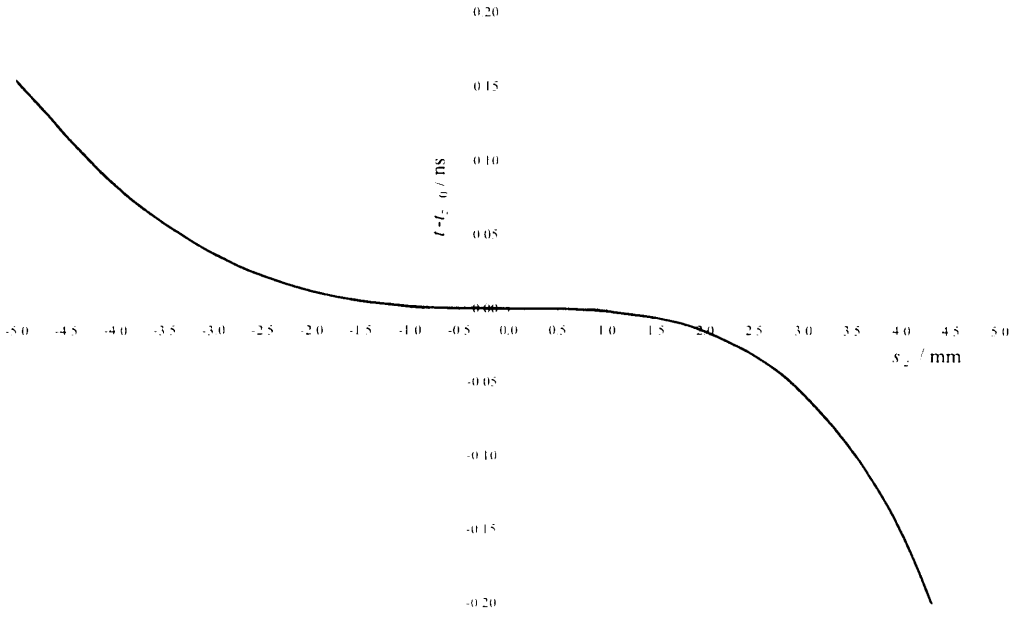

Figure 7.3 2nd-order space-focussing using a Eland-type source.

The focussing of the Eland source is such that across much of the source, differences in initial z-position have a negligible effect on flight times. This compares very favourably to a Wiley-McLaren spectrometer of the same total length (Figure 7.4).

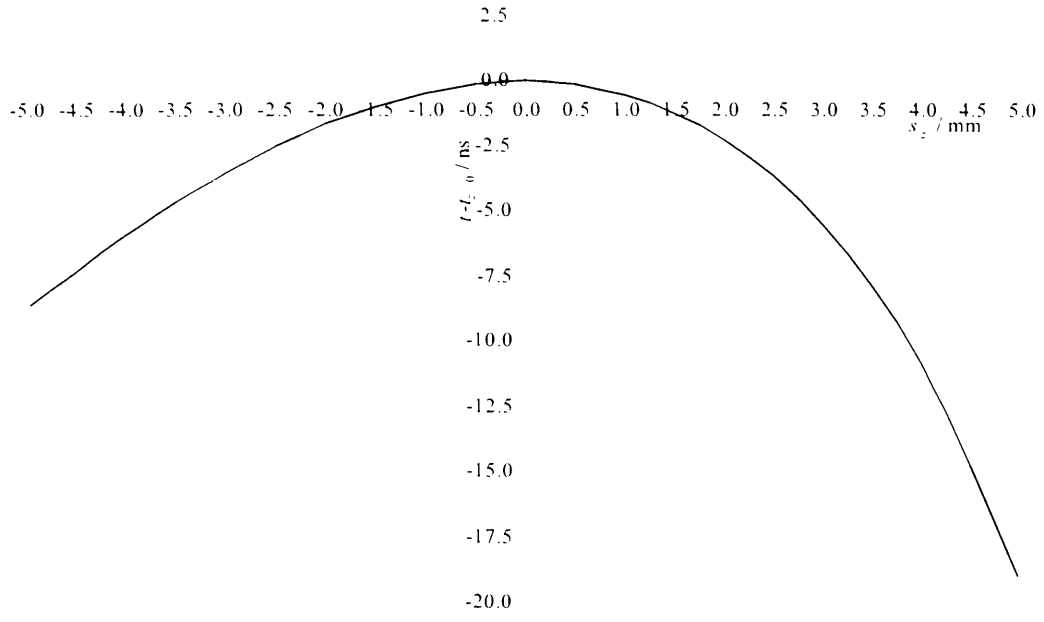

Figure 7.4 1st-order space-focussing using a Wiley-McLaren source.

An additional benefit of introducing an extended acceleration region is that velocity imaging optics, of the type used in the positive-particle collector of a VIPCO spectrometer (see Chapter 1), can be incorporated, with the ability to operate each arrangement independently of the other. In this manner, the source optics of the spectrometer comprise *both* grid and aperture electrodes and may be operated so as to achieve traditional time-of-flight behaviour (with second-order space-focussing) or velocity imaging.

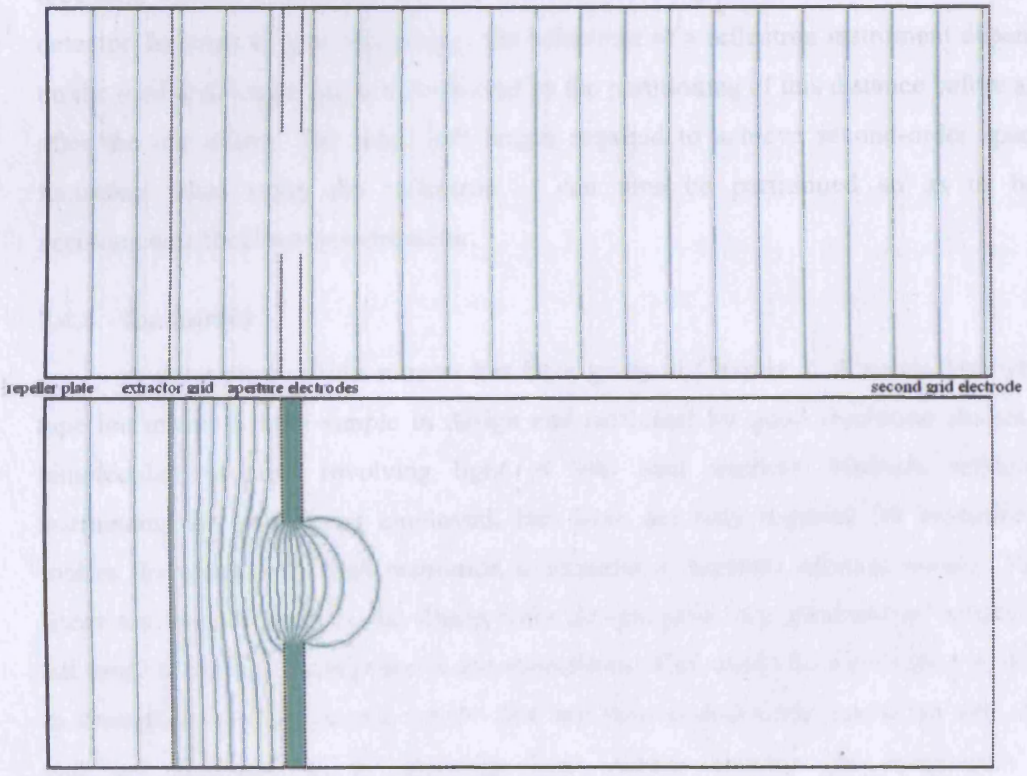

Figure 7.5 Equipotentials in the source and acceleration regions in normal mode (top image) and velocity imaging mode (bottom image).

In 'normal' operation, the aperture electrodes may be tuned to maintain a linear electric field across the acceleration region, while in VMI mode, the apertures are sufficiently distant from each grid electrode that the curvature of the electric field is not significantly curtailed (Figure 7.5). This combination of source optics is not possible

with the original VMI arrangement, because the first aperture electrode would be very close to the extractor grid, which would curtail the electrostatic lens.

It is perhaps surprising how close the voltages required for second-order focussing are to producing the same magnitude of electric field in both the source and acceleration regions. Indeed a single stage source in these dimensions is capable of reasonably good space-focussing, albeit of zeroth order.

7.4.3. Drift length

In a reflectron instrument the ion mirror can be tuned to provide good energy focussing without imposing a restriction on the drift length between the mirror and the detector. In terms of space-focussing, the behaviour of a reflectron instrument depends on the total drift length and is not affected by the partitioning of this distance before and after the ion mirror. The total drift length required to achieve second-order space-focussing when using the reflectron can thus be partitioned so as to best accommodate the linear spectrometer.

7.4.4. Ion mirror

A description of ion mirrors has been given in Chapter 1. A single Mamyrin-type ion mirror is both simple in design and sufficient for good resolution studies of bimolecular reactions involving light (< 100 amu species). Multiple reflectron instruments are sometimes employed, but these are only required for biomolecule studies for which very high resolution is required to separate adjacent masses. Non-linear ion mirrors, such as the Zhang-Enke design, give very good energy resolution, but tend to amplify divergence in ion trajectories. This would be a particular problem in crossed-beam experiments, where ions my have considerable transverse velocities and are produced in a relatively large source volume (in comparison to photodissociation experiments).

7.4.5. Detector size

When considering the size of detector required to ensure complete collection of all product ions, we must determine the range of positions that product ions may have when reaching the plane of the detector. There are four factors that affect the final position of an ion:

i) the initial transverse (x or y) velocity;

ii) the initial position;

iii) the flight time;

iv) the additional transverse (x) velocity imparted by the ion mirror.

The initial position of an ion is only important if product ions are formed over a large range perpendicularly to the time-of-flight axis, as is the case with the present experimental arrangement. The introduction of either axial injection of the dication beam or a molecular beam would render the range of initial ion positions of little importance.

The flight times of ions are determined by the electric fields employed, which are chosen to provide good mass resolution, although if necessary the applied voltages could be increased to reduce flight times. The transverse displacement of an ion is, of course, the product of its initial transverse velocity and its flight time, plus a contribution from the transverse acceleration imparted by the ion mirror, and is, neglecting variations in initial position, what determines where a given ion hits the detector. The transverse acceleration imparted by the ion mirror is of course proportional to the reflection angle, so the reflection angle should be as small as possible whilst preventing the source optics from interfering with the path to the detector. When using the reflectron settings listed in Table 7.2, a reflection angle of approximately 7° is sufficient for this purpose and a detector 100 mm in diameter will comfortably collect ions with an initial LAB frame energy of up to 5 eV in the $\pm x$-direction (kinetic energy in the z-direction does not affect the transverse displacement of an ion). The LAB frame velocity of product ions depends on their speed in the centre-of-mass frame (which is dependent on their masses and the energy released by the reaction), the collision energy of the system and the direction of the product COM velocities with respect to the motion of the centre-of-mass, as demonstrated in Chapter 2. The maximum LAB frame velocity in the x-direction, can thus be reduced by using axial injection of the dication beam, so that the motion of the centre-of-mass is in the z-direction rather than the x-direction. This reduces the maximum LAB frame x-velocity for an ion j from $v_{CM} + w_j$ to simply w_j, where w_j is the COM speed of the ion, but the range remains $\pm w_j$ in both cases. By eliminating v_{CM} from the LAB frame x-

velocity, the ideal position of the detector is not affected by the collision energy of the system.

7.4.6. Position-sensitive detection

Traditionally, imaging experiments such as ion-imaging and VELMI have used a phosphor screen in front of a CCD camera to achieve position-sensitive detection. This technique has two principal shortcomings, viz. a phosphor screen has a low repeat rate by the very nature of phosphorescence, and the electronic captured image must be subjected to considerable mathematical treatment to recover the 3D distribution of product ions. Both of these problems are overcome by the use of a delay-line anode detector, such as is employed by Price et al[9], which records the arrival position of each ion on an event-wise basis. This will allow the apparatus to record two-dimensional coincidence information, further enhancing its multiplexing ability.

7.4.7. Summary

By collating the conclusions reached in the preceding sections, we can propose a design for a powerful time-of-flight mass spectrometer, based on the one currently in use but with a number of major modifications. The source optics may be adapted from the Wiley-McLaren arrangement to an arrangement capable of second-order space-focussing. Aperture electrodes capable of velocity imaging may be added, without affecting the linear-field operation. A two-stage Mamyrin ion mirror may be added to further improve mass resolution and allow analysis of the decay of metastable ions. The reflectron set-up also permits second-order space-focussing.

Suggested parameters for an improved spectrometer are shown in Table 7.2. These parameters afford second-order space-focussing at both the linear detector and the reflectron detector. In linear mode, the grids that comprise the ion mirror are held at the same potential as the drift tube and the total drift length equals the distance between the end of the acceleration region and the entrance to the ion mirror plus the length of the ion mirror. It is only total drift length that affects the space-focussing properties of the spectrometer so that in reflectron mode, the partitioning of this into the first and second drift regions is unimportant; the ratio between l_{ff1} and l_{ff2} is chosen so that the ion mirror can be fitted in while retaining second-order focussing in linear mode.

parameter	setting (linear mode)	setting (reflectron mode)
l_s	20 mm	20 mm
ΔV_s	+400 V	+400V
l_a	130 mm	130 mm
ΔV_a	+2717 V	+2803 V
l_{tf}(total drift length)	321 mm	(160 + 410) mm
l_t	n/a	15 mm
ΔV_t	n/a	-526 V
l_k	n/a	125 mm
ΔV_k	n/a	-6645 V

Table 7.2 Suggested parameters for an improved spectrometer.

When not in use, the aperture electrodes must be tuned so as to maintain a linear field in the acceleration region. In velocity imaging mode, voltages of -1.76 E_s and -6.47 E_s on the first and second apertures respectively achieves good velocity imaging.

A scale diagram of the proposed design is shown in Figure 7.6.

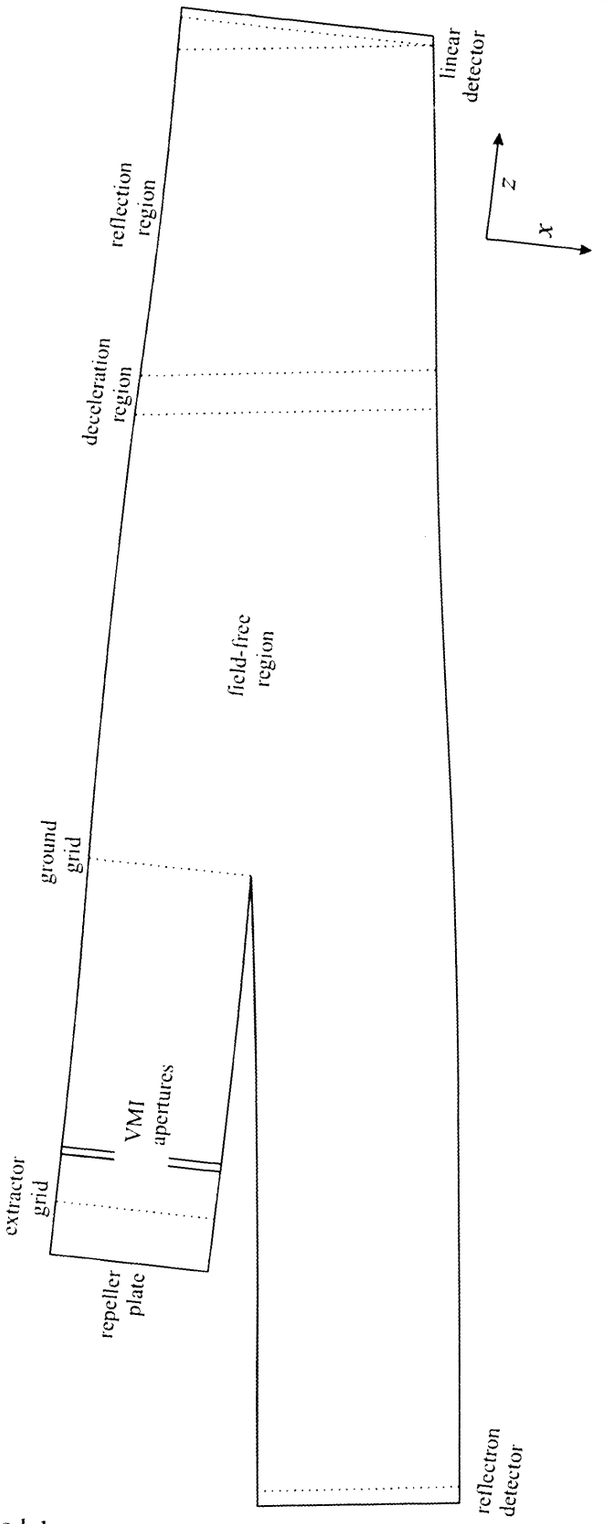

Figure 7.6 Proposed design of a new reflectron TOF mass spectrometer.

7.5. Conclusion

In this chapter we have considered in turn a number of features that are important in the operation of a TOF mass spectrometer and put them together to arrive at a modified design for the present experimental apparatus. Should this design be put into practice in the future, the experiment would become a much more powerful tool for the study of dication reactions. Replacing the effusive injection of the neutral reactant with a molecular beam would, by greatly reducing the reaction volume, make the processing of measured intensities much simpler. Experiments using the aperture electrodes of the re-designed source optics would be able to measure ion energies and thus clarify the electronic states of product ions, which at present can only be guesstimated, and also allow the energy liberated by each reaction channel to be calculated. The use of the reflectron would provide improved mass resolution, which at present can be barely adequate when observing light species containing hydrogen (for example, HCl^{2+}), and allow the past observations of metastable decay to be revisited and better understood. .

7.6. References

[1] S.M. Harper, W.-P. Hu and S.D. Price, *J. Chem. Phys.* **120:** 7245 (2004)
[2] S.M. Harper, W.-P. Hu and S.D. Price, *J. Chem. Phys.* **121:** 3507 (2004)
[3] J.R. Stairs, T.E. Dermota, E.S. Wisniewski and A.W. Castleman, *Int. J. Mass Spectrom.* **213:** 81 (2002)
[4] J. StahlZeng, F. Hillenkamp and M. Karas, *Eur. Mass Spectrom.* **2:** 23 (1996)
[5] C.R. Ponciano and E.F. da Silveira, *J. Phys. Chem. A* **106:** 10139 (2002)
[6] D. Ioanoviciu, *Rapid Commun. Mass Spectrom.* **9:** 985 (1995)
[7] *Mathematica* v.5, copyright Wolfram Research, 1999-2003
[8] *Simion3D*, copyright Bechtel BWXT Idaho, 1999
[9] S.M. Harper, S.W.P. Hu and S.D. Price, *Meas. Sci. Technol.* **13:** 1512 (2002)

Précis

This thesis has described the development and successful implementation of a new methodology for the analysis of measured ion intensities in an orthogonal time-of-flight mass spectrometer. In addition to providing the ability to extract reaction cross-sections for all ionic products of bimolecular reactions, the framework of this methodology is transferable to other apparatus employing an effusive gas inlet and the detailed understanding of the source environment gained will make the development of an analytical model for any new spectrometer much simpler than would have otherwise been the case.

Observations of a number of dication-neutral collision systems has yielded, in addition to electron transfer processes,two bond-forming reactions that produce a doubly charged product. The cross-sections of these reaction channels are weak, approximately two orders of magnitude weaker than electron transfer, but nonetheless clearly and unambiguously visible in TOF spectra. Few examples of such doubly charged chemical products have been reported in the literature, but the very different energetics of the systems reported here that produce ArS^{2+} and CCl^{2+} strongly suggests that energetics requirements are not nearly as restrictive as has been previously thought and perhaps the scarcity of long-lived dication states is the reason behind limited observation of doubly charged products.

Finally, a new design for a reflectron time-of-flight mass spectrometer has been proposed, that will be much more powerful than the present apparatus providing improved mass resolution and the ability to measure energy and angular distributions simultaneously and on an event-wise basis. Implementation of this design has the potential to overcome all the difficulties and limitations that have been encountered with the present experiment over recent years. We may thereby look to continue to develop our understanding of the reactive chemistry of atomic and molecular dications in years to come.

Appendix A

Wiley and McLaren derived their time-of-flight equations in terms of energies[1], rather than accelerations and velocities that were used to describe flight times in Chapter 2. This Appendix outlines how Wiley and McLaren reached their focussing conditions for TOF mass spectrometers, and the subsequent observations made by Eland[2].

An ion of charge q with initial energy U_0 will increase its energy as it passes through an electric field of magnitude E, such that at the point of detection its energy will be the sum of its initial energy and the energy gained in the source (s) and acceleration (a) regions:

$$U = U_0 + qd_s E_s + qd_a E_a \tag{A.1}$$

Recalling the relationship between speed and energy:

$$v^2 = \frac{2U}{m} \tag{A.2}$$

The time taken to traverse the source region may be expressed as:

$$t_s = \frac{\sqrt{\frac{2U_0}{m} + \frac{qE_s d_s}{m}} \pm \sqrt{\frac{2U_0}{m}}}{\frac{qE_s}{m}}$$

$$= \frac{\sqrt{2m}}{qE_s}\left(\sqrt{U_0 + qE_s d_s} \pm \sqrt{U_0}\right) \tag{A.3}$$

where the + and − signs correspond to initial velocities directed away and towards the detector, respectively. Using the same principles:

$$t_2 = \frac{\sqrt{2m}}{qE_2}\left(\sqrt{U} - \sqrt{U_0 + qE_1 l_1}\right) \tag{A.4}$$

and:

$$t_3 = \frac{l_3}{\sqrt{2U/m}} = l_3 \frac{\sqrt{2m}}{2\sqrt{U}} \tag{A.5}$$

For simplicity, we will now assume that $U_0 = 0$ so that Equation (A.1) becomes:

$$U = q(l_1 E_1 + l_2 E_2) \tag{A.6}$$

and also define a parameter k:

$$k = \frac{\frac{1}{2} l_1 qE_1 + l_2 qE_2}{\frac{1}{2} l_1 qE_1} \tag{A.7}$$

In subsequent equations it is useful to note two other equivalent expressions of k:

$$k = 1 + \frac{l_2 E_2}{\frac{1}{2} l_1 E_1} \tag{A.8}$$

$$k = \frac{U}{\frac{1}{2} l_1 qE_1} \tag{A.9}$$

Substituting Equation (A.9) into Equation (A.3) gives us:

$$\begin{aligned} t_1(U_0 = 0) &= \sqrt{\frac{ml_1}{qE_1}} \\ &= \tfrac{1}{2} l_1 \sqrt{\frac{1}{\frac{1}{2} l_1 qE_1}} \sqrt{2m} \\ &= l_1 \sqrt{k} \sqrt{\frac{m}{2U}} \end{aligned} \tag{A.10}$$

Similarly Equation (A.4) becomes:

$$
\begin{aligned}
t_1(U_0 \neq 0) &= \frac{\sqrt{2m}}{qE_1}\left(\sqrt{U} - \sqrt{\tfrac{1}{2}l_2 qE_2}\right) \\
&= \frac{\sqrt{2m}}{qE_1}\left(\sqrt{U} - \sqrt{\frac{U}{k}}\right) && \leftarrow \text{using } \tfrac{1}{2}l_2 qE_2 = \frac{U}{k} \\
&= \frac{\sqrt{2m}}{qE_1}\sqrt{\frac{U}{k}}\left(\sqrt{k}-1\right) \\
&= \sqrt{\frac{m}{2U}}\frac{2U}{qE_1\sqrt{k}}\left(\sqrt{k}-1\right) && \leftarrow \text{using } \sqrt{2U} = \frac{2U}{\sqrt{2U}} \\
&= \sqrt{\frac{m}{2U}}\frac{2\left(\tfrac{1}{2}l_2 qE_2 k\right)}{qE_1\sqrt{k}}\left(\sqrt{k}-1\right) \\
&= \sqrt{\frac{m}{2U}}\frac{2l_1\sqrt{k}}{k-1}\left(\sqrt{k}-1\right) && \leftarrow \text{since } k = 1 + \frac{l_1 E_1}{\tfrac{1}{2}l_2 E_2} \Rightarrow \frac{\tfrac{1}{2}E_2}{E_1} = \frac{l_1}{k-1} \\
&= \sqrt{\frac{m}{2U}}\frac{2l_1\sqrt{k}\left(\sqrt{k}-1\right)}{\left(\sqrt{k}+1\right)\left(\sqrt{k}-1\right)} && \leftarrow \text{using } (k-1) = \left(\sqrt{k}+1\right)\left(\sqrt{k}-1\right) \\
&= \sqrt{\frac{m}{2U}}\frac{2l_1\sqrt{k}}{\sqrt{k}+1}
\end{aligned}
\tag{A.11}
$$

Finally, the drift time is more simple:

$$
\begin{aligned}
t_2 &= \frac{l_2}{\sqrt{2U/m}} \\
&= \sqrt{\frac{m}{2U}}l_2
\end{aligned}
\tag{A.12}
$$

So, by adding the time spent in each stage, we arrive at the total flight time:

$$
t_{\text{total}} = \sqrt{\frac{m}{2U}}\left(l_2\sqrt{k} + \frac{2l_1\sqrt{k}}{\sqrt{k}+1} + l_2\right)
\tag{A.13}
$$

Now to find the position at which ions of differing initial position pass each other, we set $dt_{\text{total}}/dz = 0$, which gives the point where first-order space-focussing occurs:

$$t_{\mathrm{ff}} = t_{\mathrm{S}} k^{\frac{1}{2}} \left(1 - \frac{l_{\mathrm{a}}}{\frac{1}{2} l_{\mathrm{S}} (k + k^{\frac{1}{2}})} \right) \tag{A.14}$$

Alternatively, the total flight time can be expressed in terms of velocities and accelerations, as favoured by Eland:

$$t_{\mathrm{total}} = \frac{v_1 - v_0}{a_{\mathrm{s}}} + \frac{v_2 - v_1}{a_a} + \frac{l_{ff}}{v_2} \tag{A.15}$$

Since the acceleration is inversely proportional to the ion mass, the turnaround time v_0 / a_{s} is directly proportional to the initial ion momentum. The velocities acquired by the first and second grids are:

$$v_1^2 = v_0^2 + 2a_{\mathrm{s}} \left(\tfrac{1}{2} l_{\mathrm{s}} - \Delta z \right) \tag{A.16}$$

$$v_2^2 = v_1^2 + 2a_{\mathrm{a}} l_{\mathrm{a}} \tag{A.17}$$

where Δz is the z-displacement of the initial ion position from the centre of the source, positive values being towards the detector.

References

[1] W.C. Wiley and I.H. McLaren, *Rev. Sci. Instrum.* **26:** 1150 (1955)

[2] J.H.D. Eland, *Meas. Sci. Technol.* **4:** 1522 (1993)

Appendix B

The following *Mathematica* script was written to implement the analysis derived in Chapter 4. A number of annotations are included in the script, delimited "(*...*)" and highlighted in blue; some further explanatory notes are included in text boxes. Outputs have been omitted.

```
(*Assumes product ions are singly charged. For a doubly charged product you
need to insert a factor of 0.5 in the function L1 or L2 as appropriate.
x and z are both zero at the centre of the source region.
Check all inputs highlighted in green are correct before running.*)

(*Constants*)
Na=6.02 10^23;
q=1.602 10^-19;
amu=1.66 10^-27;

(*Masses of dication and neutral*)
md=36;
mn=28;
(*Masses of product ions immediately after collision*)
m1=35;
m2=29;

Elab=.;        (*lab frame collision energy (2x source block voltage) in eV*)
theta=.;       (*angle of the initial product velocity relative to the dication
               velocity vector, in the xz plane*)

vd[E_]:=(10^-4Sqrt[2 E q/md / amu]);     (*dication velocity in cm/μs*)
vcom[E_]:=(md vd[E]/(md+mn));            (*velocity of the com in cm/μs*)

(*COM frame collision energy in eV*)
Ec[E_]:=(0.5 ((md mn) amu/(md+mn)) (vd[E] 10000)^2)/q;

KER[E_]:=Ec[E]+3.8;
```

The exothermicity of the reaction is assumed to be close to the centre of the Reaction Window (~3.8eV). The kinetic energy release is here defined as the sum of the exothermicity and the com frame collision energy.

```
(*com frame x-velocities of product ions in cm/μs*)
v1com[K_]:=(10^-4Sqrt[K q/(amu(0.5 m1 +(0.5 m1^2/m2)))])
v2com[K_]:=(10^-4 Sqrt[K q/(amu(0.5 m2+(0.5 m2^2/m1)))])

(*lab frame x-velocities of product ions in cm/μs*)
vx1lab[E_,K_,theta_]:=(vcom[E]+(Cos[theta Pi/180] v1com[K]))
vx2lab[E_,K_,theta_]:=(vcom[E]+(Cos[theta Pi /180]v2com[K]))
```

```
(*spectrometer details*)
sourcelength= 0.02; (*in m*)
acclength=0.01;      (*in m*)
aperturelength=0.07; (*in m*)
driftlength=0.295;   (*in m*)
sourcepd=400;        (*volts*)
accpd=1230;          (*volts*)
extractordiam=3;     (*in cm*)
aperturediam=2.6;    (*in cm*)
detectordiam=4;      (*in cm*)
```

In addition to the source details, the diameters of the detector and the unused optics in the drift tube are required for calculating possible ion

```
accsource[m_]:=(sourcepd q/(m amu sourcelength)); (*source region
                                                   acceleration in m/s^2*)
vextractor[m_]:=(Sqrt[2 accsource[m]sourcelength/2]); (*z-velocity at first grid
                                                   in m/s*)
tsource[m_]:=(vextractor[m]/accsource[m]); (*source region flight time in s*)

accacc[m_]:=(accpd q/(m amu acclength));     (*acceleration region
                                              acceleration in m/s^2*)
vgnd[m_]:=(Sqrt[vextractor[m]^2 + 2 accacc[m]acclength]);  (*z-velocity at
                                              2nd grid in m/s*)
tacc[m_]:=((vgnd[m]-vextractor[m])/accacc[m]); (*acceleration region flight
                                              time in s*)
taperture[m_]:=(aperturelength/vgnd[m]) (*time passing through drift tube
                                              optics in s*)
tdrift[m_]:=(driftlength/vgnd[m]); (*total field-free region flight time in s*)
```

(*source position limits to pass obstacles*)

Here we calculate the upper and lower limits of x for an ion to pass through the first grid (the 2nd grid is wider and is not a limiting factor) OR the unused optics in the drift tube OR hit the detector. lowerlimit and upperlimit are then the limits to successfully do all three.

```
extractorlowerlimit[v_,m_,E_,K_]:=((-0.5 extractordiam)-(v tsource[m] 10^6))
extractorupperlimit[v_,m_,E_,K_]:=((0.5 extractordiam)-(v tsource[m] 10^6))

aperturelowerlimit[v_,m_,E_,K_]:=((-0.5 aperturediam)-(v (tsource[m]+tacc[m]
      +taperture[m]) 10^6))
apertureupperlimit[v_,m_,E_,K_]:=((0.5 aperturediam)-(v (tsource[m]+tacc[m]
      +taperture[m]) 10^6))

detectorlowerlimit[v_,m_,E_,K_]:=((-0.5 detectordiam)-(v (tsource[m]+tacc[m]
      +tdrift[m]) 10^6))
detectorupperlimit[v_,m_,E_,K_]:=((0.5 detectordiam)-(v (tsource[m]+tacc[m]
      +tdrift[m]) 10^6))

lowerlimit[v_,m_,E_,K_]:=Max[extractorlowerlimit[v,m,K,E],aperturelowerlimit
      [y, m,K,E],detectorlowerlimit[v,m,K,E]]
upperlimit[v_,m_,E_,K_]:=Min[extractorupperlimit[v,m,K,E],apertureupperlimit
```

```
[v,m,K,E],detectorupperlimit[v,m,K,E]]
```

Now we calculate the image lengths of the dication and the two products.

```
L[v_,m_,E_,K_]:=upperlimit[v,m,K,E]-lowerlimit[v,m,K,E]     (*imaged length
                                                             in cm*)
Ld[v_,m_,E_,K_]:=L[vd[E],md/2,E,K] (*/2 denotes double charge*)
L1[v_,m_,E_,K_]:=L[vx1lab[E,K],m1,E,K]     (*insert /2 if product is doubly
                                            charged*)
L2[v_,m_,E_,K_]:=L[vx2lab[E,K],m2,E,K]
```

Some more definitions of variables.

```
x=.;
t=.;
r0=1.5; (*minimum distance between gas needle and dication beam in cm*)
inlet=-3.0; (*x-position of gas inlet in cm*)
xd0=-3.7; (*position of the front of the dication beam front at t=0 in cm*)
T=9.5; (*pulse off time in μs*)
xs1=-3.7;     (*the physical width of the source region
xs2 =2.5;     i.e. where you allow ions to be formed*)

Nn=((Cos[ArcTan[(x-inlet)/r0]])^1/((x-inlet)^2+r0^2));
(*Nn is the function describing the number density distribution of the neutral
gas. In the form {Nn=(Cos[ArcTan[(x-a)/b]]^3)/b^2}, a = inlet and b = r0*)

xd[t_,E_]:=((vd[E] t)+xd0) (*position of dication beam front with time*)
```

We now need to find the time-dependent imaged length, $l(t)$.

```
(*l(t) based solely on the various aperture dimensions*)
xmintheory[t_,v_,m_,E_,K_]:=(lowerlimit[v,m,E,K]+v (t-T))
xmaxtheory[t_,v_,m_,E_,K_]:=(upperlimit[v,m,E,K]+v (t-T))

(*now checking whether xd is a limiting factor*)
xmindic[t_,v_,m_,E_,K_]:=Min[xmintheory[t,v,m,E,K],xd[t,E]]
xmaxdic[t_,v_,m_,E_,K_]:=Min[xmaxtheory[t,v,m,E,K],xd[t,E]]

(*now checking whether width of source is a limiting factor*)
xmindima[t_,v_,m_,E_,K_]:=(If[xmindic[t,v,m,E,K]≤xs1,xs1,xmindic[t,v,m,E,K]])
xmaxdima[t_,v_,m_,E_,K_]:=(If[xmaxdic[t,v,m,E,K]≤xs1,xs1,xmaxdic[t,v,m,E,K
                                                                  ]])
xmindimb[t_,v_,m_,E_,K_]:=(If[xmindima[t,v,m,E,K]≥xs2,xs2,xmindima[t,v,m,E
                                                                  ,K]])
xmaxdimb[t_,v_,m_,E_,K_]:=(If[xmaxdima[t,v,m,E,K]≥xs2,xs2,xmaxdima[t,v,m
                                                                  ,E,K]])

xmin[t_,v_,m_,E_,K_]:=(xmindimb[t,v,m,E,K])
xmax[t_,v_,m_,E_,K_]:=(xmaxdimb[t,v,m,E,K])
```

xmin and xmax are the limiting x-values of $l(t)$ in cm.

```
Nnbar[t_,v_,m_,E_,K_]:=(If[xmax[t,v,m,E,K]>xmin[t,v,m,E,K],NIntegrate[Nn,{x,
xmin[t,v,m,E,K],xmax[t,v,m,E,K]}],0])
```

Nnbar is the average number density of the neutral gas between xmin and xmax (NB a factor of $1/l$ is omitted and recovered later).

```
Emin=5;
Emax=16;
```

Defines the lab frame collision energy range.

```
intlNnbar[v_,m_,E_,K_]:=(NIntegrate[Nnbar[t,v,m,E,K],{t,0,T},PrecisionGoal→
        2,AccuracyGoal→1])
```

intlNnbar is the integral of Nnbar with respect to time between 0 and T. (NB a factor of l is omitted).

```
(*intlNbar is thus: Int[Int[Nn]dx]dt. Note tnat for speed the factors of 1/l in
Nnbar and l in intlNnbar have been omitted*)
```

```
(*incorporating
scattering*)
```

These functions describe the angular scattering of the products. The first pair are Lorentzian profiles which approximate data for SET reactions. The second pair are symmetric, but normalized to the Lorentzians. Of course any functional may be used.

```
f1[m_,E_,K_]:=(NIntegrate[intlNnbar[vx1lab[E,KER[E],theta],m,E,K]*(1000/(30
        Pi(1+((theta-10)/30)^2))),{theta,0,180},PrecisionGoal→2,AccuracyGoal
        →1])
f2[m_,E_,K_]:=(NIntegrate[intlNnbar[vx2lab[E,KER[E],theta],m,E, K]*(1000/(30
        Pi (1+((theta-70)/30)^2))),{theta,0,180},PrecisionGoal→2,AccuracyGoal
        →1])

(*
f1[m_,E_,K_]:=(NIntegrate[intlNnbar[vx1lab[E,KER[E],theta],m,E,K]*(3.04),
        {theta,0,180},PrecisionGoal\[Rule]2,AccuracyGoal→1])
f2[m_,E_,K_]:=(NIntegrate[intlNnbar[vx2lab[E,KER[E],theta],m,E,K]*(3.04),
        {theta,0,180},PrecisionGoal→2,AccuracyGoal→1])
  *)
```

```
(*INTENSITIES*)
```

In order to obtain reaction cross-sections, experimental data must be entered. Only one example is included here.

```
(* CO+ *)
R[m2,5]=5.43; R[m2,6]=6.73; R[m2,7]=7.09;
R[m2,8]=6.82; R[m2,9]=7.19;R[m2,10]=7.25;
R[m2,11]=8.56;R[m2,12]=9.86; R[m2,13]=10.9;
R[m2,14]=11.1;R[m2,15]=11.6;R[m2,16]=13.0;
```

Based on what we learnt in Chapter 4, we finally have our reaction cross-section:

$$\sigma' = \frac{R^{\text{true}} L_{\text{d}}}{v_{\text{d}} f}$$

```
(*CROSS SECTIONS*)
sigma[E_,K_]:=(R[m,E]*Ld[vd[E],md,E,KER[E]])/(vd[E]*f1[35,E,KER[E]])

(*IMPORTANT: m1 & m2 (inputted at the start) are the MASSES of products
IMMEDIATELY AFTER COLLISION (these are used to calculate velocities).
However, when calling f1 & f2 (above) use the MASS-TO-CHARGE RATIO of
the FINAL products*)
```

Appendix C

The following *Mathematica* script was written to calculate the space-focussing properties of a reflectron instrument. Variables have been labelled in the manner adopted in the thesis, but with some differences due to formatting constraints. Outputs have been omitted and explanatory notes are included in text boxes.

```
a=.
ls=.
la=.
lff1=.
lt=.
lk=.
lff2=.
lp=.
accs=.
acca=.
acct=.
acck=.
accp=.
dvs=.
dva=.
dvt=.
dvk=.
dvp=.

z=.
m=.
q=.
ts=.
a = 0.5 ls - z
theta=8 3.141592654/ 180

accs=q dvs/(m ls)
ts= (2 accs a)^0.5 /accs
acca = q dva/(m la)
ta = (((2 accs a) +(2 acca la))^0.5 -(2 accs a )^0.5)/acca
tff1 = lff1/(((2 accs a)+(2 acca la))^0.5)
acct=q dvt / (m lt)
tt=((((2 accs a)+(2 acca la))(Cos[theta])^2+(2 acct lt))^0.5-(((2 accs a)+(2 acca
      \la))(Cos[theta])^2)^0.5)/acct
acck=q dvk/(m lk)
tk=-((((2 accs a)+(2 acca la))(Cos[theta])^2+(2 acct lt))^0.5)/acck
tff2=lff2/((((2 accs a)+(2 acca la))(Cos[theta])^2)^0.5)
accp= q dvp/(m lp)
```

Defines lengths (l), accelerations (acc), potential differences (dv) and other parameters. "=." defines a variable without assigning a value to it.

a is the *z*-distance that an ion travels through the first electric field; z is the initial *z*-displacement of an ion from the centre of the source.

Calculates the acceleration produced by each electric field and the flight time of an ion through each stage of the spectrometer. These constituent flight times allow the total flight time to be calculated.

z=0
ls=0.02
la=0.13
lff1=0.16
lt=0.015
lk=0.125
lff2=0.41
lp=0.0065
dvs=400
dva=2802.9
dvt=.
dvk=.
dvp=100
diff2
diff1

FindRoot[{diff2==0,diff1==0},{dvt,-440},{dvk,-6617}]

Here the user can input the values of experimental parameters, leaving to undefined. SI units are used.

Instructs the prog find a solution wh diff1=diff2=0, by adjusting two var Each variable mu inputted with an estimate value; du the large number variables involved calculation, the es must be reasonab if the program is a solution.

By assigning the values outputted by the program to the appropriate variables, and plotting t as a function of z, the space-focussing properties of the apparatus can be visualized.